# Hyper-resolved fluorescence microscopy with STM

Benjamin Doppagne

Benjamin Doppagne. Hyper-resolved fluorescence microscopy with STM. Physics [physics]. Université de Strasbourg, 2020. English. NNT : 2020STRAE005 . tel-03967816

**HAL Id: tel-03967816**

**https://theses.hal.science/tel-03967816v1**

Submitted on 1 Feb 2023

# UNIVERSITÉ DE STRASBOURG

École doctorale
Physique, chimie-physique
ED 182
Université de Strasbourg

*ÉCOLE DOCTORALE Physique et Chimie-Physique (ED182)*

**Institut de Physique et Chimie des Matériaux de Strasbourg**

**THÈSE** présentée par :

**Benjamin DOPPAGNE**

soutenue le : **03 février 2020**

pour obtenir le grade de : **Docteur de l'université de Strasbourg**

Discipline/ Spécialité : Nano-Physique

# Hyper-Resolved Fluorescence Microscopy with STM

**THÈSE dirigée par :**

**M. SCHULL Guillaume** Directeur de Recherche, IPCMS-CNRS, Université de Strasbourg

**RAPPORTEURS :**

**M. LOUNIS Brahim** Professeur, LP2N-CNRS, Université de Bordeaux

**M. NATTERER Fabian** Professeur, Physik-Institut, Université de Zurich

---

**AUTRES MEMBRES DU JURY :**

**Mme BOER-DUCHEMIN Elizabeth** Professeure, ISMO-CNRS, Université Paris-Sud

**M. ROBERT Vincent** Professeur, Institut de Chimie-CNRS, Université de Strasbourg

**M. JACQUES Vincent** Chargée de Recherche, L2C-CNRS, Université de Montpellier

# Acknowledgements

If someone had told me when I was young that I would end up by doing a thesis in Physics, I would not have believed it. If some people know early what they want to do, my path was slightly non-linear, but finally after so many year of studies and almost four years here at the IPCMS I can say : I am a doctor. My biggest concern before starting my thesis was to be in a pleasant environment, and after my first discussion with Guillaume, I had an excellent feeling. In the end, I feel that I had made the right decision to join his team. Even though this manuscript is my thesis, nothing would have been possible without the fantastic peoples whom I was fortunate to work with. During those three years of PhD, I had the feeling to work in a family business with perfectly complementary members, and I would like to start by thanking them in this (too) short acknowledgement section.

First, I would like to thank "the dad" Guillaume Schull for having accepted to be my supervisor. I know that I am not the easiest student to manage and I can be (a lot) stubborn sometimes, but thanks to your capacity to adapt yourself to the people you manage, I genuinely believe that you were the best supervisor for me. Beside the fact that you have incredible human quality, you teach me everything and push me when I needed it. I will lie if I say that it was always pleasant for me, but it was necessary, and I always felt that you were here and I think it is the most important for a PhD student. I could not explain how much I am grateful to have the opportunity to work with you. Thanks a lot for everything.

A second person was essential during this thesis: "the uncle" Fabrice Scheurer. You were like a second supervisor to me, and I can't enumerate the number of time you solved my problems in the lab almost instantaneously. I admire your capacity to look in detail about everything and never trust my calculations without questioning every aspect. But above all, I was delighted to know you as a person, and I will remember the nice moments where we had to hide from Guillaume to discuss thermodynamics or physics entirely outside of our research topic.

Of course, I can not explain the quality of work that I had without mentioning "the mom" Virginie Speisser. It is impossible to list the things for which you helped me because you were available for basically everything, from the lab's problems to even income taxes. I think all of the team members will be agree with this title of "mom of the team". Thanks a lot for your kindness.

Upon joining the team, one person has helped me a lot to find my place: "the older brother" Michael or M.C Chong for the purists. You teach me everything I know about STM, and you explained to me how research is working. I remember during my first steps in the lab when I was bothering you with plenty of questions, you always took the time to explain everything. You were my guide in the world of research, but you have become a true friend. Thanks for your sense of humor and your kindness, I was lucky to work with you and know you as a person.

As I mentioned before, this section is too short to explain how much all of my colleagues were nice to me, but one person is very special for me: "the little brother" Luis Parra-Lopez. I cannot count how many times small discussions at the coffee break end up two hours later in crazy talks, which was not always appreciated by the bosses. From the human point of view, your good mood and your jokes were still helpful in the bad days and after more than three years laughing together, you have become one of my best friends. Thanks a lot.

I also want to thank another "uncle" Michelangelo Romeo for the development of the different software used during this work, especially the one used for the photon map acquisition. Thanks for your good mood and your (terrible) jokes during coffee time.

During my time here, I saw the family grew a lot since many members joined Guillaume's team. Shuiyan Cao who joined us as a post-doc and was always full of energy. Thanks for introducing me to the Chinese culture and for your kindness and your good daily mood. Anna Roslawska who joined us a bit later, also as a post-doc. I really enjoyed to work with you, you are an example for me, and I think you have a bright future in this team. I also discovered an adorable person, and I am sincerely happy to know you. Song Jang the last post-doc to join us. Thanks for your good mood and your joie de vivre. And finally, Kirill Vasilev, the youngest member of the team. I was glad to share a bit of my experimental knowledge with you and laugh with you every day. I think you have the capacity to do a great job in this team.

I would like to thanks the other members of the STM team: the spin guys. First Laurent Limot, the boss of the group, for his (dark) humor and his pieces of advice. My two office mates: Benjamin "Big Ben" Verlhac and Léo "Yeso" Garnier. Thanks Big Ben for your dark humor which makes me laugh a lot during my time here, I am still jealous of your skills in paint. Thanks Yeso for the opportunity you gave me to transform my car into a "recup' mobile" and for the fun moments we spent together. Of course, I keep the best member of the team for the end: "the piezo bane" Nicolas or "NTM" for the purists, who was here at the beginning of my thesis and who came back as a visiting post-doc at the end. Thanks for your kindness and your capability to make a day better just by being here.

I want to thank peoples who are not direct members of the team but with whom we collaborate. A special thank goes for Stephane who was my teacher at the "agregation preparation" and presented me to Guillaume. I really enjoyed all the discussions that we had together about science and other topics. I also want to thank Alex and Hervé for their theoretical contributions in this work, and for the many discussions we had. I want to thank our collaborators, outside of the IPCMS, Javier Aizpurua and Tomas Neumann for their theoretical contribution in the Hyper-Resolved Fluorescence Microscopy Map.

I want to thank all the jury members who accepted to review this thesis : Brahim Lounis, Fabian Natterer, Elizabeth Boer-Duchemin, Vincent Robert and Vincent Jacques. I appreciated your constructive remarks about this manuscript and the discussion we had during the PhD defence.

I want to thank the workshop members, especially Jean-Georges Faullumel and Bernard Muller, for their efficiency, whenever there was a need to build or fix a piece of the machine. I also thank Emmanuel Sternitzky for his help to fix many electronics problems we had.

My time here was also punctuated by break moments during lunch and coffee time with other students with whom I spent a lot of moments. I hope I will not forget someone on the list. Thanks to Matias, Ruben, Mauricio, Etienne, François, Olivia, Guillaume F., Kerstin, Guillaume C., Donald and Ulrich.

During my schooling, I was often in doubt about my capacity. Hopefully, I had the opportunity to know some teacher who believed in me and encouraged me to pursue. Thank you, Mrs Von-euw, Mr Catin, Mr Henry, Mr Cieslak, Mr Petit-frêre and Mr Crastes, your encouragement meant a lot for me and I believe that this thesis have been possible, somehow, thanks to you. I want to address special thanks for two professors: Marguerite Barzoukas and Thierry Charitat, for their support and their continuous availability during the preparation of the agregation, it is because of our discussion that I decided to give a try in research.

Coming from a modest family, I was not predisposed to make long studies, and I never thought I would arrive at this point. Luckily, my family was always incredibly supportive and enabled me to pursue my goals at every steps of my career. Especially you mom, I know that whatever I could do, you would have been proud of me, I own you everything, you are the best.

I want to thank all of my friend for their support during this thesis.

At last but not least, I really want to thank the person who shared my life during this thesis, thank you Primmie, for your comprehension during those long four years. Thanks for the meals that were waiting for me after a long day of measurement and for your support.

# Contents

**Résumé** **1**
0.1 Microscope à effet tunnel . . . . . . . . . . . . . . . . . . . . . . . . . 3
0.2 Processus d'émission de lumière dans une jonction STM . . . . 5
0.3 Microscopie de Fluorescence Hyper-Résolue . . . . . . . . . . . 6
0.4 Spectroscopie vibronique avec une résolution sub-moléculaire . 9
0.5 Electrofluorochromisme à l'échelle de la molécule unique. . . . 11
Contrôle de la durée de vie de l'espèce redox . . . . . . . 13
Contrôle de la durée de vie de l'exciton associée aux deux espèces redox . . . . . . . . . . . . . . . . . . . . . 13

**Introduction** **17**

**1 Scanning Tunneling Microscopy** **21**
1.1 Scanning Tunneling Microscopy . . . . . . . . . . . . . . . . . . . 21
1.1.1 Working principle of the scanning tunneling microscope 21
1.1.2 Expression of the tunnel current . . . . . . . . . . . . . . . 23
Bardeen's model of the tunnel current . . . . . . . . . . . 23
Model of Tersoff and Hamann. . . . . . . . . . . . . . . . . 28
Expression of the tunnel current in the WKB approximation 31
1.1.3 Practical STM image recording. . . . . . . . . . . . . . . . 32
1.1.4 Scanning tunneling spectroscopy . . . . . . . . . . . . . . . 33
1.1.5 Example : STM image and STS on single molecule . . . . 33
1.2 Experimental setup . . . . . . . . . . . . . . . . . . . . . . . . . . . 35
1.2.1 Microscope and preparation . . . . . . . . . . . . . . . . . 35
The microscope . . . . . . . . . . . . . . . . . . . . . . . . . 35
Tip and sample preparation. . . . . . . . . . . . . . . . . . 35
1.2.2 Optical setup . . . . . . . . . . . . . . . . . . . . . . . . . . 37
The light collecting system . . . . . . . . . . . . . . . . . . 37
The light analyzing system. . . . . . . . . . . . . . . . . . . 39

**2 Light Emission process in a STM junction** **43**
2.1 Basic principle of light emission in an STM junction . . . . . . . 43
2.1.1 An STM junction from an electromagnetic point of view 44
Electromagnetic description of the sample surface. . . . . 45
Electromagnetic description of the tip-sample junction. . 47
2.1.2 Light emission process mechanism . . . . . . . . . . . . . 49
2.1.3 Molecular exciton in a plasmonic nanocavity . . . . . . 50
2.2 Light emission from single molecules . . . . . . . . . . . . . . . . 52
2.2.1 STM-Induced light emission from adsorbed molecules . 52
2.2.2 Several strategies to decouple molecules . . . . . . . . . 53

2.2.3 Timeline of STM-Induced single-molecule fluorescence . 54
2.3 Overview of STM-Induced phthalocyanine fluorescence on NaCl 57
2.3.1 Inter molecular coupling . . . . . . . . . . . . . . . . . . . . 57
Homogeneous molecular coupling . . . . . . . . . . . . 57
Heterogeneous molecular coupling . . . . . . . . . . . . 59
2.3.2 NCP-exciton coupling . . . . . . . . . . . . . . . . . . . . . 61
2.3.3 Single-photon emission . . . . . . . . . . . . . . . . . . . . 64
2.3.4 Excitation mechanism . . . . . . . . . . . . . . . . . . . . . 65
2.4 Summary . . . . . . . . . . . . . . . . . . . . . . . . . . . . . . 69

**3 Hyper-Resolved Fluorescence Microscopy 71**
3.1 STM-F spectroscopy . . . . . . . . . . . . . . . . . . . . . . . . 71
3.1.1 Description of the system . . . . . . . . . . . . . . . . . . 71
General properties . . . . . . . . . . . . . . . . . . . . . 71
3.1.2 STM-F spectroscopy on $H_2Pc$ . . . . . . . . . . . . . . . . . 73
3.2 Hyper-Resolved Fluorescence Microscopy . . . . . . . . . . . . 74
3.2.1 Spatial mapping of the fluorescence signal . . . . . . . . 74
3.2.2 Origin of the spatial variation . . . . . . . . . . . . . . . . 76
Description of the excitation process . . . . . . . . . . . 76
Description of the emission process. . . . . . . . . . . . 77
Simulations and results . . . . . . . . . . . . . . . . . . 80
3.2.3 Fluorescence identification of each tautomer . . . . . . . 81
3.3 Description of the tautomerization process . . . . . . . . . . . . 82
3.3.1 Dynamic of the tautomerization process . . . . . . . . . . 82
3.3.2 Impact of the NaCl island on the $H_2Pc$ fluorescence spectra . . . . . . . . . . . . . . . . . . . . . . . . . . . . . . 85
3.4 Tautomerization mechanism . . . . . . . . . . . . . . . . . . . . 89
3.4.1 Similarities between fluorescence and tautomerization processes . . . . . . . . . . . . . . . . . . . . . . . . . . . 89
3.4.2 Additional data supporting an excited-state mediated mechanism . . . . . . . . . . . . . . . . . . . . . . . . . . 93

**4 Vibronic spectroscopy with sub-molecular resolution 97**
4.1 STM-F spectroscopy on a zinc phthalocyanine molecule . . . . . 98
4.1.1 Presentation of the system . . . . . . . . . . . . . . . . . . 98
4.1.2 Narrowing the emission line by dipole-dipole coupling. 99
4.1.3 Vibronic fingerprint from STM-F spectroscopy . . . . . . 102
4.2 Electronic contributions to the ZnPc dimer emission . . . . . . . 104
4.2.1 Dipole-dipole coupling modes . . . . . . . . . . . . . . . . 104
4.2.2 HRFM maps . . . . . . . . . . . . . . . . . . . . . . . . . . 105
4.3 Vibronic spectroscopy with sub-molecular resolution . . . . . . 107
4.3.1 Impact of the electronic contribution on the vibronic spectrum . . . . . . . . . . . . . . . . . . . . . . . . . . . . . 107
4.3.2 Impact of the tip position on the vibronic signal . . . . . 109
4.3.3 Explanation of the vibronic spatial variation: Herzberg-Teller coupling . . . . . . . . . . . . . . . . . . . . . . . . . 112
4.3.4 Case of $H_2Pc$ . . . . . . . . . . . . . . . . . . . . . . . . . . 113

**5 Electrofluorochromism at the single-molecule level** **117**
5.1 STM-F spectroscopy on a zinc phthalocyanine molecule . . . . 118
5.1.1 Presentation of the system . . . . . . . . . . . . . . . . . . 118
5.1.2 Vibrational signature of the charged molecule . . . . . . 120
5.2 Control of the respective emission of the charged and neutral molecule . . . . . . . . . . . . . . . . . . . . . . . . . . . . . . 121
5.2.1 Charge lifetime . . . . . . . . . . . . . . . . . . . . . . . . 122
5.2.2 Emission lifetime . . . . . . . . . . . . . . . . . . . . . . . 124
5.3 Mechanism . . . . . . . . . . . . . . . . . . . . . . . . . . . . . 125
5.3.1 Impact of the metallic substrate on the fluorescence . . . 126
Voltage dependency . . . . . . . . . . . . . . . . . . . . . 126
Current dependency . . . . . . . . . . . . . . . . . . . . . 128
5.3.2 Impact of the energy level alignment . . . . . . . . . . . 130
5.3.3 Plasmon-exciton coupling . . . . . . . . . . . . . . . . . . 133
5.3.4 General mechanism . . . . . . . . . . . . . . . . . . . . . 135

**Conclusion** **139**

**Bibliography** **155**

**List of figures** **159**

**Publications and presentations** **161**

# Résumé

Les spectroscopies optiques constituent de puissantes méthodes expérimentales qui fournissent des informations précises concernant la structure chimique de molécules organiques. Néanmoins, ces techniques sont en général utilisées pour analyser des échantillons constitués d'un très grand nombre de molécules, où l'information portée par chaque molécule est diluée dans le signal total. Ainsi, obtenir le signal optique provenant d'une unique molécule constitue une sorte de limite ultime en terme d'analyse chimique. Cela permet non seulement d'obtenir des informations à propos de la molécule elle-même, mais surtout d'utiliser cette dernière comme une sonde locale de son environnement direct. A la fin des années 80, Moerner and Orrit ont atteint cette limite ultime en mesurant le spectre optique d'une unique molécule [82, 87], accomplissant ainsi une première étape vers le développement des techniques de microscopie de fluorescence super-résolues. En dépit de nombreuses innovations, ces techniques semblent pourtant avoir atteint une résolution spatiale de l'ordre de la dizaine de nanomètre, soit un ordre de grandeur de plus que la taille typique d'une molécule organique. En conséquence, même si le spectre optique d'une unique molécule constitue un moyen efficace pour sonder son environnement, connaître de manière exacte ce dernier pour en comprendre en retour l'effet sur la molécule reste impossible.

L'objectif de cette thèse est d'utiliser un Microscope à effet tunnel (STM) pour exciter électriquement l'émission de fluorescence (STM-F) de molécules uniques. L'avantage de cette technique est double : il est possible d'obtenir le spectre de fluorescence d'une unique molécule et en même temps, de contrôler et visualiser directement son environnement direct.

Le premier signal optique excité par STM et provenant d'une unique molécule, a été reporté dans le papier fondateur de Qiu et al. [92] en 2003. Le système étudié était constitué de molécules uniques de porphyrine, découplées d'un subtrat métallique NiAl par une fine couche d'oxyde jouant le role d'isolant. Dans ces travaux, les auteurs ont observé une variation substantielle du spectre optique en fonction de la position relative de la pointe par rapport à la molécule et du site d'adsorption de cette dernière. Malheureusement, derrière ces résultats prometteurs est caché un problème majeur : la raie principale d'émission observée ne correspond pas à l'énergie de fluorescence attendue pour cette molécule. Une explication possible à cette observation étant que la couche d'oxyde ne permet pas de découpler suffisament la molécule du substrat métallique, ce qui induit une perte des propriétés intrinsèques de la molécule.

En 2016, Michael Chong le précédent étudiant en thèse dans notre équipe a développé une innovante configuration expérimentale où une molécule de porphyrine est suspendue entre la pointe et le substrat par des fils moléculaires d'oligothiophène [20]. Dans cette configuration, une fine raie d'émission

correspondant à la fluorescence de la molécule est observée. De plus, la raie principale de fluorescence est accompagnée d'une série de raies de plus faibles intensités associées à des modes d'émission vibronique. Ce résultat suggère qu'une empreinte chimique de la molécule sondée peut être obtenue à l'échelle de la molécule unique et sans avoir recours à une excitation lumineuse. Malheureusement dans cette configuration, puisque la molécule est suspendue entre la pointe et le substrat, la résolution spatiale est perdue rendant impossible une étude approfondie des variations à l'échelle sub-moléculaire de cette empreinte chimique.

Peu après cette publication, Zhang *et al* [129] ont reporté des expériences où le spectre de fluorescence de molécules de phtalocyanine de zinc pouvait être obtenu en découplant ces dernières d'un substrat d'argent Ag(111) par une fine couche de NaCl. En construisant des arrangements linéaires de plusieurs molécules, les auteurs ont observé l'apparition de plusieurs pics de fluorescence associés à différents modes de couplage excitoniques intermoléculaire. En utilisant la m ême technique et quasiment au même moment, Imada *et al* [49] ont montré qu'il était possible d'observer l'émission de fluorescence d'une molécule de phtalocyanine ($H_2Pc$) en l'excitant indirectement via un transfert d'énergie provenant d'une seconde molécule adjacente (MgPc) excitée par les électrons tunnels de la pointe STM.

Cette méthode efficace permettant d'obtenir le spectre de fluorescence d'une molécule unique, couplée à la possibilité de sonder et de contrôler l'environnement local de la molécule, a ouvert la voie à l'étude de questions intrigantes :

D'où vient la résolution sub-moléculaire observée dans les expériences de fluorescence induite par STM (STM-F) ? Comment l'orientation du moment dipolaire de transition de la molécule influence, à cette échelle, l'émission de photons en champ lointain ? Que peut-on apprendre de cette information ?

Les spectres vibroniques obtenus grâce aux spectroscopies vibrationnelles de type Raman, sont souvent considérés comme une empreinte chimique de l'objet sondé. Si une telle signature peut être obtenue grâce à la STM-F, comme cela est suggéré par le résultat de Chong et al., comment cette signature varie lorsque l'acquisition est réalisée à différentes positions à l'intérieur même de la molécule ? Plus fondamentalement, quel est le sens physique du spectre optique acquis à l'intérieur d'une molécule ? De nombreuses publications ont démontré la possibilité d'utiliser le STM pour contrôler l'état de charge d'atomes ou de molécules [99, 67, 36, 115]. Peut-on utiliser le STM pour contrôler l'état redox d'une molécule fluorescente et en même temps sonder ses propriétés optiques ?

Le but de cette thèse est de tenter d'apporter des réponses à ces questions. Le présent manuscrit sera divisé en cinq différents chapitres.

Le chapitre 1 présente le principe de fonctionnement de la microscopie à effet tunnel, ainsi que le dispositif expérimental utilisé dans le cadre de cette thèse.

Le chapitre 2 présente le principe de fonctionnement de l'émission de lumière par STM, tout d'abord d'une manière générale au sein de jonction tunnel métal-métal pour introduire les modes électromagnétiques particulièrement localisés dans la jonction STM, appelés plasmons de nano-cavité. Ensuite, le principe de l'émission de fluorescence de molécules uniques au sein de la nano-cavité ainsi que l'état de l'art du domaine est présenté.

Le chapitre 3 est le premier chapitre expérimental de cette thèse, où le concept de Microscopie de Fluorescence Hyper-Résolue est présenté (HRFM : Hyper Resolved Fluorescence Microscopy). En particulier une étude systématique de l'influence de la position de la pointe sur le spectre de fluorescence est menée et démontre que l'origine de la résolution spatiale provient essentiellement des modes de plasmons localisés grâce aux derniers atomes de la pointe STM. Cette technique de microscopie est ensuite utilisée pour identifier et suivre en temps réel la dynamique d'un processus de tautomerisation d'une unique molécule de phtalocyanine ($H_2Pc$).

Le chapitre 4 est le second chapitre expérimental de cette thèse. Dans ce chapitre, une étude réalisée sur des arrangements linéaires de molécules de phtalocyanine de zinc (ZnPc) montre que la spectroscopie STM-F permet d'obtenir une signature vibrationnelle, à l'instar de la spectroscopie Raman, à l'échelle de la molécule unique et sans avoir recours à une excitation lumineuse. Une étude plus poussée, au moyen de cartes HRFM, montre que la variation spatiale de cette signature vibrationnelle est pilotée par la symétrie du mode de vibration considéré.

Le chapitre 5 est le dernier chapitre expérimental de cette thèse. Dans ce chapitre, le STM est utilisé pour contrôler l'état de charge d'une molécule unique de phtalocyanine de zinc et en même temps sonder ses propriétés optique par spectroscopie STM-F. Pour la première fois, la signature vibrationnelle d'une unique molécule chargée est obtenue et montre des différences notables avec celle de l'espère neutre. Un contrôle de l'émission respective des deux espèces redox est réalisé, en modifiant l'épaisseur de NaCl, permettant ainsi un contrôle de la durée de vie de la molécule chargée et en contrôlant la réponse plasmonique de la nanocavité, permettant ainsi de contrôler la durée de vie de l'exciton. Une étude comparative de l'émission des deux espèces redox sur un substrat d'or et d'argent, ainsi qu'une étude en fonction de la position de la pointe par rapport à la molécule, sont réalisées afin d'étudier le mécanisme d'excitation à l'oeuvre.

## 0.1 Microscope à effet tunnel

### Principe du microscope à effet tunnel

En 1982 Binnig et Rohrer démontrent la possibilité d'obtenir, à l'échelle atomique, des topographies de surfaces conductrices. L'appareil ayant permis cette prouesse technique, porte le nom de microscope à effet tunnel (STM). Ce dernier est composé d'une pointe métallique, séparée d'une surface conductrice d'une distance de l'ordre de 1 nm, aux bornes desquelles est appliquée une différence de potentiel inférieure au travaux de sortie des métaux constituants de la pointe et de la surface. Dans ces conditions et d'un point de vue classique, aucun courant ne peut exister puisque la différence de potentiel n'est pas suffisante pour extraire un électron d'une des deux électrodes. En revanche, d'un point de vue quantique les électrons se comportent comme des ondes, ainsi il est possible de montrer que la probabilité pour un électron de passer de l'une à l'autre des électrodes n'est pas nulle et varie de manière exponentielle avec la distance : un faible courant électrique (de l'ordre de 1 nA), appelé **courant tunnel** peut exister dès lors que la distance entre la pointe et la surface est bien inférieure à 1 nm. En première approximation le courant peut s'exprimer comme suit :

$$I_t = |\psi|^2 \propto e^{-2\rho z} \tag{1}$$

Où $\phi$ est le travail de sortie des métaux constitutifs de la pointe et la surface, $E \leq eV$ l'énergie donnée aux électrons et $z$ la distance pointe-surface. Pour les métaux typiques utilisés en STM, tels que l'or ou l'argent, une variation de 1 Ådonne lieu à une variation du courant tunnel d'un ordre de grandeur. En balayant la surface et en contrôlant la position de la pointe pour garder le courant tunnel à une valeur de consigne, au moyen de tubes piezo-électriques, les mouvements verticaux de la pointe sont enregistrés et permettent de reconstruire une topographie de la surface avec une résolution atomique.

## Influence des états électroniques de la pointe et de la surface sur le courant tunnel

### Courant tunnel

L'expression précédente du courant tunnel (1) ne tient pas compte des états électroniques de la pointe et de la surface. Tersoff et Hamann [118] ont montré que dans le formalisme de Bardeen [3] il est possible d'obtenir une expression plus précise du courant tunnel :

$$I_t \propto \int_0^{eV} dE \rho^P(E - eV)\rho^S(\mathbf{r_0}, E) \tag{2}$$

Où $\rho^P$ et $\rho^S$ sont les densités locales d'états de la pointe et de la surface respectivement. Cette expression montre que le courant tunnel est directement sensible aux états électroniques de la surface et donc qu'une image STM est en réalité une convolution entre la topographie de la surface et sa densité d'état.

### Spectroscopie tunnel

En dérivant l'expression 2, il est possible d'obtenir la **conductance différentielle** donnée par :

$$\frac{dI_t}{dV}(V) \propto \rho^S(\mathbf{r_0}, eV) \tag{3}$$

Cette expression montre que la conductance différentielle $dI/dV$ est directement proportionnelle à la densité d'état de la surface à l'énergie $eV$. La spectroscopie tunnel (STS) exploite directement cette relation. En mesurant cette conductance différentielle tout en faisant varier la tension appliquée $V$, des résonnances de conductance vont apparaitre aux énergies caractéristiques des états électroniques de la surface. En particulier dans le cadre de cette thèse, une expérience de STS réalisée sur des molécules uniques découplées du substrat métallique par une fine couche isolante de NaCl permet de révéler la position en énergie des orbitales HOMO (orbitale plus haute occupée) et LUMO (orbitale plus basse vacante).

### Dispositif expérimental

La suite du chapitre présente le dispositif expérimental utilisé dans le cadre de cette thèse. Le dispositif expérimental consiste en un microscope à effet tunnel basse température Omicron, refroidi à l'hélium liquide et permettant de travailler à 4.6K. La tête STM est équipée d'une lentille qui permet de collecter la lumière émise dans la jonction. La lumière ainsi redirigée vers l'extérieur peut être analysée spectralement au moyen d'un spectromètre et d'une caméra CCD, mais également temporellement grâce à un système HBT composé d'un séparateur de faisceau et de deux détecteurs de photons uniques (photodiodes à avalanche). Le taux de collection final est estimé à 2-5 % de la lumière émise dans la jonction.

## 0.2 Processus d'émission de lumière dans une jonction STM

Sous une différence de tension de l'ordre de $V = 2$ V un électron traversant la jonction tunnel porte une énergie qui correspond à la longueur d'onde de la lumière visible ($\lambda = 600$ nm). D'un autre côté, l'apex de la pointe STM est constitué de structures métalliques de taille $d \ll \lambda$. Ce genre de structure peut se comporter comme un transducteur qui convertit l'énergie extrêmement localisée dans la jonction en photon dans le champ lointain, à l'instar d'une antenne dans d'autres domaines du champ électromagnétique.

### Emission de lumière dans une jonction métal-métal

Plus précisément, l'hybridation entre les oscillations plasmons de la pointe, couplées avec celles de l'échantillon, donne lieu à des modes électromagnétiques particulièrement confinés dans la jonction tunnel appelés **Plasmons de nanocavité** (NCP). Ces modes de plasmons peuvent être excités par des transitions tunnels inélastiques qui concernent, au mieux, une fraction de l'ordre d'un millième des électrons participant au courant tunnel total. Ces modes peuvent se désexciter radiativement en émettant un photon. Le spectre qu'il est possible de mesurer dans ces conditions présente une émission large bande caractéristique des modes de plasmons de la nano-cavité et présentant un seuil quantique correspondant à la tension appliqué dans la jonction (énergie maximale des électrons susceptibles d'exciter les modes de plasmons). L'émission de photons par les électrons tunnels peut être formellement résumée par la règle d'or de Fermi :

$$\Gamma(\nu) = \frac{2\pi}{\hbar^2} | \langle i|\hat{\mu}|f\rangle |^2 \rho_{NCP}(\nu = E_i - E_f, M) \tag{4}$$

Où $\langle i|\hat{\mu}|f\rangle$ est le moment dipolaire de transition associé à la transition tunnel inélastique et $\rho_{NCP}$ la densité de modes de plasmons de nano-cavité présent à l'énergie de la transition.

### Emission de fluorescence d'une molécule unique dans une jonction STM

Si les électrons tunnels représentent le terme source de l'émission de lumière, la jonction STM peut être vue comme une cavité plasmonique qui va fortement amplifier les transitions inélastiques. Dans ce type de cavité, une molécule fluorescente portée dans son état excité peut voir son rendement d'émission fortement amplifié par les modes électromagnétiques de la cavité. Le taux d'émission de fluorescence peut donc également être résumé par une règle d'or de Fermi telle que celle décrite précédemment. Le mécanisme d'excitation de la molécule sera discuté en détail au cours du manuscrit.

La suite du chapitre présente une partie historique de

## 0.3 Microscopie de Fluorescence Hyper-Résolue

Ce chapitre présente des expériences de fluorescence induites par STM (STM-F) réalisées sur des molécule de phtalocyanine ($H_2Pc$) découplées d'un substrat Ag(111) par une fine couche tri-atomique de NaCl. Les résultats expérimentaux principaux de ce chapitre, consistent en une cartographie de l'intensité des raies de fluorescence en fonction de la position de la pointe. Les cartes expérimentales, nommées carte de Microscopie de Fluorescence Hyper-Résolue (HRFM : Hyper-Resolved Fluorescence Microscopie), sont comparées à un modèle théorique et permettent de comprendre l'origine de la variation spatiale à l'échelle sub-moléculaire des spectres de fluorescence.

### Spectroscopie de fluorescence induite par STM

Le spectre de fluorescence typique de la molécule d'$H_2Pc$ présentent deux raies principales d'émission, appelées $Q_x$ et $Q_y$ et qui sont associées respectivement, aux moments dipolaires de transition alignés le long de l'axe des hydrogènes de la molécule (axe $x$) et l'axe perpendiculaire (axe $y$) [49, 83, 50]. Des spectres STM-F réalisés en différent endroits de la molécule montrent une duplication des raies principales $Q_x$ et $Q_y$, non reportée dans la littérature. Parallèlement, les images STM de l'orbitale LUMO révèlent une inversion des axes de symétrie, due au mouvement concerté des hydrogènes centraux (tautomérisation [68]), de la molécule lorsque cette dernière est soumise à une tension $V$ = -2.5V (tension utilisée pour réaliser les spectres STM-F). Ces observations suggèrent une connexion entre le processus de tautomérisation et la duplication des raies de fluorescence observée dans les spectres.

## Cartographie HRFM

Pour comprendre l'origine de cette duplication qui apparait lorsque l'excitation est réalisée à différents endroits de la molécule, une cartographie HRFM est réalisée dans un premier temps sur la première raie $Q_x$. La carte obtenue présente une structure de dipôle avec deux doubles lobes intenses et opposés, ainsi qu'un centre plus sombre (Fig. 3.6(a)). Superposée à cette structure, une forme à huit lobes provenant de la structure de l'orbitale HOMO (orbitale contribuant principalement au transport du courant tunnel) est également observée.

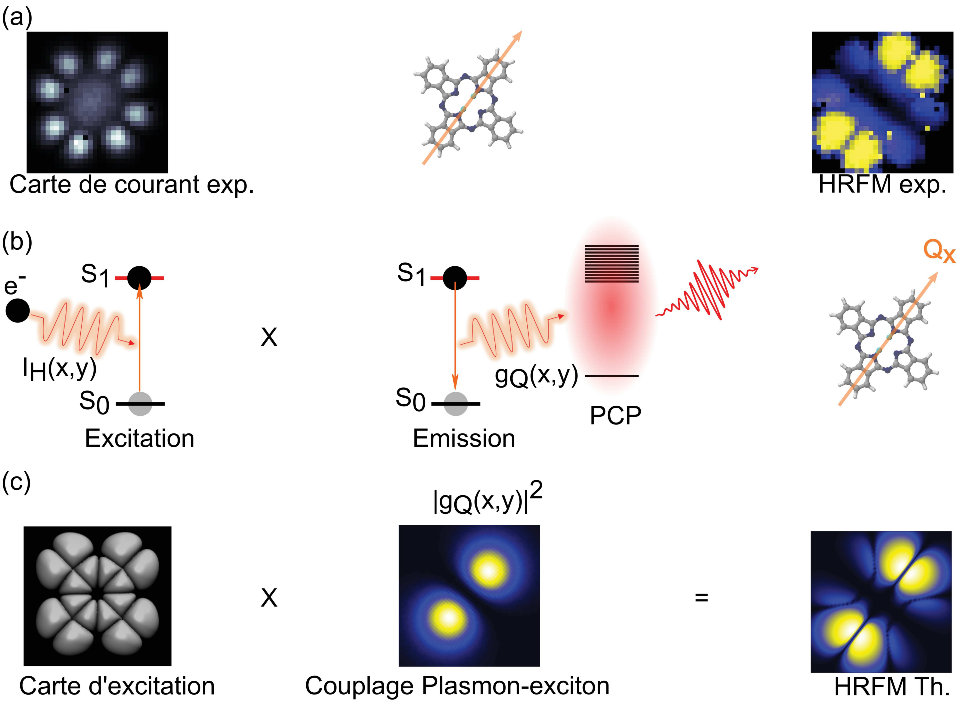

**Figure 1: Carte HRFM de la raie $Q_x$ de fluorescence de la molécule de $H_2$Pc** (a) Carte de courant expérimentale, orientation du moment dipolaire de transition $Q_x$ et carte HRFM de la raie $Q_x$. (b) Schèma representant le processus d'excitation par les électrons tunnels et le processus d'émission piloté par les plasmons de la pico-cavité. (c) Cartes théoriques d'excitation, d'émission et carte HRFM totale théorique.

Pour comprendre ces observations, les résultats expérimentaux sont comparés à un modèle théorique construit par nos collaborateurs Javier Aizpurua et Tomas Neuman de San Sebastian en Espagne. Ce modèle estime la probabilité de détecter un photon de fluorescence comme le produit de la probabilité d'exciter la molécule par la probabilité de désexcitation de cette dernière Fig. 3.6(b). Ces deux probabilités sont calculées point par point de la manière suivante :

- La probabilité d'exciter la molécule est proportionnelle au courant traversant l'orbitale HOMO divisé par le courant total (efficacité d'excitation). La carte d'excitation (Fig. 3.6(c)) est ainsi très similaire à la carte en courant de l'orbitale HOMO.

- La probabilité de désexcitation est proportionnelle au module carré de la constante de couplage entre l'exciton et les plasmons localisés dans la jonction tunnel. La carte de désexcitation représente ainsi la variation du couplage entre l'exciton et les plasmons en fonction de la position de la pointe.

Le point extrêmement important de ce calcul concerne la localisation des plasmons dans la jonction. En effet, les plasmons de nano-cavité sont habituellement considérés comme étant confinés dans un volume de l'ordre de plusieurs dizaines de nm$^3$ [50]. Des résultats récents de spectroscopie Raman exaltée par effet de surface (SERS) [111], obtenus sur des molécules disposées entre une nanoparticule et un film d'or, montrent que quelques atomes disposés sur la nanoparticule suffisent à amplifier très fortement le champ électromagnétique dans des volumes inférieurs à 1 nm$^3$. Cet effet, nommé par les auteurs "pico-cavité" a été transposé dans nos expériences.

Le très bon accord entre l'expérience et la théorie montre deux choses :

- L'existence de la pico-cavité dans la jonction STM.
- Que les variations sub-moléculaire d'un spectre optique dépendent essentiellement du couplage entre le moment dipolaire de transition de la molécule et les plasmons confinés dans la pico-cavité.

Ainsi nos cartes de HRFM représentent une image optique du moment dipolaire de transition de la molécule et permettent donc d'en identifier l'orientation. En sachant que pour la molécule d'$H_2Pc$ les dipôles $Q_x$ et $Q_y$ sont orthogonaux les cartes HRFM réalisées sur chacune des raies de fluorescence de la molécule permettent d'associer, sans ambiguïté, la duplication des raies de fluorescence aux deux tautomères respectifs de la molécule.

## Description du processus de tautomérisation

Un suivi temporel de l'émission respective de chacun des deux tautomères est réalisé au moyen de détecteurs de photon unique. Un signal en créneau est observé sur chacun des détecteurs et permet de confirmer que les deux tautomères n'émettent jamais en même temps. Une analyse statistique est réalisée en calculant la fonction de corrélation du deuxième ordre $g^2(\tau)$. Cette fonction permet d'estimer la probabilité de détecter une paire de photon séparées d'un délai $\tau$. L'analyse des fonction d'autocorrélations et de corrélations croisées permettent de déduire la durée de vie de chaque tautomère. Une différence significative de durée de vie est observée pour les deux tautomères, ce qui confirme que la molécule ressent un environnement légèrement différent dans les deux formes tautomères.

Une analyse plus poussée de l'interaction entre la molécule et son environnement est réalisée par imagerie STM de haute résolution. Ces images montrent que les différences observées pour les deux tautomère (énergie de fluorescence et durée de vie) est due à une modulation de l'environnement local de la molécule en raison d'une adsorption différente sur un Moiré électronique résultant de l'incommensurabilité du réseau de NaCl sur l'argent Ag(111).

### Etude du mécanisme de tautomérisation

Finalement un mécanisme de tautomérisation implicant l'état excité de la molécule est proposé. Ce mécanisme repose sur trois arguments principaux :

- Le taux de tautomérisation et l'intensité de fluorescence présentent une dépendance similaire avec le courant tunnel.
- Le processus de tautomérisation apparait lorsqu'un seuil en tension correspondant à l'énergie de fluorescence est atteint. Cet argument est confirmé en réalisant des expériences similaires sur une autre molécule (Naphtalocyanine).
- La tautomérisation peut être induite par une excitation "à distance" via le couplage entre les plasmons et l'exciton moléculaire.

### Conclusion

A travers cet exemple du suivi optique d'un processus de tautomérisation avec une résolution spectrale, spatiale et temporelle, ce chapitre illustre le concept de microscopie de fluorescence hyper-résolue (HRFM). Cette technique repose sur l'unique combinaison de la résolution spectrale offerte par la spectroscopie optique et la résolution spatiale offerte par le microscope à effet tunnel. L'extrême résolution spatiale obtenue dans les images optiques n'est pas seulement due à l'extrême localisation du courant tunnel, mais surtout au confinement extrême des modes de plasmons dans la pico-cavité formée par la jonction STM.

## 0.4 Spectroscopie vibronique avec une résolution sub-moléculaire

Les spectroscopies Raman [40], proche infra-rouge [11] et de fluorescence à basse température [84], sont de puissantes méthodes expérimentales permettant d'obtenir le spectre de vibration de molécules organiques. Comme les raies observées dans ces spectres sont relatives aux modes de vibration caractéristiques de l'espèce sondée, ces spectres sont souvent considérés comme une empreinte chimique de cette dernière.

En raison de leur caractère non-invasif, les spectroscopies vibrationnelles constituent des méthodes clefs d'analyse chimique dans un large spectre de domaines scientifiques tels que la chimique organique, la biologie, la médecine, l'étude des matériaux ou encore les sciences médico-légales [51, 7]. Fondamentalement, obtenir le spectre de vibration d'une unique molécule constitue la limite ultime en terme d'analyse chimique résolue spatialement. Ce chapitre s'intéresse à la possibilité d'obtenir une telle information à cette échelle.

## Spectroscopie STM-F sur des molécules de phtalocyanine de zinc

Des expériences de STM-F sont réalisées sur des molécules de phtalocyanine de zinc (ZnPc), découplées d'un substrat Ag(111) par une fine couche bi-atomique de NaCl et des arrangements linéaires de plusieurs molécules. Les spectres réalisés montrent une augmentation de l'intensité, un affinement ainsi qu'un décalage vers le rouge de la raie principale de fluorescence lorsque le nombre de molécules dans l'arrangement augmente. Ce phénomène, reporté par Zhang *et al.*[129], est une conséquence du couplage excitonique (dipôle-dipôle) intermoléculaire. Cet affinement permet de mettre en évidence une série de raies dans la partie de plus basse énergie du spectre et qui n'a pas été reporté dans les précédentes études. Une comparaison avec un spectre Raman, acquis sur une poudre de ZnPc par l'équipe de Stéphane Berciaud de l'IPCMS, montre que ces raies correspondent aux modes d'émission vibronique de la molécule de ZnPc. Enfin, une comparaison avec des calculs DFT permet d'assigner chacune des raies vibroniques aux modes normaux de vibration de la molécule de ZnPc et d'en déduire les représentations irréductibles de symétries associées.

## Emission purement électronique associée aux modes de couplage excitonique

Une analyse systématique des spectres en fonction de la position de la pointe est conduite sur un dimère de ZnPc.

Cette étude permet tout d'abord de mettre en évidence l'existence de 5 modes d'émission dans la partie du spectre de plus haute énergie, dont l'intensité varie fortement en fonction de la position de la pointe. Ces observations sont en très bon accord avec les résultats publiés par Zhang *et al.* [129], où les auteurs ont associé ces modes d'émission aux différents modes de couplage excitonique intermoléculaire. Pour étudier plus en détails la façon dont l'intensité de ces modes d'émission varie avec la position de la pointe, des cartes HRFM sont réalisées. Une comparaison avec des cartes théoriques d'émission, similaires à celle présentées dans le chapitre précédent, permet de comprendre l'origine de ces variations : pour un mode donné l'émission est pilotée par le couplage entre l'exciton supramoléculaire et les plasmons de la pico-cavité.

## Spectroscopie vibronique avec une résolution sub-moléculaire.

Le signal vibronique obtenu dans les spectres de STM-F constitue une empreinte chimique de l'espèce sondée. Cette partie s'attache à répondre à la question : comment l'empreinte chimique varie lorsque l'acquisition est réalisée à l'intérieur même de la molécule ? L'étude des spectres en fonction de la position de la pointe révèle deux choses importantes :

- L'évolution de l'intensité du signal vibronique ne semble pas dépendre de l'intensité des modes d'émission purement électronique.

- Pour être comparé à un spectre Raman et donc pouvoir assigner notre spectre à un spectre vibronique, ce dernier doit toujours être tracé en fonction du décalage avec la raie d'émission associée au mode de couplage de plus basse énergie (dipôles alignés et en phase).

Une étude plus détaillée révèle que l'intensité du signal vibronique présente une variation significative en fonction de la position de la pointe. De manière surprenante cette variation semble reliée à la symétrie du mode de vibration considéré. Des cartes HRFM réalisées sur chacun de ces modes confirment ces observations : les modes appartenant à la même représentation irréductible de symétrie présentent un schèma similaire et qui reflète cette dernière. Ces cartes confirment également que la variation spatiale du signal vibronique n'est pas corrélée à celle des modes purement électroniques. Ces résultats montrent qu'une empreinte chimique, auparavant considérée comme caractéristique de la molécule sondée, présente des variations au sein même de cette dernière. Finalement, une discussion est menée dans le cadre de la théorie du couplage Herzberg-Teller (couplage vibronique) pour expliquer les observations expérimentales. Dans cette théorie, les observations expérimentales peuvent être rationalisées de la manière suivante : le mouvement de vibration de la molécule contamine la transition vibronique avec une superposition de moments dipolaires de transition associés à des états excités de plus haute énergie de la molécule. Ainsi, la transition vibronique porte des caractéristiques de cette superposition déterminée par des règles de symétrie. La carte HRFM qui est caractéristique du couplage entre le moment dipolaire de transition de l'émission vibronique et des plasmons de pico-cavité présente ainsi un schéma qui reflète la symétrie du mode de vibration concernée et qui diffère fortement des cartes acquises pour les modes purement électroniques.

### Conclusion

Ces résultats montrent que notre méthode permet d'obtenir, sans ambigüité, l'empreinte chimique d'une molécule unique sans avoir recours à une excitation lumineuse. Plus important encore, cette empreinte chimique varie de manière substantielle lorsque l'on excite l'une ou l'autre des sous parties de la molécule. La possibilité d'obtenir de telles informations optiques, combinée avec une haute résolution spatiale, montre que la microscopie de fluorescence hyper-résolue constitue une méthode puissante pour étudier des phénomènes physiques à une échelle inatteignable par d'autres techniques plus conventionnelles.

## 0.5 Electrofluorochromisme à l'échelle de la molécule unique.

L'interaction entre l'état redox d'une molécule et ses propriétés optiques est d'une importance cruciale pour les applications tels que les écrans, les capteurs ou encore des systèmes de mémoire basés sur des molécules organiques [1].

D'un point de vue fondamental, la compréhension de cette interaction revêt d'une importance particulière dans des phénomènes biologiques tels que la photosynthèse, où l'état redox des molécules impliquées joue un rôle crucial dans le mécanisme de transfert d'énergie intermoléculaire.
Les propriétés optiques des différents états redox de molécules sont en général adressées par spectro-électrochimie, qui consiste à sonder les propriétés optiques d'un large nombre de molécules dans des cellules électrochimiques [52]. Des résultats récents montrent qu'il est possible d'atteindre la limite de la molécule unique avec ces techniques [48]. En revanche, obtenir à l'échelle de la molecule unique une signature chimique d'une espèce redox, par exemple son empreinte vibrationnelle, s'avère toujours difficile experimentalement. De telles signatures ont été observées récemment par Spectroscopie Raman Exaltée par Effet de Surface (SERS) [23, 130], mais au prix d'un contact direct entre les électrodes et la molécule, ce qui affecte les propriétés intrinsèques de cette dernière. L'environnement STM quant à lui, a prouvé être une plateforme idéale pour contrôler et sonder l'état de charge d'atomes ou de molécules [99, 115, 114] avec une précision atomique. L'objectif de ce chapitre est de montrer qu'il est possible de combiner cette approche avec la spectroscopie STM-F pour étudier l'interaction entre l'état redox d'une molécule et ses propriétés optiques.

## Spectroscopie STM-F sur une molécule de phtalocyanine de zinc

Des expériences de STM-F sont réalisées sur des molécules uniques de phtalocyanine de zinc (ZnPc), découplées d'un substrat Au(111) par une couche tri-atomique de NaCl. Un spectre réalisé à une tension $V$ = -2.5V montre la raie de fluorescence typique de la molécule (1.89 eV), ainsi qu'une raie plus étroite et plus intense à plus basse énergie (1.52 eV). Une comparaison avec la littérature permet d'assigner cette raie à la fluorescence du radical cation de la molécule de ZnPc. Un spectre réalisé à tension positive ($V$ = +2.5 V) montre quant à lui seulement l'émission de fluorescence de l'espèce neutre, ce qui est cohérent avec l'impossibilité de charger positivement la molécule dans ce cas. Les spectres STM-F permettent également d'obtenir le signal vibronique émis par la molécule chargée. Une comparaison de ce signal avec celui obtenu sur l'espèce neutre montre une différence significative entre les deux spectres. Ce résultat montre que la spectroscopie STM-F permet d'obtenir sans ambigüité une empreinte chimique précise des deux espèces redox d'une unique molécule.

## Contrôle de l'émission respective des deux espèces redox

Les expériences précédentes ont montré la possibilité d'obtenir le spectre de fluorescence des deux espèces redox de la molécule de ZnPc et d'en extraire une empreinte chimique permettant de les caractériser sans ambigüité. Cette partie s'intéresse au moyen de contrôler l'émission respective des deux espèces.

### Contrôle de la durée de vie de l’espèce redox

L’évolution des spectres STM-F acquis sur une unique molécule de ZnPc est étudié en fonction de l’épaisseur de la couche de NaCl. Les spectres acquis sur la molécule reposant sur le métal ou une unique couche atomique de NaCl montrent l’émission large bande caractéristique des plasmons de nano-cavité, suggérant un découplage électronique de la molécule insuffisant. Un spectre acquis sur une bicouche présente une faible émission de fluorescence comparable en intensité pour les deux espèces. Lorsque l’acquisition est réalisée pour une tri couche de sel, l’émission de fluorescence pour les deux espèces est plus intense, ce qui suggère un bien meilleur découplage électronique comparé au cas précédent. Plus intéressant encore, l’émission de fluorescence de l’espèce chargée devient dominante. Cette tendance s’accentue sur la tétra couche puisque seulement cette dernière devient observable dans ce cas, ce qui suggère que la molécule reste dans l’état chargé positivement la plupart de son temps. Finalement, ces résultats montrent que l’émission des deux espèces redox peut être modulée en contrôlant la durée de vie respective des deux espèces redox de la molécule.

### Contrôle de la durée de vie de l’exciton associée aux deux espèces redox

La géométrie de la jonction, essentiellement la forme de la pointe, est modifiée pour moduler la réponse spectrale de la nano-cavité plasmonique. Lorsque cette dernière est choisie pour être résonnante avec l’émission de fluorescence de la molécule neutre (resp. chargée), cette dernière est fortement amplifié au détriment de l’émission de la seconde espèce. Cet effet est connu sous le nom d’effet Purcell : la durée de vie de l’exciton est réduite par la forte densité de mode électromagnétique disponible à l’énergie de la transition. Ces résultats montrent ainsi qu’il est possible de contrôler l’émission respective des deux espèces redox en modifiant la durée de vie de l’exciton associé.

## Mécanisme d’excitation

Dans cette partie une étude comparative de l’influence du substrat (or ou argent) sur la fluorescence des deux espèces redox, est réalisée pour étudier en détail le mécanisme d’excitation. Il apparait que l’alignement des orbitales frontières HOMO et LUMO, qui est spécifique à chacun des deux substrats en raison de leur différent travaux de sortie, joue un rôle crucial dans l’excitation des deux contributions. De plus, il semble que différents mécanismes d’excitation contribuent à l’excitation de l’émission de l’espèce neutre en fonction du substrat. De manière surprenante, les résultats suggèrent un mécanisme d’excitation impliquant deux électrons dans le cas d’un substrat d’or; et à contrario, un mécanisme à un électron dans le cas de l’argent. Il est à noter que ce dernier a été suggéré, indépendamment par d’autres équipes [132] et également pour une molécule différente [16]. Une étude du couplage plasmon-exciton en fonction de la distance latérale pointe molécule est réalisé. Alors que l’émission de fluorescence de la molécule neutre peut être excité à distance, comme cela a été montré dans de nombreuses études [50, 134], celle de la molécule chargée ne peut être excitée que lorsqu'un recouvrement des orbitales de la pointe et de la molécule est possible, ce qui est cohérent avec la nécessité de charger directement la molécule. De manière surprenante, une dépendance avec la polarité du couplage plasmon-exciton de la molécule neutre est également observé. Enfin, les observations expérimentales sont résumées par un mécanisme phénoménologique prenant en compte les différents couplages existant entre : l'exciton, les plasmons et les électrons tunnels inélastiques.

## Conclusion

Ces résultats montrent qu'il est possible de contrôler l'état redox d'une molécule unique et en même temps de venir sonder le spectre de fluorescence de chacune des espèces redox. En particulier, il est possible d'obtenir sans ambigüité l'empreinte chimique de ces deux espèces. L'environnement hautement contrôlable de la jonction tunnel permet également de moduler finement leur émission en contrôler la durée de vie de l'espèce chargée en contrôlant l'épaisseur de NaCl ou la durée de vie de l'exciton associé en contrôlant la réponse plasmonique de la jonction tunnel. L'étude comparative sur différent substrat ainsi que celle du couplage plasmon-exciton a permis de mettre en évidence la richesse physique de ces expériences et d'en déduire différents mécanismes d'excitation. Finalement, notre approche permet d'étudier l'interaction entre l'état redox d'une molécule et ses propriétés optiques avec une précision presque atomique. Cette aptitude pourrait être extrêmement valorisable dans l'élucidation de mécanisme de transfert d'énergie intermoléculaire, où l'état redox des molécules joue un rôle crucial, tels que ceux impliqués dans la photosynthèse ou les cellules photovoltaïques.

# Conclusion Générale

D'un point de vue fondamental le travail mené durant cette thèse a permis d'étudier les processus d'interaction lumière-matière à une échelle inatteignable par les techniques optiques classiques. Nous avons pu expliquer (chapitre 3) comment et pourquoi le spectre optique d'une molécule, en particulier son spectre vibronique (chapitre 4), varie lorsque une sous partie de la molécule est excitée. D'un point de vue plus appliqué, nous avons montré que la microscopie de fluorescence hyper-résolue couplée à des mesures temporelles constitue un formidable outil pour suivre la dynamique de réaction chimique simple telle que la réaction de tautomérisation (chapitre 3). Nous avons montré qu'il était possible, à l'échelle de la molécule unique, de contrôler l'état redox d'une molécule et de venir sonder en même temps ses propriétés optiques (chapitre 5). Ces derniers travaux pourraient contribuer à l'élucidation des mécanismes de conversion d'énergie impliquant des réactions redox photo-induites, tels que ceux observés dans des processus biologiques tels que la photosynthèse.

Finalement, l'essence même de la Microscopie de Fluorescence Hyper-Résolue réside dans la possibilité de confiner et de contrôler la lumière à des échelles presque atomique dans un environnement parfaitement connu via le

STM. Cette possibilité revêt d'une importance particulière dans le domaine grandissant de la nanophotonique et nous pouvons prévoir une adaptation de cette approche expérimentale avec une source d'excitation purement optique sans pertes de la résolution spatiale. D'un autre côté, l'utilisation des électrons comme source d'excitation offre de nombreuses possibilités. En particulier l'utilisation de pointe fonctionnalisées, tel que des pointes magnétiques [125], permet d'entrevoir la possibilité d'accéder à l'état triplet d'une molécule unique afin d'étudier l'interaction entre les processus de fluorescence et de phosphorescence à l'échelle atomique.

# Introduction

Optical spectroscopies are powerful methods to obtain precise information regarding the chemical structure of organic molecules. However, such techniques are generally addressed over a large assembly of molecules, where information about individual molecules is diluted in the averaged signal. Therefore, gathering the optical signal which originates from a single molecule constitutes the ultimate limit in terms of chemical analysis. This allows not only to obtain information on the molecule itself but above all to use this latter as a local probe of its direct environment. In the late 80s, Moerner and Orrit reached this ultimate limits by performing optical detection and spectroscopy of single molecules [81, 87, 82], a first step towards the development of the super-resolved fluorescence microscopy. Despite many improvements, such optical techniques seem to have attained a spatial resolution an order of magnitude higher than the typical molecular size. Consequently, even though a single-molecule optical spectrum constitutes a probe of its local environment, knowing the exact nature of this latter to understand its interplay with the molecule remains impossible.

In this thesis, we propose to use a Scanning Tunneling Microscope to electrically address the fluorescence (STM-F) of single molecules [92, 20, 129]. The advantage of this approach is double: we can obtain a single-molecule fluorescence spectrum with sub-molecular precision, and at the same time, control and directly visualise its local environment.

The first single-molecule optical signal induce by STM has been reported by Qiu *et al.* [92] in 2003, where they detected for the first time, an optical spectrum of a single porphyrin molecule excited by the tunneling electrons coming from an STM tip. The authors reported substantial variations in the optical spectrum as a function of the tip position above the molecule and the adsorption site of this latter. However, behind this promising result is hidden a major problem: the emission lines observed in the spectrum does not match with the expected fluorescence energy for this molecule. The hybridization between the molecular and the metallic substrate states leads the molecule to lose its intrinsic properties. Therefore, to observe an intrinsic optical signal of the molecule, this latter has to be decoupled from the metallic substrate. In the work of Qiu *et al.*, this decoupling was achieved by separating the molecule from the substrate by a thin layer of oxide, which played the role of an insulator. One can suppose that this oxide was not sufficient to preserve the intrinsic properties of the molecule. In 2016, Michal Chong a former PhD student in our team developed an innovative experimental configuration, where a porphyrin molecule was suspended between the tip and the sample by molecular oligothiophene wires [20]. In this configuration, sharp emission lines associated with the molecule fluorescence were observed. Additionally, the main emission line was accompanied by smaller intensity features, associated with vibronic emission modes. This result suggested that a chemical fingerprint could be obtained at the single-molecule level without light excitation. Unfortunately, in this suspended configuration the spatial resolution is lost, and make an impossible further investigation about the sub-molecular variation of such fingerprint. Shortly after, Zhang *et al.* developed an experimental configuration where they obtained the fluorescence spectrum of Zinc-phthalocyanine single molecules, decoupled from an Ag(111) substrate by a thin layer of NaCl. By building linear arrangements of molecules, the authors observed features in the spectra associated with an inter-molecular excitonic coupling. Nearly at the same time Imada *et al.* [49], investigated energy transfer between two adjacent Mg and $H_2$ -phthalocyanine molecules, by using the same decoupling method.

This convenient method to obtain a single-molecule fluorescence spectrum, together with the capability to probe and control the local environment of the molecule, opened the way to the investigation of intriguing questions : Where does the sub-molecular resolution observed in STM-F experiments come from? How the orientation of the molecule transition dipole moment influence, at this scale, the light emitted in the far-field? What would we learn from that?

Vibronic spectra obtain in Raman or Infrared spectroscopies are often considered as a chemical signature of the probed species. If such signature can be obtained with STM-F, as it has been suggested by Chong *et al.* [20], how does this signature vary when the signal is recorded at different excitation positions inside the molecule? More fundamentally, what is the physical meaning of an optical spectrum of the inside of a molecule?

Many publications reported the capability to use STM to control the charge state of single atoms or molecules [99, 67, 36, 115]. Can we use the STM to control the redox state of a single molecule, and at the same time, probe its optical properties?

The goal of this thesis is to attempt to answers to these questions, therefore the manuscript will be divided into five chapters.

**Chapter 1** will be dedicated to presents the basic STM principles and the setup used in our experiments.

**Chapter 2** will be dedicated to presents how light can be generated in an STM junction. First, a description of the particular electromagnetic modes localized in the STM junction, called **Nanocavity-Plasmons**, is presented. Then, the different parameters to obtain a single-molecule fluorescence signal in such an environment are discussed. A last part of the chapter is dedicated to presents an overview of the recent STM-F experiments realized with the NaCl decoupling method.

**Chapter 3** is the first chapter of results, where I present the concept of **Hyper-Resolved Fluorescence Microscopy** (HRFM). I report STM-Induced fluorescence experiments carried out on a single $H_2Pc$ molecules adsorbed on a NaCL/Ag(111) sample. STM-F spectroscopy is performed and reveals duplication of the two main fluorescence lines of the molecule, which are associated with a tautomerization process. HRFM maps (*i.e* maps showing the variation of the fluorescence signal as a function of the tip position) are realized on those lines and discussed with a theoretical model. It shows that the spatial variation of the fluorescence signal is essentially due to the coupling between the molecule transition dipole moment and plasmonic modes confined in a scale much smaller than the molecule. Thanks to this interpretation HRFM maps are used to identify the respective fluorescence lines of each tautomer, through their dipole orientations. A temporal analysis of the fluorescence signal emitted by the two tautomers is realized and allows to perform a complete tracking of the tautomerization dynamics. Finally, a tautomerization mechanism involving the excitonic state of the molecule is discussed. The work presented in this chapter has been recently accepted for publication.

In **Chapter 4**, I report the possibility to use HRFM to obtain a single molecule chemical fingerprint with sub-molecular resolution. STM-F experiments are carried out on single ZnPc molecules adsorbed on a NaCl/Ag(111) sample. Spectra recorded on a linear arrangement of this molecule show a narrowing of the main emission line, due to an inter-molecular dipole coupling, which allows observing well-resolved features in the lower energy region. Comparison with spectroscopic data shows that these features correspond to vibronic emission lines, that can be assigned to vibrational normal modes of the ZnPc molecule. HRFM maps realized on the vibronic contributions reveal a pattern related to the vibrational modes symmetry, which demonstrates a sensitivity of the chemical fingerprint at the sub-molecular level. Finally, these observations are discussed and rationalized in the vibronic coupling theory framework. The work presented in this chapter has been partially published in 2017 [29].

The **Chapter 5** presents an investigation of the interplay between the redox states of a single molecule and its optical properties. STM-F experiments are carried out on single ZnPc molecules adsorbed on a NaCl/Au(111) sample. Beside the fluorescence line observed for the ZnPc molecule, a red-shifted and sharper line is observed in the STM spectra. Based on a comparison with the literature, we found that this line corresponds to the fluorescence emission of the radical cation of ZnPc. Comparison between spectra recorded at a positive or negative voltage, confirms that this line appears only when it is possible to extract an electron from the molecule HOMO orbitals. A vibrational signature of the charged molecule is obtained and presents substantial differences compared to the neutral one. Then, the respective emission of each redox species is controlled by tuning the insulator thickness and the plasmonic response of the STM nanocavity. Investigation of the fluorescence emission of both redox species as a function of the tip-molecule lateral distance is performed to highlight the different mechanism at plays in this system. Finally, the last part is dedicated to discuss with more details about these mechanisms. The work presented in this chapter has been partially published in 2018 [28].

# Chapter 1

# Scanning Tunneling Microscopy

## 1.1 Scanning Tunneling Microscopy

### 1.1.1 Working principle of the scanning tunneling microscope

In 1982 Binnig and Rohrer publish an astonishing paper [9] where they obtained, for the very first time, topographies of different surfaces at the atomic scale. For this achievement, they developed a new tool: the Scanning Tunneling Microscope (STM). After this success, the STM allowed them to observe in real space the 7×7 surface reconstruction of Si(111) [8]. This has ended several years of theoretical and experimental controversy about the structure of this latter (Fig 1.1), showing the important potential of this new technique which became one of the most important tools in surface science.

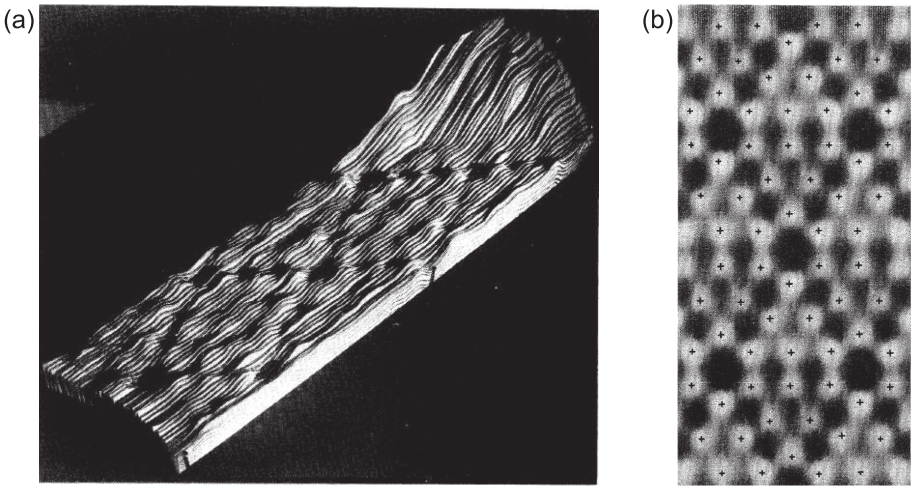

**Figure 1.1: Image of the surface reconstruction of Si(111) with STM** (a) Relief form of the original recordings of two complete 7×7 units cells. (b) Top view of (a) The two diagonals of the unit cell are 29 ± 4 Å and 46 ± 1 Å in good agreements with the crystallographic values at that time ( 26.88 Å and 46.56 Å respectively.). Reproduced from [8]

Binnig and Rohrer gave a very clear description of the STM working principle [9]:

"*The principle of the STM is straightforward. It consists essentially in scanning a metal tip over the surface at* ***constant*** *tunnel current as shown in Figure 1.2. The displacements of the metal tip given by the voltages applied to the piezo drives then*

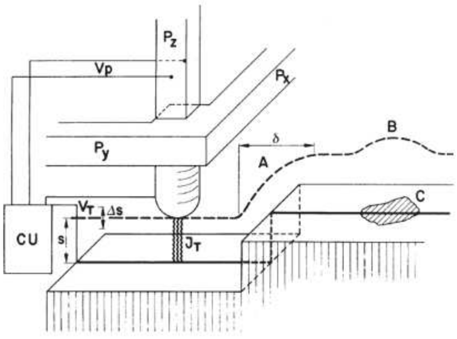

FIG. 1. Principle of operation of the scanning tunneling microscope. (Schematic: distances and sizes are not to scale.) The piezodrives $P_x$ and $P_y$ scan the metal tip $M$ over the surface. The control unit (CU) applies the appropriate voltage $V_p$ to the piezodrive $P_z$ for constant tunnel current $J_T$ at constant tunnel voltage $V_T$. For constant work function, the voltages applied to the piezodrives $P_x$, $P_y$, and $P_z$ yield the topography of the surface directly, whereas modulation of the tunnel distance $s$ by $\Delta s$ gives a measure of the work function as explained in the text. The broken line indicates the $z$ displacement in a $y$ scan at ($A$) a surface step and ($B$) a contamination spot, $C$, with lower work function.

**Figure 1.2: Description by Binnig and Rohrer of the working principle of the STM.** Reproduced from [8]

*yield a topographic picture of the surface. The very high resolution of the STM rests on the strong dependence of the tunnel current on the distance between the two tunnel electrodes, i.e, the metal tip and the scanned surface.*"

To understand the strong distance-dependency of the tunneling current, let's describe with a very simple model what occurs in the junction constituted by the tip and the sample of the STM.

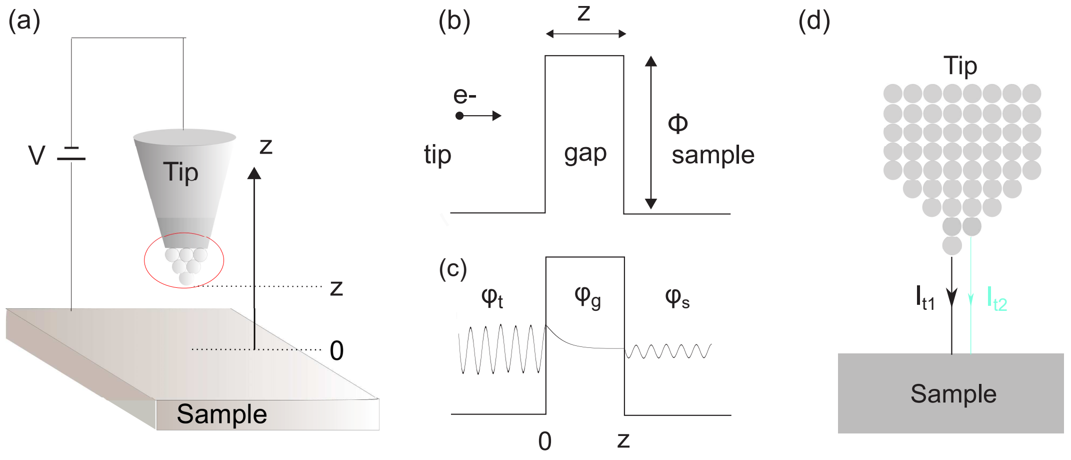

**Figure 1.3: Origin and description of the tunnel current.** (a) Sketch of the STM junction. (b) Energetic sketch of the junction from a classical point of view. (c) Energetic sketch of the junction from a quantum point of view. (d) Description of the apex of the tip (red circle in (a)).

The two electrodes (the tip and the sample) are separated by a distance $s$ of the order of 10 Å (Fig.1.2 (a)). A voltage $V$ of the order of 1 V is applied between the two electrodes. For an electron the gap existing between the tip and the surface constitutes a potential barrier, whose height corresponds (Fig.1.2 (b)) to the metal workfunction $\Phi$ *i.e* the energy necessary to extract an electron from the metal to the vacuum). For typical metals used in STM experiments, this energy is $\approx 5$ eV.

In the gap region, the energy of the electron ($E = 1$ eV with a bias of 1 V) is smaller than the potential ($V = \Phi \sim 5$ eV). This means that its kinetic energy is negative: from a classical point a view the gap region is forbidden for the electron, therefore it cannot cross the junction. However, in a quantum point of view, the electron behaves like a wave. Mathematically this wavefunction satisfies the following Schrodinger equation:

$$\frac{-\hbar^2}{2m}\frac{d^2\psi_{el}(z)}{dz^2} + V(z)\psi_{el}(z) = E\psi_{el}(z) \tag{1.1}$$

In the gap region $V(z) = \Phi$ and $E < V$ leading to a solution of the form:

$\psi_g(z) = Ae^{-\rho z}$ with $\rho = \sqrt{\frac{2m(\phi - E)}{\hbar^2}}$

This means that in the gap region there is an evanescent wave, whose amplitude decays exponentially with the distance. With $E$ = 1 eV and $\Phi$ = 5 eV the decay length can be evaluated as: $l = \frac{1}{\rho} \approx 1$ Å
This decay length is in the order of the width of the barrier. Consequently, this wave is eventually transmitted in the sample (Fig.1.2 (c)) with a probability that decays exponentially with the distance. The electron can cross the junction: this is the tunnel effect. Therefore the so-called tunnel current is given by:

$$I_t = |\psi|^2 \propto e^{-2\rho z} \tag{1.2}$$

From this expression, we obtain that if z increases by 1 Å $I_t$ will increase by a factor 10. To understand qualitatively the high spatial resolution of STM, in figure 1.3(d) we represent the last few atomic planes of the tip apex. If we compare the tunneling current corresponding to an atom of the closest plane to the surface ($I_{t1}$) to the one of the second closest ($I_{t2}$), there is more than one order of magnitude difference. Therefore, the total tunnel current is mainly due to the last atom, and consequently extremely localized in the (x,y) plane. Even if this model cannot provide a satisfying expression for the tunnel current $I_t$, it gives the physics behind the high resolution of the STM: the exponential decay of $I_t$ with the tip-sample distance $z$. A small variation of $z$ will induce a strong variation of $I_t$. Scanning the sample with the tip while measuring those variations will eventually provide a topography of the scanned sample.

## 1.1.2 Expression of the tunnel current

### Bardeen's model of the tunnel current

In the previous part, we have seen how it is possible to obtain topographies at the atomic scale with STM. The contrast observed in these topographies lies essentially on the gap width $s$ (tip-sample distance). However, since the tunnel current consists of electrons flowing from the tip (resp. sample) to the sample (resp. tip), it is necessary to take into account the start and arrival quantum states of the electron. As an example, one can cite the famous work done by Crommie *et al.* [24] on quantum corrals.

In this work, the sample consists of Fe atoms deposited on a Cu(111) surface. The authors observed in the STM images standing waves patterns resulting from the scattering (Fig.1.4 (a)) or the confinement of surface state electrons (Fig.1.4 (b)). These examples show that STM images are strongly affected by the

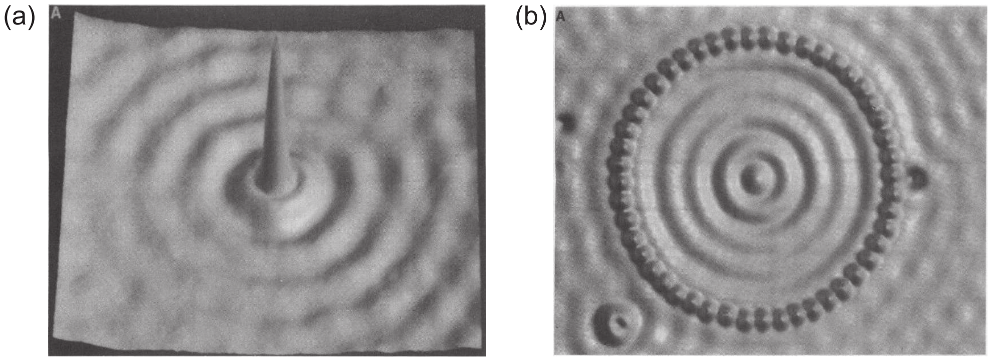

**Figure 1.4:** Electronic standing waves probed by STM. (a) STM image of a single Fe atom deposited on a Cu(111) surface. The concentric rings are standing waves due to the scattering of surface state electrons. (b) STM image of a ring of 48 Fe atoms deposited on a Cu(111) surface. The standing wave pattern is due to the closure of the ring that confines electrons inside t,he ring.

electronic states of the sample which have to be integrated into the expression of the tunnel current $I_t$.

In this paragraph, we will derive the one-dimensional expression of the tunnel current $I_t$ in the Bardeen formalism [3, 18]. The idea of this approach is to describe the state of an electron tunneling across the junction, which is delocalized on the two electrodes (tip and sample), on the basis set of states which are localized on the tip and the sample considered as two separated systems (Fig.1.5). Note that for the moment we are describing a symmetric situation between the two electrodes, especially we are not taking into account the shape of the tip.

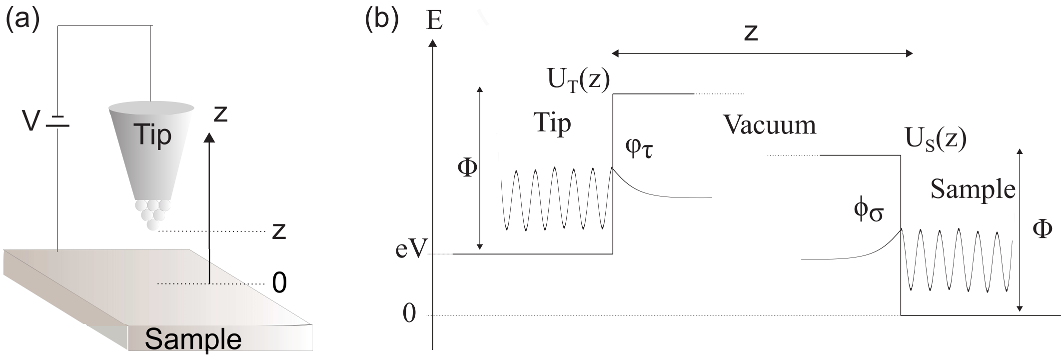

**Figure 1.5: Description of a STM junction and model of Bardeen.** (a) Sketch of the STM junction (tip-vacuum-sample junction). The tip and the sample are separated by a distance z. A voltage $V$ is applied between the tip and the sample. We considered that the tip is grounded ($V = 0$) while the sample is maintained at $V$. (b) Energetic sketch of the STM junction. When $z \to \infty$, wavefunctions in both electrodes decay in the vacuum. When $z$ is small enough tunneling is possible.

We first consider both electrodes as two separated systems ($z \to \infty$).

Assuming that the transport in the junction is essentially in the $z$ direction, the generic wavefunction $\Psi(\mathbf{r},t)$ of an electron in the tip satisfies the Schrodinger equation :

$$i\hbar\frac{\partial\Psi(\mathbf{r},t)}{\partial t}=\Big[-\frac{\hbar^2}{2m}\frac{\partial^2}{\partial z^2}+U_T(z)\Big]\Psi(\mathbf{r},t) \tag{1.3}$$

Where $U_T$ is the potential which is seen by the electron in the tip (Fig. 1.5(b)). From this equation the eigen wavefunctions of the tip are:

$$\Psi_\tau(\mathbf{r},t)=\psi_\tau(\mathbf{r})e^{-\frac{i}{\hbar}E_\tau t} \tag{1.4}$$

Where $\psi_\tau$ is the spatial part of the eigen wavefunctions that decay in the vacuum (Fig. 1.5(b)). It satisfies the equation :

$$\Big[-\frac{\hbar^2}{2m}\frac{\partial^2}{\partial z^2}+U_T(z)\Big]\psi_\tau(\mathbf{r})=E_\tau\psi_\tau(\mathbf{r}) \tag{1.5}$$

Similarly, the generic wavefunction $\Psi(\mathbf{r},t)$ of an electron in the sample satisfies the Schrodinger equation :

$$i\hbar\frac{\partial\Psi(\mathbf{r},t)}{\partial t}=\Big[-\frac{\hbar^2}{2m}\frac{\partial^2}{\partial z^2}+U_S(z)\Big]\Psi(\mathbf{r},t) \tag{1.6}$$

Where $U_S$ is the potential which is seen by the electron in the sample (Fig. 1.5(b)).
From this equation the eigen wavefunctions of the sample are :

$$\Phi_\sigma(\mathbf{r},t)=\phi_\sigma(\mathbf{r})e^{-\frac{i}{\hbar}E_\sigma t} \tag{1.7}$$

Where $\phi_\sigma$ is the spatial part of the eigen wavefunctions that decay in the vacuum (Fig. 1.5(b)). It satisfies the equation :

$$\Big[-\frac{\hbar^2}{2m}\frac{\partial^2}{\partial z^2}+U_T(z)\Big]\phi_\sigma(\mathbf{r})=E_\sigma\phi_\sigma(\mathbf{r}) \tag{1.8}$$

We have now two basis set of wavefunctions :

- The ensemble $\{\Psi_\tau\}_\tau$ is a basis of the tip states as an isolated system.
- The ensemble $\{\Phi_\sigma\}_\sigma$ is a basis of the sample states as an isolated system.

In Bardeen's tunneling theory it is assumed that the two sets of wavefunctions are orthogonal :

$$\langle\Psi_\tau|\Phi\sigma\rangle=0 \tag{1.9}$$

If $z$ is small enough (the order of the decay length defined in the previous paragraph) the two electrodes get coupled. The generic wavefunction $\Psi(\mathbf{r},t)$ of an electron, which is now delocalized on the two electrodes, satisfies the equation :

$$i\hbar\frac{\partial\Psi(\mathbf{r},t)}{\partial t}=\Big[-\frac{\hbar^2}{2m}\frac{\partial^2}{\partial z^2}+U_T(z)+U_S(z)\Big]\Psi(\mathbf{r},t) \tag{1.10}$$

Since the tip and the sample are now coupled $\Psi_\tau$ and $\Phi_\sigma$ are no more stationary states of the coupled system. Consequently, an electron prepared at $t = 0$ in a state $\psi_\tau$ (starting from the tip) will not evolve according to 1.4, it has a chance to be transferred in a state of the sample. The state $\Psi(\mathbf{r}, t)$ of this electron can thus be written as :

$$\Psi(\mathbf{r}, t) = \psi_\tau(\mathbf{r})e^{-\frac{i}{\hbar}E_\tau t} + \sum_{\sigma=1}^{+\infty} c_\sigma(t)\phi_\sigma(\mathbf{r})e^{-\frac{i}{\hbar}E_\sigma t} \tag{1.11}$$

Since $\Psi(\mathbf{r}, t = 0) = \psi_\tau$, it gives the following condition :

$$\forall\, \sigma, c_\sigma(t = 0) = 0 \tag{1.12}$$

By injecting the expression 1.11 in 1.10 the evolution equation for the $c_\sigma$ coefficients is :

$$i\hbar \sum_{\sigma=1}^{+\infty} \frac{dc_\sigma(t)}{dt}\phi_\sigma e^{-\frac{i}{\hbar}E_\sigma t} = U_S\psi_\tau e^{-\frac{i}{\hbar}E_\tau} + U_T \sum_{\sigma'=1}^{+\infty} c_{\sigma'}(t)\phi_{\sigma'}(\mathbf{r})e^{-\frac{i}{\hbar}E_{\sigma'} t} \tag{1.13}$$

The second term in the equation 1.13 is a second-order quantity, therefore, the dynamic is driven mainly by the first term: the potential of the sample acting on the "starting" state. Keeping the first order term and using the condition 1.9, the projection of 1.13 leads to the evolution equation for $c_\sigma$ :

$$\frac{dc_\sigma}{dt} = -\frac{i}{\hbar}\langle\phi_\sigma|U_S|\psi_\tau\rangle\, e^{-\frac{i}{\hbar}(E_\tau - E_\sigma t)} = -\frac{i}{\hbar}M_{\sigma\tau}e^{-\frac{i}{\hbar}(E_\tau - E_\sigma t)} \tag{1.14}$$

Where we defined the **tunneling matrix element** $M_{\tau\sigma}$ :

$$M_{\tau\sigma} = \langle\phi_\sigma|U_S|\psi_\tau\rangle = \int d^3\mathbf{r}\phi_\sigma^*(\mathbf{r})U_S(\mathbf{r})\psi_\tau(\mathbf{r}) \tag{1.15}$$

Bardeen has shown [3] that it is possible to express this matrix element as:

$$M_{\tau\sigma} = \frac{\hbar^2}{2m}\int d\mathbf{S}\{\psi_\tau^*(\mathbf{r})\nabla(\phi_\sigma(\mathbf{r})) - \phi_\sigma(\mathbf{r})\nabla(\psi_\tau^*(\mathbf{r}))\} \tag{1.16}$$

Where $\nabla$ is the gradient operator. The physical interpretation of the tunneling matrix element is the following: it is a flux of the probability current.

Using 1.12 and integrating 1.14 over time gives :

$$c_\sigma(t) = M_{\tau\sigma}\frac{e^{-\frac{i}{\hbar}(E_\tau - E_\sigma)t} - 1}{E_\tau - E_\sigma} \tag{1.17}$$

Starting from the tip in a state $\psi_\tau$ the probability to find the electron in the sample in the state $\phi_\sigma$ after a time $t$ is therefore :

$$P_{\tau\sigma}(t) = |c_\sigma(t)|^2 = |M_{\tau\sigma}|^2\frac{4sin^2(\frac{\Delta Et}{2\hbar})}{\Delta E^2} \tag{1.18}$$

Where $\Delta E = E_\tau - E_\sigma$. Introducing the function $\delta_t$ defined as :

$$\delta_t(\Delta E) = \frac{2\hbar sin^2(\frac{\Delta E t}{2\hbar})}{\pi t(\Delta E)^2} \tag{1.19}$$

This function can be consider as a Dirac delta function if $t$ is long enough : $\lim\limits_{t \to +\infty} \delta_t(\Delta E) = \delta(\Delta E)$. In our case if we assume that the tunneling time $t$ is such that $t >> \frac{2\hbar}{\Delta E}$ we can write then :

$$P_{\tau\sigma}(t) = \frac{2\pi}{\hbar}|M_{\sigma\tau}|^2\delta(E_\tau - E_\sigma)t \tag{1.20}$$

From this one can define the *transition rate* $\gamma_{\sigma\tau}$ as :

$$\gamma_{\tau\sigma} = \frac{dP_{\tau\sigma}(t)}{dt} = \frac{2\pi}{\hbar}|M_{\tau\sigma}|^2\delta(E_\tau - E_\sigma) = \frac{2\pi}{\hbar}|\langle\phi_\sigma|U_S|\psi_\tau\rangle|^2\delta(E_\tau - E_\sigma) \tag{1.21}$$

This expression is very similar to the well known Fermi Golden rule which is obtained in the time-dependant perturbation theory [117]. It describes the probability per unit of time of tunneling from a tip state $\Psi_\tau$ to a sample state $\Phi_\sigma$. The delta function imposes an important condition on the tunneling process : $E_\tau = E_\sigma$, it has to be an elastic process. We often speak about **elastic tunneling** process in this case because we will see later that an **inelastic tunneling** process is also possible and has important consequences especially in the framework of this thesis.

Even though this expression seems familiar, we want to point out that what has been done so far is not a "standard" time-dependant perturbation theory. As stated before $\{\Psi_\tau\}_\tau$ are eigenstates of the *tip* Hamiltonian $H_T$ and $\{\Phi_\sigma\}_\sigma$ are eigenstates of the *sample* Hamiltonian $H_S$. Consequently the concatenation of those two sets of states **does not** form a complete orthogonal basis of the eigenspace of the $\{tip + sample\}$ Hamiltonian $H_{T+S}$. Therefore, equation 1.14 is not sufficient to determine the "real" wavefunction $\Psi(\mathbf{r}, t)$. This is a fundamental weakness of Bardeen's theory. However in the "weakly" coupled regime *i.e*, the tip and the sample are still far, even though still in the tunneling regime the approach of Bardeen has produced reliable results [47, 62].

Eventually, to write the complete expression of the transition rate from the tip to the sample we have to take into account two things :

- A voltage $V$ is applied to the sample (Fig. 1.5).
- Tunneling can occurs only from occupied states of the tip to unoccupied states of the sample. The transition rate has to be multiplied by the probability : $f_{E_F+eV}(E_\tau)(1 - f_{E_F}(E_\sigma))$. Where $f_\mu$ is the Fermi-Dirac distribution given by $f_\mu(E) = \frac{1}{e^{\frac{(E-\mu)}{k_B T}}+1}$. $E_F$ corresponds to the Fermi level of the sample (or both tip and sample when $V$ = 0).

Doing so the transition rate from the tip to the sample reads :

$$\gamma_{\tau\sigma}^{T\to S} = \frac{2\pi}{\hbar}|M_{\tau\sigma}|^2\delta(E_\tau - E_\sigma) \times f_{E_F+eV}(E_\tau)(1 - f_{E_F}(E_\sigma)) \tag{1.22}$$

Since so far we have not made a difference between the two electrodes, the transition rate from the sample to the tip can be easily deduced :

$$\gamma_{\sigma\tau}^{S\rightarrow T} = \frac{2\pi}{\hbar}|M_{\sigma\tau}|^2\delta(E_\tau - E_\sigma) \times f_{E_F}(E_\sigma)(1 - f_{E_F+eV}(E_\tau)) \tag{1.23}$$

We can associate two elementary currents to the two transition rates :

$$\begin{aligned} \delta I_{\tau\sigma}^{T\rightarrow S} &= e \times \gamma_{\tau\sigma}^{T\rightarrow S} && (1.24) \\ \delta I_{\sigma\tau}^{S\rightarrow T} &= e \times \gamma_{\sigma\tau}^{S\rightarrow T} && (1.25) \end{aligned}$$

Where $e$ is the elementary charge of the electron.

Finally we can write the total current that cross the junction by simply summing up those two elementary currents over all states of the tip and the sample :

$$\begin{aligned} I_t &= 2 \times \sum_{\tau\sigma} \delta I_{\tau\sigma}^{T\rightarrow S} - 2 \times \sum_{\sigma\tau} \delta I_{\sigma\tau}^{S\rightarrow T} && (1.26) \\ I_t &= \frac{4\pi e}{\hbar} \sum_{\tau\sigma} |M_{\tau\sigma}|^2 \delta(E_\tau - E_\sigma)\{f_{E_F+eV}(E_\tau) - f_{E_F}(E_\sigma)\} && (1.27) \end{aligned}$$

Where the factor 2 is introduced to take into account the spin. We assume that $|M_{\tau\sigma}|^2 = |M_{\sigma\tau}|^2$.

### Model of Tersoff and Hamann.

So far no assumption has been done regarding the shape or the structure of the tip. The main contribution of Tersoff *et al.* [118] is assuming that the states $\psi_\tau$ of the tip are spherical waves. In other words the authors assumed the following expression for $\psi_\tau$ :

$$\psi_\tau(\mathbf{r}) = C_\tau \frac{e^{-\rho_\tau|\mathbf{r}-\mathbf{r_0}|}}{|\mathbf{r}-\mathbf{r_0}|} \tag{1.28}$$

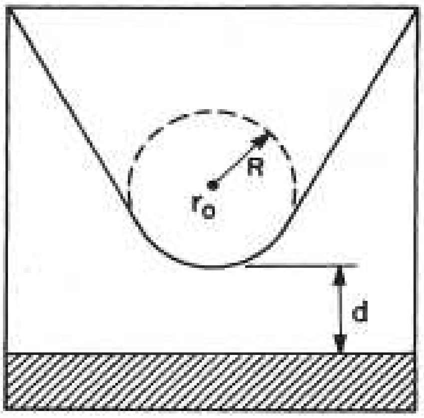

**Figure 1.6: Sketch of the tip geometry assumed by Tersoff and Hamann.** The end of the tip is assumed to be a sphere or radius $R$. The center of the sphere is located to $\mathbf{r_0}$, the tip-sample distance is d. Reproduced from [118].

With $\rho_\tau$ the decay constant defined in the first paragraph. $\rho_\tau = \sqrt{\frac{2m(\Phi-E_\tau}{\hbar^2}}$ where $\Phi$ is the work function.

With this expression for $\psi_\tau$ they showed that the tunneling matrix element can be written as follow :

$$M_{\tau\sigma} \propto \phi_\sigma(\mathbf{r_0}) \tag{1.29}$$

By introducing a continuous summation in 1.27 we get :

$$I_t = \frac{4\pi e}{\hbar} \int_{-\infty}^{+\infty} dE \sum_{\tau\sigma} |M_{\tau\sigma}|^2 \delta(E_\tau - E)\delta(E - E_\sigma)\{f_{E_F+eV}(E) - f_{E_F}(E)\} \tag{1.30}$$

Substituting 1.29 in this expression we end with :

$$I_t \propto \int_{-\infty}^{+\infty} dE \rho^T_{E_F+eV}(E)\rho^S_{E_F}(\mathbf{r_0}, E)\{f_{E_F+eV}(E) - f_{E_F}(E)\} \tag{1.31}$$

Where $\rho^S$ is the **Local Density of States of the sample (LDOS)** defined by : $\rho^S_{E_F}(\mathbf{r_0}, E) = \sum_\sigma |\phi_\sigma(\mathbf{r_0})|^2 \delta(E - E_\sigma)$ and $\rho^T$ is the density of state of the tip $\rho^T$.

Finally, by using the Fermi level of the sample as a reference ($E_F$) we can use the following identities :

- $f_{E_F+eV}(E) = f_{E_F}(E - eV)$
- $\rho^T_{E_F+eV}(E) = \rho^T_{E_F}(E - eV)$

We can write an integrated form of the tunneling current in the following way :

$$I_t \propto \int_{-\infty}^{+\infty} dE \rho^T(E - eV)\rho^S(\mathbf{r_0}, E)\{f(E - eV) - f(E)\} \tag{1.32}$$

All experiments of this thesis have been performed at low temperature $T \approx 4K$. Therefore the Fermi-Dirac distribution can be approximated by an heavyside function. The final expression of the tunnel current reads :

$$I_t \propto \int_0^{eV} dE \rho^T(E - eV)\rho^S(\mathbf{r_0}, E) \tag{1.33}$$

This expression shows that the tunneling current is directly related to the local density of state of the sample. Therefore electronic states of the sample will affect drastically the STM images. We can resume by saying that an STM image is a topography convoluted with the density of state of the probed surface.

Even though expression 1.33 allows one to understand the origin of the STM sensitivity to the sample electronic states, it does not highlight the dependency of the tunneling probability with the energy.

In the framework of the situation described Fig.1.7, an other expression of $I_t$ can be obtained in the semi-classical Wentzel-Kramers-Brillouin theory (WKB) [120] :

$$I_t \propto \int_{-\infty}^{+\infty} dE \rho^T(E - eV)\rho^S(E)\{f(E - eV) - f(E)\}T(z, E, V) \tag{1.34}$$

The interest of this expression compared to 1.33 is that it makes appear $T$ the transmission coefficient which depends on the shape of the barrier. $\rho^T$ and $\rho^S$ are the density of states of the tip and the sample respectively. Considering the tip apex as a single atom it is possible to assume that only the s-states play a role, this leads to a rather "flat" density of state. At low temperature condition, the previous expression can be written :

$$I_t \propto \int_0^{eV} dE \rho^S(E)T(z, E, V) \tag{1.35}$$

For a trapezoidal shape such as the one described in Fig.1.7 (c) and (d) it is possible to express the transmission as follows :

$$T(z, E, V) \propto e^{-2z\sqrt{\frac{2m}{\hbar^2}(\Phi - E + \frac{eV}{2})}} \tag{1.36}$$

This expression shows that the higher the electron energy the higher the probability to tunnel (which is represented by the arrows in Fig.1.7 (c) and (d). It allows us also to recover the exponential dependency of the tunnel current with the tip-sample distance $z$ that confers the high sensitivity of the STM.

### Expression of the tunnel current in the WKB approximation

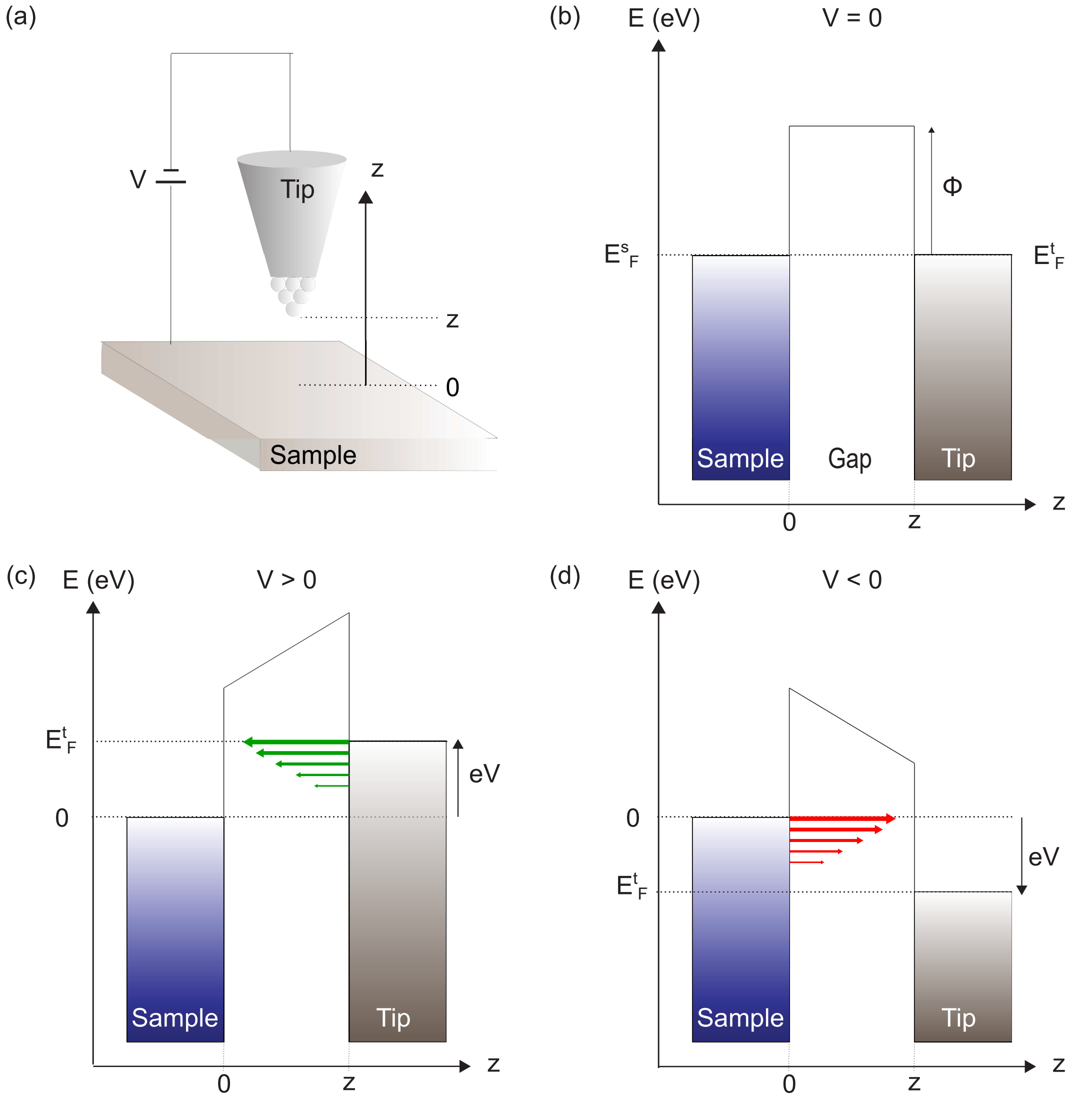

**Figure 1.7: Description of a metal-metal tunnel junction.** (a) Sketch of an STM junction that consists of applying a voltage between a metal tip and a metal sample. By convention, the electric potential $V$ is applied to the sample. (b) Energetic sketch of the tunnel junction at $V = 0$. The blue rectangle (resp. grey) represents the energy band of the sample (resp. tip). The gap between the tip and the sample is energetically modelled by a potential barrier with a height corresponding to the work function of the metal $\Phi$. At $V = 0$, the Fermi levels of the sample and the tip are aligned. (c) Energetic sketch of the tunnel junction at $V > 0$. The Fermi level of the sample is considered as the reference of energy ($E^s_F = 0$). If $V > 0$ the energy of electrons in the sample is changed by a term $-eV$ with respect to $E^t_F$. The Fermi level of the tip is above the Fermi level of the sample. Electrons are flowing from the occupied states of the tip to the unoccupied states of the sample (green arrows). (d) Energetic sketch of the tunnel junction at $V < 0$. If $V < 0$ the energy of electrons in the sample is changed by a term $-e(-V) = eV$ with respect to $E^t_F$. The Fermi level of the tip is below the Fermi level of the sample. Electrons are flowing from the occupied states of the sample to the unoccupied states of the tip (red arrows).

Finally one can simply describe the tunneling process in an STM junction as follow :

- If $V > 0$ the electrons are flowing from the filled states of the tip to the empty states of sample: the empty states of the sample are probed 1.7 (c).
- If $V < 0$ the electrons are flowing from the filled states of the sample to the empty states of the tip: the filled states of the sample are probed 1.7 (d).

### 1.1.3 Practical STM image recording.

Previously we have described how an STM junction is working. The origin of STM sensitivity relies on the exponential dependency of the tunnel current $I_t$ with the tip-sample separation $z$.

To move the tip with atomic-scale precision, this latter is fixed on a piezoelectric tube that can move in the three directions of space by applying three corresponding voltages (Fig. 1.8 (a)). This operation is performed utilizing a control unit (C.U.) that essentially controls all the physical parameters used to operate the STM. The C.U. applies the voltage $V$ to the junction and measures the tunnel current $I_t$ after conversion by a pre-amplifier.

The STM images can be recorded in two modes:

- In the constant height mode, the tip is maintained at a constant z-piezo extension (Fig. 1.8 (b)) while the tip is scanning in the (x,y) plane. Concomitantly, the value of the tunnel current is registered for each position of the tip. The representation of the function $I_t(x,y)$ gives an image (often referred to current-image) of the surface.
- In the constant current mode, the z-direction of the tip is adjusted during the scan to keep $I_t$ by the means of a feedback loop acting on the voltage $V_z$ applied on the piezo tube $V_z$ (Fig. 1.8 (c)). In the same time, the displacement of the tip $\Delta z$ is registered for each position (x,y) of the tip. The representation of the function $\Delta z(x,y)$ yields a topographic image of the surface.

In practice, the constant current is preferred because it allows imaging large scale areas and non-flat surfaces without risking to damage the tip. The constant current mode was the one used by Binnig and Roher to obtain the $7 \times 7$ Si surface image [8].

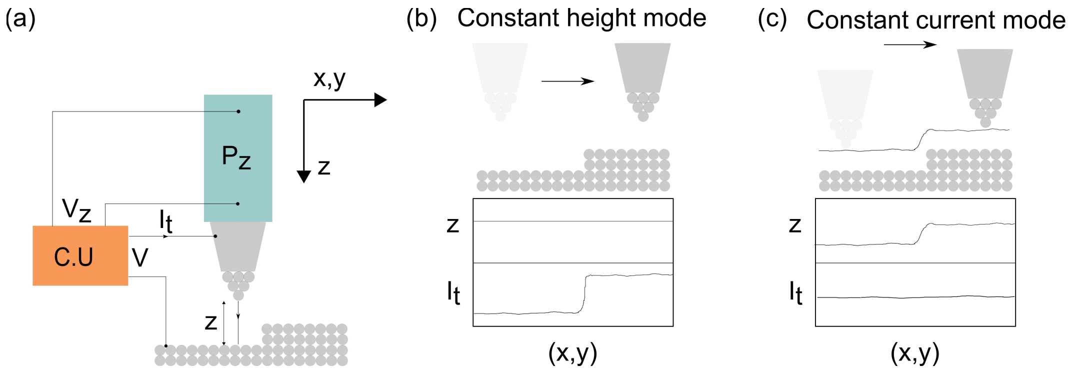

**Figure 1.8: Operation of STM imaging.** (a) Sketch of the tip displacement system. The metal tip is fixed on a piezo tube which can be moved in the three directions of space. A voltage $V$ is applied between the sample and the tip, the tunneling current $I_t$ is amplified and then measured. The displacement of the tip is performed by applying 3 different voltages $V_{x,y,z}$ (only the z-direction is represented here for simplicity) in the three direction x,y,z of the piezo tube. (b) Constant height mode. The z-distance is held constant by maintaining a constant voltage $V_z$ on the piezo tube. (c) Constant current mode. In this mode, a feedback loop is used to systematically adjust the z-distance.

### 1.1.4 Scanning tunneling spectroscopy

From expression 1.33 we see that the value of the tunnel current is strongly dependant of the LDOS of the sample. This expression explains why we can visualize electronic state such as surface states of the sample like the ones shown in Fig. 1.4. However, with this integrated form we lose spectral information about these states.

If we differentiate expression 1.33 with respect to V and if we assume that the density of state of the tip is constant we obtain :

$$\frac{dI_t}{dV}(V) \propto \rho^S(\mathbf{r_0}, eV) \tag{1.37}$$

The value of the **differential conductance** $\frac{dI_t}{dV}(V)$ is directly proportional to the value of the sample LDOS at the energy $eV$. The Scanning Tunneling Spectroscopy (STS) utilizes this relation to obtain spectral information on the sample. An STS experiment consists essentially to measure the differential conductance while sweeping the voltage $V$. Therefore the existence of a sample state at an energy $E$ will induce an increase of the differential conductance for $V = \frac{E}{e}$ so a peak in the so-called differential conductance spectrum.

### 1.1.5 Example : STM image and STS on single molecule

When a molecule is directly adsorbed on a metallic surface, the electronic states of the molecule are hybridized with the ones of the metal surface. Therefore one cannot access to the intrinsic electronic properties of the molecule. An approach, used in this thesis, to obtain characteristic electronic features of a single molecule is to decouple the molecule from the metal surface by a thin layer of an insulator such as NaCl [99, 101, 100, 116] (Fig. 1.9 (a)). In such a way, the current and the differential conductance (see expression 1.33 and 1.37) are directly sensitive to the "molecular LDOS". In this manuscripts, we will often consider two particular states of the molecule: the **Lowest Unoccupied Molecular Orbital** (LUMO) which is above the Fermi level and the **Highest Occupied Molecular Orbital** (HOMO) which is below the Fermi level (Fig. 1.9 (b)).

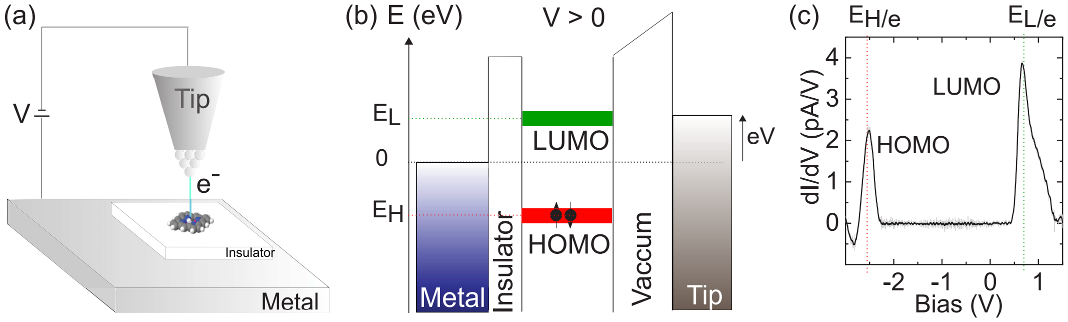

**Figure 1.9: Tunneling through molecular orbitals.** (a) Sketch of the STM junction. The insulating layer is usually several atomic layers thick. (b) Energetic sketch of the double barrier junction. (c) Experimental differential conductance obtained on a single free-base phthalocyanine molecule decoupled from an Ag(111) surface by a thin layer of NaCl.

At a voltage $V_L = \frac{E_L}{e}$ a conductance resonance will appear in the differential conductance spectrum, because tunneling takes place into the molecule LUMO(Fig. 1.9 (c)). Similarly, at a voltage $V_H = \frac{E_H}{e}$ a resonance corresponding to the HOMO appears in the spectrum (Fig. 1.9 (c)).

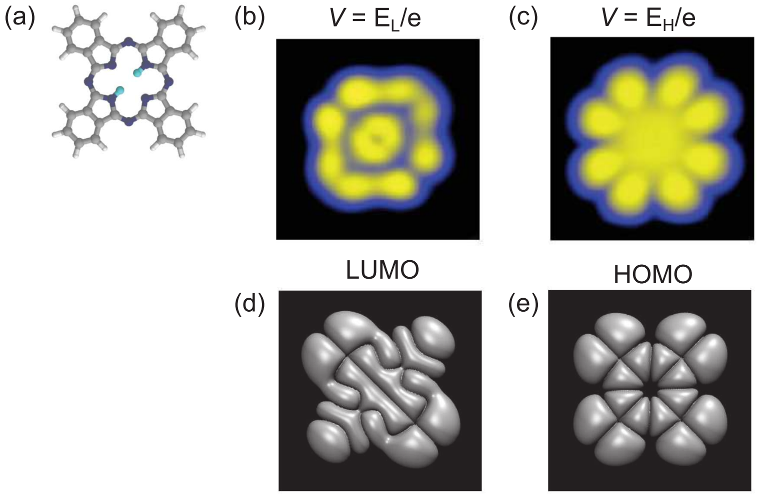

**Figure 1.10: Voltage dependency of STM images.** (a) Topological structure of an $H_2Pc$ molecule. (b) STM image of the $H_2Pc$ LUMO orbital (3 × 3 nm$^2$; $V$ = +0.5V; $I$ = 10pA). (c) STM image of the $H_2Pc$ HOMO orbital (3 × 3 nm$^2$; $V$ = -2.5V; $I$ = 10pA). (d) LUMO orbital obtained by DFT. (e) HOMO orbital obtained by DFT.

Because of the strong increase in the differential conductance, if the voltage $V_L$ (resp. $V_H$) is used for imaging, the main channel of conduction is the one tunneling through the LUMO orbital (resp. HOMO). The remaining pattern in the image (Fig. 1.10 (b) resp. Fig. 1.10 (c) will, therefore, be extremely impacted by the structure of the LUMO itself (Fig. 1.10 (d)) (resp. HOMO (Fig. 1.10 (e) ).

## 1.2 Experimental setup

### 1.2.1 Microscope and preparation

**The microscope**

The experiments of this thesis have been done with a low-temperature commercial Omicron STM 1.11. The STM head (sample and tip) is cooled down by thermal contact with a cryostat filled with helium. This cryostat is shielded with a cryostat filled with nitrogen to protect the He-cryostat from thermal radiation. The STM chamber is kept in Ultra High Vaccum (UHV) conditions by the means of an ionic pump. In the low temperature working regime the base pressure is $P = 5 \times 10^{-11}$ mbar and the sample is kept at a stable temperature of 4.7 K.

When the STM head has reached the thermal equilibrium, it can be decoupled from the He-cryostat to dump the noise coming from external vibrations. This is done by the means of three metallic springs and an eddy current damping stage. Besides, the whole STM is also decoupled from the ground by four pneumatic cylinders. Under these conditions, the "mechanical" noise on the $z$ measurement can be reduced down to 3 pm (peak to peak).

The STM chamber is equipped with a Kentax evaporator with 3 independent crucibles that allow us to evaporate organic molecules directly on the cooled (4.7 K) sample, to avoid molecular diffusion on the surface.

**Tip and sample preparation.**

The STM chamber is connected via a valve to a preparation chamber that allows us to prepare tips and samples. This preparation chamber is kept under UHV conditions (base pressure : $1 \times 10^{-10}$ mbar). The chamber is equipped with an argon ion gun used to sputter the samples and a heating system used for samples annealing. The preparation chamber is equipped with a molecular evaporator with four different crucibles that allows us to mainly evaporate organic compound and different types of salts.

We insert samples and tips from the outside in the preparation chamber through a load-lock chamber which is pumped to reach preliminary vacuum of $\approx 10^{-7}$ mbar.

**Tip preparation.**

The tips used in the framework of this thesis are tungsten tips. Sharp tips are obtained by conducting an electrochemical etching with a NaOH solution on a 0.25 mm diameter tungsten wire [32]. Once the tip is inside of the preparation chamber, it is eventually annealed and sputtered to remove all possible contamination on the tip.

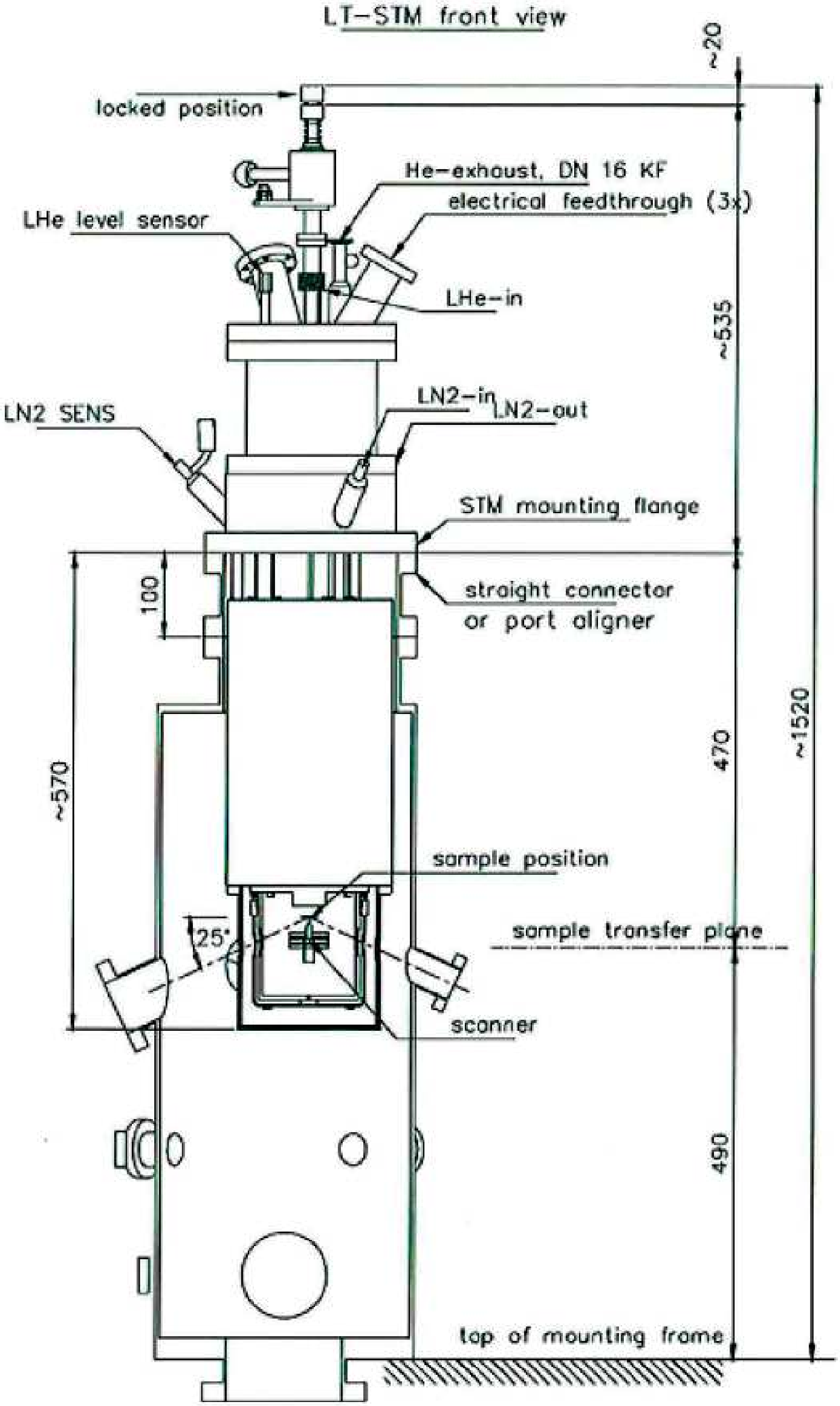

**Figure 1.11: Scheme of the LT-STM Omicron.** Source : Omicron GmbH

To obtain a satisfying plasmonic response (see next chapter) the tungsten tip is indented in the working surface (gold or silver) to cover it with the corresponding metal.

**Sample preparation**

The samples used during this thesis are Au(111) and Ag(111) substrates which are covered with atomic layers of NaCl. This extra layer of salt is used as an insulator to electronically decouple the probed molecule from the metallic substrate. The molecules studied in this work are essentially phthalocyanine molecule ($H_2$PC and ZnPc).

Typical sample preparation starts by cleaning the substrate with several cycles of sputtering and annealing. The sputtering is realized with an ionic gun that creates and accelerates $Ar^+$ ions toward the sample. This step of sputtering is needed to remove dirt and remaining compounds coming from previous experiments. But, it also removes several layers of the metallic substrates, creating defects on the surface. That is why the second step of annealing is necessary. By heating the sample at a temperature of $\approx$ 350 °C it allows the metal atoms to diffuse and create large terraces along with the cutting plane of the sample (here (111)) and also to segregate some remaining dirt trapped in the bulk. These sputtering-annealing cycles are repeated until the substrate is clean.

When this is done, the thermal evaporation (under a crucible temperature of $\approx$ 300 °C) of the salt can be realized. Once the needed amount of salt is deposited on the surface, a last annealing can be done on the substrate essentially to modify the thickness of the salt clusters (from 2 to 8 atomic layers thickness).

Finally, the investigated molecules are deposited directly in the STM chamber on the cooled sample via thermal evaporation as well. The evaporation flux during all thermal evaporation is measured employing a quartz balance. This allows us to adjust the evaporation time and control in a very reproducible way the amount of salt and molecules on the sample.

## 1.2.2 Optical setup

### The light collecting system

As we will describe it in the next chapter, under a voltage $V \approx 2$V the tunneling electrons have enough energy to generate light emission from the plasmonic modes of the STM junction. Our STM has been equipped with an entire optical setup to collect and analysed the light emitted in the junction. This setup consists of collecting the light by mean of a lens (L1) placed so that the tip-sample junction is at the focal point (Fig. 1.12). Doing so, the collimated beam will pass through the two cryostat windows and sent outward of the STM chamber. Once the beam is outside it can be split into two paths (red and blue arrows in Fig. 1.12) by a flipping mirror (M).

- In the first path (blue arrow) the collimated beam is focused into an optical fiber by a lens (L2), then transported to a spectrometer coupled to a charge-coupled device (CCD) camera to obtain an optical spectrum.

- In the second path (red arrow) the collimated beam is split by the mean of a beamsplitter (BS), then focused by the lens (L3) and (L4) into optical fibers leading to two Single Photon Counters (SPC1 and SPC2).

This optical setup allows us to obtain both spectral (with the spectrometer and the CCD) and temporal resolution (with the SPC detectors).

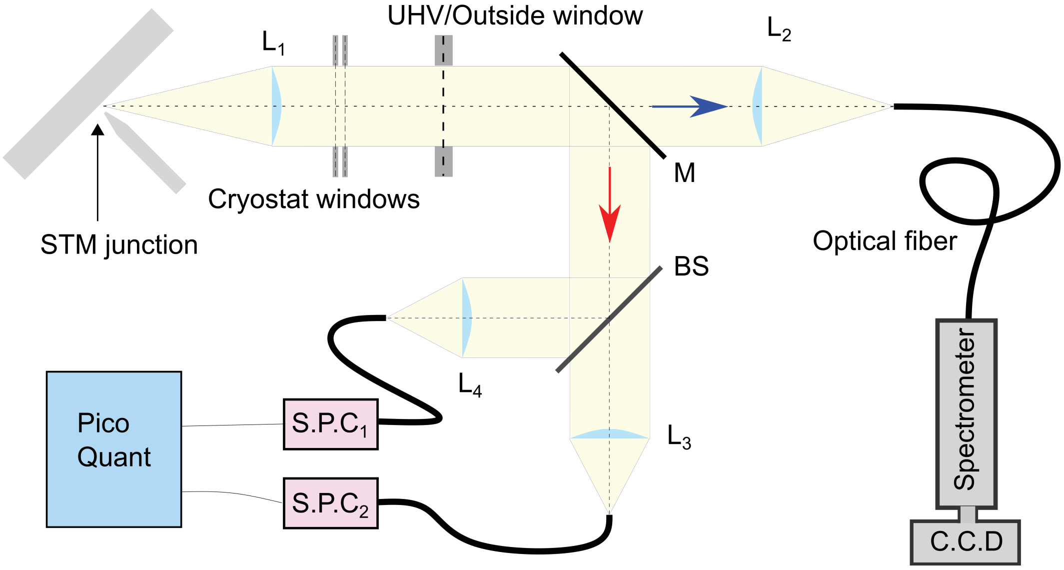

**Figure 1.12: Sketch of the optical setup.**

**The collecting system in the STM head.**
The collecting system in the STM head which has been developed by Keizer et al. [53] is directly provided by Omicron. The lens (L1) (diameter $d = 9.9$ mm; focal $f = 15.0$ mm; numerical aperture $N.A = 0.543$) is fixed with an angle $\theta = 25°$ with respect to the sample. This value of 25° is taking into account the calculated angular distribution of emission for a metal-metal STM junction (maximum for $\theta = 30°$ and symmetrical around the tip axis [5]) and the space required for the lens which is limited by the design of the STM head. The amount of light which is collected depends essentially on the solid angle covered by the lens. We estimate that in the actual configuration 6 to 10 % of the light emitted in the junction is collected by the lens.

**The collecting system outside of the STM head.**
The two BK7 glass cryostat windows and the UHV window have a transmission of more than 90% in the 400-1000 nm range. On the main optical path (blue arrow in Fig. 1.12 the focusing lens (L2) is an achromatic doublet from Thorlabs (AC254-050-B; diameter $d = 25$ mm; focal $f = 50$ mm; transmission represented Fig. 1.13 (a)). The optical fiber (OF1) is a bundle of 7 optical fibers (diameter of 200 $\mu$m, see transmission Fig. 1.13 (b)). These fibers are disposed in circle in the side of (L2) to optimize the coupling with the focused light. On the other optical path (red arrows Fig. 1.12) the mirror (M) used is a Thorlabs gold-coated mirror (diameter $d = 25$ mm). The beam splitter (BS) is a Thorlabs cube beam splitter 700-1100 nm ( transmission Fig. 1.13 (c)). The two focusing

lenses (L3) and (L4) are the same as (L1). The two optical fibers (OF2) and (OF3) are Excelitas QC6 multimode fibers (diameter $d = 100\ \mu$m).

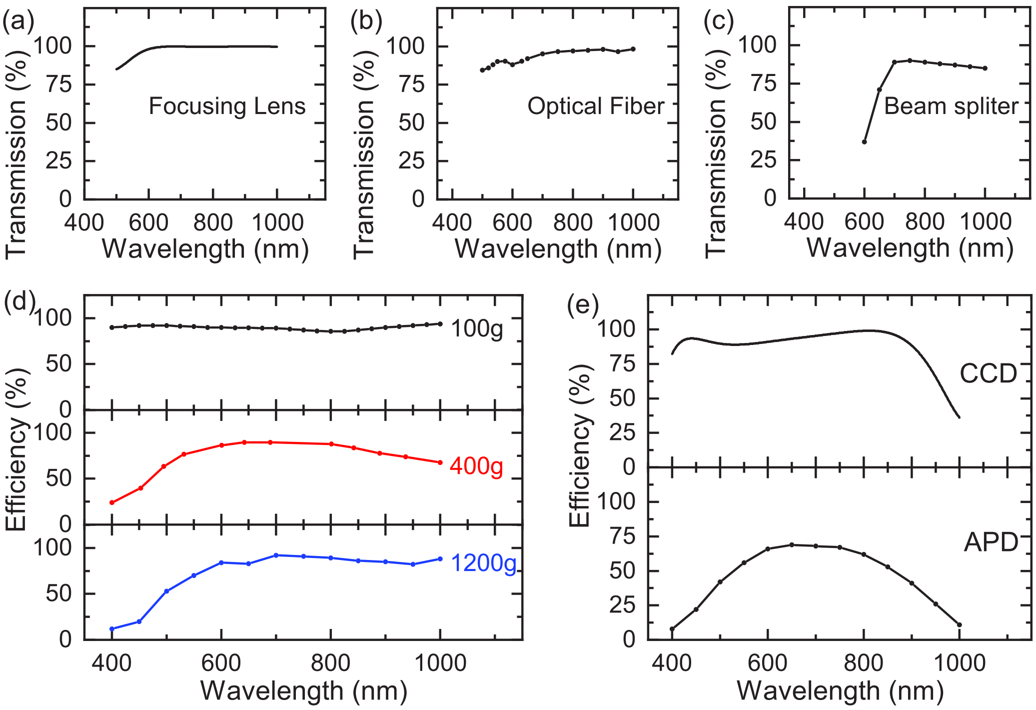

**Figure 1.13: Transmission and efficiency of the optical components.** (a) Focusing lens transmission as a function of the wavelength (Thorlabs AC 254-050-B) (b) Transmission of the optical fiber (SEDI ATI 7 × 200 Vis-IR). (c) Transmission of the beam splitter (Thorlabs cube beam splitter 700-1100 nm) (d) Efficiency of the three different gratings. (e) Efficiency of the CCD camera (top pannel) and the APD (lower pannel).

### The light analyzing system.

#### Spectral analysis with the spectrometer and the CCD camera.

We used an Acton SP2300 spectrometer coupled with a Pylon Excelon 100BR CCD together provided by Princeton instrument (efficiency Fig. 1.13 (e)) [1]. To optimize the light coupling from the optical fiber (OF1) to the spectrometer, the bundle of fibers is disposed in a line and directly put in front of the spectrometer entrance slit. Therefore, the illuminated slit becomes the optical source analyzed by the spectrometer. The spectrometer is equipped with three different gratings (efficiency given in Fig. 1.13 (d)). The first one has 100 grooves/mm and is blazed at 750 nm. The second one has 400 grooves/mm and is blazed at 850 nm. The last one has 1200/mm grooves and is blazed at 780 nm. Once the light

---

[1] Some data have been obtained with a similar setup composed of a Pylon Excelon 400BR and an Isoplane 320 spectrometer also from Princeton instrument.

coming from the illuminated slit is diffracted by the grating , we observe (by the mean of a projecting lens with a focal $f$ = 300 mm) the first-order diffraction pattern on the rectangular CCD sensor of the camera ($l_x$ = 100 pixels; $l_y$ = 1340 pixels; pixel size : 20 $\times$ 20 $\mu$m). The orientation of the sensor is chosen to match its x-direction with the direction of the slit, in the direction of each band appearing in the diffraction pattern. Then, the 100 pixels of each 1340 rows of the sensor are binned to build a spectrum which gives a number of counts for each row. If a range of wavelength $\Delta\lambda$ is observed on the sensor the wavelength step $\delta\lambda$ is therefore given by :

$$\delta\lambda = \frac{\Delta\lambda}{1340} \tag{1.38}$$

For a given grating and at a fixed incident angle, the angular deviation with the wavelength at the first order is :

$$\frac{d\theta}{d\lambda} = \frac{d}{cos(\theta)} \tag{1.39}$$

Where $\theta$ is the observation angle and $d$ the number of grooves per mm. We see that the dispersion over the CCD sensor is proportional to the number of grooves per mm. Since the CCD sensor size is fixed, a grating with higher dispersion will reduce the observable range of wavelength $\Delta\lambda$ on the sensor and therefore increase the resolution. Since the angle $\theta$ is limited by the size of the sensor and the focal $f$ of the projecting lens of the spectrometer, by integrating 1.39 the wavelength range can be evaluated as:

$$\Delta\lambda = \frac{2(sin(\theta_{max}) - 1)}{d} \tag{1.40}$$

With $\theta_{max}$ the maximum observation angle which is given by:

$$\theta_{max} = Arctan(\frac{L}{2f}) \tag{1.41}$$

Where L is the size of the sensor in the y-direction ($L$ = 1340 $\times$ 20 $\mu$m). The wavelength range for each grating is summarized in the tabular Fig. 1.14.

| Grating | Δλ (nm) | δλ (nm) | Resolution (nm) | Resolution (meV) |
|---|---|---|---|---|
| 100 g/mm | 890 | 0.7 | 2.4 | 7 |
| 400 g/mm | 220 | 0.2 | 0.6 | 1.8 |
| 1200 g/mm | 74 | 0.06 | 0.2 | 0.6 |

**Figure 1.14: Comparison of the three different gratings.** The resolution in meV is calculated at a central wavelength of 650 nm as an example.

Because of the Rayleigh criterion, the entrance slit opening has a drastic effect on the resolution. However, we are often looking for weak signals, so the resolution has to be trade-off for a sufficient luminosity. In our experiments, the slit is opened at 70 $\mu$m. The wavelength calibration is performed with a He-Ar lamp (Princeton instruments). Finally, the spectral resolution of the entire setup is deduced by measuring the FWHM of a spectral lamp specific ray which is extremely narrow. These experimental resolution are given in the table of Fig. 1.14.

In brief, we are using the 100 grooves/mm grating for measuring a signal on a large range of wavelength, while the 400 grooves/mm is used to obtain more detailed spectroscopic data such as vibronic spectra. In some cases the 1200 grooves/mm grating is used to resolve very fine features. One has to note that we can easily turn from one grating to another during the experiment. Taking into account the transmission and the efficiency of each component in the collecting chain, we estimate that we collect 2-5 % of the light emitted in the junction.

**Temporal analysis with the Single Photon Counters**

The single-photon counters used for temporal measurements are Si-avalanche Photodiodes (Excelitas SPCMS-AGRH-FC). They can detect single photons over the wavelength range of 400-1060 nm (see efficiency Fig. 1.13 (e)) and allows to obtain temporal traces with an important time resolution. Moreover, the setup is designed to perform Hanbury Brown and Twiss interferometry experiment, that we will describe later in the manuscript.

# Chapter 2

# Light Emission process in a STM junction

Under a bias voltage $V \approx 2$ V a tunneling electron carries an energy that corresponds to visible light (wavelength $\lambda \approx 600$ nm). On another hand, the apex of the STM tip is made of metallic structures of size $d \ll \lambda$. Therefore, like antennas in other electromagnetic domains, those metallic structures can play a role of a transducer that converts the extremely localized energy carried by tunneling electrons into visible light in the far-field. More precisely, we will see in this chapter that it is the unique combination of the tip apex with the metallic surface that allows converting any type of "localized energy" such as molecular excitation into far-field photons.

## 2.1 Basic principle of light emission in an STM junction

The first observation of light emission from tunneling electrons has been reported in 1976 by Lambe *et al.* in a metal-insulator-metal junction [64]. In this experiment, a first electrode made of aluminium is oxidized at the surface. This oxide layer (thickness of approximately 30 Å) plays the role of an insulating gap. A counter electrode (made from Ag, Au, Pb or In) is directly positioned on this insulator to build the tunneling junction. The authors observed a quantum cutoff in the light spectrum obtained under different voltage conditions (Fig. 2.1(a)). This cutoff condition, $h\nu < eV$, where $\nu$ is the frequency of the emitted photon, shows that the photon energy is limited by the maximum energy accessible by the tunneling electrons. The authors also mentioned the necessity to create roughness on the counter electrode surface, *i.e* small metallic nanostructures, to observe light emission. Therefore, the emission of photons can be only due to an **inelastic tunneling process** where electrons lose their energy in the barrier. This energy is transfer to localized electromagnetic mode associated with the metallic roughness, that will eventually decay in the far-field by emitting a photon (Fig.2.1(b)). Few years after the invention of STM, Gimzewski *et al.* obtained similar results directly in an STM junction [41], opening the way to **STM-Induced Light Emission** STM-LE experiments. The highly controllable environment of the STM junction allowed then to make a big step forward in the understanding of this process.

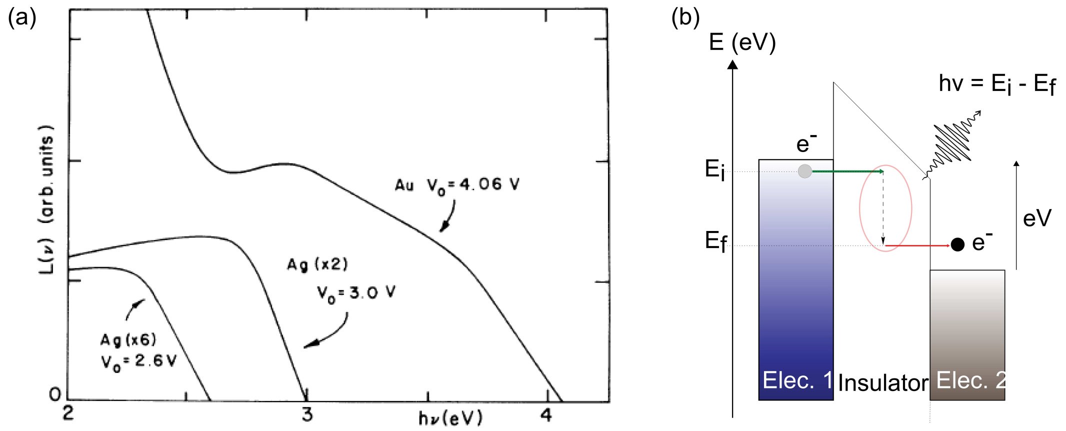

**Figure 2.1: Light emission from a metal-insulator-metal junction.** (a) Spectra obtained under different voltages for different metals. Adapted from [64] (b) Sketch depicting the emission of a photon by an inelastic electron.

### 2.1.1 An STM junction from an electromagnetic point of view

STM-Induced light emission (STM-LE) has allowed obtaining a better understanding of the electromagnetic modes of the junction that are involved in the emission process.

Recording series of spectra obtained with a tungsten tip over different metal surfaces (Ag(111), Au(110) and Cu(111)), Berndt *et al.* [6] investigated the influence of the metal used in the junction on its optical response. Spectra obtained in such conditions reveal a light emission characterized by a broadband peak (Fig. 2.2 (a)). The wavelength of the peak maximum is around 550 nm for the Ag(111) surface, 600 nm for Au(110) and 650 nm for Cu(111). These observations show that the wavelength of the broadband peak is strongly dependent on the metal composition of the junction. Meguro *et al.* [75] investigated the influence of the tip shape on the emission. They used gold tips with different shapes, characterized by Scanning Electron Microscopy (SEM), to perform STM-LE spectra over an Au(111) surface. Depending on the tip apex shape, and thus the junction geometry, the authors observed drastic differences in the STM-LE spectra (Fig. 2.2 (b) and Fig. 2.2 (c)).

These two examples show that two parameters influence the electromagnetic properties of the STM junction: the chemical nature of the STM junction (*i.e.* the metals used for the tip and the surface) and its geometry. This latter depends essentially on the shape of the tip since STM experiments are performed on flat surfaces. To understand more these observations, let us describe the particular electromagnetic modes existing in the STM junction and which are involved in the light emission process.

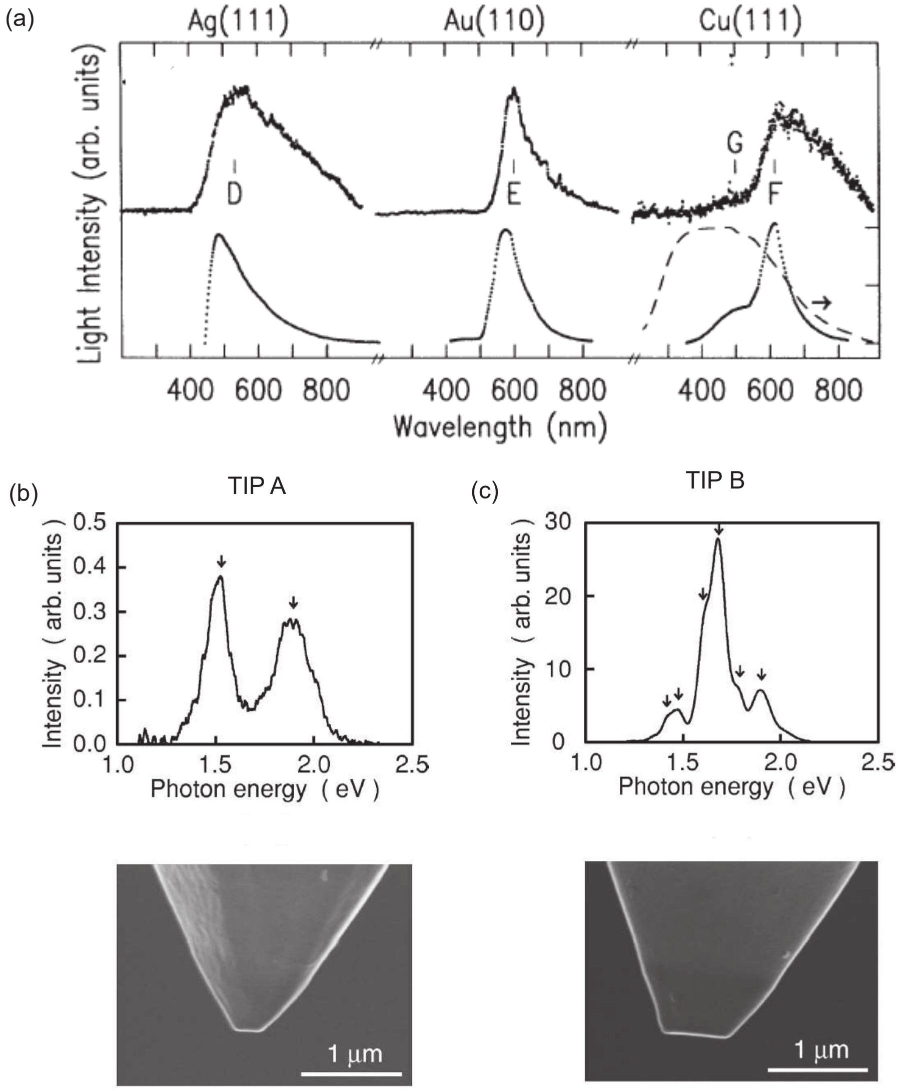

**Figure 2.2: Influence of the tip shape and composition of the STM junction on the STM-LE spectrum.** (a) Spectra obtained with the same tungsten tip above different metallic surfaces. Adapted from [6] (b) and (c) Top panel: STM-LE spectra obtained with two different tips, labelled Tip A and Tip B. Bottom panel: SEM image of the two different tips. Adapted from [75]

### Electromagnetic description of the sample surface.

When a metal is subject to an electromagnetic field, the collective oscillation of the conduction electrons gives rise to so-called plasma waves. These waves are a solution of the Maxwell equations and oscillate at the plasma pulsation:

$$\omega_p = \sqrt{\frac{ne^2}{\epsilon_0 m}} \tag{2.1}$$

where $n$ is the density of free electrons in the metal, $\epsilon_0$ the dielectric constant of the vacuum, and $m$ the mass of the electron. In the quantum regime, plasma waves are quantized with an associated quasiparticle of energy $\hbar\omega_p$, which is called **plasmon** [1].

Due to the skin effect, an incident field cannot penetrate the metal over a distance greater than the order of several $\delta = \sqrt{\frac{2}{\omega\mu_0\mu_m\sigma}}$ (skin depth), with $\omega$ the pulsation of the incident field, $\mu_0$ the magnetic permeability of the free space, $\mu_m$ the relative metal permeability and $\sigma$ the metal conductivity.

For a metal, under optical field irradiation, this skin depth is a few hundreds of nanometers.

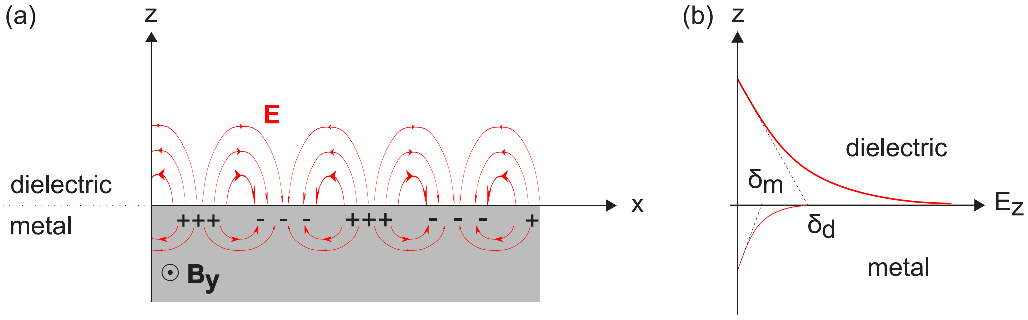

**Figure 2.3: Description of the Surface Plasmon Polariton (SPP).** (a) Sketch depicting the structure of the SPP wave. Collective oscillations of conduction charges are localized in the vicinity of the metal surface. The generated field is both transferal and longitudinal. Red arrows represent the electric field. (b) The evanescent character of the electric field z component. $\delta_d$ and $\delta_m$ are the decay lengths of the latter in the dielectric and the metal respectively.

Therefore, the collective oscillations generated by the field excitation are mostly localized at the vicinity of the metal surface. At the interface between a metal and a dielectric, described by a relative permittivity $\epsilon_m$ and $\epsilon_d$ respectively, the solutions of the Maxwell equations are called **Surface Plasmons (SP)** (Fig. 2.3 (a)). In return, these charge oscillations generate an electromagnetic (EM) field. In the metal, and the dielectric (here the vacuum) the electric field is evanescent in the direction perpendicular to the sample (Fig. 2.3 (b)).

The coexistence of the SP with its induced EM field is a physical object called **Surface Plasmon Polariton (SPP)** [2] [131, 95, 61]

These SPPs are surface waves, propagating along with the metal-dielectric interface, and oscillating in a pulsation range varying with the wavevector **k** from $\omega_{SPP} = 0$ to [95, 131] :

$$\omega_{SPP}^{max} = \frac{\omega_P}{\sqrt{1+\epsilon_{rd}}} \tag{2.2}$$

For noble metals such as silver or gold due to the low losses (small imaginary dielectric function), SPP may carry strong resonant oscillations under excitation

---

[1] In the following part of this thesis we will follow the usual way to talk about these generics collective oscillations by calling them simply "plasmon".

[2] One has to note that an SP cannot exists without generating an electromagnetic field. Therefore an SP is a "conceptual" part of the real object that is the SPP. Often the term SP is used but refers to SPP.

by visible light [10, 103]. One has to note that regardless of any incident field, these modes can be excited by different ways: prism coupling, grating coupling or, in our study, with tunneling electrons [103].

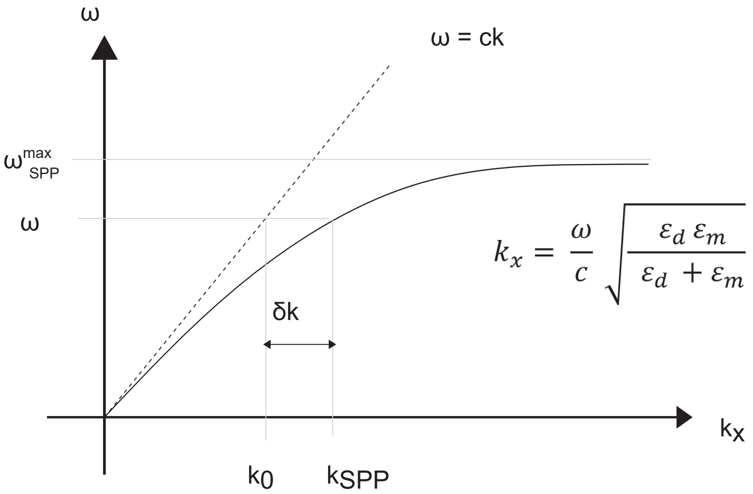

**Figure 2.4: Dispersion relation of SPP (dark line).** The dashed line corresponds to the dispersion relation for a free propagating electromagnetic field. $\delta k$ is the impulsion mismatch between SPP and the photon.

Since SPP are propagating waves, an excitation leads preferentially to a propagation [123]: they are non-radiative by nature. To allow for SPP conversion to a photon both energy and momentum have to be conserved. However, we can see that the dispersion relation is quite different between SPP and photons: for the same energy, there is a mismatch $\delta k$ in impulsion (Fig. 2.4). For a resonance appearing at $\omega$, if the mismatch $\delta k$ is compensated, the energy of the SPP can be converted into a photon in the far-field. The presence of a roughness on the surface that breaks the translation symmetry, the use of a prism or a grating may compensate this mismatch and allow the SPP to decay radiatively [103, 59, 61].

### Electromagnetic description of the tip-sample junction.

Fig 2.5 (a) shows an SEM image of a tip that has been used in our experiments, actually one of the best in terms of light emission. Even though the tip shape seems chaotic over a micrometer range it may still provide high-quality images and optical response. The "tip apex" is surrounded by a red circle, and is constituted by a small piece of metal which have a size smaller than one-tenth of a micrometer.

To understand the electromagnetic properties of the tip apex, let us model it in a first approximation by a small metallic particle with sub-optical-wavelength size (Fig. 2.5 (b)). For such a geometry, charge oscillations described for the case of the planar sample are confined in the three directions of space (Fig. 2.5 (b)). Due to this confinement, these particular plasmons are called **Localized Surface Plasmon (LSP)** [131].

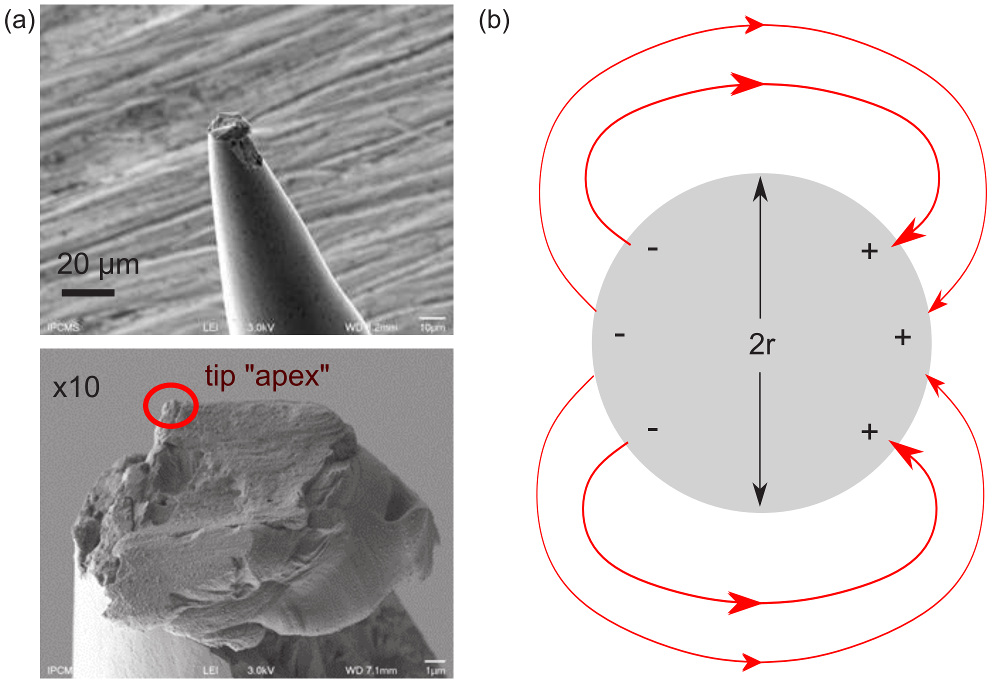

**Figure 2.5: Description of Localized Surface Plasmons confined in the sub-wavelength size tip apex.** (a) Scanning Electron Microscopy image of a tungsten tip covered with silver. The tip apex area (red circle) presents metallic structures smaller than 0.1 micrometer. (b) Sub-wavelength size metallic sphere model of the tip apex. Charge oscillations are confined in the sphere. The red arrows represent the generated electric field lines.

One has to note that LSP and SPP are a different kind of plasmons [131, 10, 89]. SPPs are propagative waves by nature, which means that excitation will lead preferentially to propagation along with the interface between the metal and the vacuum. LSP however, due to their confinement, cannot propagate along with the interface. Therefore, while SPP excitation needs compensation of the momentum mismatch to be radiative, LSP can effectively decay radiatively [131]. For a given metal, LSP modes are conditioned by the shape and the size of the particle in which they are confined. Tuning the geometry particle made of noble metals, such as gold or silver, may give rise to strong resonances with light in the visible range [126].

From an electromagnetic point of view, the STM junction in the tunneling regime can be seen as a nano-particle separated from the sample plane by a distance $d \approx 1$ nm. In such geometry (often mentioned as nanoparticle-on-mirror NPoM), the plasmonic modes (SPP and LSP) of the two nano-structures hybridize to create new modes of plasmons localized in the nano-gap [90, 94, 110]. Since these modes are confined in a cavity-like geometry (Fig. 2.6), they are often called **Nano-Cavity Plasmon** (NCP) modes.

Under an incident light, such as the one produced by a laser, NCP contained is the nanogap of such nano-structure, may strongly enhance the EM field locally. For this reason, that particular geometry has attracted considerable interest. For example, it allowed recently to observed light-matter strong coupling of a single molecule at room temperature [19] and has also many potentials application such as biosensing [110], or quantum information [93]. For the domain of scanning probe microscopy, this effect is for example used in **Tip-Enhanced Raman Scattering** (TERS) experiments [66, 133].

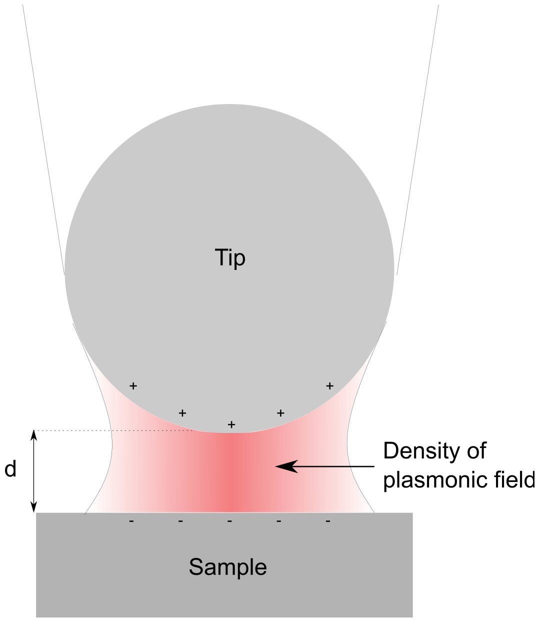

**Figure 2.6: Formation of nano-cavity plasmons.**

### 2.1.2 Light emission process mechanism

Now we can obtain an intuitive picture of how light can be emitted in a metal-metal STM junction. Because of the high density of electromagnetic modes available in the junction, inelastic transitions may occur during the tunneling process, leading to excitation of an NCP mode (Fig. 2.7 (a)) with the following condition: $\hbar\omega_{NCP} = E_i - E_f$, where $E_i$ and $E_f$ are respectively the initial and final electron energies.

Eventually, this excited NCP mode will decay by emitting a photon in the far-field with the condition: $h\nu = \hbar\omega_{NCP}$. Fig. 2.7 (b) presents the NCP typical STM-LE spectrum recorded by locating a gold tip above a gold Au(111) surface under a voltage $V = 2$ V. It shows a broadband emission with a quantum cutoff at $E = 2$ eV. This spectral shape is a consequence of two things. On a first hand, electrons able to undergo an inelastic transition have an energy which is between $E = 0$ to $E = eV$. On another hand, the NCP eigenmodes form a continuum, which is modulated by the nanocavity geometry. Therefore, the corresponding optical spectrum will exhibit a broadband emission characteristic of the NCP modes and presenting a cutoff at $eV$ (Fig. 2.7 (b)). Since the NCP modes result from the coupling between SPP and LSP modes (Fig. 2.7 (c)), changing the tip shape will change the LSP eigenmodes and thus those of the NCP.

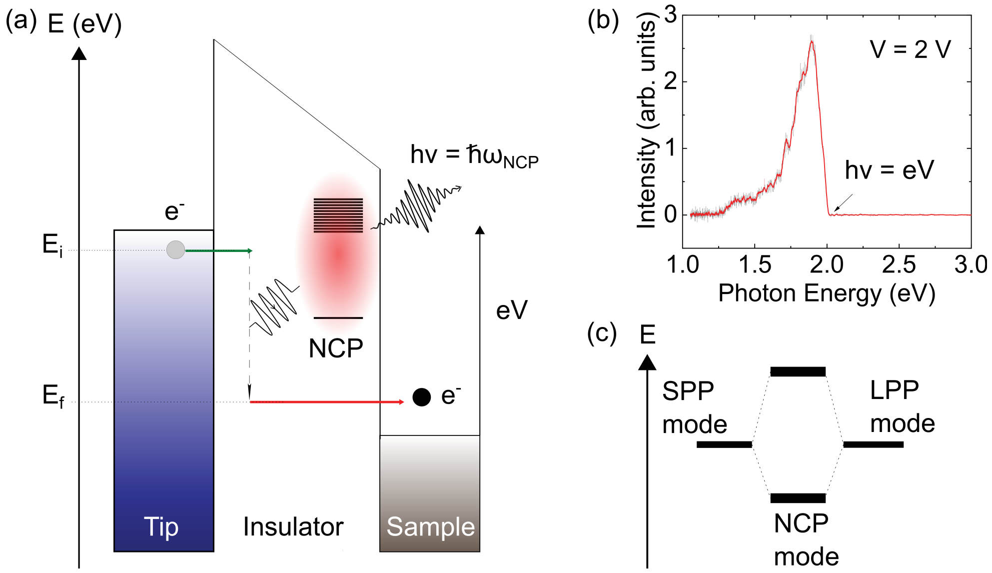

**Figure 2.7: Light emission process in a metal-metal junction.** (a) An inelastic tunneling transition excites an NCP mode that decays into a photon in the far field. (b) Broadband emission spectrum of the NCP at a bias voltage $V = 2$ V. The spectral shape depends on the spectral density of the NCP modes. The spectrum shows a quantum cutoff at $h\nu = 2$ eV. (c) Energetic sketch illustrating the hybridization between LSP and SPP that generate NCP modes.

Light emission in an STM-junction has been studied theoretically by Rendell *et al.*, and they showed that the emission is characterized by a dipole located in the nanogap, and directed along the tip axis [98, 97]. In this model, the maximum emission intensity is found at $\approx 60°$ to the tip axis.

Mathematically the light emission process by the tunneling electrons can be resumed by the Fermi Golden rule [30] giving the rate of emission at a given frequency $\nu$ :

$$\Gamma(\nu) = \frac{2\pi}{\hbar^2} |\langle i|\hat{\mu}|f\rangle|^2 \rho_{NCP}(\nu = E_i - E_f, M) \tag{2.3}$$

Where $\langle i|\hat{\mu}|f\rangle$ is the transition dipole moment associated to the inelastic transition of an electron starting from a state $\langle i|$ to a state $\langle f|$ and $\rho(\nu, M)$ is the local density of electromagnetic states available around the frequency $\nu = E_i - E_F$ . Finally, the emission is a product of two terms: one related to the inelastic transition and one related to the EM environment.

The chemical nature of metal composing the tip and the sample have also a drastic impact on the plasmonic oscillations, and thus the enhancement factor. Due to their small imaginary dielectric constant, noble metals such as gold or silver are the best materials to use to achieve STM-Le experiments [10].

### 2.1.3 Molecular exciton in a plasmonic nanocavity

Since the topic of this manuscript is mostly about single-molecule fluorescence, here we describe how an excited molecule in the vicinity of the NCP of the STM junction may generate a fluorescence photon that can be detected in the far-field. We will come back later on the excitation mechanism, but for the moment let's assume that tunneling electrons may provide an effective excitation of the molecule. This description relies on an analogy with the common explanation of the spontaneous emission phenomenon, where the presence of the free propagating field modes allows a decay of the molecule excited state into the EM field and thus lead to an emission of photons.

Let us consider a molecule in its excited state $|e\rangle$ located in the plasmonic nanocavity (Fig. 2.8 (a)).

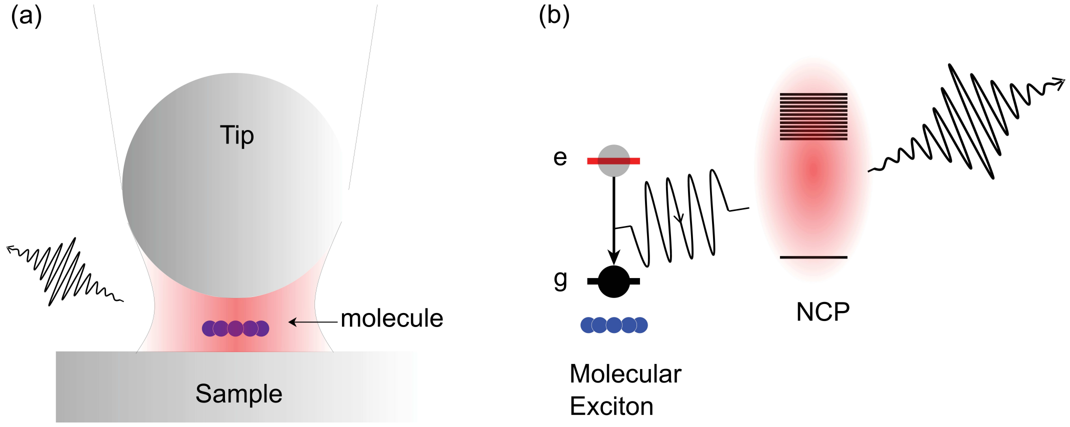

**Figure 2.8: Decay of a molecular excitation in a plasmonic nanocavity.** (a) A molecule is placed in the gap on the STM junction. (b) The molecular excitation decays toward NCP modes due to fluctuations of the plasmonic vacuum. NCP excitations decay into photons in the far-field at the molecular exciton energy.

Due to the high volume density of EM modes (*i.e.* NCP modes,) in the cavity, the molecular excitation (**exciton**) will interact strongly with the plasmonic vacuum fluctuations, and thus decay by populating an NCP excited mode. In such configuration, the population of the molecular excited state follows a time dependency $\propto e^{-\Gamma t}$, where $\Gamma$ is the decay rate. According to the Fermi golden rule, the decay rate of the exciton in the NCP environment is given by:

$$\Gamma = \frac{2\pi}{\hbar^2}\left|\mu_{eg}\right|^2 \rho_{NCP}(\omega_{eg}, M) \tag{2.4}$$

where $\mu_{eg} = \langle g|\hat{\mu}|e\rangle$ is the molecule transition dipole moment and $\rho_{NCP}(\omega_{eg}, M)$ the local density of electromagnetic states (LDOS) available around the frequency $\omega_{eg}$. Since the local density of state of NCP is much larger than the one of the free propagating field, the exciton decay rate is tremendously increased in the nanocavity [3]. Once the decay has excited an NCP mode, this one will decay at its turn by emitting a photon in the far-field at the energy of the exciton. A fluorescence signal of the molecule can be therefore detected. The decay of the excited NCP modes into the far-field is extremely fast compared to the decay of the exciton into the NCP. Therefore the total rate of emission is mainly

---

[3] Note that the direct decay toward free propagating field still exists but is extremely weak compare to the decay toward the NCP and then can be neglected in our experiments.

limited by the decay rate of the exciton, and thus can be approximated by the expression 2.4.

From the expression 2.4 we can see that the rate of emission of a molecular excitation can be dramatically increased by the presence of an important NCP LDOS at the exciton energy. This effect is the well-known Purcell effect [91].

It is important to remark that plasmonic decay includes both radiative and non-radiative decay. Therefore, a molecular excitation is not converted into photon in the far-field with 100% efficiency. This is usually expressed via the quantum yield $\eta$, given by:

$$\eta = \frac{\Gamma^{rad}}{\Gamma} \tag{2.5}$$

where $\Gamma^{rad}$ is the part of the decay rate which results into an effective emission of photon in the far field.

Note also that this description does not take into account the intrinsic non-radiative decay of the molecular excitation. We will see in the next part that this non-radiative decay is an experimental difficulty to the overpass to observe fluorescence emission in our STM junction.

## 2.2 Light emission from single molecules

### 2.2.1 STM-Induced light emission from adsorbed molecules

Few years after the pioneering experiments on bare metals, STM-LE experiments have been extensively carried out to obtain an intrinsic optical signal of a single molecule. The common approach in these early experiments consists of deposing a small number of molecules to obtain islands of monolayer thickness. Various species of molecules and different metal substrates have been used [112, 27, 25]. The first experiment of this kind was reported by Berndt *et al.* [4] with $C_{60}$ molecules adsorbed on a Au(111) surface. An STM image of such an island is shown in the top panel of figure 2.9(a). The STM image shows a lattice of protuberances that correspond to the $C_{60}$ molecules. At each pixel of the image, the authors recorded the optical signal with a photodiode to obtain an intensity map (usually called **photon map**), which is represented in the bottom panel of Figure 2.9(a). The photon map shows a lattice of bright spots, whose positions correspond to the protuberances observed in the STM image. This shows that the STM-LE signal is strongly impacted by the presence of $C_{60}$ molecules. This is also confirmed by the correlated line extracted from the STM image and the photon map (Fig. 2.9(b)). STM-LE spectrum [105] acquired, on the $C_{60}$ layer and the Au(111) reveal broad features in both cases, but centered at different energies (Fig. 2.9(c)). This observation suggests that the $C_{60}$ molecule modifies the NCP emission signal rather than produce its intrinsic optical signal. This modification can be explained by the presence of molecular states in the junction that open new channels for inelastic transitions as it was confirmed later [25, 107, 44].

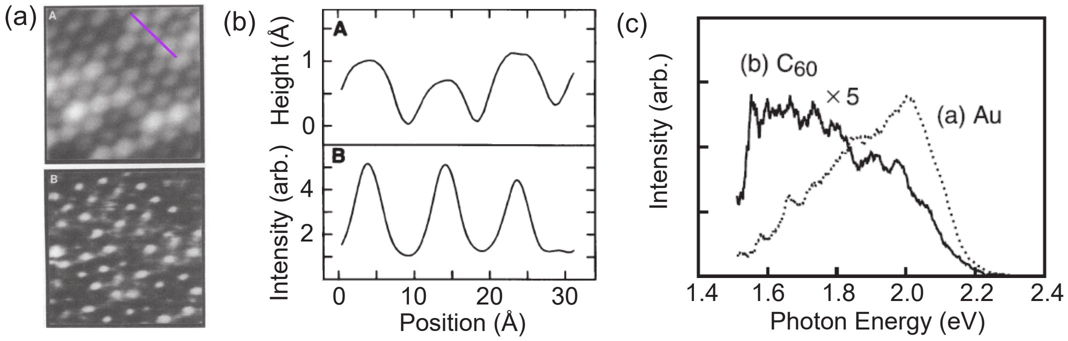

**Figure 2.9: STM-LE on $C_{60}$ molecules adsorbed on a Au(111) surface.** (a) STM image of the $C_{60}$ monolayer island (top panel) and intensity map of the STM-LE signal (bottom panel). (b) Top panel: height profile along the line in the STM image in (a). Bottom panel: STM-LE intensity along the same line. (adapted from [4]) (c) STM-LE spectrum acquired with the tip located on top of a $C_{60}$ molecule of the island compared to the spectrum acquired on the bare Au(111) surface (adapted from [105]).

In paragraph 2.1.3 we described how a fluorescence photon can be generated in the far-field from an excited molecule placed in the STM plasmonic nanocavity. This process supposes that the main channel of decay for the molecule is towards the NCP modes. However, in some configurations much faster decay channels exist leading to the so-called **quenching** of the fluorescence. It is the case when a molecular exciton is in contact with a metal surface: dissipation occurs by the creation of electron-hole pairs in the metal [61].

Although we have not yet mentioned how the molecule can be excited, we can already say that some mechanisms invoke the creation of electron-hole pairs by direct injection into the molecular orbital. If the molecule is in direct contact with the metal, the strong electronic state hybridization will lead to a charge transfer faster than the time needed for the electron-hole pair creation, making this type of excitation impossible.

One can conclude that to both excite the molecule and observe its radiative emission, the molecule has to be decoupled from the metallic substrate.

### 2.2.2 Several strategies to decouple molecules

To avoid the molecular radiative emission quenching in STM-LE experiments, several strategies have been employed to decouple molecules from the metallic substrate.

The first one consists in using multilayers of molecules as a spacer to decouple the molecules of the top layer [26, 27, 76, 45]. While spectra characteristic of the fluorescence of the probed molecule have been reported in this configuration, one can hardly associate the fluorescence signal to a given molecule, as any of the molecules of the 3D molecular cluster may act as an emitting center. Nevertheless, this approach has allowed identifying defects in $C_{60}$ multilayers which were shown to behave like single-photon emitters [45].

The second approach consisting of decoupling the molecule with a thin insulating layer of oxide [92, 127, 127, 65] or sodium chloride. Compared to the previous method, it is possible to selectively probe an isolated molecule adsorbed on this layer. Another advantage is the capability to specifically address a different part of the molecule, thanks to the high spatial resolution provided by STM. Moreover, in this configuration, it is possible to investigate the impact of the direct molecular environment on its optical properties.

Sodium chloride decoupling is, so far, the most efficient way to preserve fluorescence signal from a single molecule in STM-LE experiments. It allowed dipole-dipole coupling "imaging" [129], energy transfer investigations [49], vibronic spectroscopy [29], investigation of the exciton-plasmon interaction [134, 50], demonstration of the single-photon emitter behavior of single phthalocyanine molecules [132], investigation of the interplay between the redox state and the fluorescence [28], investigation of light emission from a triplet state [17, 54] and finally investigation of the influence of the NCP on the single-photon source character of a linear arrangement of molecules [73].

Finally, the last decoupling method is to use molecular wires allowing to suspend the emitting molecule between the tip and the sample [96, 20, 21]. Although this method is extremely difficult experimentally, it has two main advantages. The first benefit is that it allows controlling continuously the decoupling, simply by playing with the wire length and the lifting height [20]. The second benefit is that, in this configuration, the dipole of the emitter is colinear with the NCP dipole, allowing a much better plasmon-exciton coupling. This may potentially, give rise to strong coupling effect between the NCP and the emitter [109, 124]. Unfortunately, the main problem of this configuration is the loss of any spatial resolution, since the emitter is suspended between the tip and the sample.

### 2.2.3 Timeline of STM-Induced single-molecule fluorescence

In this paragraph, I will resume the main experiments carried out to obtain STM-induced single-molecule fluorescence until the year 2016, the date at which Zhang *et al.* [129] proposed a convenient way to obtain a single-molecule fluorescence signal. This result is the starting point of my PhD work.

**In 2003**, Qiu *et al.* obtained for the first time the electrically-driven optical signal coming from a single Zn(II)-etioporphyrin (ZnEtio) decoupled from a NiAl(100) substrate by a thin layer of $Al_2O_3$ oxide (Fig. 2.10 (2003) (a)). The authors found a variation of the optical signal as a function of a tip position at a sub-molecular scale. Furthermore, molecules occupying different adsorption sites exhibit different optical signatures (Fig. 2.10 (2003) (b)). This demonstrates a strong impact of the tip position on the STM-LE signal and sensitivity of this signal to the surrounding environment.

**In 2008**, by using the same decoupling method, similar observations were reported by Wu *et al.* [127] on an Mg-porphyrin molecule.

**In 2010**, Chen *et al.* [15] performed a more systemic study of optical signal variation as a function of the tip, on the same system (Fig. 2.10 (2010) (a). First they observed two different main peaks depending of the tip position (Fig. 2.10 (2010) (b)).

Photon maps recorded at the energy of these peaks reveal dipole-like patterns with a bright area on the symmetric lobes and a dark center (see photon map in Fig. 2.10 (2010) (b)). The explanation given by the authors is the following: at the lobe position, the presence of NCP and molecular dipoles yields a net total dipole moment that radiates in the far-field. However, when the tip is located in the center the total dipole moment is almost zero. This qualitative analysis is supported by theoretical calculations and allows to reproduce the contrast observed in the experimental photon maps.

An important remark is that in these experiments the luminescence signal cannot be attributed to the fluorescence of the molecule. Indeed, the main emission line energy does not match with the fluorescence energy obtain with conventional optical methods. One of the reasons could be the strong interaction between the molecule and the oxide used to decouple the molecule.

**In 2016**, Chong *et al.* [20] developed an innovating method where a porphyrin molecule is suspended between the tip and the sample by an oligothiophene wire (Fig. 2.10 (2016) (a)). Simply by lifting step by step the wire, and thus varying the decoupling between the porphyrin molecule and the substrate, the authors demonstrated a continuous variation from a broadband emission (molecule adsorbed on the substrate) to a narrow line emission, corresponding to the fluorescence of the molecule. It is important to note that it was the first time that STM-LE signal on a single-molecule could be unambiguously attributed to its fluorescence. With this method, the authors were able to obtain a fluorescence emission with a linewidth of ≈ 2.5 meV. Last but not least, the main fluorescence line (associated with the so-called 0-0 transition) is accompanied by much weaker lines at lower energy (Fig. 2.10 (2016) (b)). Comparison with calculated Raman modes suggests that those lines correspond to different vibronic modes of the molecule.

We want to point out the implications of the results of this work: first, single-molecule fluorescence can be induced by STM and second, vibrational information can be obtained **without** light excitation. Unfortunately, in this suspended configuration the spatial resolution is lost, making impossible further studies on the impact of the tip position on the vibrational signature of the probed molecule.

Finally the ideal system was proposed by Zhang *et al.* [129], where sodium chloride was used to decouple single Zn-phthalocyanine (ZnPc) molecules from a Ag(100) substrate (Fig. 2.10 (2016) (a)). The STM-LE signal obtained on a single ZnPc shows a sharp fluorescence emission peak in very good agreement with photoluminescence measurement on the same molecule in a frozen matrix.

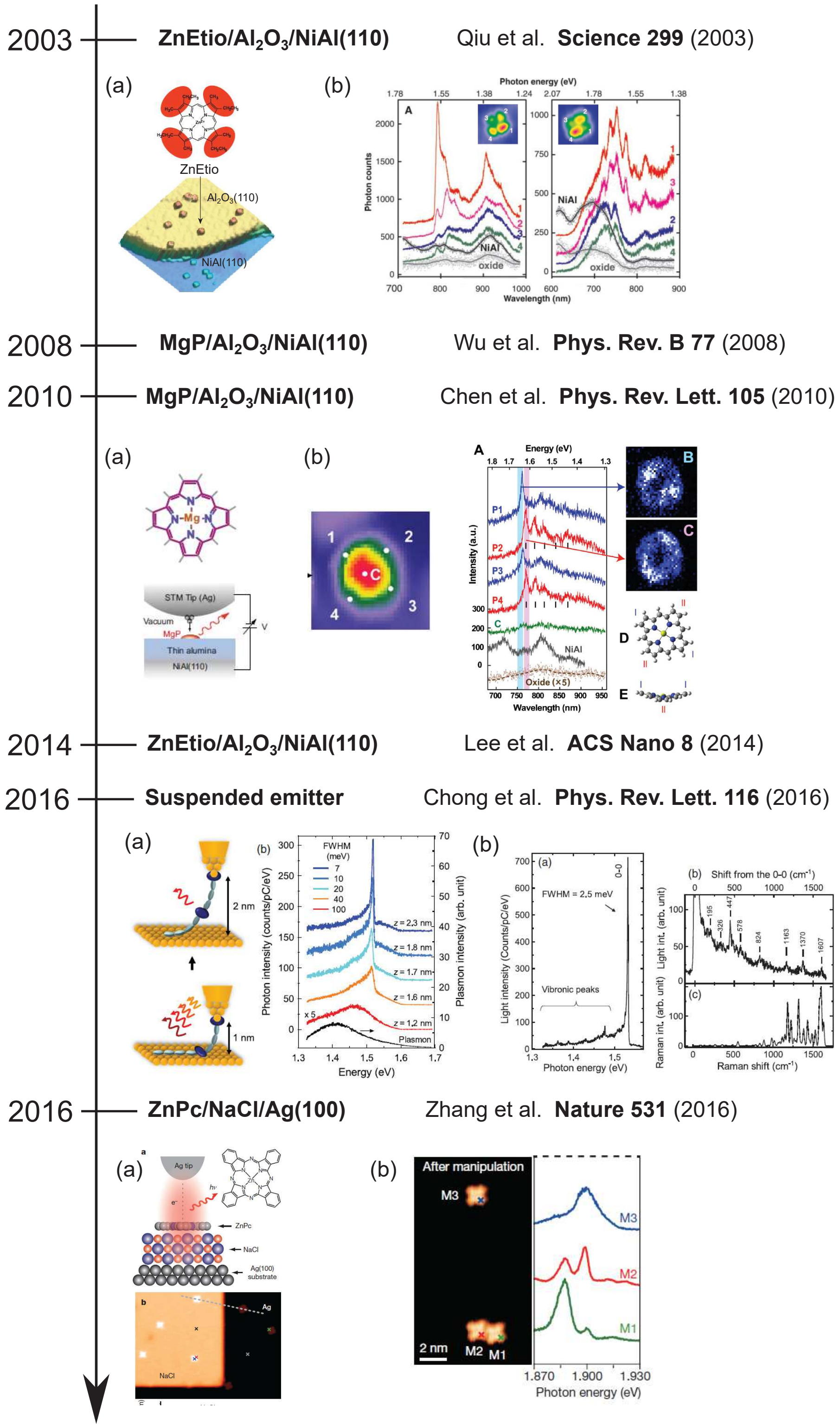

**Figure 2.10: Timeline of STM-Induced single molecule fluorescence experiments..**

By building artificial dimer of molecules, the authors also observed features in the STM-LE spectra which were assigned to inter-molecular dipole-dipole coupling (Fig. 2.10 (2016) (b). This convenient method to obtain a fluorescence signal of a single molecule, together with the spatial resolution offered by STM opened the way to the fascinating investigation of light-matter interaction at the single-molecule level.

## 2.3 Overview of STM-Induced phthalocyanine fluorescence on NaCl

In this part, we will focus on the most recent STM-Induced Fluorescence (STM-F) results of single-molecule decoupled by a NaCl layer. Most of these experiments have been carried out with phthalocyanine molecules on a silver substrate.

### 2.3.1 Inter molecular coupling

**Homogeneous molecular coupling**

As we have mentioned above, the experimental configuration developed by Zhang *et al.* allowed them to probe inter-molecular dipole coupling between two identical ZnPc molecules. When the two ZnPc molecules are in "contact" (dimer configuration), five different peaks, all shifted to the red or the blue with respect to the single-molecule emission line, can be identified in the spectra (Fig. 2.11 (b)). The authors attributed those to the existence of five different excitonic coupling modes resulting from the dipole moment interaction (Fig. 2.11 (c)). Photon maps of these modes reveal specific patterns delocalized over the whole dimer. This observation suggests a **coherent** excitonic coupling between the two ZnPc molecules.

The lowest energy mode (mode 1) is particularly interesting. It corresponds to the coupling between molecular dipoles oriented along the same direction and oscillating in phase. The corresponding peak is red-shifted with respect to the emission line of the monomer and is much narrower than this latter. Interestingly, the authors showed that this trend continues when a third and a fourth molecule is added to the dimer (Fig. 2.12 (a)). The authors suggested that this observation is a consequence of the increasing strength of the coupling with the number of molecules. Photon maps of this particular mode for the dimer, trimer and tetramer reveal that it is delocalized over the whole architecture (Fig. 2.12 (b)), suggesting that the coherence is maintained on such structure.

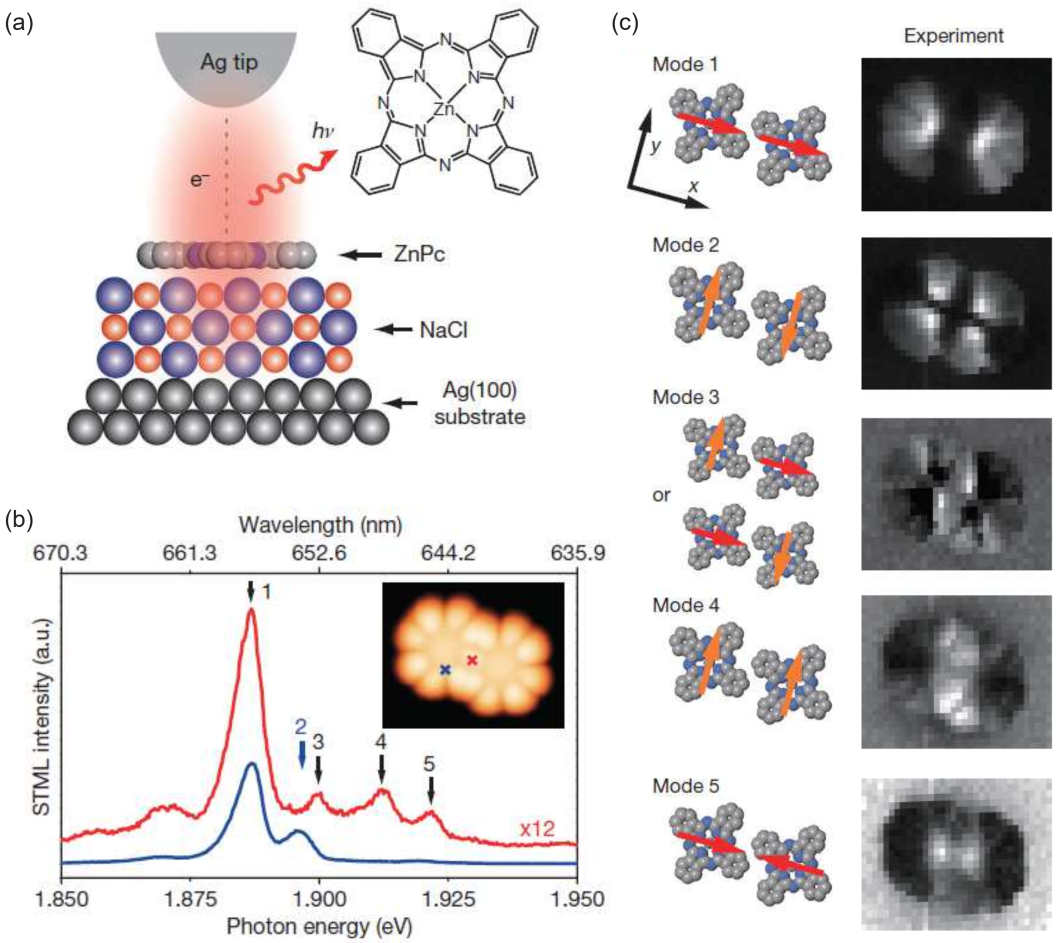

**Figure 2.11: Coherent dipole-dipole coupling.**(a) A ZnPc molecule is decoupled from a Ag(100) surface by a three atomic NaCl layers. (b) STM-LE spectra of a ZnPc dimer excited at the corresponding colored cross in the STM image inset. The five different peaks correspond to five different coupling modes. (c) Experimental maps for the five peaks compared with theoretical maps. Adapted from [129]

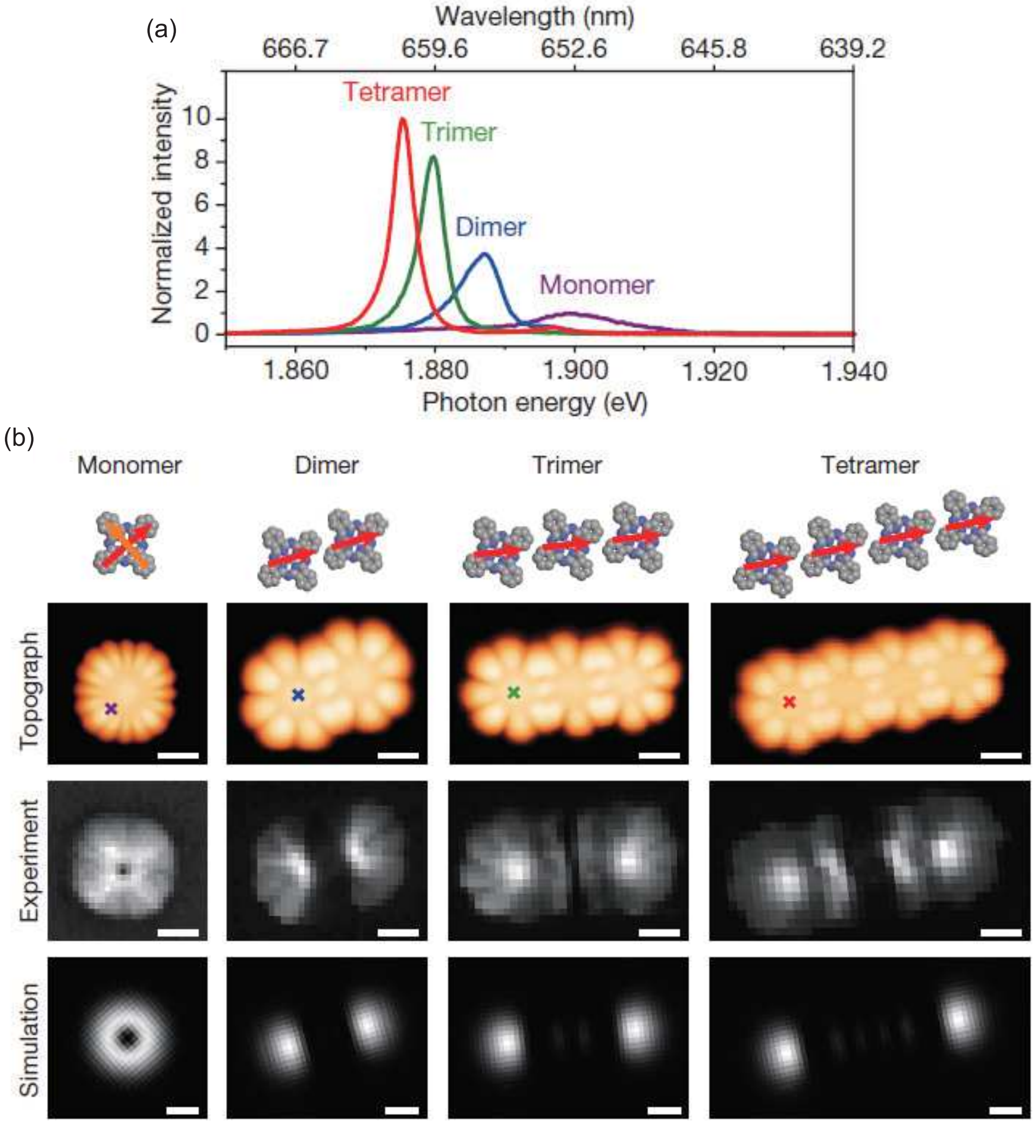

**Figure 2.12: Evolution of the lowest energy coupling mode as a function of the number of molecules.** (a) Top pannel: Spectra of a monomer, dimer, trimer and tetramer of $ZnPc$. Spectra are acquired at the cross-marked position in (b). Intensities are normalized by the monomer one. (b) Corresponding experimental photon maps compared to the simulated maps. Adapted from [129].

### Heterogeneous molecular coupling

Nearly at the same time Imada *et al.* published a paper where they investigated the intramolecular coupling in a heterogeneous dimer made from a $H_2Pc$ and a $MgPc$ molecule (Fig. 2.13 (a)). An important remark regarding the two molecules used is that the $H_2Pc$ has a C2 symmetry while $MgPc$ has a C4 symmetry (Fig. 2.13 (a)). The STM-F spectrum recorded on $H_2Pc$ (Fig. 2.13 (b))reveals two main emission lines ($Q_x$ and $Q_y$) which are associated to the two different dipole moments of the molecule, directed along the $x$ and $y$ axis. On another hand, an STM-F spectrum recorded on $MgPc$ reveal only one line ($Q$) since for a C4 symmetry the $Q_x$ and $Q_y$ dipoles are equivalent.

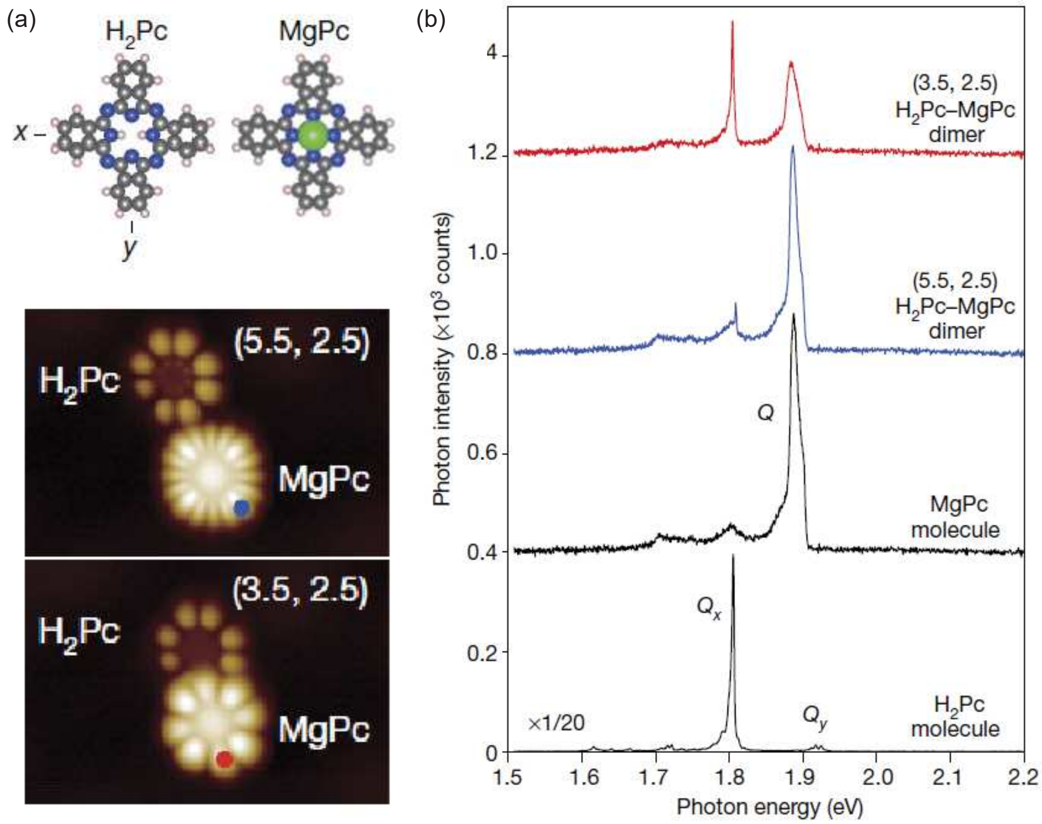

**Figure 2.13: Intermolecular energy transfer via dipole-dipole interaction.** (a) Sketch of the experiment. (b) Dimer of $H_2Pc$ and $MgPc$ molecules. (c) STM-LE spectra obtained. The two top spectra are acquired at the position marked by a dot in (b). Adapted from [49].

When the two molecules are close enough, a spectrum acquired with the tip located above the $MgPc$ lobe presents two lines (Fig. 2.13 (b)). One corresponds to the $Q$ line of $MgPc$, the second one appears at the energy of the $H_2Pc$ $Q_x$ line. This suggests that once the $MgPc$ molecule is driven into its excited state, it can decay by emitting a photon at $Q$ line energy, or by exciting the $H_2Pc$ $Q_x$ transition via **energy transfer**.

Interestingly, the authors identified two regimes of energy transfer. The low-RET [4] regime (blue spectrum Fig. 2.14 (a)) where the emission mainly comes from the $MgPc$ molecule, and the high-RET regime where the $MgPc$ $Q$ line is reduced to the benefit of the $H_2Pc$ $Q_x$ emission (red spectrum Fig. 2.14 (a)). Note that both regimes are found on the same system and with the same tip position. To find out the origin of this behavior, the authors recorded STM images in the two regimes. These images reveal an inversion of the $x$ and $y$ axis of the $H_2Pc$ molecule, between the high RET and low RET regimes (Fig. 2.14 (b)). This inversion is due to the tautomerization process, where the two inner hydrogen atoms swap their position in a concerted way. In the high-RET regime, the $H_2Pc$ $Q_x$ dipole is directed along the dimer axis. It can, therefore, couple efficiently with the $MgPc$ $Q$ dipole, allowing an efficient energy transfer. In the

---

[4] RET stands for Resonant Energy Transfer

low-RET regime the two dipoles are almost perpendicular reducing drastically the coupling, hence the energy transfer efficiency.

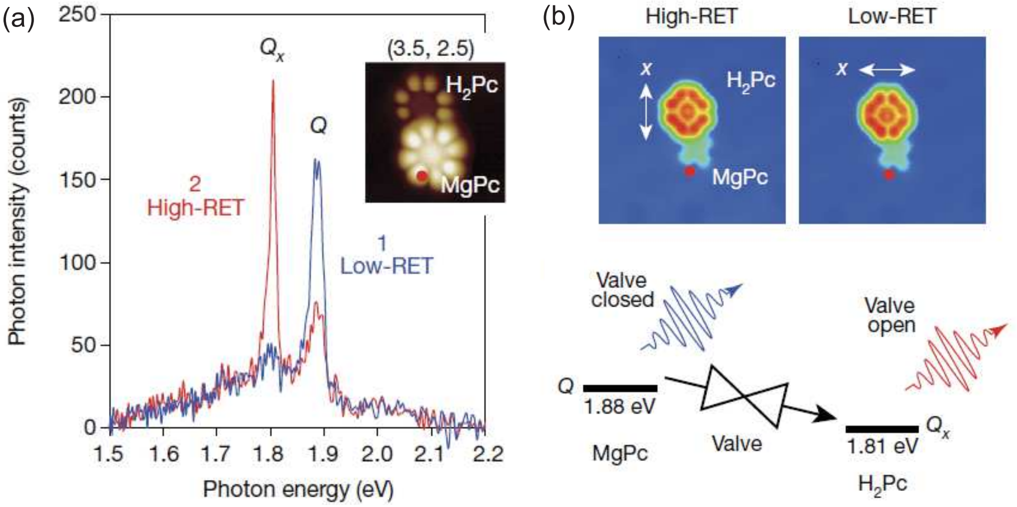

**Figure 2.14: Energy transfer controlled with dipoles respective orientations.** (a) Spectra illustrating the two regimes of energy transfer. The two spectra are acquired a the position marked by a dot in the STM image inset. (b) STM images of the dimer in the two energy transfer regimes. The LUMO image of the $H_2Pc$ molecule shows a symmetry axis related to the orientation of the $Q_x$ transition. Adapted from [49]

### 2.3.2 NCP-exciton coupling

Imada *et al.* [50] investigated the spatial dependency of the NCP-exciton coupling. The authors performed experiments where the tip (hence the NCP) is located several nanometers away from the molecule (Fig. 2.15 (a)). As a reference, the typical spectrum with the tip above the molecule is presented in figure 2.15 (b). The authors recorded a series of STM-F spectra with the tip located from 1 to 5 nm away from the center of the molecule (Fig. 2.15 (c)). When the tip is located at 5 nm the STM-F spectrum presents the typical broadband emission of the NCP (black spectra Fig. 2.15 (d)). When the tip-molecule distance reaches $\approx 3$ nm the spectrum (number 3 in figure 2.15(d)) presents dip features at the energy of both $Q_x$ and $Q_y$ transitions. These features evolve progressively to an asymmetric dip-peak shape when the tip gets closer to the molecule (Fig. 2.15 (d)). This dip-peak shape is interpreted as follows: the molecule can absorb the NCP energy and decay toward this latter; in a coherent interaction, these two processes may interfere leading to this asymmetric dip-peak shape. Indeed, this asymmetric feature is a signature, called Fano resonance, entirely specific to the coherent interaction between a discrete-state system (here the molecule) and a continuum of states (here the NCP) [33, 78, 72]. Therefore, the evolution of the Fano resonance shape presented figure 2.15(d) represents a direct measure of the impact of the tip-molecule distance on the coherent NCP-exciton coupling.

An interesting remark regarding these experiments is the significant change of emission regime when the tip goes from outside to above the molecule (Fig. 2.15).

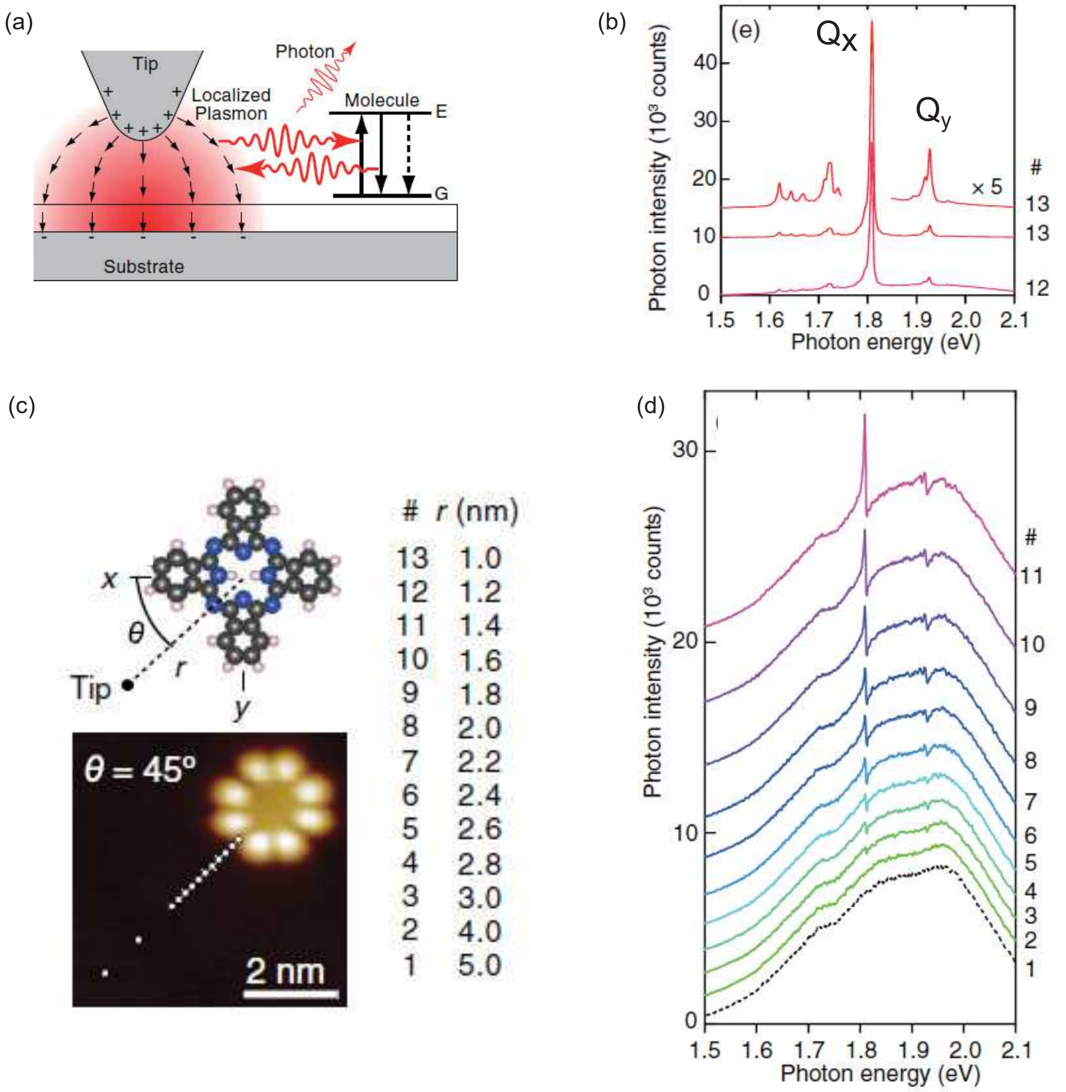

**Figure 2.15: Investigation of the NCP-exciton interaction as a function of the tip-molecule distance** (a) Sketch depicting the NCP-molecule interaction while the tip is located next to the molecule. (b) Reference STM-LE spectra acquired above the $H_2Pc$ molecule for the three last positions in (c). (c) Tip positions for the spectra presented in (b)and (d). Adapted from [50]

In the same vein Zhang *et al.* published a study, where they demonstrated how this coherent interaction between exciton and plasmon can be controlled spatially and spectrally [134]. The experiment is carried out on $ZnPc$, whose STM-F spectrum is shown figure 2.16 (a).

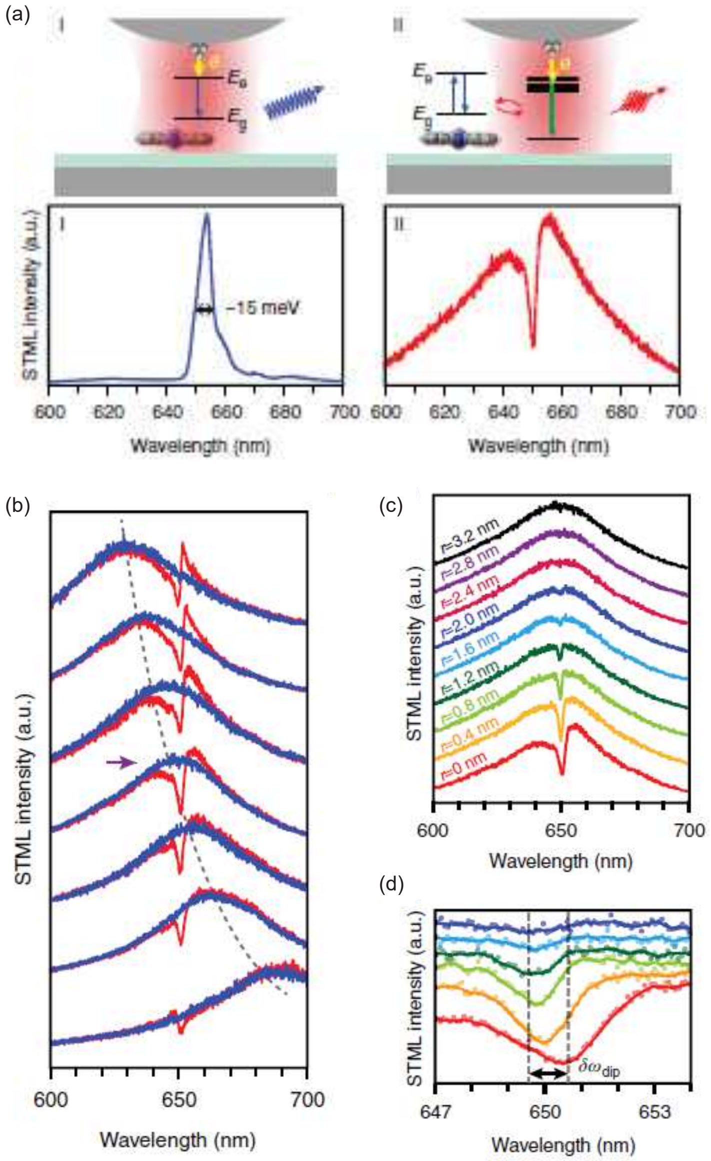

**Figure 2.16: Observation of Fano resonance.** (a) Sketch of the experiment. When the tip is above the molecule the spectrum shows the typical fluorescence line of the $ZnPc$ molecule (first spectrum). When the tip is far from the molecule, the typical NCP broadband emission is observed (last spectrum). when the tip is close ($\approx$ 1 nm) but outside the molecule, Fano resonance appears. (b) Fano resonance shape as a function of the detuning between NCP and the molecule. (c) Fano resonance shape as a function of the tip-molecule distance (top panel). The shift of the Fano resonance as a function of the distance, due to the Lamb shift.- (bottom panel). Adapted from [134]

Like Imada *et al.*, the authors observe a Fano resonance when the tip is located at several nanometer away from the molecule. Interestingly the shape of the Fano resonance exhibits an asymmetric dip structure, which is quite different from the one observed by Imada *et al.*. In fact, by tuning the NCP broadband response from low to high energy (compared to the exciton energy), the authors observed that the Fano resonance shape goes gradually from a dip to dip-peak (Fig. 2.16 (b)).

Fig. 2.16 (c) shows a series of different spectra recorded at different tip positions away from the molecule. The dip depth increase when the tip is closer to the molecule suggesting an increase of the NCP-exciton coupling. Moreover, the authors observe a shift of the dip toward the lower energy with increasing coupling strength (reducing tip-molecule distance) (Fig. 2.16 (d)). The explanation given by the authors is that this shift comes from the Lamb effect resulting from the interaction between the exciton and the quantum fluctuations of the plasmonic vacuum. One has to note that the lamb shift is tremendous compared to the usual value observed in other systems, because of the very high density of the electromagnetic field in the nanocavity.

### 2.3.3 Single-photon emission

Single-photon emitters (SPE) are light sources that can emit only one photon at a time, leading potentially to the capability to produce one photon on demand. Due to this property, SPEs are key components in the development of quantum technologies, from quantum cryptography to quantum computing [71]. The common way to characterize a single-photon emission process is to use a Hanbury-Brown and Twiss (HBT) interferometer [14]. The principle of this setup is to equally split the signal coming from the emitters with a beamsplitter (Fig. 2.17 (a)). Then, the two beams are directed to two different single-photon detectors (SPD), commonly avalanche photo-diodes. These laters allow precise temporal tracking of the photon emission. The two signals are analysed conjointly in a start-stop configuration. The arrival of a first photon on the first SPD (start SPD) triggers a timer which will stop when a second photon arrives on the second SPD (stop SPD). The delay time $\tau$ between the start and the stop is recorded, and the process is reiterated many times. The histogram of the different times $\tau$ recorded on a large number of events constitutes an accurate representation of the second-order correlation function $g^2(\tau)$. This function estimates the probability to detect photon pairs separated by a delay $\tau$

For an SPE, we expect the correlation function to be zero at a short time since two photons can never be emitted at the same time. However, for long times we expect an uncorrelated relation between the two photons, and therefore the correlation function to be 1. Consequently, the typical correlation function for an SPE presents a typical dip structure at $\tau = 0$ with exponential-shaped flanks, called anti-bunching. The time constant $\tau_0$ obtained by an exponential fit represents the typical time between two-photon arrivals, while the depth value of the dip ($g^2(0)$) characterizes the "quality" of the SPE ($g^2(0) = 0$ for an ideal SPE). In "classic" laser-induced HBT experiments, because of the fast excitation process, the emission lifetime is the bottleneck of the excitation-emission process. Therefore, the time constant $\tau_0$ corresponds essentially to the emission lifetime. However, we will see that this assumption is not necessarily verified in STM-F experiments.

In 2017, Zhang *et al.* performed HBT experiments on a single $ZnPc$ molecule excited by STM. (Fig. 2.17 (a)).

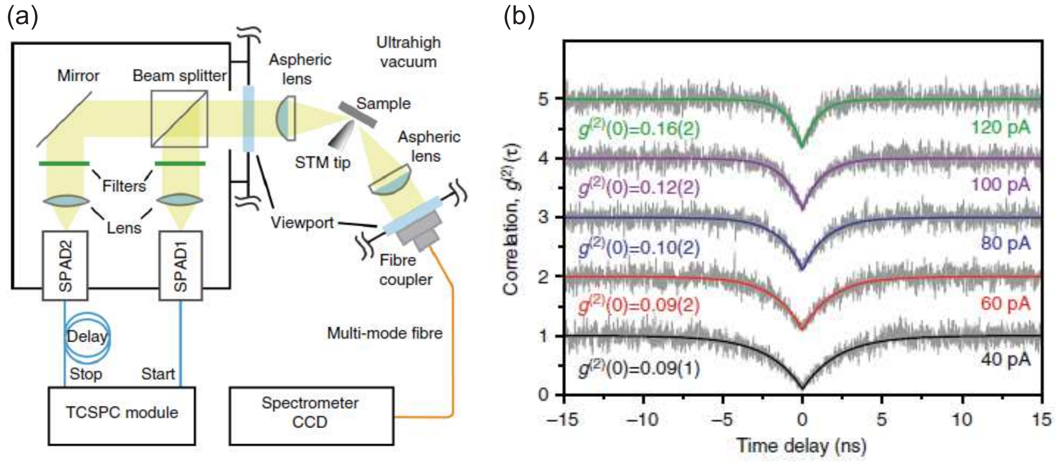

**Figure 2.17: Single photon emission from a $ZnPc$ molecule.** (a) Experimental setup. (b) Second-order correlation function as a function of the time delay for different tunneling currents. Adapted from [132]

The second-order correlation function, measured at different tunneling currents (Fig. 2.17 (b), presents the typical anti-bunching structure with a time constant $\tau_0$ of the order of 1 ns. This demonstrates, unambiguously, the "single-photon source" character of the $ZnPc$ electroluminescence. Interestingly, the time constant $\tau_0$ decreases significantly as a function of the tunnel current. This is interpreted by the authors as an enhancement of the radiative decay rate since the tip gets closer with increasing tunnel current. However, because of the high Purcell enhancement, the value of the time constant $\tau_0$ in the nanosecond range is surprisingly high compare to what we would expect. Indeed, if the fluorescence lifetime is typically in the order of 1 ns, the high enhancement ratio achieved in our system (several orders of magnitude), suggested an emission lifetime reduced in the same proportion.

An explanation, not suggested by the authors, could be that the process is not limited by the emission lifetime itself. Indeed, if we consider an excitation via charge injection, for instance, a transient charged state could be the bottleneck of the excitation-emission process. Therefore, the time constant $\tau_0$ measured experimentally could be somehow related to the lifetime of this transient charged state.

### 2.3.4 Excitation mechanism

In this paragraph, I will present briefly the two type of excitation mechanisms that are usually considered in STM-F single-molecule experiments.

The first mechanism which has been proposed is called **carrier injection mechanism** [92, 129, 49, 54]. This mechanism supposes a direct formation of an exciton inside the molecule by sequential injection of an electron in the LUMO state and a hole in the HOMO state (Fig. 2.18 (a)). This electron-hole pair formation is then followed by recombination and photon emission. To be effective this mechanism requires, at least, an alignment of the HOMO state [5]

---

[5] We will discuss this crucial aspect later in the manuscript.

(resp. LUMO) with the Fermi level of the tip (resp. sample) to allow the carrier injection , which supposes a similar voltage drop in both side of the junction under the applied bias (Fig. 2.18 (a)).

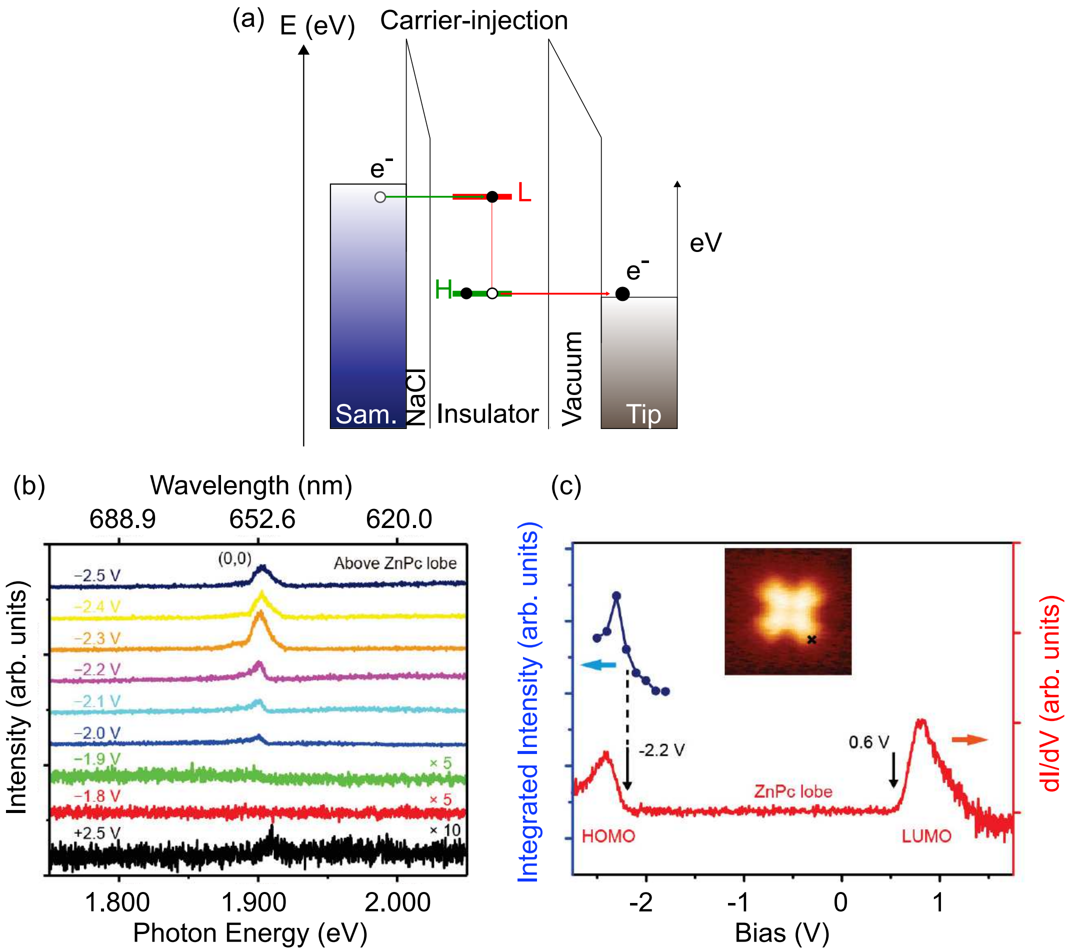

**Figure 2.18:** Carrier injection mechanism at negative bias voltage. (a) Energy sketch of the mechanism. An electron is injected from the sample in the LUMO and a hole is injected from the tip in the HOMO. A voltage drop is present on both sides of the junction. (b) Voltage dependency of the STM-LE intensity of a single $ZnPc$. (c) Comparison of the voltage dependency of the integrated STM-LE intensity and the differential conductance of a single $ZnPc$. (b) and (c) are adapted from [129].

This mechanism is experimentally supported by the voltage dependency of the STM-F intensity which is related to the energy position of the molecular orbitals. As an example, Fig. 2.18 (b) presents the STM-F voltage dependency of the $ZnPc$ molecule, from the work of Zhang *et al.* [129]. While the molecular exciton energy is $h\nu \approx 1.89$ eV, the emission starts to be significant around -2.0 V (electron energy $\leq 2$ eV), which correspond to the HOMO orbital onset (Fig. 2.18 (c)).

The second mechanism, called **energy transfer mechanism**[26, 108, 20], does not need a specific orbital level alignment. Similarly to the NCP luminescence mechanism (see paragraph 2.1.2), the molecular excitation is generated via an energy transfer from an electron tunneling inelastically (Fig. 2.19 (a)). In this picture, the only restrictive condition is that the electrons have to carry enough energy to excite the molecule, which is characterized by the quantum relation: $e|V| \geq h\nu$.

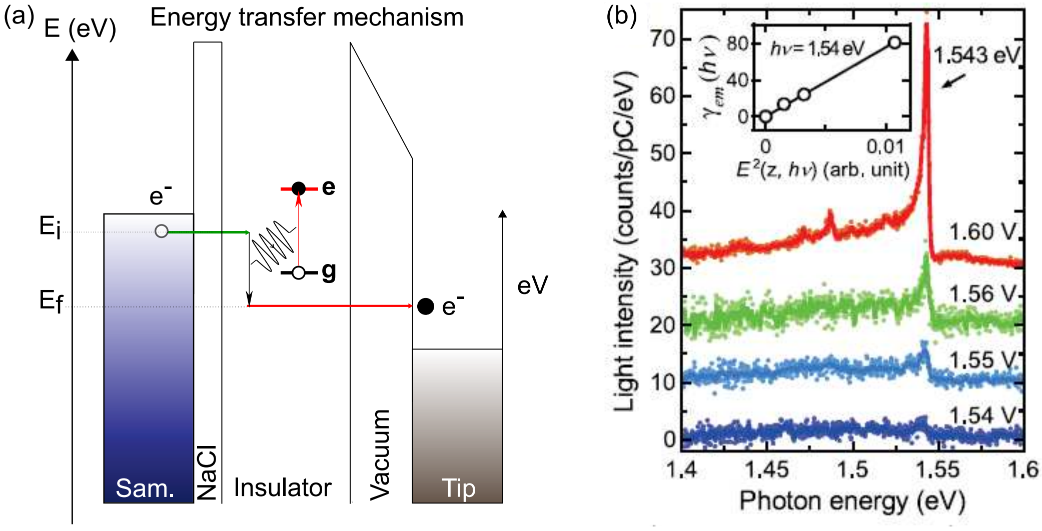

**Figure 2.19:** Energy transfer mechanism (a) Energy sketch of the mechanism. The inelastic tunneling transition is resonant with the molecular exciton with the condition $E_i - E_f = h\nu$. Therefore the energy threshold is given by $e|V| \geq h\nu$. (b) Voltage dependency of the STM-LE intensity of a suspended porphyrin molecule. Adapted from [20]

.

This is illustrated in Figure 2.19 (b) by the voltage dependency of the STM-LE intensity, from the work of Chong *et al.* [20]. One can see that the fluorescence onset voltage is perfectly matching with the fluorescence energy ($eV = h\nu$). Note that this energy transfer mechanism has often been explained as a plasmon-mediated mechanism [26, 108, 20]: a tunneling electron excites an NCP mode which can excite the molecule.

The two types of mechanisms have been suggested independently. However, Imada *et al.* have first suggested the possibility of an interplay between the two mechanisms. This conclusion relies on the observation of different emission regimes. First, they observe a drastic increase of the STM-LE intensity when the tip goes from outside of the molecule to above [50] (see paragraph 2.3.2). This suggests a more effective excitation when the tunnel current can cross the molecule. One has to note that it could also be due to the position of the molecule in the plasmonic nanocavity, which drastically affects the radiative decay of the molecular exciton [6]. Second, they observe two different voltage regimes in the STM-LE intensity [49] when the tip is placed above the molecule. The second point has been investigated deeply in the work of Chen *et al.* [16], where they studied STM-F intensity of a single $H_2Pc$ molecule as a function of the voltage (Fig. 2.20 (a)).

---

[6] I will discuss this aspect in the next chapter.

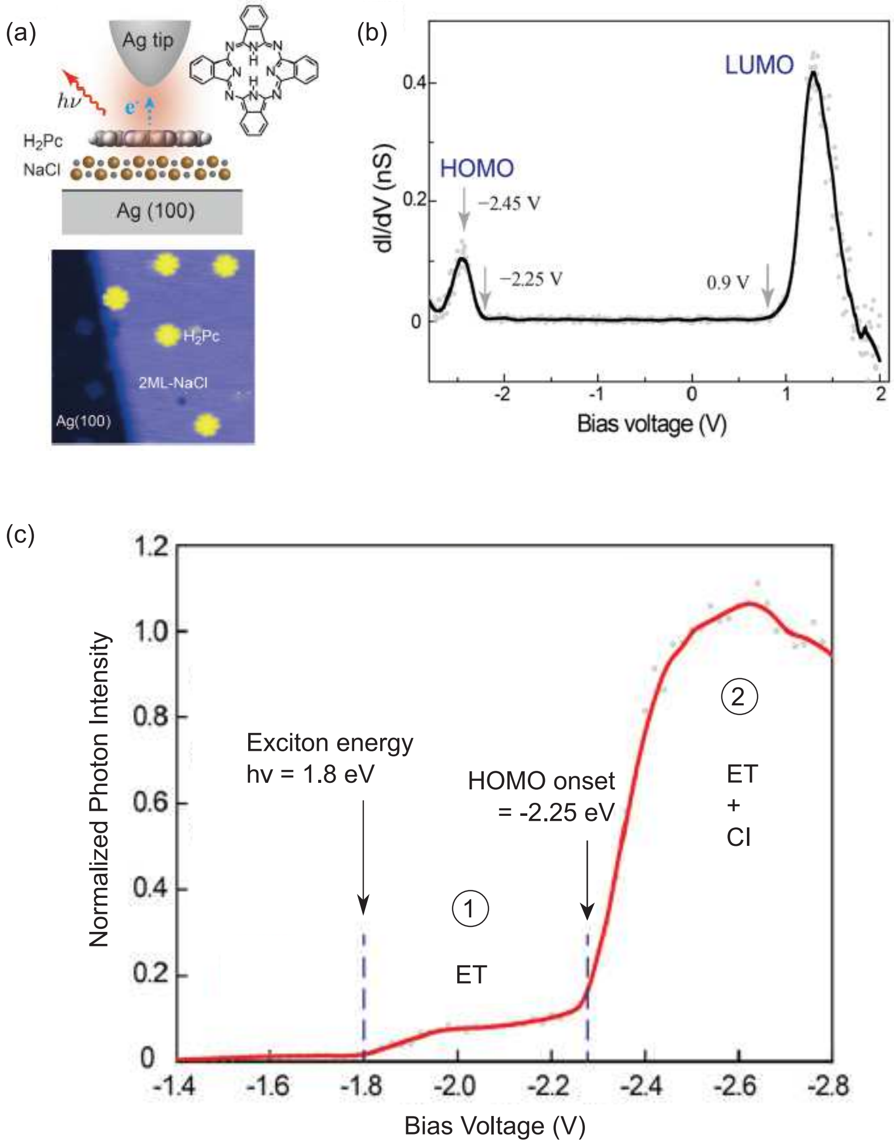

**Figure 2.20:** STM-LE of a single $H_2Pc$ molecule as a function of the voltage. (a) Sketch of the experiment. (b) Differential conductance as a function of the voltage. The resonance peak at negative voltage (resp. positive) corresponds to the HOMO state (resp. LUMO). (c) STM-LE as a function of the voltage. Adapted from [16]

On the one hand, the differential conductance spectrum ($dI/dV$) shows a peak at the negative voltage that corresponds to the HOMO of the $H_2Pc$ molecule (Fig. 2.20 (b)). The voltage onset of this peak is ≈ -2.25 V. On the other hand, the STM-LE intensity as a function of the voltage reveals two onsets (Fig. 2.20 (c)). The first onset is observed at ≈ -1.8 V, which corresponds to the molecular exciton energy ($h\nu = 1.8$ eV). The second onset is observed at ≈ -2.25 V, which corresponds to the onset of the HOMO in the $dI/dV$ spectrum (see Fig. 2.20 (b)). This suggests two different regimes of excitation. A first regime of excitation (labelled 1 in figure 2.20 (c)) for -2.25V $\leq V \leq$ -1.8 V where only the ET mechanism is possible. And a second regime (labelled 2 in figure 2.20 (c)) for $V \leq$ -2.25V where both ET and CI mechanisms are possible. Noticeably, the photon yield in the second regime is much larger than in the first one.

The authors suggest that this is proof that the CI injection is the dominant mechanism as soon as a tunneling through the molecular state is possible.

## 2.4 Summary

The STM environment provides both an excitation source, thanks to tunneling electrons, and an amplifier medium thanks to the specific electromagnetic modes called Nanocavity-Plasmon (NCP) confined in the STM junction. This unique combination, together with a sufficient molecular decoupling from the electrodes can be used to obtain fluorescence emission from a single molecule. The early experiments [92, 127, 15, 65], although very promising, have failed to provide an unambiguous single-molecule fluorescence signal. For the very first time, Chong *et al.* [20] obtained such a signal, thanks to an innovative decoupling technique where the molecular emitter was suspended between the tip apex and the surface by molecular wires. Moreover, in this work vibrational signatures could be observed. Unfortunately, in this suspended configuration the STM spatial resolution is lost, forbidding further imaging investigations. The NaCl decoupling method developed by Zhang *et al.* [129], allowed to obtain the fluorescence signal of a single phthalocyanine molecule while preserving the imaging capability of the STM. In this configuration, Zhang *et al.* [129] as well as Imada *et al.* [49] have shown that the emission of two coupled molecules is mainly driven by the molecular dipole moment interaction, but is also dependent of the tip position. The same teams [134, 50] have also investigated the NCP-molecule interplay, showing that the molecule can be "remotely excited" by the NCP. Furthermore, single-photon emission from a single $ZnPc$ has also been demonstrated by Zhang *et al.* [132]. From these works [49, 50, 134, 17], different regimes of emission could be found. These two regimes depend on the tip position as well as the voltage (*i.e* tunneling electron energy) applied to the junction.

Yet a lot of questions remain.

- How does the dipole moment of a single molecule influence, at this scale, the light emitted in the far-field?
- What kind of information would we learn from this?
- How can we explain the fact that the emission strongly depends on the tip position?
- Is it due to the local excitation provided by the extreme localization of the tunneling current?
- Vibrational features are usually considered as a specific fingerprint of a molecule in spectroscopic methods such as infrared or Raman spectroscopy. How does this vibrational signature vary when the signal is acquired at different excitation positions in the molecule?
- More fundamentally, what is the physical meaning of an optical spectrum of the inside of a molecule?

- Since the STM allows to inject electric charges directly inside the molecule, can we use this property to control the redox state of a single molecule, and at the same time characterize this redox state optically?

The goal of my thesis is to attempt to provide answers to these questions. The following part of the manuscript will present the main results obtained during these three years.

# Chapter 3

# Hyper-Resolved Fluorescence Microscopy

In this chapter, I report STM-F experiments carried out on a single free-base phthalocyanine molecule $H_2Pc$. STM-F spectra reveal duplication of the two main fluorescence lines of the molecule, which is associated with a tautomerization process. Hyper-Resolved Fluorescence Microscopy maps (*i.e* maps showing the variation of the fluorescence signal as a function of the tip position) are realized on those lines and discussed with a theoretical model to confirm that the spatial variation of the fluorescence signal is essentially due to the coupling between the molecule transition dipole moment and plasmonic modes confined on a scale much smaller than the molecule. Thanks to this interpretation HRFM maps are used to identify the fluorescence lines of each tautomer. A temporal analysis of the fluorescence signal is presented and allows tracking the tautomerization dynamics. Finally, a tautomerization mechanism involving the excitonic state of the molecule is discussed.

## 3.1 STM-F spectroscopy

### 3.1.1 Description of the system

**General properties**

The experiments presented in this chapter have been carried out on single free-base phthalocyanine molecules ($H_2Pc$) decoupled from an Ag(111) substrate by a thin layer (3 atomic layers) of NaCl (Fig. 3.1 (a)). The $H_2Pc$ molecule presents two main axes of symmetry. The first axis (x-axis) is aligned with the two inner hydrogens of the molecule while the second axis (y-axis) is perpendicular to this direction (Fig. 3.1 (a)). Figure 3.1 (b) presents a large scale STM image of four $H_2Pc$ molecules adsorbed on a three-monolayer NaCl island grown on Ag(111). Molecules on the bare metallic surface are faintly visible while they present a bright eight-lobe pattern on the NaCl island. This indicates that the molecular electronic properties are preserved on NaCl, thanks to an excellent electronic decoupling from the surface. A differential conductance spectrum acquired on a molecule adsorbed on the NaCl island presents two peaks (Fig. 3.1 (c)). The peak at negative voltage corresponds to the HOMO state ($E_{HOMO} \approx$ -2.5 eV) while the peak at positive voltage corresponds to the LUMO state ($E_{LUMO}$ = 0.7 eV). A STM image of the HOMO can be realized under a voltage $V$ = -2.5

V while the LUMO is imaged with a voltage $V = 0.7$ V (inset Fig. 3.1 (c)). The HOMO image presents an eight-lobe pattern with a four-fold symmetry, while the LUMO image presents a two-fold symmetry pattern. Figure 3.1 (d) presents a comparison between these images and the spatial projections of the HOMO and LUMO orbitals obtained with Density Functional Theory (Fig. 3.1 (d)). The good agreement between STM images and DFT calculations confirms the preservation of the intrinsic electronic properties of the molecule. Interestingly, DFT calculations show that the nodal axis observed in the LUMO is found to be the y-axis (Fig. 3.1(a)) of the $H_2$Pc molecule. Therefore the STM image of the LUMO allows one to identify the two symmetry axis of the molecule.

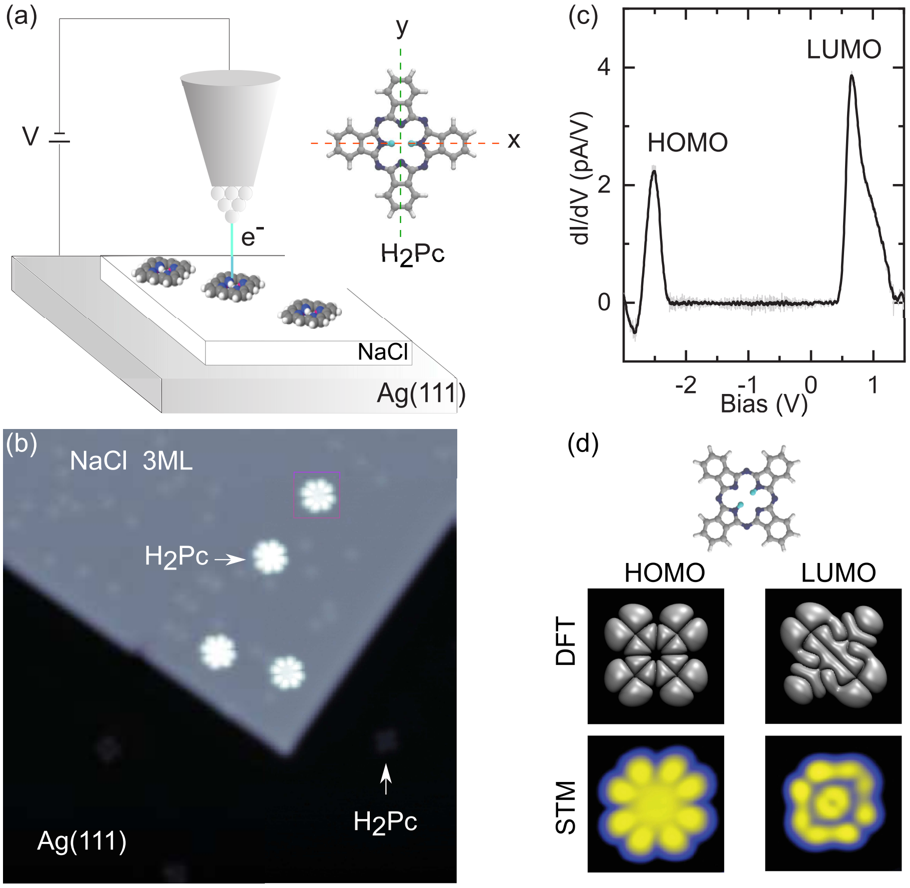

**Figure 3.1: STM measurement on $H_2$Pc molecules decoupled from a Ag(111) substrate by a thin layer of NaCl.** (a) Sketch of the experiments. The two axes of the $H_2$Pc molecule are labelled x and y. (b) Large scale STM image ( $30 \times 30$ nm$^2$; $V$ = -2.5 V; $I_t$ = 10 pA) of $H_2PC$ molecules adsorbed on a NaCl island resting on bare Ag(111) surface. (c) Differential conductance spectrum acquired on the molecule surrounded by a purple square in (b). (d) Comparison between DFT calculations and experimental STM images of the HOMO ($V$ = -2.5 V; $I_t$ = 10 pA) and the LUMO ($V$ = 0.7V; $I_t$ = 10 pA). The nodal axis of the LUMO corresponds to the y axis defined in (a).

### 3.1.2 STM-F spectroscopy on $H_2Pc$

Figure 3.2(a) presents three STM-F spectra (labeled 1, 2, and 3) recorded under a negative voltage ($V$ = -2.5 V) at the three corresponding positions indicated in Fig. 3.2(b). The first spectrum (labelled 1) recorded on a branch of the $H_2Pc$ molecule presents an intense emission line at $\approx$ 1.80 eV and a weaker line at $\approx$ 1.92 eV. These two lines can be assigned to the two first optical transitions of the $H_2Pc$ molecule named $Q_x$ and $Q_y$ respectively [83]. While the $Q_x$ emission line is associated to the transition dipole moment directed along the hydrogen axis (Fig. 3.2(c)), the $Q_y$ emission line is associated to the perpendicular transition dipole moment. Another spectrum recorded on the same molecule at the perpendicular branch (position 3) shows similar spectral features but with a 20 meV shift of the $Q_x$ line towards higher energies. Eventually, the last spectrum recorded between the two branches (spectrum 2) shows that this shift originates from a duplication of the $Q_x$ line. Interestingly, one observes in the STM images of the LUMO two different patterns presenting its typical two-fold symmetry but tilted by 90° (Fig. 3.2(d)). A switch from one pattern to another is often observed after a scan at a negative voltage ($V$ = -2.5V the same voltage as used in the STM-F spectra). This suggests that a scan at negative voltage induces a swapping between the x-axis and the y-axis, a phenomenon called tautomerization which has been previously observed, by STM, on similar systems [68, 58, 60, 12, 63]. Therefore, the two different patterns can be assigned to the two different tautomers of the $H_2Pc$ molecule (bottom panel of Fig. 3.2(c)).

The observation of this tautomerization process together with the duplication of the $Q_x$ lines, at a negative voltage, suggests that the two lines may correspond to the fluorescence emission of each tautomer. To investigate this hypothesis further, the next section will focus on the detailed variation of the STM-F signal as a function of the tip position.

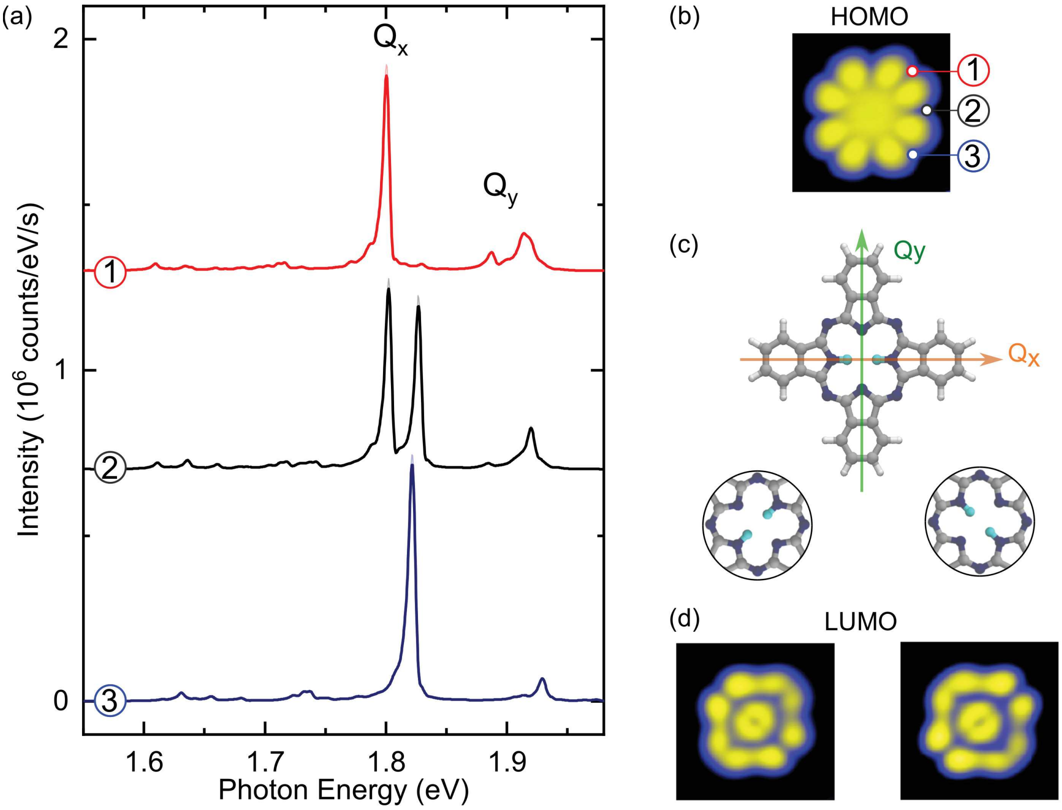

**Figure 3.2: STM-F spectroscopy of individual $H_2Pc$ molecules** (a) STM-F spectra recorded ($V$ = -2.5 V; $I$ = 100 pA; acquisition time $t$ = 120 s) with the tip located at the three positions indicated in (b). (b) STM image ($V$ = -2.5V; $I$ = 10 pA; 3 × 3 $nm^2$) of the HOMO. (c) Sketch of the $H_2Pc$ molecule and zoom on the central part of the molecule highlighting the structure of the two tautomers. (d) STM images ($V$ = +0.55 V; $I$ = 10 pA; 3 × 3 $nm^2$) of the LUMO. Two patterns tilted by 90° from each other may be observed in the image of a same molecule, corresponding to the two tautomers.

## 3.2 Hyper-Resolved Fluorescence Microscopy

### 3.2.1 Spatial mapping of the fluorescence signal

To further investigate the connection between tautomerization and fluorescence we realized a spatial mapping of the fluorescence signal. This procedure, that we call **Hyper-Resolved Fluorescence Microscopy** (HRFM), is realized by recording an STM-F spectrum at each pixel of the image of the molecule (current map Fig. 3.3(a)). For a given fluorescence line, these maps show the variation of its intensity as a function of the tip position.

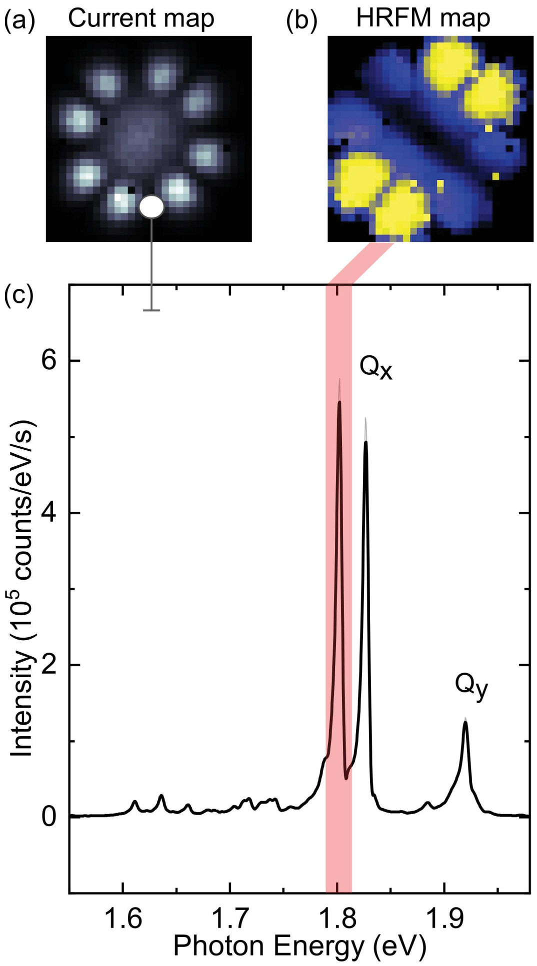

**Figure 3.3: Spatial mapping of the fluorescence signal.** (a) Current map ($V$ = -2.5 V; 2.5 × 2.5 nm$^2$) defining the grid (30 × 30 pixels) used for the mapping. This map is acquired simultaneously with the HRFM map. (b) HRFM map recorded for the first duplicated $Q_x$ line indicated by a red band in (c). Integration band : 1.798 < $h\nu$ < 1.811 eV. (c) STM-F spectrum ($V$ = -2.5 V; $I$ = 100 pA; acquisition time $t$= 120 s) acquired at the position marked by a circle in the current map (2.5 × 2.5 nm$^2$; $V$ = -2.5V) displayed in (a).

The mapping is realized on a grid of 30×30 pixels which is sufficient to resolve the HOMO structure of the molecule in the STM-constant height image (Current map in Fig. 3.3(a)). One has to note that the complete mapping of the molecule takes approximately 14 hours, which explains why we cannot use a better resolution. These measurements are conducted at constant-height (constant tip-sample distance) to prevent distance-related artefacts in the HRFM map. Under this condition, the current varies a lot with the tip position (see the current map in Fig. 3.3(a)), and thus the light intensity. To correct this effect, the fluorescence signal is therefore normalized by the tunneling current at each position. Fig. 3.3(b) presents the HRFM map recorded at the energy of the first duplicate line (red band in Fig. 3.3(c)). The map presents bright features on two opposite sides of the molecule, separated by a darker nodal axis. Superimposed to these features one can identify an eight-lobe structure which seems to be related to the one of the HOMO pattern (Fig. 3.3(a)).

To explain these observations it is necessary to understand the physical origin of the variation of the fluorescence signal as a function of the tip position. Based on a comparison with a theoretical model, the next part of this section will be focused on this aspect.

### 3.2.2 Origin of the spatial variation

The fluorescence process results from an excitation process followed by an emission stimulated by the quantum fluctuations of the electromagnetic field. As we presented it in paragraph 2.1.3, in our case the excitation is driven by the tunneling electrons while the emission is driven by the coupling between the molecular excitation and the **Nanocavity-plasmons** NCP (Fig. 3.4).

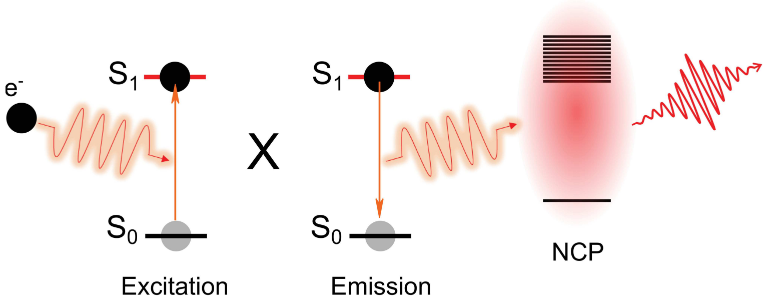

**Figure 3.4: Fluorescence process in a STM junction**

Therefore, the number of photons $Y_{det.}$ detected in the far-field for a given tip position $(x, y)$ is:

$$Y_{det.}(x, y) \propto \eta_{exc.}(x, y) \times \eta_{em.}(x, y) \tag{3.1}$$

where $\eta_{exc.}(x, y)$ is the electron-driven excitation efficiency and $\eta_{em.}(x, y)$ the plasmon-driven emission efficiency when the tip is located at the position (x,y).

Our collaborators Javier Aizpurua and Tomas Neuman built a theoretical model based on this formula to reproduce the experimental HRFM maps presented previously.

#### Description of the excitation process

Assuming that the excitation is due to tunneling electrons, the excitation efficiency $\eta_{exc.}$ represents the flux of tunneling electrons able to excite the molecule (let's call it excitation current $I_{exc.}$) divided by the total flux of electrons flowing in the junction (*i.e* the total tunneling current $I_{tot}$) :

$$\eta_{exc.} = \frac{I_{exc.}}{I_{tot}} \tag{3.2}$$

To evaluate $I_{exc.}$ we have to take into account that the STM-F spectrum is acquired at a voltage $V$ = -2.5 V which corresponds to resonant tunneling through the HOMO (see differential spectrum Fig. 3.2(c)). In the previous chapter (see **??**), based on several experimental evidence [49, 50, 16], we have mentioned that, under this condition, the light intensity is increased by an order of magnitude compared to a non-resonant condition (*i.e.* when the voltage is low enough so that the HOMO does not contribute to the transport). Therefore, we assume that the excitation mainly results from the tunneling of electrons through the HOMO, meaning that $I_{exc.} \propto I_H$, where $I_H$ is the tunneling current passing through the HOMO channel. The spatial dependence of $I_H$ is obtained from the fact that $I_H$ is proportional to the local density of states of the molecule and thus:

$$I_H(x,y) \propto |\Psi_{HOMO}(x,y)|^2 \tag{3.3}$$

where the term $|\Psi_{HOMO}(x,y)|^2$ is the squared modulus of the HOMO wave function evaluated at the constant-height tip position $(x, y, z = z_0)$.

Finally, by assuming that the transport mainly occurs through the HOMO channel the total current reads: $I_{tot} = I_H + I_{BG}$, where $I_{BG}$ is the small background current resulting from transport through other channels. For this background current, we assume that it is independent of the tip position in the (x,y) plane, and small compares to $I_H$.

Eventually, the expression of the excitation efficiency at position (x,y) is given by:

$$\eta_{exc.}(x,y) \propto \frac{I_H(x,y)}{I_H(x,y) + I_{BG}} \tag{3.4}$$

From this expression we can build an excitation efficiency map of $\eta_{exc.}(x,y)$ based on the HOMO map calculated by DFT, and by introducing the small current background $I_{BG}$.

### Description of the emission process.

The emission process results from the coupling between the molecular excitation and the electromagnetic field through the Purcell effect [91]. In most cases, the size of the emitter is much smaller than the electromagnetic-field variation scale. For instance, the coupling strength $g$ between an emitter and the electromagnetic field in a "regular" optical cavity is often evaluated as [85]:

$$\hbar g \approx -\mathbf{p_{eg}} \cdot \mathbf{E}(M) \tag{3.5}$$

where $\mathbf{p_{eg}}$ is the dipole moment of the optical transition of the emitter and $\mathbf{E}(M)$ the local electric field evaluated at the position of the emitter. This coupling, and thus the emission decay, is strongly enhanced by the presence of high-density optical cavity modes which are resonant with the molecular optical transition.

From this expression the emission efficiency is simply:

$$\eta_{em.} \propto |g|^2 \tag{3.6}$$

However, when the value of the electromagnetic field varies on a scale comparable to the size of the emitter this description fails. In our experiments, the spatial extension of the NCP is, therefore, a crucial parameter to evaluate if we want to understand their impact on the spatial variation of the emission. Until recently, the consensus was that plasmonic structures can confine the electromagnetic field within a volume typically of the order of 10 nm$^3$ [106]. This value is in agreement with the discussion of the paragraph 2.3.2, where we discussed the possibility to remotely excite the molecule through NCP-exciton coupling. Especially, Imada *et al.* showed that it was possible to excite the molecule fluorescence with a tip located at 3 nm away from the molecule center, which would correspond to an NCP volume of a few tens of nm$^3$. However, atomic-scale simulations have predicted that plasmonic confinement to atomic scales [2] could arise if one takes into account atomic features in such structures. This prediction has been demonstrated experimentally by Benz *et al.* [111]. In this work, the authors show that atomic features, assembled or disassembled by laser irradiation inside a plasmonic cavity, formed by a gold nanoparticle and a gold film, could strongly affect the Raman spectrum of a single molecule located inside the cavity, due to the highly localized plasmonic field. To visualise the concept, Fig. 3.5(a) presents the theoretical simulation used by the authors to confirms the experimental observations. The top panel presents the near-field map calculated for a gold nanoparticle in front of a gold film. The presence of atomic protrusions highly increases the electromagnetic field density in the vicinity of the protrusions. To highlight this effect, the bottom panel of Fig. 3.5(a) shows a comparison between the in-gap field enhancement in presence of the **pico-cavity** (red line), due to the atomic protrusions, and without this pico-cavity (dashes black line).

A complete transposition of these results can be done to our system, and allow making assumptions regarding the electromagnetic properties of the junction. In addition to the NCP described previously, we assume that the last few atoms of the tip apex (which are necessary to carry out STM images) generate a second cavity called **pico-cavity** which confine the so-called **pico-cavity plasmons** (PCP) modes to volumes of the order of 1 nm$^3$ (Fig. 3.5(b)). In this situation, the spatial extension of the electromagnetic field is much smaller than the emitter size, and therefore we cannot estimate the coupling strength with the expression 3.5. In the model developed by our collaborators (see reference [85] for details), the coupling strength $g_Q$ between a plasmonic mode of the pico-cavity and the molecular excitation of the $Q$ transition ($Q$ is $Q_x$ or $Qy$) is calculated as:

$$g_Q(\mathbf{r}) = \iiint d^3\mathbf{r}'\rho_Q(\mathbf{r}')\phi(\mathbf{r}' - \mathbf{r}) \tag{3.7}$$

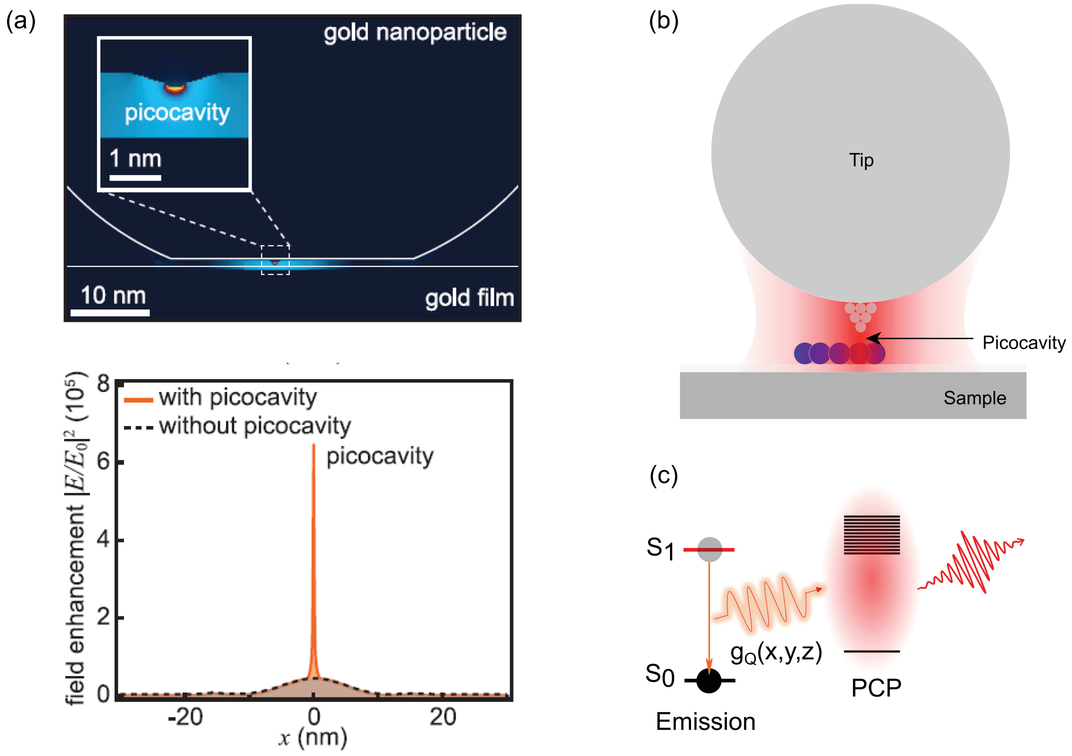

**Figure 3.5: Description of the emission process** (a) Simulations of the system used by Benz *et al.* consisting of a gold nanoparticle and a gold film. Top panel: 3D map of the near-field intensity with an enlarged view of the pico-cavity showing strong enhancement of the field localized in the vicinity of atomic protrusions. Bottom panel: Comparison of the field enhancement with (red line) and without (dashed line) the pico-cavity. Adapted from [111]. (b) Sketch of the STM junction taking into account the pico-cavity formed by the last atoms located at the tip apex. (c) Sketch depicting the fluorescence emission as a local coupling, at the tip position (x, y), between the molecular excitation and the highly localized pico-cavity-Plasmons.

This expression represents an overlap integral of the excitonic transition-charge density $\rho_Q$ and the scalar potential $\phi$ of the plasmonic excitation which is confined in the pico-cavity. Note that the plasmon mode is chosen to be resonant with the optical transition (*i.e* $\hbar\omega_p = h\nu$). The scalar potential is calculated in a geometry that takes into account the atomic-size protrusion at the tip apex which thus gives the sub-molecular confinement of the PCP. This overlap integral is evaluated for each tip position (x,y) for a given tip height, yielding the spatial mapping of the coupling strength between the molecular optical transition and the PCP (Fig. 3.5(c)). Finally, the spatial dependence of the emission efficiency $\eta_{em.}(x,y)$ for a given optical transition $Q$ is:

$$\eta_{em.}(x,y) \propto \left|g_Q(\mathbf{x},\mathbf{y})\right|^2 \tag{3.8}$$

where the coupling strength is evaluated for a given tip height.

### Simulations and results

Fig. 3.6 shows the results of the simulation for a $Q_x$ transition of the $H_2Pc$ molecule. Figure 3.6(a)) recalls the differents steps of the fluorescence process: excitation (left panel) by the tunneling electrons, and emission (right panel) driven by the coupling with PCP.The theoretical map ($Y_{det.}(x,y)$) is a convolution of the excitation map ($\eta_{exc.}(x,y)$ calculated via 3.4), with the emission map ($\eta_{em.}(x,y)$ calculated via 3.8). These three maps are displayed in Fig. 3.6(c). The excitation map presents a HOMO-like pattern whereas the emission map presents a dipole-like pattern with two lobes, directed along the $Q_x$ dipole of the $H_2Pc$ molecule (Fig. 3.6(b)). The comparison between the theoretical and experimental maps shows an excellent agreement (Fig. 3.6(d)).

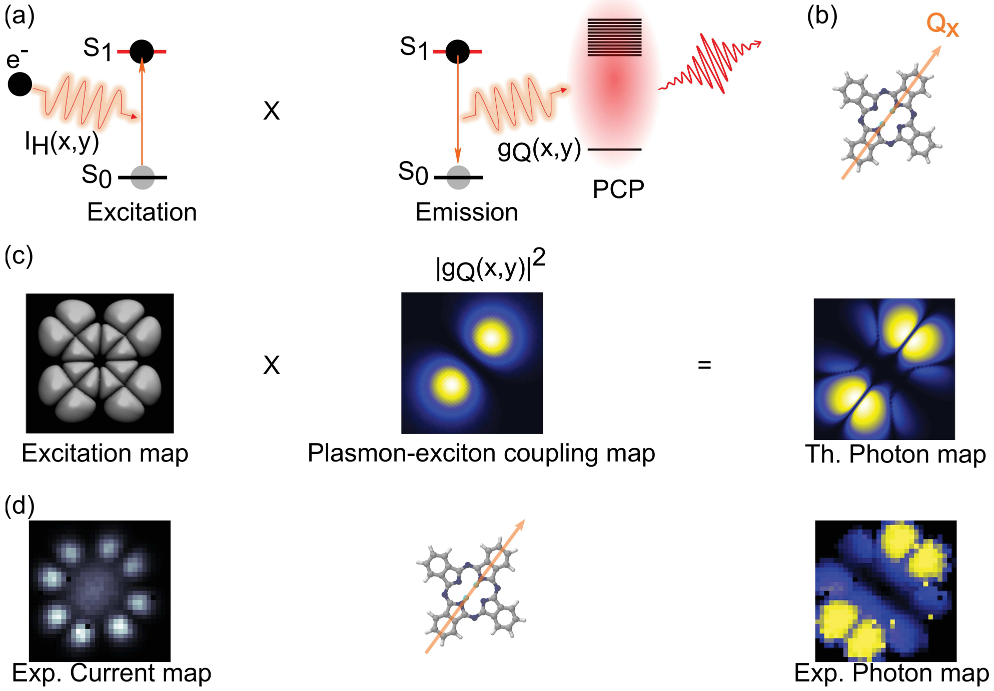

**Figure 3.6: Modelisation of the $Q_x$ HRFM map** (a) Sketch depicting the fluorescence process. (b) Orientation of the transition moment dipole of the $Q_x$ transition. (c) Theoretical map obtained as a convolution of the excitation map and the emission map. The emission map is the square absolute value of the plasmon-exciton coupling map. (d) Experimental map.

This excellent agreement between theoretical and experimental HRFM maps has several consequences regarding the information that we can extract from the HRFM maps presented in figure 3.3. The reminiscent pattern of the HOMO confirms that the excitation is mainly driven by direct tunneling into the HOMO. On another hand, the dipole-like pattern is direct visualisation of the variation of the emission efficiency as a function of the tip position. The emission is increased (resp. decreased) at the extremities (center) of the molecular dipole because of the better (resp. worse) coupling with the plasmonic pico-cavity modes. Due to the high localization of these modes, on a scale much smaller than the molecule itself, an HRFM map constitutes what might be called an optical image of the molecule transition-dipole moment. This means that the spatial mapping of the STM-F signal that we term Hyper Resolved Fluorescence Microscopy can be considered as an optical microscopy technique with close-to atomic-scale spatial resolution.

Furthermore, the excellent agreement between experiment and theory confirms, *aposteriori* the existence of the pico-cavity in the STM junction.

### 3.2.3 Fluorescence identification of each tautomer

Thanks to the understanding provided by the previous discussion, one can apply the HRFM technique to the other contributions observed in the STM-F spectra (see paragraph 3.1.2). In Fig. 3.7(b) we display the HRFM maps (panel noted Exp.), as well as the corresponding theoretical maps (panel noted Theory) for the four contributions, noted $Q_{x1}$, $Q_{x2}$, $Q_{y1}$, and $Q_{y2}$, that appear in the spectrum of Fig. 3.7(a). For all the maps, a similar "dipole like" pattern is observed. Since an HRFM map recorded for a given fluorescence line allows to directly visualise the corresponding transition dipole moment orientation, for a given configuration of the $H_2Pc$ molecule, the $Q_x$ and $Q_y$ maps will, therefore, present a perpendicular pattern. Upon this consideration one can conclude that the $Q_{x1}$ and $Q_{y1}$ (resp. $Q_{x2}$ and $Q_{y2}$) lines are associated to tautomer 1 (resp. tautomer 2) of the $H_2Pc$ molecule (Fig. 3.7(b) and (c)). To emit at different energies, the two otherwise equivalent tautomers must experience a slightly different environment. This is confirmed by the substantial difference observed in the $Q_x - Q_y$ gaps of the two tautomers. Tautomer 1 has a $Q_x - Q_y$ gap of $\approx 0.17$ eV whereas it is $\approx 0.10$ eV for tautomer 2. Interestingly, this latter is very close to the one observed in cryogenic matrices [83]. This suggests that the molecule is submitted to additional constraints in the structure of tautomer 1 compared to the structure of tautomer 2.

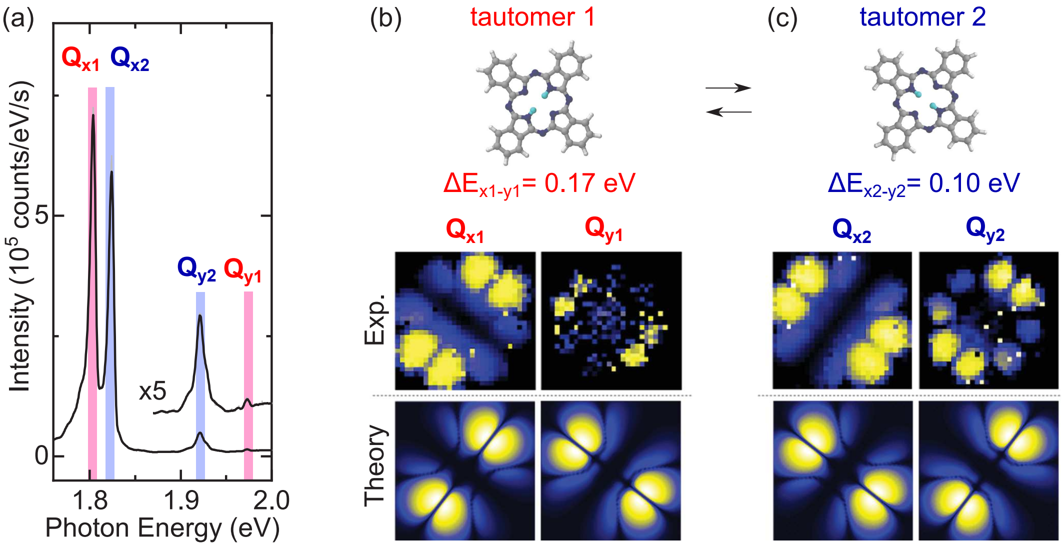

**Figure 3.7: Identification of the two tautomers with Hyper-Resolved Fluorescence Microscopy.** (a) STM-F spectrum ($V$ = -2.5 V, $I$ = 100 pA, acquisition time $t$ = 180 s) acquired at the position marked by a circle in the current image ($2.5 \times 2.5$ nm$^2$, $V$= -2.5 V) in inset. In (b) and (c) we display the chemical structure of tautomers 1 and 2, the associated HRFMs for the main contributions ($Q_{x1}$ : 1.798 $< h\nu <$ 1.811 eV , $Q_{y1}$ : 1.972 $< h\nu <$ 1.981 eV , $Q_{x2}$ : 1.824 $< h\nu <$ 1.832 eV, and $Q_{y2}$ : 1.923 $< h\nu <$ 1.941 eV) identified in (a) together with their related simulated maps.

## 3.3 Description of the tautomerization process

HRFM maps allowed us identifying the fluorescence associated with each tautomer. In this section we will provide a temporal analysis of the fluorescence signal, first to confirm our interpretation and second to understand further the dynamic of the process.

### 3.3.1 Dynamic of the tautomerization process

Thanks to the fluorescence line assignments for each tautomer realized in paragraph 3.2.3, a temporal tracking of their respective emission can be carried out. To do so, the fluorescence signal is separated with a beam splitter in two paths. These two paths are spectrally filtered with a narrow bandwidth (Fig. 3.8(a)) at the energies of, respectively, the $Q_{x1}$ and $Q_{x2}$ lines and eventually sent towards avalanche photo-diodes (APDs), which allow recording a temporal trace of the signal (dead time $\approx$ 100 ns). Figure 3.8(b) shows 200 ms of temporal traces of the $Q_{x1}$ and $Q_{x2}$ emission lines (Fig. 3.8 (b)) and the tunneling current which has been recorded simultaneously. Note that one bar in the fluorescence traces corresponds to the detection of one photon by the detector. The emission stream, for both $Q_{x1}$ and $Q_{x2}$, consists of a bunch of photons emitted during a time of the order of 10 ms, followed by a "dead time" of a similar duration where only a few photons are detected. We can notice that the two tautomer emissions are anti-correlated, which means that the emission bunch of one tautomer appears during the "dead time" of the other. This confirms that the

$Q_{x1}$ and $Q_{x2}$ photons are not emitted at the same time, thus the $Q_{x1}$ and $Q_{x2}$ contributions correspond to the fluorescence emission of the different tautomers of the $H_2Pc$ molecule. This phenomenon is also confirmed by the telegraphic noise observed in the temporal trace of the tunneling current. This kind of signal in the current temporal trace is similar to what has been already observed on similar systems [68] and is due to the difference of the local conductance between the two tautomers. From the data presented in figure 3.8(b), we can also see that the plateau of emission from the $Q_{x2}$ transition (tautomer 2) seems slightly longer than the one of tautomer 1. This suggests that the molecule spends more time in the tautomer-2 form than in the tautomer-1 form.
To obtain quantitative information about the tautomer lifetime we performed, on the $Q_{x1}$ and $Q_{x2}$ fluorescence signals, correlation measurement by HBT interferometry [69]. More precisely, we measured the second-order correlation function $g^{(2)}(\tau)$, which estimates the probability to observe photon pairs separated by a delay time $\tau$ [69, 71]. One has to note that this approach has been recently used in STM-F experiments to characterize molecular fluctuations [88, 77] and single-photon sources [76] [132].

Two types of second-order correlation functions are displayed in figure 3.8(d): We displayed the functions $g^{(2)}_{11}(\tau)$ and $g^{(2)}_{22}(\tau)$, which are the second order **auto-correlation** functions of the intensity of respectively the $Q_{x1}$ and $Q_{x2}$ fluorescence lines. These functions estimate the probability to detect a pair of photons, whose detection times are separated by a time delay $\tau$, and which are emitted from the same fluorescence transition [69]. For instance, $g^{(2)}_{11}(\tau)$ estimates the probability to detect a pair of photons coming from tautomer 1 separated by a delay $\tau$. These functions are generally defined as:

$$g^{(2)}_{ii}(\tau) = \frac{\langle I_{Q_{xi}}(\tau) I_{Q_{xi}}(t+\tau)\rangle}{\langle I_{Q_{xi}}(t)\rangle^2} \tag{3.9}$$

where index $i$ stands for 1 or 2, and $I_{Q_{xi}}$ is the intensity of the $Q_{xi}$ line. Experimentally, the $g^{(2)}_{ii}(\tau)$ function is approximated by the histogram function of delay times for each pair of photons appearing in the photon stream of the $Q_{xi}$ trace (Fig. 3.8(b)).

We also display the cross-correlation function $g^{(2)}_{12}(\tau)$ which is defined by:

$$g^{(2)}_{12}(\tau) = \frac{\langle I_{Q_{x1}}(\tau) I_{Q_{x2}}(t+\tau)\rangle}{\langle I_{Q_{x1}}(t)\rangle \langle I_{Q_{x2}}(t)\rangle} \tag{3.10}$$

This function estimates the probability to detect a photon emitted from the $Q_{x2}$ transition (tautomer 2) at a time $\tau$ after the detection of a photon emitted from the $Q_{x1}$ transition (tautomer 1). Experimentally, this function is also approximated by the histogram function of delays time between each possible pair of tautomer1-tautomer2 photon.

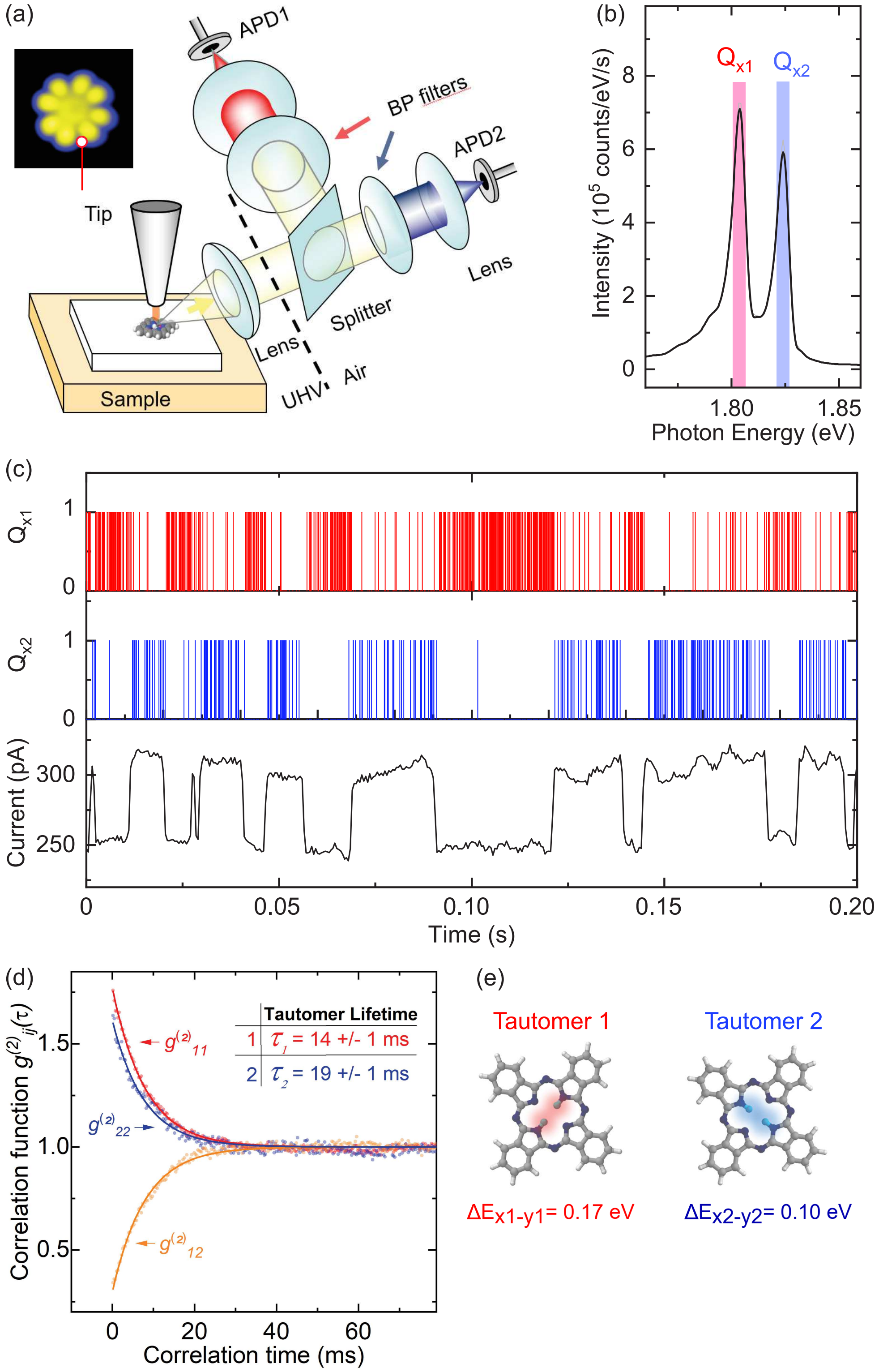

**Figure 3.8: Temporal tracking of the tautomerization process** (a) Sketch of the time resolved setup. Inset: STM image of the molecule ($V$ = -2.5 V; $I$ = 10 pA; 3.5 × 3.5 nm$^2$. (b) Reference fluorescence spectrum showing the $Q_{x1}$ (tautomer 1) and the $Q_{x2}$ (tautomer 2) lines. (c) Temporal traces acquired ($V$ = -2.5 V; current set point: $I$ = 250 pA) simultaneously on APD1 and APD2, corresponding respectively to the $Q_{x1}$ (tautomer 1) and the $Q_{x2}$ (tautomer 2) transitions. These traces are recorded at the position marked by a circle on the STM image in (a). (d) Second order auto-correlation $((g^{(2)}_{ii}(\tau))$ and cross-correlation $((g^{(2)}_{12}(\tau)$ functions of the APD signals displayed in (b). (e) Sketch depicting the two tautomers and their respective $Q_x - Q_y$ gap.

For short delay times $\tau$, auto-correlation functions (Fig. 3.8(d)) reveal a bunching ($g_{ii}^{(2)}(\tau) > 1$) while the cross-correlation function presents an anti-bunching ($g_{12}^{(2)}(\tau) < 1$). For larger delay times, an uncorrelated emission ( $g_{ii}^{(2)}(\tau) = g_{12}^{(2)}(\tau) = 1$) characterizes both functions. The anti-bunching observed in the cross-correlation function confirms that the two tautomers do not emit at the same time. This is confirmed by the bunching observed in the auto-correlation functions, which shows that the molecule remains a certain time in a given tautomer configuration and undergoes several excitation-emission cycles before switching in the other configuration.

These correlation functions can be fitted with a single exponential decay, $g_{ij}^{(2)}(\tau) = 1 + Ae^{-k\tau}$, where k is the tautomer switching frequency. From these fits, we used a two-level system model, based on [69], to evaluate the lifetime of each tautomer. For a current of 250 pA, these lifetimes are $\tau_1 \approx 14$ ms for tautomer 1 and $\tau_2 \approx 19$ ms for tautomer 2, which means that tautomer 2 configuration is energetically more favourable than tautomer 1. This is consistent with the difference observed in the $Q_x - Q_y$ gap which suggested that the molecule experiences different interactions with its environment, depending on the tautomer form (Fig. 3.8(e)).

To investigate this hypothesis, the next paragraph will focus on a detailed analysis of the near molecular environment.

### 3.3.2 Impact of the NaCl island on the $H_2$Pc fluorescence spectra

STM-F spectra acquired on different $H_2$Pc molecules have revealed different energy separations between the $Q_{x1}$ and $Q_{x2}$ emission lines. Overall one can observe three different behaviours. Fig. 3.9(a) shows three STM-F spectra recorded on three different molecules, focused in the energy region of the $Q_x$ peak. The first spectrum (labeled type 1), where no splitting is observed, corresponds to the situation reported by Imada *et al.* [49] [50]. Type 2 spectrum shows an energy difference of $\approx 5$ meV between the $Q_{x1}$ and $Q_{x2}$ peaks while type 3, **which is the case investigated in this chapter**, shows a higher energy difference of $\approx 15$ meV. The STM image with the three molecules on which have been acquired these spectra is presented figure 3.9 (b). Except for a darker center for the type 3 molecule compared to type 2 and type 1, no other information can be extracted from the regular STM image. Assuming that the different behaviours may be due to a different adsorption site, we imaged the same area with a CO functionalized tip (Fig. 3.9 (c)). This tip functionalization procedure consists in picking a carbon monoxide molecule at the tip apex [1] to achieve atomic resolution [42]. This image reveals protrusions that correspond to the chlorine atoms of the top NaCl layer [79]. In this way, it is possible

---

[1] As discussed in the first chapter, tunneling current is essentially due to the coupling between the s-orbitals of the atom constituting the tip apex with the state of the sample. Using a molecule such as CO allows one to replace the s-orbitals of the tip with $\pi$-orbitals. Since the $\pi$-orbitals are highly confined along the CO molecule axis one can achieve better confinement of the tunneling electrons in this direction and thus a better spatial resolution.

to determine the adsorption site for each of the three $H_2Pc$ molecules with atomic-scale precision. All three molecules are adsorbed on the Na top sites with the $H_2Pc$ molecular axis oriented along the [100] and [010] directions of the NaCl(001) layer, similar to what has been reported by Miwa *et al.* [79]. From this observation, one can conclude that the adsorption site of the $H_2Pc$ molecule with respect to the NaCl lattice is not responsible for the three behaviours that are observed.

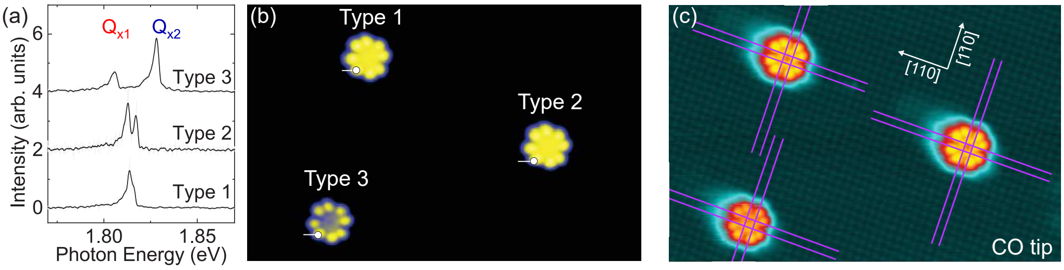

**Figure 3.9: Description of the three different behaviours observed in the STM-F spectra.** (a) STM-F spectra ($V$ = -2.5 V; $I$ = 200 pA; acquisition time $t$ = 300 sec) acquired on three different molecules. Spectra are acquired on the three molecules whose STM image is presented in (b). (b) STM image (20 × 14.2 $nm^2$; $V$ = -2.5 V; $I$ = 10 pA) of the three types of molecules. The arrows show the position at which the three spectra in (a) have been acquired. (c) Same image as (b) with a CO functionalized tip. The purple lines are directed along the chlorine atom alignments.

To better understand why the type 3 molecule appears less bright, figure 3.10 presents another data set which focuses on type 2 and type 3 molecules. Figure 3.10(a) shows an STM image of four molecules, deposited on a NaCl island. The molecules labeled 2 and 3 present a bright contrast while those labeled 1 and 4 seem darker. STM-F spectra acquired on these four molecules are presented figure 3.10(b). The molecules with a darker contrast (1 and 4) present a splitting greater than 15 meV which corresponds to a type 3 behaviour. Conversely, the brighter molecules (2 and 3) present a similar splitting of approximately 5 meV and thus are of type 2. To understand the origin of the difference in the contrast observed between type 2 and type 3 molecules, we recorded differential conductance spectra on the four molecules (Fig. 3.10(c)). The peaks corresponding to the HOMO of the type 2 molecules are shifted toward higher voltage compare to those of type 3, explaining the difference in the contrast observed in the STM images realized at a voltage $V$ = -2.5 V (see inset Fig. 3.10(c)). To understand further these observations we performed a high-resolution STM image on the sodium chloride. This image (inset Fig. 3.10(a)) is realized at high current and low voltage ($I$ = 100 pA; $V$ = -100 mV) to obtain details which are not provided by the large scale image. With these parameters, the tip is much closer to the surface, which makes it impossible to image the salt and the molecules together. For this reason, the high-resolution image is realized nearby the molecules and superimposed afterwards on the large scale image. Compared to the CO-tip image presented in figure 3.9(c), this image shows a linear **Moiré pattern**, which has been reported previously by Heidorn *et al.* [46]. This Moiré pattern is a consequence of the incommensurability of the NaCl lattice (square lattice) with the Ag(111) lattice (hexagonal lattice). Heidorn *et al.* showed that this Moiré is of electronic nature, meaning that the corrugation in the pattern results from a local modulation of the electrostatic potential. To check if different positions on the Moiré pattern may explain the lifting of the energy degeneracy between the two tautomers, (hence different fluorescence lines), figure 3.10(d) presents the same image as figure 3.10(a) but with an overlaid structure of grey lines that follow the Moiré pattern. Molecules 2 and 3 (type 2) occupy the layer of the exact same position on the Moiré pattern while molecules 1 and 4 (type 3) occupy different positions (see enlarged view in Fig. 3.9(e)). Therefore two molecules, although having the same type of adsorption site, may not be equivalent because they occupy different positions with respect to the Moiré pattern. Therefore, they may experience different local interactions with the NaCl, which affects their electronic properties, and thus their fluorescence spectrum. If now we add another degree of freedom, due to the tautomerization, one can understand that the two tautomers will emit at slightly different fluorescence energies. This also explains why the tautomer-2 form seems slightly more favourable than the tautomer-1 form.

These results show that a single-molecule STM-F spectrum may provide interesting new information regarding the direct environment of the emitting molecule, additionally to the structure and topography provided by conventional STM. In this way, a complete picture can be obtained at a scale unreachable by conventional optical techniques.

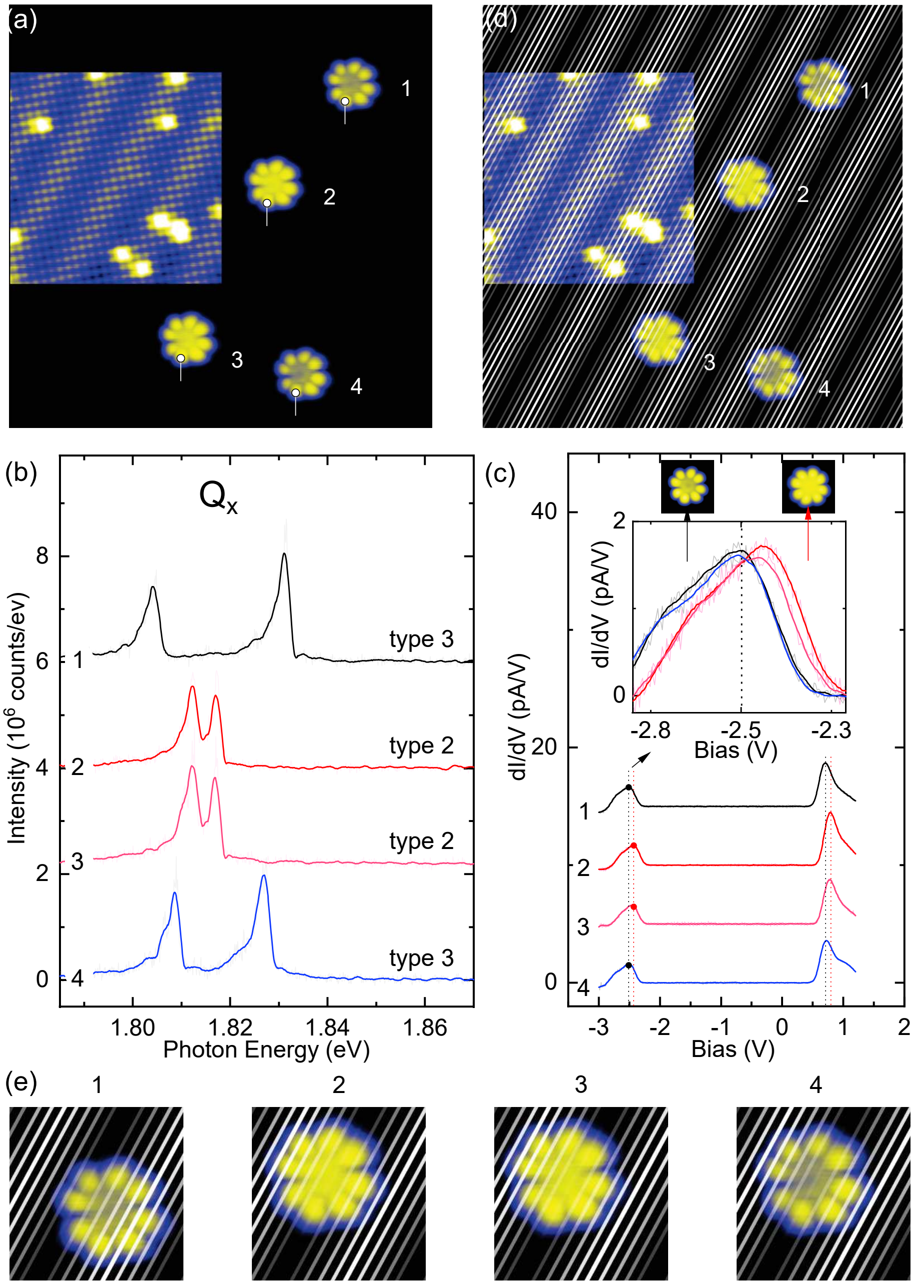

**Figure 3.10: Influence of the molecule position on the Moiré pattern.** (a) STM image (20 × 20 $\text{nm}^2$, $V$= -2.5 V) of four $H_2Pc$ molecules. The position of the atomically resolved STM image in inset (10 × 10 $\text{nm}^2$, $V$= -100 mV) has been precisely adjusted with respect to the larger STM image. (b) STM-F spectra acquired at $V$ = -2.5 V, $I$ = 200 pA, acquisition time $t$ = 120 s on the 4 molecules imaged in (a). (c) $\mathrm{d}I/\mathrm{d}V$ spectra acquired on the four molecules imaged in (a). (d) Same STM image as in (a) with an overlaid superstructure of gray lines that follow the linear Moiré pattern.

## 3.4 Tautomerization mechanism

### 3.4.1 Similarities between fluorescence and tautomerization processes

Figure 3.11(a) displays three data sets of temporal traces ($Q_{x1}$, $Q_{x2}$, and tunneling current) recorded at a setpoint current of $\approx$ 100 pA (top panel), $\approx$ 150 pA (middle panel), and $\approx$ 250 pA (bottom panel). Comparison between these three data sets shows that the tautomerization switching rate increases as a function of the tunneling current.

To obtain quantitative information about this current dependence of the switching rate, we realized the same correlation measurement as those presented Fig.3.8 with a range of different tunneling currents going from 10 pA to 400 pA. Figure 3.11(b) displays the switching rate, extracted from the fit of the $g^{(2)}$ functions, as a function of the tunneling current. The switching rate $k$ varies with the current $I$ as a power of 1.3. This super-linear behaviour is surprising if we consider an electron-activated process generally considered in similar systems [68]. Interestingly, a very close power law (1.2) is found for the variation of the light intensity with the tunneling current, which is consistent with other STM-F experiments on the same molecule [16].

This intriguing similarity in the current dependency of the fluorescence intensity and switching rate, suggests a connection between the fluorescence excitation and the tautomerization process (Fig. 3.11(c). To further investigate the connection between these two processes, we performed a series of voltage dependence experiments in different conditions. Figure 3.12(a) presents temporal traces of the tunneling current acquired at different voltages. These traces show the typical telegraphic noise, resulting from the change of the local conductance upon switching from one tautomer to the other. A reduction of the switching rate is observed when the absolute value of the voltage is reduced. Moreover, a voltage onset for the tautomerization process is observed at $V \approx$ -1.8 V. Similarly, series of fluorescence spectra acquired at different voltages, are displayed in figure 3.12(b). The threshold for the fluorescence emission is found around $V \approx$ -1.8V which is consistent with the energy of the $Q_x$ line. One can note a second threshold at $V \approx$ -2.4 V, where the light intensity increases strongly, which is due to the direct tunneling into the HOMO. The observation of the same voltage threshold in the current traces and the fluorescence signal may indicate that the tautomerization process occurs during an excitation/emission cycle of the molecule.

To confirm this assumption, we acquired a series of STM-F spectra at different voltages with the tip located at $\approx$ 1.2 nm away from the molecule (Fig. 3.12(c)). In this configuration, no direct tunneling through the molecule is possible. However, it has been shown that the molecule can be driven in its excited state (see paragraph 2.3.2) via coupling with the plasmons and may give a fluorescence signal without direct tunneling in the molecule [50, 134, 56]. The most striking observation is that the fluorescence duplication, thus the tautomerization process, still appears in this configuration.

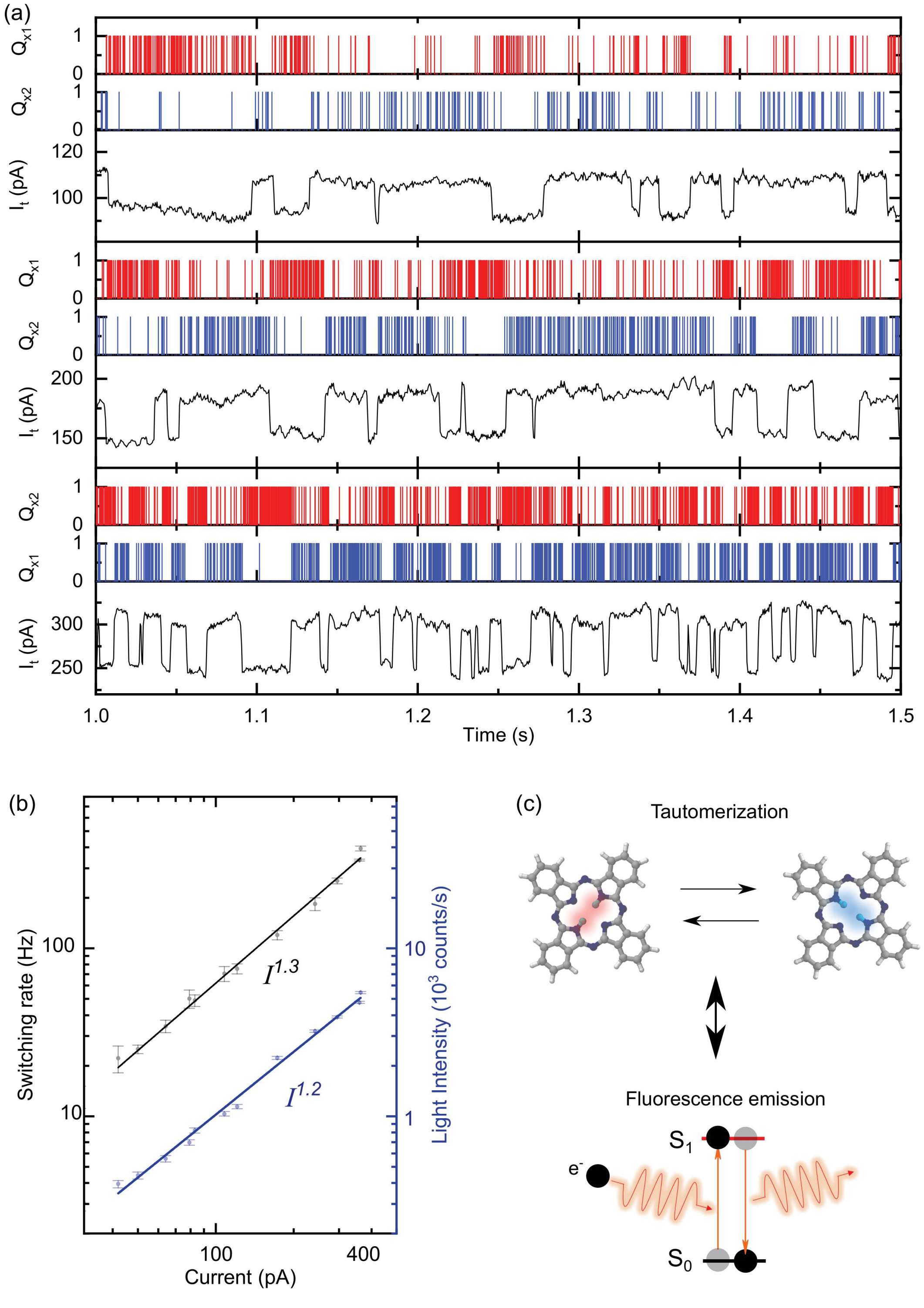

**Figure 3.11: Evolution of the tautomerization switching rate as a function of the current.** (a) Temporal traces of the $Q_{x1}$ and $Q_{x2}$ lines, and of the tunneling current ($V$ = -2.5 V). (b) Evolution of the switching rate (dark line) and the light intensity (blue line) as a function of the tunneling current. (c) Sketch illustrating the connection between tautomerization and fluorescence excitation.

This shows that the tautomerization process can occur even without direct tunneling into the molecule.

These observations confirm further a connection between the fluorescence emission and the tautomerization process. Overall, we can summarize several observations supporting such connection:

- The current dependencies for the fluorescence emission and the tautomerization switching rate are very close.
- The voltage onset is similar for the apparition of the tautomerization and the fluorescence.
- The tautomerization can be excited at distance via a coupling between the excitonic state and the plasmons.
- The voltage onset, found at $V$ = -1.8 V, matches the energy of the first optical gap $Q_x$ ($E_{Q_x}$ = 1.8 eV) of $H_2Pc$.

Altogether, these observations suggest that the tautomerization occurs during a fluorescence excitation-emission cycle. In this picture, the tautomerization process would be mediated by the excited state of the molecule, similarly to what was deduced from laser-induced tautomerization experiments [122]. Note that this mechanism was not considered in previous STM-induced tautomerization measurements, because optical information about the fluorescence was not available. In fact, throughout these experiments, different mechanisms were invoked: current-induced [68], thermally and vibrationally induced [60], scattering with hot carrier [63, 58] and even photo-generated carrier in the substrate bulk to excite the tautomerization [12].

The following paragraph presents additional data, to support our interpretation and attempt to exclude all the above mechanisms.

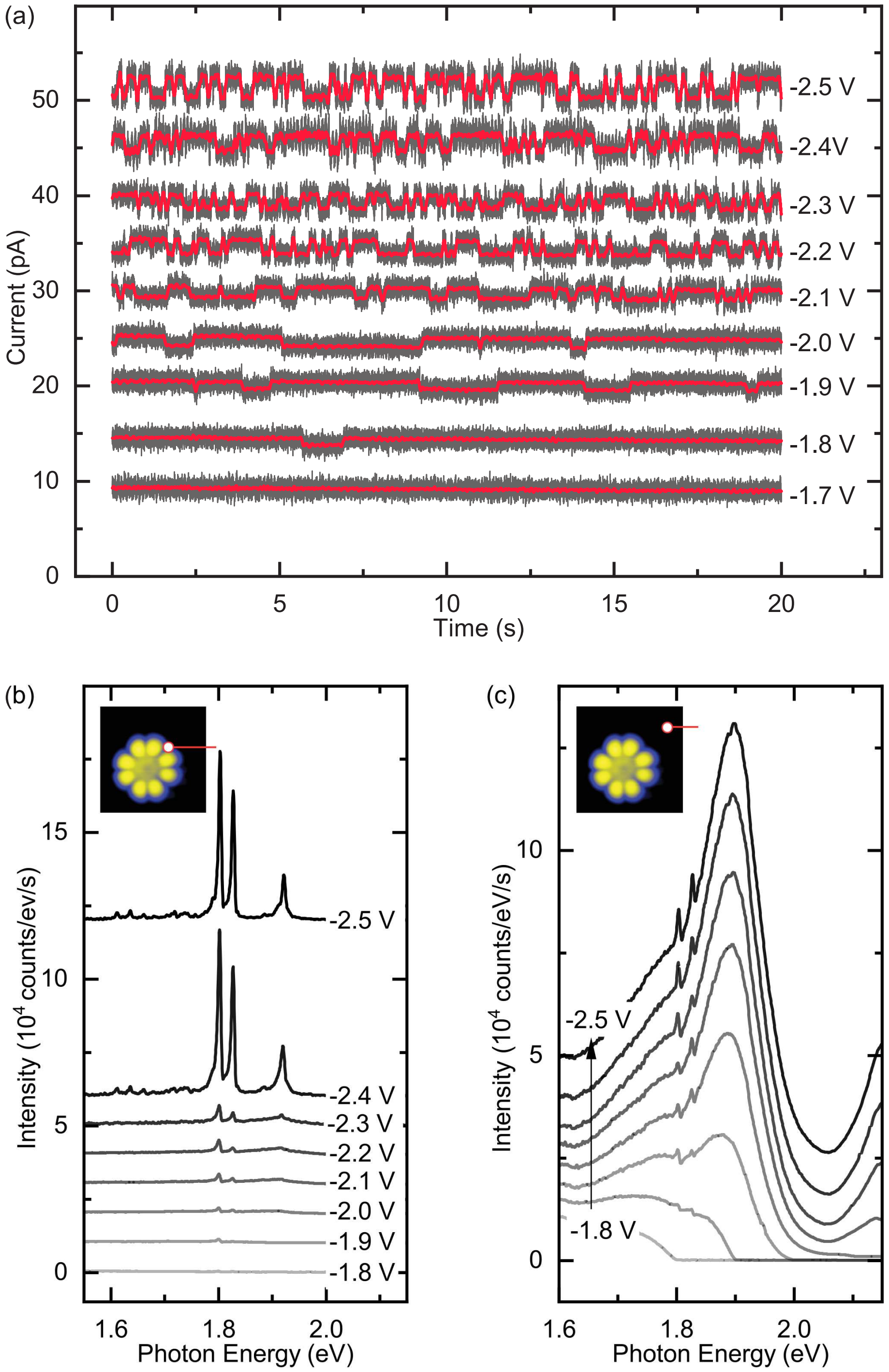

**Figure 3.12: Voltage onset of the tautomerization process.** (a) Current traces at different voltages (initial current setpoint $I$ = 10 pA). (b) Series of fluorescence spectra ($I$ = 10 pA; acquisition time $t$ = 180 s) acquired at different voltages at the position marked by a dot in the STM image in inset. (c) Series of fluorescence spectra ($I$ = 600 pA; acquisition time $t$ = 180 s) acquired at different voltages at the position marked by a dot in the STM image in inset.

### 3.4.2 Additional data supporting an excited-state mediated mechanism

While a direct electron excitation mechanism [68] cannot be excluded when the tip is located above the molecule, it cannot occur when the tip is located outside. However, it has been shown that remote excitation of the tautomerization can be obtained on a molecule adsorbed on the bare metal [63] [58]. In these works, this "at distance" excitation is explained by hot electrons, injected in a surface state of the sample, which may travel along the surface to induce tautomerization through inelastic scattering. To check if this mechanism occurs in our case, we acquired differential conductance spectrum (displayed Fig. 3.13(b)) on NaCl and the bare Ag(111) substrate (Fig. 3.13(a)) to identify the energy position of the surface state. Indeed, at the voltage used in our experiments ($V < 0$) this surface state could play a role for a molecule deposited on the bare Ag(111) surface. On NaCl however, the surface state (that should now be called interface state) is shifted above the Fermi level, forbidding thus direct carrier injection in the surface state at a negative voltage. Therefore, this mechanism of hot carrier travelling along the surface cannot explain our observations. One has to note that, because of the high absolute value of the tautomerization voltage threshold ($V$ = - 1.8V), we can reasonably also exclude vibrationally and thermally mediated excitation [60].

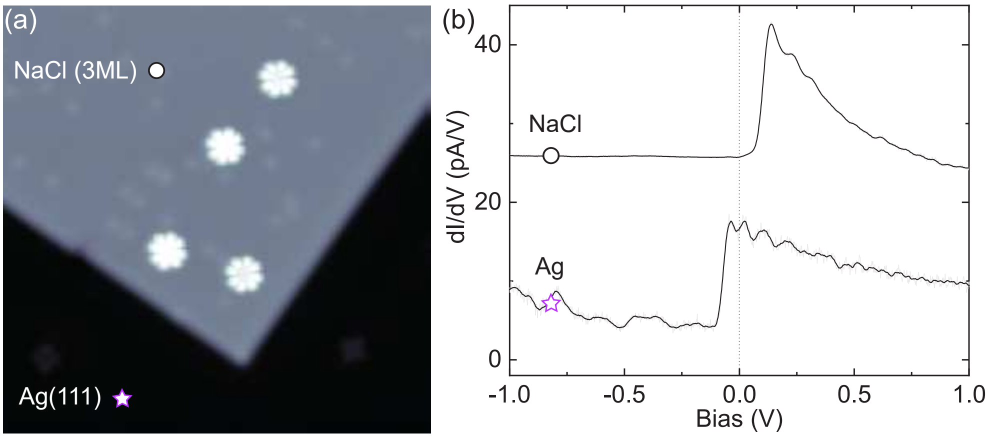

**Figure 3.13: Interface state on NaCl.** (a) STM image ($V$ = -2.5 V; $I$ = 10 pA; 30 × 30 nm$^2$) of four $H_2Pc$ molecules on a three layer NaCl island deposited on Ag(111). (b) Differential conductance spectra allowing to identify the energy position of the surface state on NaCl and Ag(111).

To support our interpretation, we carried out the same study on a very similar molecule, free-base naphthalocyanine. This molecule presents a smaller optical gap than $H_2Pc$ (*H2Nc* Fig. 3.14(a)). Like the $H_2Pc$ molecule, $H_2Nc$ presents a HOMO with a four-fold symmetry while the LUMO presents a two-fold symmetry which allows identifying two tautomers (Fig. 3.14(b)). It also presents two optical transition $Q_x$ and $Q_y$ (Fig. 3.13(c)) as expected from the literature [55]. One has to note that the $Q_x - Q_y$ gap is significantly smaller than for $H_2Pc$. Eventually, fluorescence spectra acquired with the tip located between the two branches (spectrum 2 Fig. 3.14(c)) presents also a duplication of the $Q_x$ ($E_{Q_{x1}}$= 1.61 eV; $E_{Q_{x2}}$= 1.63 eV) and $Q_y$ ($E_{Q_{y2}}$= 1.64 eV; $E_{Q_{y1}}$= 1.66 eV) transitions. Thanks to this similarity, we wanted to see if the tautomerization voltage onset still matches the first optical gap ($Q_x$) of the $H_2$Nc molecule.

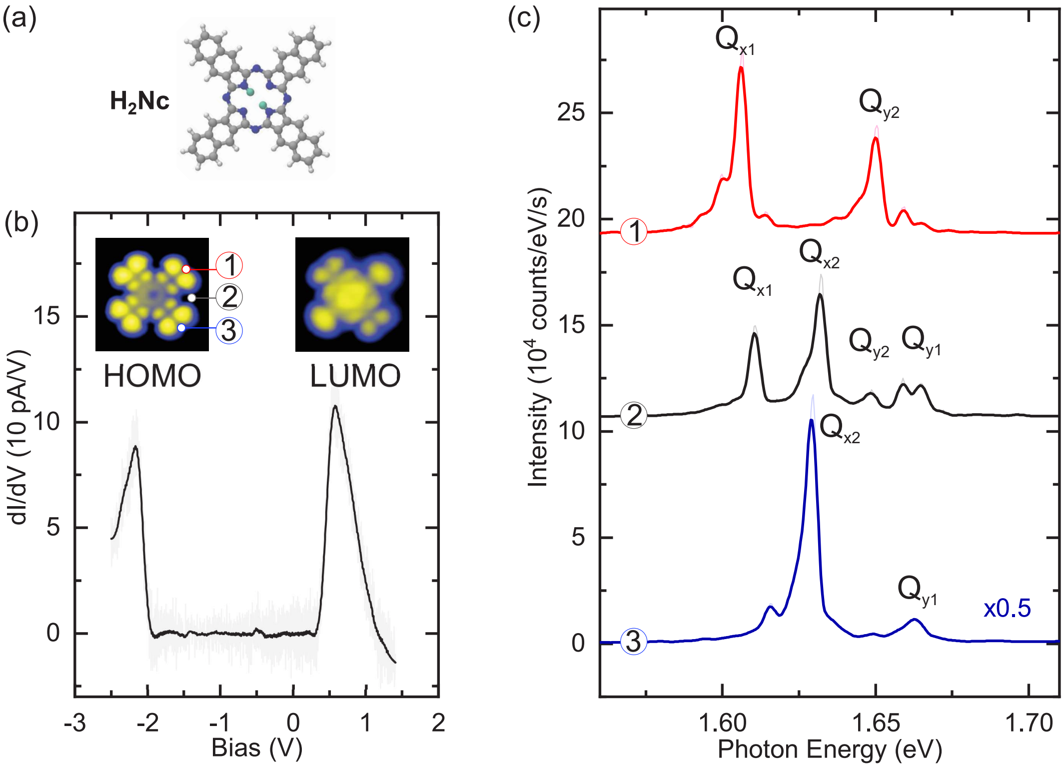

**Figure 3.14: Properties of the naphthalocyanine molecule ($H_2$Nc).** (a) Sketch of the $H_2$Nc molecule. (b) Differential conductance spectrum of a single $H_2$Nc molecule adsorbed on 3 layers of NaCl on Ag(111). Inset: STM images (3.5 × 3.5 nm$^2$) of the HOMO ($V$ = -1.9 V; $I$ = 10 pA) and LUMO ($V$ = +0.7 V; $I$ = 10 pA). (c) STM-F spectra ($V$ = -2.2 V; $I$ = 50 pA; acquisition time: $t$ = 180 s) recorded at the different tip positions marked in (b).

Fig. 3.15(a) presents a direct comparison between fluorescence spectra of $H_2$Pc and $H_2$Nc to highlight the energy difference of their optical gaps. The first $Q_x$ is observed at $\approx$ 1.61 eV for $H_2$Nc, and at $\approx$ 1.80 eV for $H_2$Pc. Figure 3.15(b) and (c) show a series of spectra at different voltages at a distance $\approx$ 1.2 nm away from the the molecule for $H_2$Pc and $H_2$Nc. In both cases, one can see the duplication of the $Q_x$ lines, and therefore the tautomerization occurs in both cases when no tunneling current goes through the molecule.

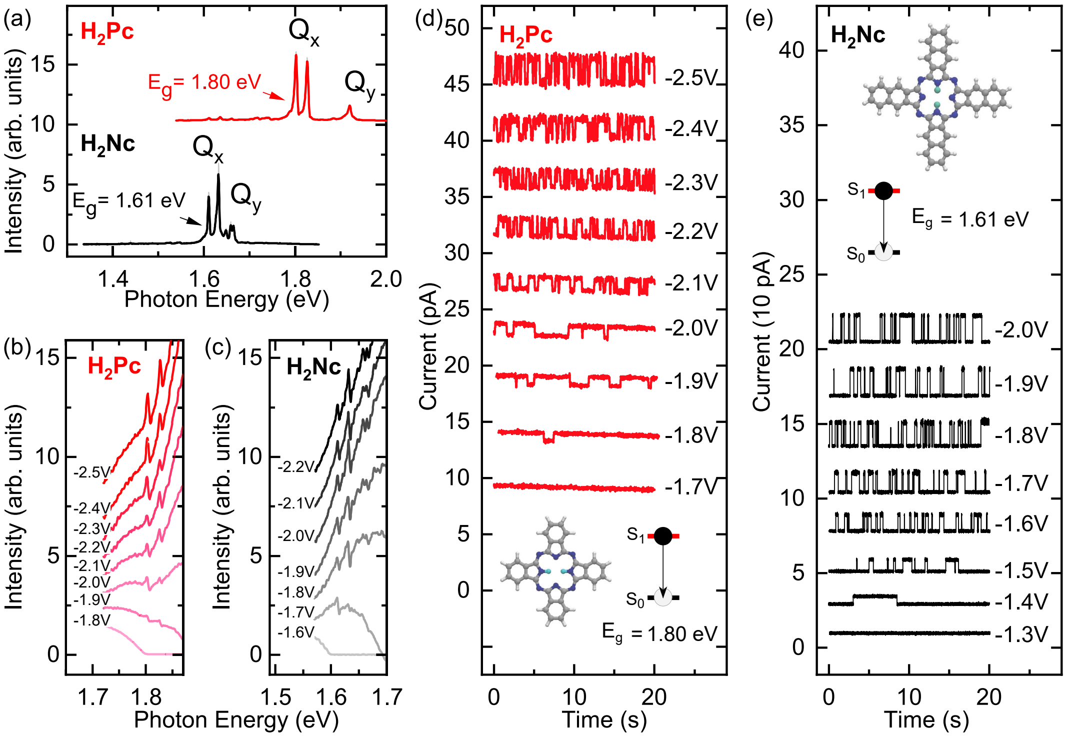

**Figure 3.15: Comparison between $H_2Pc$ and $H_2Nc$** (a) Comparison between fluorescence spectrum of $H_2Pc$ (top spectrum : $V$ = -2.5 V; $I$ = 100 pA; acquisition time $t$ = 120 s) and $H_2Nc$ (bottom spectrum : $V$ = -2.2 V; $I$ = 50 pA; acquisition time $t$ = 180 s). (b,c) Series of fluorescence spectra ($I$ = 600 pA; acquisition time $t$ = 180s) for different voltages, acquired at a distance ≈ 1.2 nm away from the molecule, for $H_2Pc$ and $H_2Nc$. A vertical offset is used for clarity. (d,e) Series of current temporal traces, for different voltages, for $H_2Pc$ and $H_2Nc$. A vertical offset is used for clarity. All the traces are acquired with an initial current setpoint of $I$ = 10 pA.

# Conclusion

In this chapter, we reported STM-F experiments carried out on a single $H_2Pc$ molecule decoupled from a silver Ag(111) substrate by a thin atomic layer of NaCl. STM-F spectra recorded at different positions of the molecule reveal duplication of the two main fluorescence lines, named $Q_x$ and $Q_y$. Spatial mapping of the fluorescence lines (HRFM map) as a function of the tip position is realized. It reveals "dipole-like" features along the main molecule axis. To understand the origin of this pattern, a theoretical model (developed by our collaborators, T. Neuman and J. Aizpurua) allowing to simulate these maps is presented. The simulated maps are obtained by a convolution of two maps: an excitation map which takes into account that the excitation is mainly driven by the electrons tunneling into the HOMO, an emission map which represents the coupling between the molecular excitation and the plasmonic modes of the junction. Based on recent results, the model assumes that the last atoms located at the tip apex play a role of a pico-cavity [111, 121], which induces an extreme localisation of the plasmonic modes within a volume of the order of 1 $nm^3$. The excellent agreement between the experimental and theoretical maps first validates *a posteriori* the existence of such a pico-cavity in our STM junction, and second, gives unprecedented insight in the comprehension of the spatial variation of a single molecule fluorescence signal induced by STM. Since this spatial variation relies essentially on the coupling between the molecular exciton and the pico-cavity modes which extend on a scale smaller than the size of the molecule, an HRFM map represents an optical image of the molecular transition- dipole moment. This interpretation allows associating the different emission lines observed in the STM-F spectra to the fluorescence emission of the two tautomers of the $H_2Pc$ molecule.

Thanks to this identification, a temporal tracking of the fluorescence signal associated with each tautomer are realized. This tracking confirms that the two tautomers do not emit at the same time. Second-order correlation function measurements are realized, which yield the lifetime of each tautomer. The lifetimes are found slightly different, confirming that the molecule experiences a slightly different local environment in the two tautomer forms. A detailed investigation of the molecular environment is realized via STM imaging. It shows that the difference observed for the two tautomers (fluorescence emission energies and lifetime) is due to a modulation of the local environment of the molecule by different positions on the NaCl/Moiré pattern, the adsorption position on top of a Na atom remaining the same.

Finally, a tautomerization mechanism mediated by the molecule excited state is proposed. This mechanism relies on three arguments: (i) a similar current dependency for the tautomerization rate and the fluorescence intensity; (ii) the fact that the tautomerization voltage onset of $H_2Pc$ matches with the energy of its lower excitonic state (supported by other data on $H_2Nc$, a molecule presenting a smaller excitonic gap); (iii)tautomerization can be excited at distance via the exciton-plasmon coupling.

In conclusion, through this example, we presented the concept of "Hyper-Resolved Fluorescence Microscopy with STM", which relies on the combination between spectral resolution provided by optical spectroscopy, and spatial resolution provided by STM. The great spatial resolution in optical images is not only due to the highly localized tunneling current but also to the pico-cavity plasmon modes confined in volumes of the order of the $nm^3$.

# Chapter 4

# Vibronic spectroscopy with sub-molecular resolution

Near-infrared [11], Raman [40], and low-temperature fluorescence [84] spectroscopies are powerful methods to obtain the vibrational spectrum of organic molecules. As the vibrational sequences observed in this spectrum are extremely characteristic of the probed species, these spectra are often considered as a chemical fingerprint of this latter. Due to their non-invasive character, vibrational spectroscopies constitute key methods for chemical analysis in a large number of scientific fields such as organic chemistry, biological, biomedical, material, environmental, and forensic science [51, 7]. Fundamentally, obtaining the vibrational spectrum of a single molecule constitutes the ultimate limit in terms of spatially resolved chemical analysis. Moreover, obtaining such information with sub-molecular precision raises a question about the meaning of a chemical fingerprint at this scale. On another hand, gathering information about the vibration of a single molecule may provide precise information regarding its direct environment. In this chapter, I report STM-F experiments carried out on single zinc phthalocyanine ($ZnPc$) molecules adsorbed on a NaCl/Ag(111) substrate. STM-F spectra recorded on a linear arrangement of this molecule show a narrowing of the main emission line, due to an inter-molecular dipole coupling, as well as resolved features in the lower energy region. A comparison with spectroscopic data shows that these features correspond to vibronic emission lines, that can be assigned to vibrational normal modes of the ZnPc molecule. Further analysis of the STM-F spectra is carried out to unravel the impact of the different inter-molecular coupling modes on the vibronic emission. It confirms that vibronic emission originates from the lower energy supra-molecular excited state. HRFM maps realized at the wavelength of the vibronic contributions reveal patterns related to the vibrational mode symmetry, thus demonstrating a chemical sensitivity down to the sub-molecular level. Additionally, these sub-molecular variations are not correlated to those of the main emission line. Finally, these observations are discussed and rationalized in the vibronic coupling theory framework.

## 4.1 STM-F spectroscopy on a zinc phthalocyanine molecule

### 4.1.1 Presentation of the system

Fig.4.1(a) shows a sketch of the experiment where the STM tip is used to excite the fluorescence of a ZnPc molecule decoupled from an Ag(111) surface by a thin layer of NaCl. Figure 4.1(b) is a large scale STM image of the sample where a single ZnPc molecule and a linear arrangement of three ZnPc are adsorbed on 2ML-NaCl/Ag(111) substrate. A differential conductance spectrum (Fig. 4.1(c)) shows the energy positions of the HOMO and LUMO orbitals, whose STM images are displayed in the inset. The LUMO presents a $4^{th}$-order symmetry, consistent with the structure of the molecule (Fig. 4.1(a)), with bright edges and a darker center. The HOMO orbital also presents a $4^{th}$-order symmetry, but with a 16-lobe structure, different from the one obtained by DFT simulations. Interestingly, the individual molecules in the linear arrangement (Fig. 4.1(b)) present an 8-lobe structure, this time very similar to the HOMO representation predicted by DFT. The difference between the experiment the structure predicted by DFT has been observed and discussed on a very similar molecule ($MgPc$) by Miwa *et al.* [79]. The authors suggested that the 16-lobe pattern results from the shuttling motion between two equivalent positions of the molecule on the surface. When the molecule is placed in the linear arrangement, this shuttling motion is blocked and the molecule recovers its "natural" 8-lobe pattern. One has to note that the same 8-lobe structure is observed when a single molecule has pined on a defect. Figure 4.1(d) displays a STM-F spectra recorded on single $ZnPc$ molecule. A strong emission line of $\approx$ 20 meV width appears at $\approx$ 1.90 eV. It corresponds to the fluorescence of the $ZnPc$ molecule [129, 83]. Note that unlike the $H_2Pc$ molecule presented in the previous chapter, the two main axes (corresponding to the two molecular branches), and therefore the two transition dipole moments of $ZnPc$ are equivalent. This means that the two excitonic states ($Q_x$ and $Q_y$, see the previous chapter) are, in principle, degenerated, giving only one fluorescence line referred to the $Q$ line.

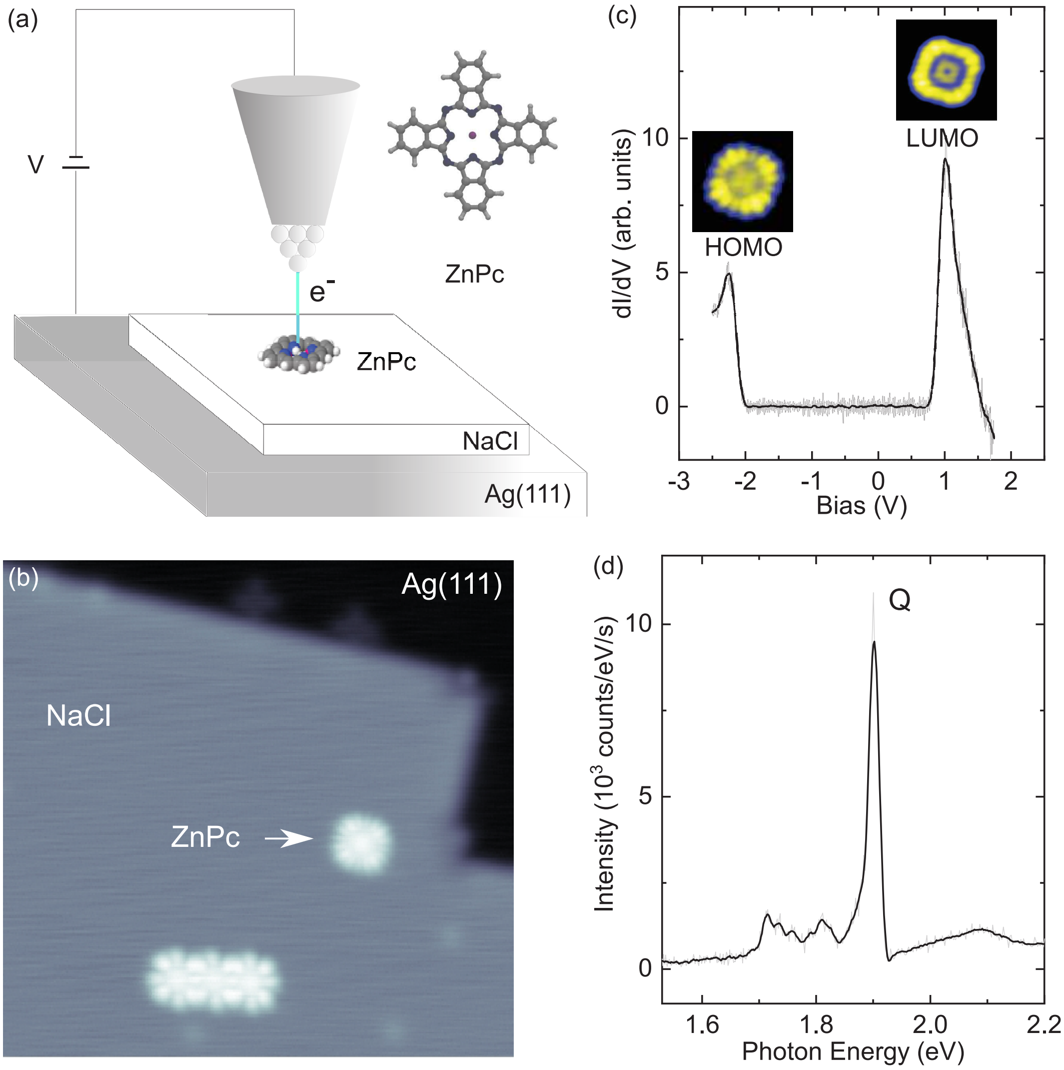

**Figure 4.1: Description of the system** (a) Sketch of the experiment. (b) Large scale image of ZnPc molecules on three-layers NaCl island on Ag(111). (c) Differential conductance spectrum of the ZnPc molecule. Inset: STM image (2.7 × 2.7 $\mathrm{nm}^2$) of the LUMO ($V$= +1 V; $I$ = 10 pA) and HOMO ($V$ = -2.2 V; $I$ = 10 pA) orbitals. (d) STM-F spectrum of the ZnPc molecule ($V$ = -2.5 V; $I$ = 300 pA; acquisition time $t$ = 180 s).

In addition to this main fluorescence line, the STM-F spectrum presents weak intensity features in the lower energy region.

To improve the resolution of these features we drew inspiration from the work of Zhang *et al.* [129] where they showed that linear arrangements of molecules (oligomers) present narrow emission lines due to the coherent intermolecular excitonic coupling.

## 4.1.2 Narrowing the emission line by dipole-dipole coupling.

Figure 4.3 displays several STM images to illustrate the tip manipulation used to build linear arrangements of ZnPc molecules. Figure 4.3(a) shows an STM image of three ZnPc molecules adsorbed on a 2ML-NaCl island. As a first step of the manipulation, the tip is located at the left edge of the central molecule at a voltage $V$ = -2.5 V. Then, the tip is approached toward the surface which leads to an increase of the tunneling current. In this configuration, the molecule feels an attractive potential which can induce a sudden displacement of the molecule under the tip. By progressively moving the tip laterally away from the molecule, one can, therefore "pull" the molecule toward a second molecule and eventually build a dimer (Fig. 4.3(b)). An STM image realized at a lower voltage ($V$ = -1.8 V), on which we superimposed the molecular structure, allows identifying the respective orientation of the individual molecules in the dimer (Fig. 4.3(c). Eventually, a third molecule is approached toward the dimer to build a trimer (Fig. 4.3(e)). The orientations of the three molecules constituting the dimer are depicted in Fig. 4.3(d).

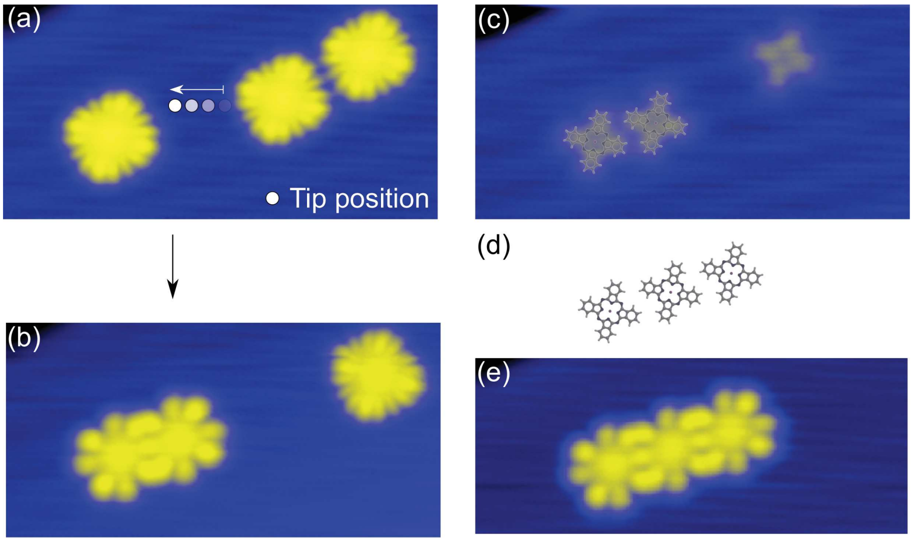

**Figure 4.2: Building ZnPc oligomers with tip manipulation** (a) STM images ($V$ = -2.5 V; $I$ = 10 pA; 10 × 4.9 nm$^2$) of three ZnPc molecules before tip manipulation. (b) Same image as (a) after manipulation, showing the built dimer of ZnPC. (c) STM image of the same area at a lower voltage ($V$ = -1.8 V) showing the molecular structure. The sketch of the molecule is superimposed on the dimer. (d) Sketch depicting the linear arrangement of the molecules in the trimer. (e) STM image of the trimer after a second manipulation.

Fig.4.3(a) displays STM images of a monomer, a dimer, a trimer, and a tetramer of ZnPc molecules built with the procedure described above. STM-F spectra recorded on the different oligomers are shown in Fig. 4.3(b). A background is subtracted to the spectra, which are eventually normalized by the plasmonic response of the STM junction. This procedure allows to get rid of the purely plasmonic emission, and also to correct the intensity of the different lines by the Purcell effect. STM-F spectra for all oligomers present an intense emission line, which corresponds to the emission of the supra-molecular exciton (see 2.3.1) resulting from the coherent coupling of the two in-line individual molecular dipoles [129] (Fig.4.3(a)). This mainline sharpens, shifts toward lower energy, and becomes more intense with the number of molecules in the oligomer. These effects have been observed previously by Zhang *et al.* [129], and are another consequence of the inter-molecular dipole coupling (see 2.3.1), that is also expected for J-aggregates [31]. For the three oligomers, a magnification of the spectra in the lower energy region reveals a well-resolved series of peaks, which were not reported in previous studies [129]. Their widths are close to the ones of the main emission line, and their energy shift seems to follow te one of the main emission line. To better visualize this effect, we display in Fig. 4.3(c) the same STM-F spectra plotted as a function of the shift with respect to the main emission line. While the weaker peaks appear at different energies depending on the molecule number in Fig. 4.3(b), Fig. 4.3(c) shows that the energy positions of the weak peak scale when the main-lines are aligned. These observations suggest that the main and weaker lines have the same common origin.

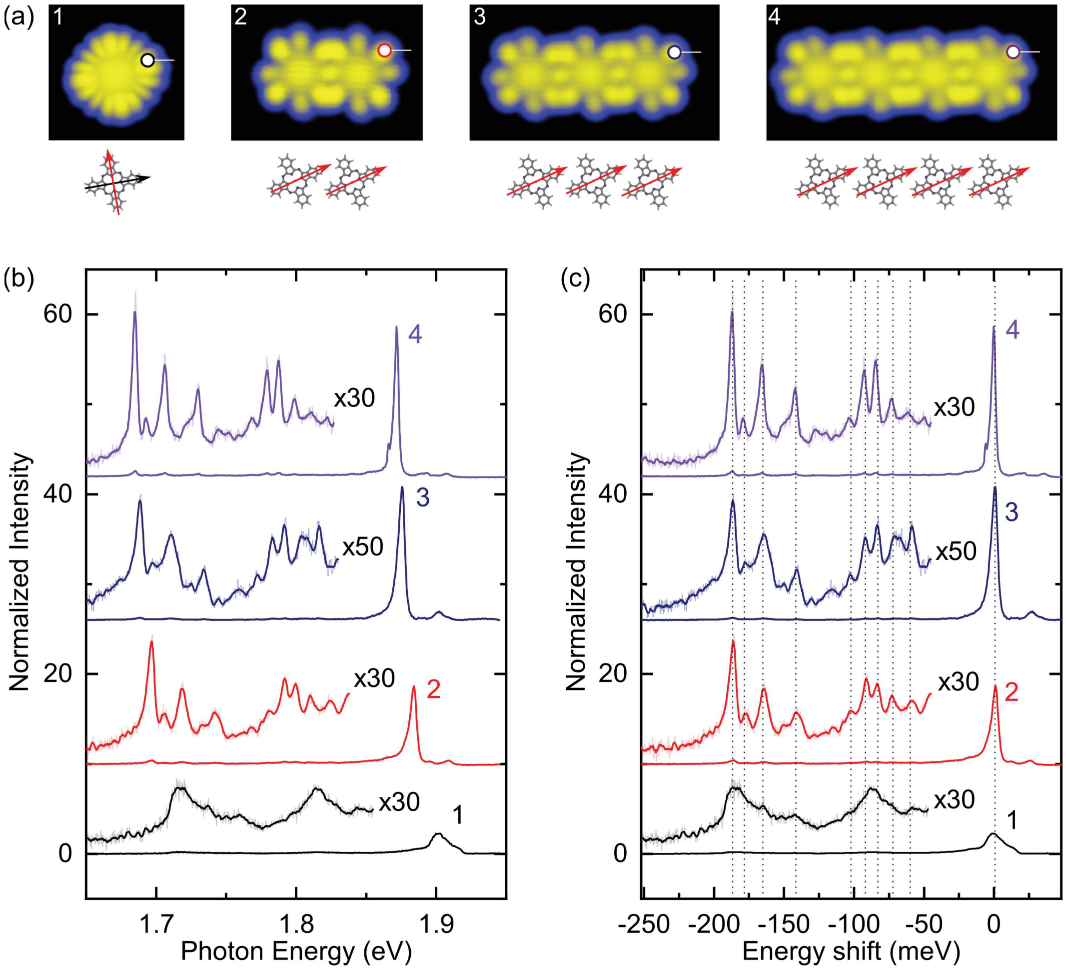

**Figure 4.3: Narrow line emission from oligomer excitonic states.** (a) STM images ($V$ = -2.5 V; $I$ = 10 pA) of a monomer, a dimer, a trimer, and a tetramer of ZnPc. Below the image is shown a sketch depicting the respective orientations of the molecules and the dipole coupling mode excited during the experiment. (b) STM-F spectra acquired on the different oligomers at the position marked in (a). The full width at half maximum of the main emission line is 14 meV for the monomer, 6 meV for the dimer, 5 meV for the trimer, and 4 meV for the tetramer. (c) Same spectra presented in (b) plotted after energy position alignment of the main emission lines.

### 4.1.3 Vibronic fingerprint from STM-F spectroscopy

Fig. 4.4(a) focuses on an STM-F spectrum recorded by locating the tip at the extremity of a ZnPc dimer (Fig. 4.4(b). This spectrum is plotted as a function of the energy shift from the main emission line (main peak energy: $E_1 = 1.883$ eV). The lower energy region of the spectrum is magnified (red) and compared to a Raman spectrum (green), recorded by colleagues from the team of Stephane Berciaud at IPCMS on a macroscopic ZnPc polycrystalline sample with an excitation laser energy of 1.96 eV (close to resonance excitation). A remarkable agreement is found between these two spectra, for the number, the energies and the intensities of the different peaks. We also have an excellent agreement with photo-luminescence spectra acquired in cryogenic matrices [83]. This observation shows that these peaks correspond to a radiative transition from the vibrational ground level $\nu = 0$ of the first excited electronic state $S_1$ (where $S_1$ indicates the excited state described by the supra-molecular exciton) to the different excited vibrational level $\nu$ of the electronic ground state $S_0$ (Fig. 4.4(c)). Because this type of transition involves a simultaneous change of the electronic and vibrational states of the molecule, they are called **vibronic transitions**, by opposition to a vibrational transition that produces an emission in the infrared and follows different selection rules. In this picture, the main emission line corresponds to the **0-0 transition** (Fig. 4.4(c)), which is a purely electronic transition (the vibrational state of the molecule remains the same upon transition). Finally, based on on a comparison with DFT [1] one can precisely assign each of these vibronic peaks to a specific vibrational mode of the ZnPc molecule. A comparison table that summarizes these different modes is presented in Fig. 4.4(b). The last column of the table indicates the irreducible symmetry representation associated with each vibrational mode of the molecule. For instance, the vibrational modes which belong to the $A_{1g}$ representation are symmetric, while the $B_{1g}$ and $B_{2g}$ modes are anti-symmetric.

This comparison shows that our STM-F spectrum constitutes an accurate vibrational signature of the probed species, without light excitation, and at the single-molecule level.

In the following, we will focus on how this spectral signature changes with the excitation (tip) position. For sake of clarity, we will first focus on the main emission line energy region, and then on the vibronic emission energy region.

---

[1] The calculations are carried out at the B3LYP/6-13G level in the full D4h geometry to determine the vibrational modes and their symmetries [39]. The calculated vibrational frequencies are scaled by 0,9613 as recommended in ref. [70]

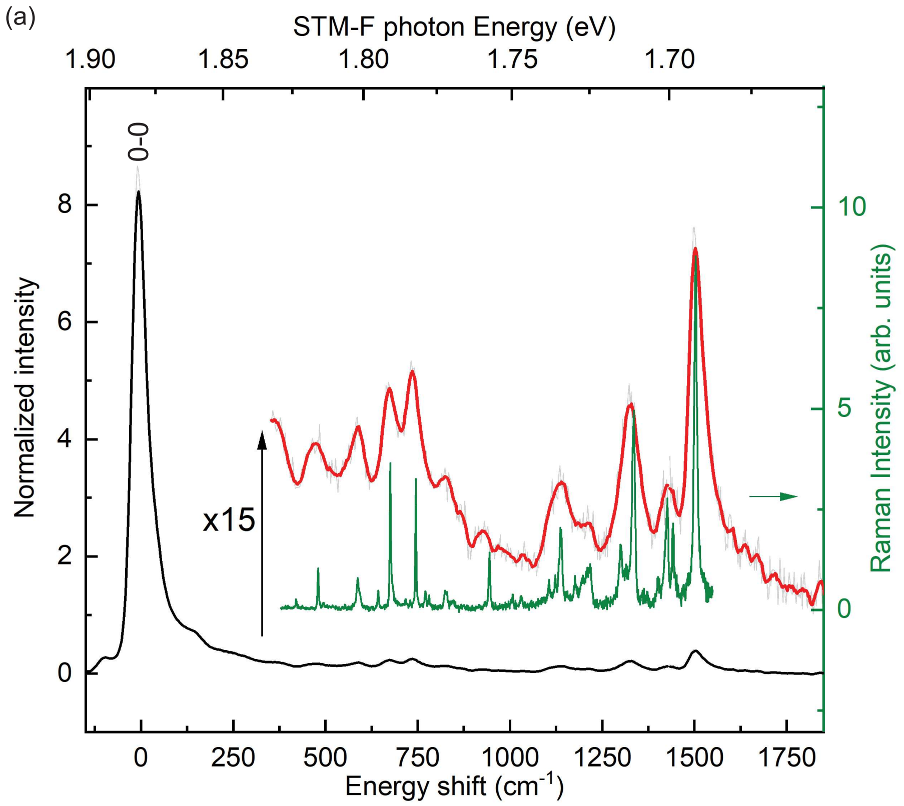

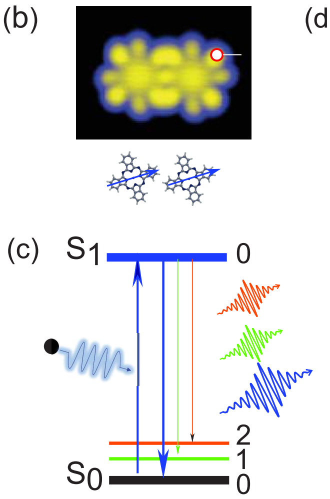

(d)

| STM-F | Raman | Ar mat. | DFT | Sym. |
|---|---|---|---|---|
| 474 | 480 | 490 | 471 | B2g |
| 587 | 588 | 598 | 579 | A1g |
| 675 | 676 | 689 | 664 | A1g |
| 733 | 745 | 751 | 734 | B1g |
| 821 | 826 | 845 | 823 | A1g |
| 924 | 944 | 945 | 923 | B2g |
| 1138 | 1137 | 1150 | 1165 | B1g |
| 1211 | 1209 | 1221 | 1195 | B2g |
| 1325 | 1335 | 1346 | 1333 | A1g |
| 1431 | 1442 | 1445 | 1429 | B2g |
| 1505 | 1503 | 1525 | 1528 | B1g |

**Figure 4.4: Assignments of the vibronic lines.** (a)STM-F spectrum recorded on a ZnPc dimer at the position marked in (b) ($V$ = -2.5 V; $I$ = 900 pA; acquisition time $t$ = 300 s); The low energy region is magnified (red spectrum) and compared to a Raman spectrum recorded on a ZnPc powder. (b) STM image of the dimer ($V$ = -2.5 V; $I$ = 10 pA; 4.6 × 4.6 nm$^2$). Sketch depicting the orientations of the molecules, and the dipole-dipole coupling mode involved in the emission. (c) Sketch depicting the 0-0 and vibronic transitions. $S_1$ indicate the supra-molecular excited state corresponding to the coupling mode described in (b). (d) Table of energy positions (energy in cm$^{-1}$) of the vibronic peaks in the STM-F and Raman spectra displayed in (c), and in the fluorescence spectra of ZnPc molecules trapped in frozen Ar matrices (taken from ref. [83]), and DFT based assignments.

## 4.2 Electronic contributions to the ZnPc dimer emission

Previously, we have shown that STM-F provides information regarding the 0-0 and vibronic lines for oligomers, thus chemical sensitivity with molecular-scale precision is gained. An advantage of STM is that the spatial resolution is such that one can consider molecules as extended objects, *i.e*, one can address different "sub-parts" of a molecule. Below we will show how our approach can provide optical information with sub-molecular resolution. We will first focus on purely electronic lines before discussing the vibronic contributions.

### 4.2.1 Dipole-dipole coupling modes

Fig. 4.5(a) shows a series of STM-F spectra, with a focus to the energy region close to the main emission line, recorded with the tip located at different positions of a ZnPc dimer (Fig. 4.5(b)). Interestingly, while the main emission line (peak 1 at $\approx$ 1.883 eV) is intense when the tip is located at the extremity of the dimer (spectra labeled 1 and 2), it becomes much weaker at the dimer bottom center (spectrum labeled 3). This latter spectrum shows also the emergence of two other peaks at higher energy (peak 3 at $\approx$ 1.901 eV and peak 4 at $\approx$ 1.908 eV). Another spectrum (labeled 4) recorded in the center of the dimer shows two other peaks (peak 2 $\approx$ 1.895 eV and 5 $\approx$ 1.918 eV). Altogether, one can identify five different emission lines whose intensities vary substantially as a function of the tip position. Eventually, the last spectrum (labeled 5) shows that these five contributions exist independently. Those five emission modes have been associated by Zhang *et al.* [129] to five possible dipole coupling modes of the molecular dimer (Fig. 4.5(c)) :

- in line - in-phase (mode 1)
- parallel - phase opposition (mode 2)
- orthogonal (mode 3)
- parallel - in-phase (mode 4)
- in line - phase opposition (mode 5)

The coupling between two molecules described by two dipoles should give, in principle, only four different modes. Therefore, the observation of five different modes, especially the orthogonal mode 3, is somehow surprising. An alternative explanation could be that one of these peaks corresponds to the hot emission [22, 26] of an excited vibronic mode of $S_1$, a contribution somehow similar to anti-Stokes emission.

For simplicity, we will refer to these five modes by simply calling them electronic modes by opposition to the vibronic modes.

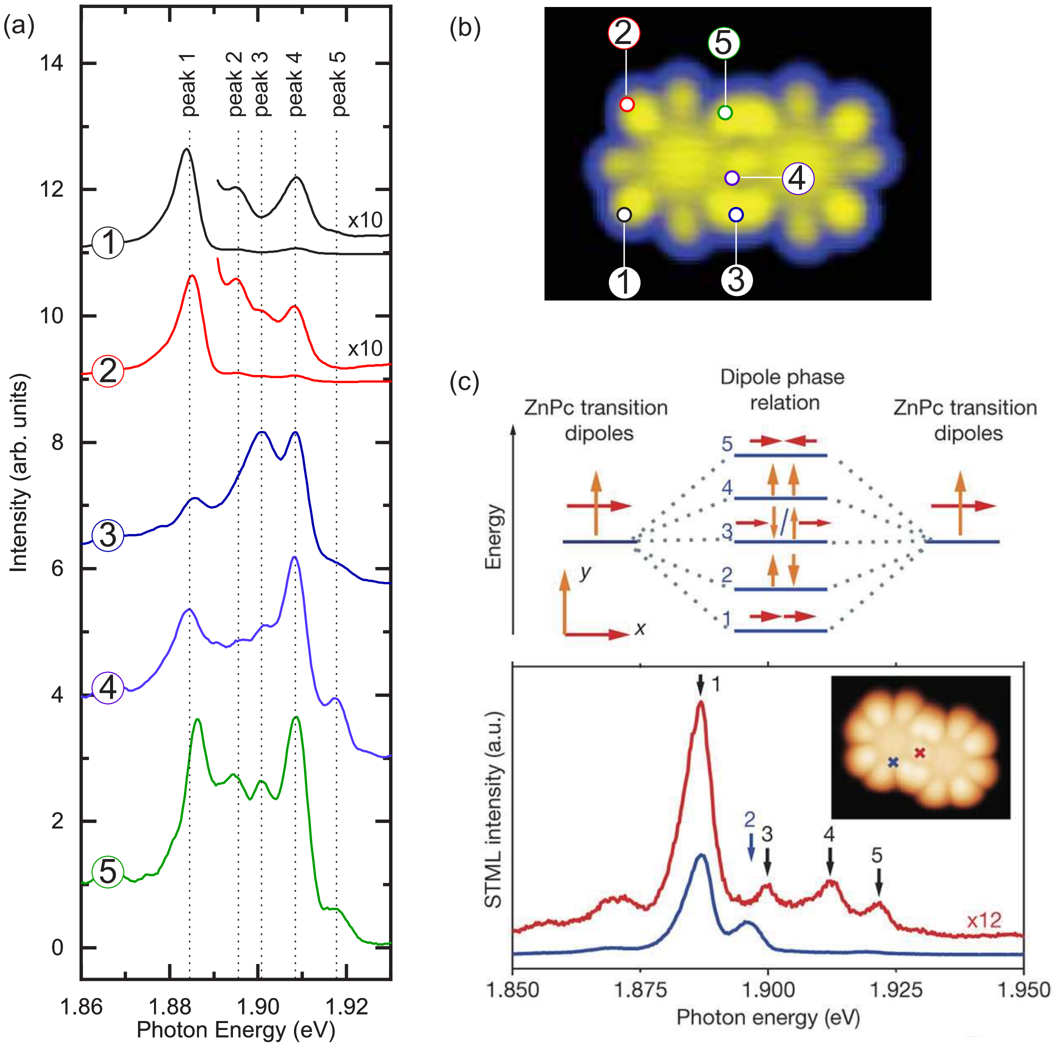

**Figure 4.5: Spatial variation of the supra-molecular exciton emission** (a) STM-F spectra recorded at the different positions marked in (b). Spectra 3, 4, and 5 are arbitrarily magnified to emphasise the different electronic modes. (b) STM images of the ZnPc dimer. (c) Sketch depicting the attribution by Zhang *et al.* of the five peaks appearing in (a) to five dipole coupling modes (Adapted from [129]).

Additionally, Fig. 4.5(a) reveals a measurable energy shift of the peaks as a function of tip position, which is particularly obvious for mode 1 ($\approx 3$ meV shift between positions 1 and 5). The shift, also called Lamb shift [104, 38, 119], is due to the interaction between the excitonic mode and the NCP, that has been reported by Zhang *et al.* [134].

### 4.2.2 HRFM maps

We recorded HRFM maps of the five electronic contributions identified in the STM-F spectra (Fig. 4.6(a). We followed the same procedure as described in paragraph 3.2.1 in the previous chapter. These maps are recorded on a $40 \times 21$ pixel grid (Fig. 4.6(b)) and eventually normalized by the tunneling current. The result for the five contributions is displayed in Fig. 4.6(c).

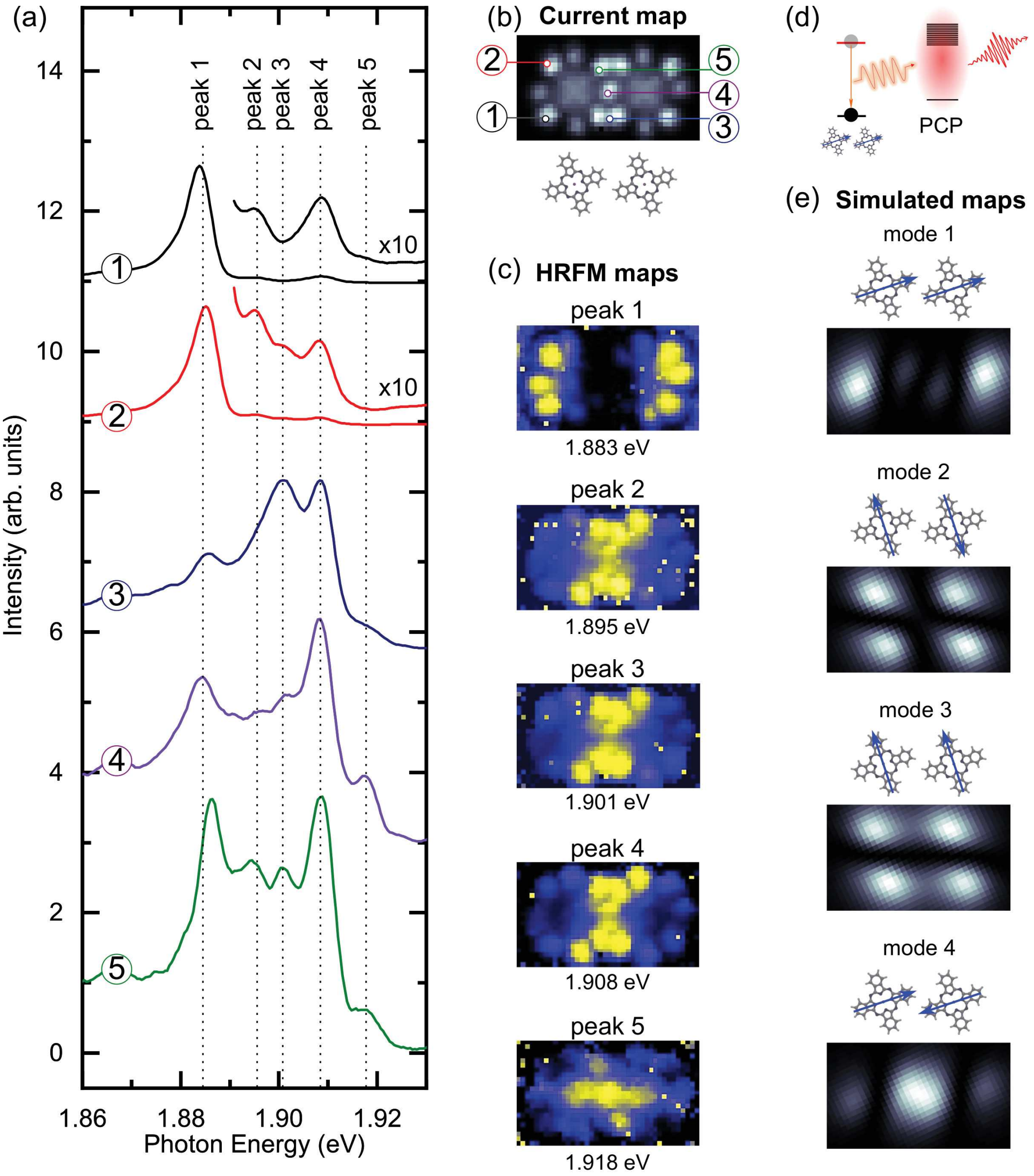

**Figure 4.6: Hyper-Resolved Fluorescence Microscopy on the four excitonic coupling modes** (a) STM-F spectra recorded at the positions marked in (b). (b) Current map recorded during the HRFM experiments ($V$ = -2.5V; 40 × 23 pixels; 3.6 × 2.1 nm$^2$). (c) HRFM maps for the different electronic modes identified in (a) ($V$ = -2.5 V; acquisition time per pixel: $t$ = 65 s). (d) Sketch depicting the coupling between the supra-molecular excitation and the pico-cavity plasmons. The coupling strength is evaluated at each position of the tip (see 3.2.1). (e) Simulated maps showing the square modulus of the coupling strength, representing the emission efficiency.

Besides, we display in Fig. 4.6(e) the theoretical emission-maps for the four possible dipole coupling modes, which are calculated by considering the coupling between the supra-molecular dipole and the pico-cavity plasmons (Fig. 4.6(d)). The map realized on peak 1 shows bright features at the extremity of the dimer with a dark contrast in between, in good agreement with the simulated emission map of mode 1 (inline - in phase). This shows that the coupling between the PCP and the supra-molecular dipole is stronger at the extremity of this latter. Note that the simulated maps do not account for the excitation rate (see paragraph 3.2.1) which may explain why the detailed structure that is reminiscent of the HOMO is not accounted for. Conversely, the map for peak 5 shows a larger signal at the center of the dimer and a darker contrast at the edges of the molecules, in reasonable agreement with the simulated map for mode 5 (inline - phase opposition). The maps realized at the energy of peaks 2, 3, and 4 present patterns with bright features in the center and along the perpendicular direction of the dimer axis. The rather similar patterns observed for these three peaks is likely due to the large energy overlap between these contributions, preventing a proper separation. This may, at least, explain the poor agreement with the theoretical maps for modes 2 and 3.

To conclude, five electronic contributions could be identified in the STM-F spectra whose intensities vary substantially depending on the tip position. The reasonable agreement between theory and experiments for modes 1 and 5, shows that HRFM maps allow observing, in real space, supra-molecular dipole transitions.

## 4.3 Vibronic spectroscopy with sub-molecular resolution

In the first section, we showed that it is possible to obtain a vibrational signature at the single-molecule level. Thanks to the capability of STM-F spectroscopy to obtain spectra with a sub-molecular precision, the following part of this chapter will be dedicated to answering the question: how does the spectroscopic chemical fingerprint vary if we address a "sub-part" of a molecule? First, we will focus on the impact of the electronic contributions on the vibronic signal, and then on the spatial variation of this latter.

### 4.3.1 Impact of the electronic contribution on the vibronic spectrum

Fig. 4.7(b) shows STM-F spectra recorded with the tip located at three different positions of a dimer (Fig. 4.7(a)). Spectra are plotted as a function of the energy shift with respect to peak 1 (inline - in phase electronic mode). The vibronic part of the spectra is magnified (×20) to highlight the different vibronic contributions.

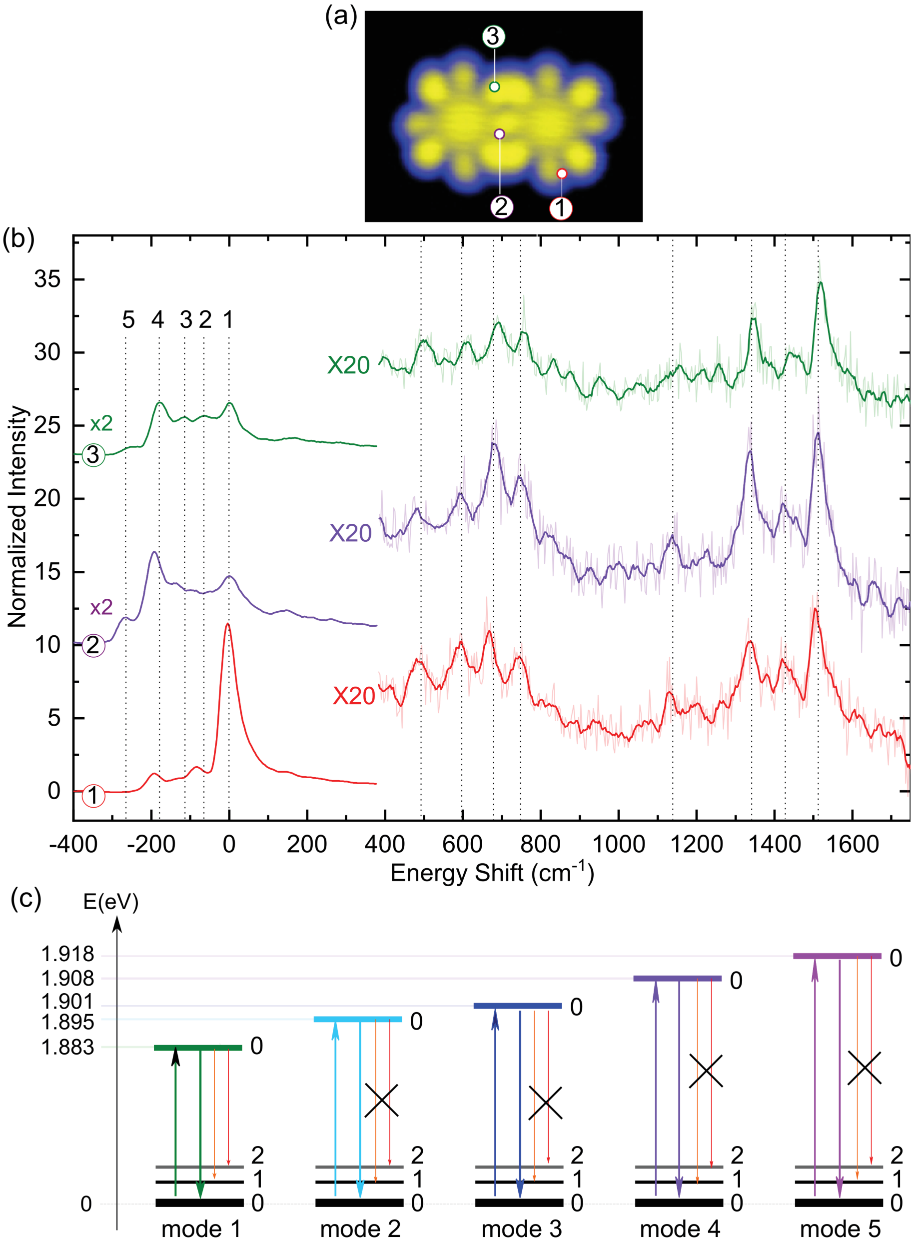

**Figure 4.7: Impact of the excitonic coupled modes on the vibronic signal** (a) STM image of a dimer. (b) STM-F spectra recorded at the three different positions marked in (a). (c) Sketch of the different transitions for the five different excitonic modes.

Spectrum 1 shows mostly an intense peak 1 and much weaker contributions from the other electronic peaks, while spectra 2 and 3 show a weaker peak 1 and a stronger contribution from the other peaks. Meanwhile, the vibronic contributions in all spectra appear at the same energy with almost the same intensity. Note that to obtain the right energy correspondence between the vibronic contributions in these spectra and the Raman spectrum (see 4.1.3), peak 1 has to be taken as the reference of the energy shifts. To summarize the observations:

- The absolute energy positions of the vibronic modes always appear at the same energy (except for a small Lamb shift, see 4.2.1) irrespective of the tip position and main peak intensities.
- If peak 1 is taken as the energy reference, the vibronic feature energies match with those given by the Raman spectrum;
- The global intensity of the vibronic signal is weakly affected by the intensities of the different electronic lines, especially peak 1.

The first and second observations suggest that vibronic contributions only arise from the radiative transition from the lower energy electronic excited state (the excitonic state in line - in-phase), while no vibronic transitions are associated to the other electronic modes (Fig. 4.7(c)). The third observation is even more surprising because if the 0-0 and the vibronic contributions arise from the same excited state one would expect that the intensities of the 0-0 and the vibronic emission evolve similarly.

### 4.3.2 Impact of the tip position on the vibronic signal

We now focus on a systematic analysis of the vibronic signal as a function of the tip position. Fig. 4.8(a) presents another set of STM-F spectra recorded at the position marked in Fig. 4.8(b). The comparison between the three vibronic spectra confirms that the number of peaks and their energy positions does not change as a function of the tip position. If the "global intensity" of the vibronic signal is of the same order of magnitude in the three spectra (which, as before, is not the case for the 0-0 line), a substantial change in the intensity of the vibronic peaks may be observed. Overall, one can identify three groups of peaks that present a similar intensity variation as a function of the tip position. There is a first group, identified by a blue ribbon, with intense peaks in spectra 1 and 3 and weaker ones in spectrum 2. A second group (grey ribbon) shows an opposite behavior with intense peaks in spectrum 2 and weaker ones in spectra 1 and 3. In the third group, (yellow ribbon), the peak intensity is almost the same in the three spectra.

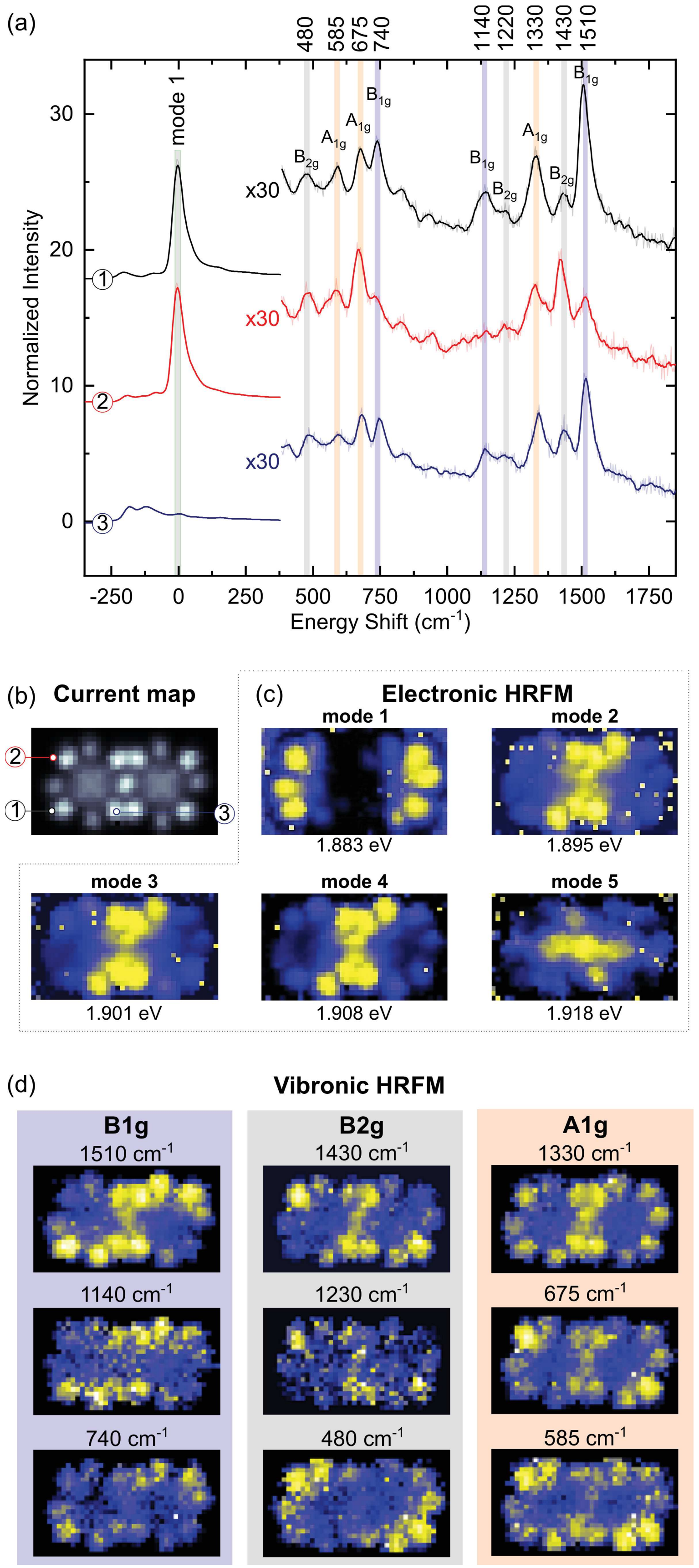

**Figure 4.8: Spatial variation of the vibronic signal.** (a) STM-F spectra acquired at the three positions of a dimer in (b). (b) Current map of the dimer. (c) HRFM maps of the electronic contributions. (c) HRFM maps of the different vibronic peaks indicated in (a).

In the top panel of Fig. 4.8(a) we indicate the irreducible representation of each vibrational mode, deduced from DFT calculations and a comparison with other available data on ZnPc [70] [83] (see table Fig. 4.4(b) for details). Interestingly, the peaks belonging to the first group (blue peaks) belong to the $B_{1g}$ representation, while the second and third group (grey and yellow peaks) belong to the $B_{2g}$ and $A_{1g}$ representations respectively. While the $B_{1g}$ and $B_{2g}$ representations correspond to anti-symmetric vibrational modes, the $A_{1g}$ one corresponds to symmetric modes of the ZnPc molecule. This suggests that the spatial variation of a vibronic peak intensity is strongly related to its symmetry.

To go further in the interpretation we recorded HRFM maps, following the method described previously, for each vibronic mode. The energy of the modes is indicated above the STM-F spectra pannel (Fig. 4.8 (a)). HRFM maps for each of these modes are given in Fig. 4.8(d). The maps of the vibronic modes belonging to the $B_{1g}$ representation (anti-symmetric vibrational modes) follow an anti-symmetric "S"-shape pattern. Conversely, an anti-symmetric "Z"-shape pattern is observed for the modes belonging to the other anti-symmetric $B_{2g}$ representation. Finally, the modes belonging to the symmetric $A_{1g}$ representation present a rather symmetric pattern with the intensity localized at the edges of the molecules.

This confirms that the HRFM map of a given vibronic emission depends on the symmetry of the corresponding vibrational mode. Interestingly, such vibronic sensitivity has not been reported in the paper of Zhang *et al.* [133] published in 2013, although the authors reported a single-molecule vibronic signal, obtained with Tip Enhanced Raman Spectroscopy. In contrast, our results (published partially in 2017), show that a vibrational signature presents spatial variation at the sub-molecular scale. Note that similar observations have been reported in the recent TERS paper (2019) of Lee *et al.* [66].

Eventually, a comparison between electronic (Fig. 4.8(c)) and vibronic (Fig. 4.8(d)) HRFM maps confirms that no obvious correlations can be found between the intensity of the electronic and vibronic contributions. Especially, eventhough the vibronic peaks and peak 1 originate from the same excited state $S_1$, HRFM maps suggest that their emission is uncorrelated.

A first naive interpretation of the vibronic maps would be that we are directly sensitive to the local density of vibrational modes, *i.e*, to the part of the molecule involved in the vibration. However, we have to keep in mind that a vibronic transition is, first of all, an optical transition. Indeed, from the study carried out in the previous chapter, we know that a HRFM map essentially shows how the transition dipole moment can efficiently couple with the pico-cavity plasmon as a function of the tip position. This means that the contrast observed in the vibronic maps is related to the spatial distribution of the dipole that carries the vibronic emission.

### 4.3.3 Explanation of the vibronic spatial variation: Herzberg-Teller coupling

The vibronic peaks that we observe in the STM-F spectra correspond to a radiative transition of the molecule from an excited state $|e,0\rangle$ to a ground state $|g,\nu\rangle$, where the first index refers to the electronic state and the second to the vibrational one. During this transition, a photon is emitted while a quantum of vibration is left in a vibrational mode $\nu$ of the molecule. To get insight into the experimental observations, let us derive the expression of the transition dipole moment of such a vibronic transition.

In the Born-Oppenheimer approximation [37] a molecular state $\Psi$ is expressed as a tensorial product of an electronic state $\phi$ and a vibrational state $\chi$. For an electronic ground state labeled $g$ and for a vibrational state identified by a quantum number $n$, the molecular state $\Psi_{g,n}$ is therefore written as:

$$\Psi_{g,n}(\{\mathbf{r_i}\},\{\mathbf{Q_j}\}) = \phi_g(\{\mathbf{r_i}\},\{\mathbf{Q_j}\})\chi_n^g(\{\mathbf{Q_j}\})$$

where $\{\mathbf{r_i}\}$ designates the electron positions and $\{\mathbf{Q_j}\}$ the set of normal mode coordinates of the vibrational eigenmodes (which contain all information on the nuclei positions).

In a first approximation, it is often considered that the electronic states do not depend of the nuclei positions $\{\mathbf{Q_j}\}$s). In this approximation (Franck-Condon picture) the generic transition dipole moment for any vibronic transition is given by:

$$\langle \Psi_{g,n}|\hat{\mu}|\Psi_{e,m}\rangle \approx \left[\langle \phi_g|\hat{\mu}|\phi_e\rangle_{\mathbf{r}}\right]_{\{\mathbf{Q_j^0}\}} \langle \chi_n^g|\chi_m^e\rangle_{\mathbf{Q}}$$

The molecular transition dipole moment is expressed as a product of a purely electronic transition dipole moment and an overlap between the starting and arrival vibrational modes.

For the (0-0) transition, assuming identical vibrational modes in the electronic ground and excited state, one can deduce from this expression the associated transition dipole moment:

$$\langle \Psi_{g,n}|\hat{\mu}|\Psi_{e,m}\rangle \approx \left[\langle \phi_g|\hat{\mu}|\phi_e\rangle_{\mathbf{r}}\right]_{\{\mathbf{Q_j^0}\}} \langle \chi_0^g|\chi_0^e\rangle_{\mathbf{Q}} \approx \left[\langle \phi_g|\hat{\mu}|\phi_e\rangle_{\mathbf{r}}\right]_{\{\mathbf{Q_j^0}\}}$$

For any other vibronic transition, we see that the dipole moment will essentially correspond to this value modulated by the overlap between starting and arrival vibrational states. For our study, this means that the pattern observed in the HRFM maps for the 0-0 and the vibronic lines should all be identical, which is not what we observed. To explain this behavior we have to move beyond the Franck-Condon picture and take into consideration the dependence of the electronic states with the nuclei positions. In other words, we have to take into account the coupling between electrons and molecular vibrations, which is often mentioned under the term **Vibronic coupling** [37].

To the first order in the displacement $\delta Q_j$ from the ground state equilibrium positions $\{\mathbf{Q_j^0}\}$, one can shows that the molecular transition dipole moment associated to the vibronic emission is given by :

$$
\begin{aligned}
&\left\langle \Psi_{g,n} \middle| \hat{\mu} \middle| \Psi_{e,m} \right\rangle \approx \left[ \left\langle \phi_g \middle| \hat{\mu} \middle| \phi_e \right\rangle_{\mathbf{r}} \right]_{\{\mathbf{Q_j^0}\}} \left\langle \chi_n^g \middle| \chi_m^e \right\rangle_{\mathbf{Q}} \\
&+ \sum_j \left\{ \sum_h \left[ \left\langle \phi_g \middle| \hat{\mu} \middle| \phi_h \right\rangle_{\mathbf{r}} \left\langle \phi_h \middle| \frac{\partial \phi_e}{\partial Q_j} \right\rangle_{\mathbf{r}} + \left\langle \frac{\partial \phi_g}{\partial Q_j} \middle| \phi_h \right\rangle_{\mathbf{r}} \left\langle \phi_h \middle| \hat{\mu} \middle| \phi_e \right\rangle_{\mathbf{r}} \right]_{\{\mathbf{Q_j^0}\}} \right\} \\
&\times \left\langle \chi_n^g \middle| \delta \hat{Q}_j \middle| \chi_m^e \right\rangle_{\mathbf{Q}}
\end{aligned}
$$

The first term corresponds to the Franck-Condon transition dipole moment, described above. The second term, usually referred to the Herzberg-Teller coupling term, involves a summation of transition dipole matrix elements over the complete basis of electronic excited states. This means that the dipole moment associated with a vibronic emission is described as a superposition of dipole moments associated with transitions from higher excited states of the molecule. In this case, the pattern observed in the HRFM maps will be characteristic of this superposition, and thus will be different from the pattern observed for the 0-0 line (lower energy excited state). The fact that the (0-0) and vibronic lines present a different HRFM pattern suggests that the Herzberg-Teller coupling term plays a dominant role in our experiment. Additionally, we point out that the different overlap integrals in the Herzberg-Teller term will be non-zero only if the integrant is symmetric. This condition will determine the composition of the superposition involved in the vibronic emission, and thus explain the pattern symmetry observed in the HRFM maps.

Note that this discussion is carried out for a single molecule of ZnPc. Extending this discussion to the dimer situation, one can propose two possible explanations for the experimental observations of the dimer:

- The vibronic emission is described by a superposition of dipoles associated with the higher energy excited states of the individual molecules in the dimer.
- This superposition is built on the higher energy states of the dimer itself, *i.e* the higher energy supra-molecular excitonic modes.

Theoretical calculations are in progress and will, hopefully, allow to chose between these two possibilities. Anyhow, one can state that the vibronic coupling is the reason for the spatial variation observed in the vibronic spectra.

### 4.3.4 Case of $H_2Pc$

To illustrate the sensitivity of the technique, Fig. 4.9 presents a set of data recorded on a single $H_2Pc$ molecule. By locating the tip at one branch of the molecule or the other (Fig. 4.9(a)), we showed that it is possible to obtain selectively the STM-F spectrum (Fig. 4.9(b)) of tautomer 1 (red spectrum) or tautomer 2 (blue spectrum) (see the previous chapter). By magnifying the low-energy region of the $Q_x$ transition, we can observe on both spectra a vibronic signal. A comparison of these two vibronic spectra with the Raman spectrum recorded on a macroscopic polycrystalline sample of $H_2Pc$ is presented Fig. 4.9(c). The blue spectrum (tautomer 2) is in excellent agreement with the Raman spectrum for the number of peaks, the energy and the intensities. However, tautomer 1 presents a substantially different vibrational spectrum. This observation suggests that the molecule is subject to additional constraints from the substrate in tautomer 1 compared to tautomer 2. Conversely, the explanation of this substantial modification of the vibronic spectrum can only be deduced from our spatial, spectral and time-resolved fluorescence experiment presented in the previous chapter. Note that a specific investigation of the vibronic spectrum as a function of the tip position is complicated by the fact that the emissions of the two tautomers become easily mixed (black spectrum Fig. 4.9(b)) for any excitation localized elsewhere than the two specific positions indicated in Fig. 4.9(a). This example shows that Hyper-Resolved Fluorescence Microscopy allows getting insight into sub-molecular phenomena, which are unreachable with any other conventional technique.

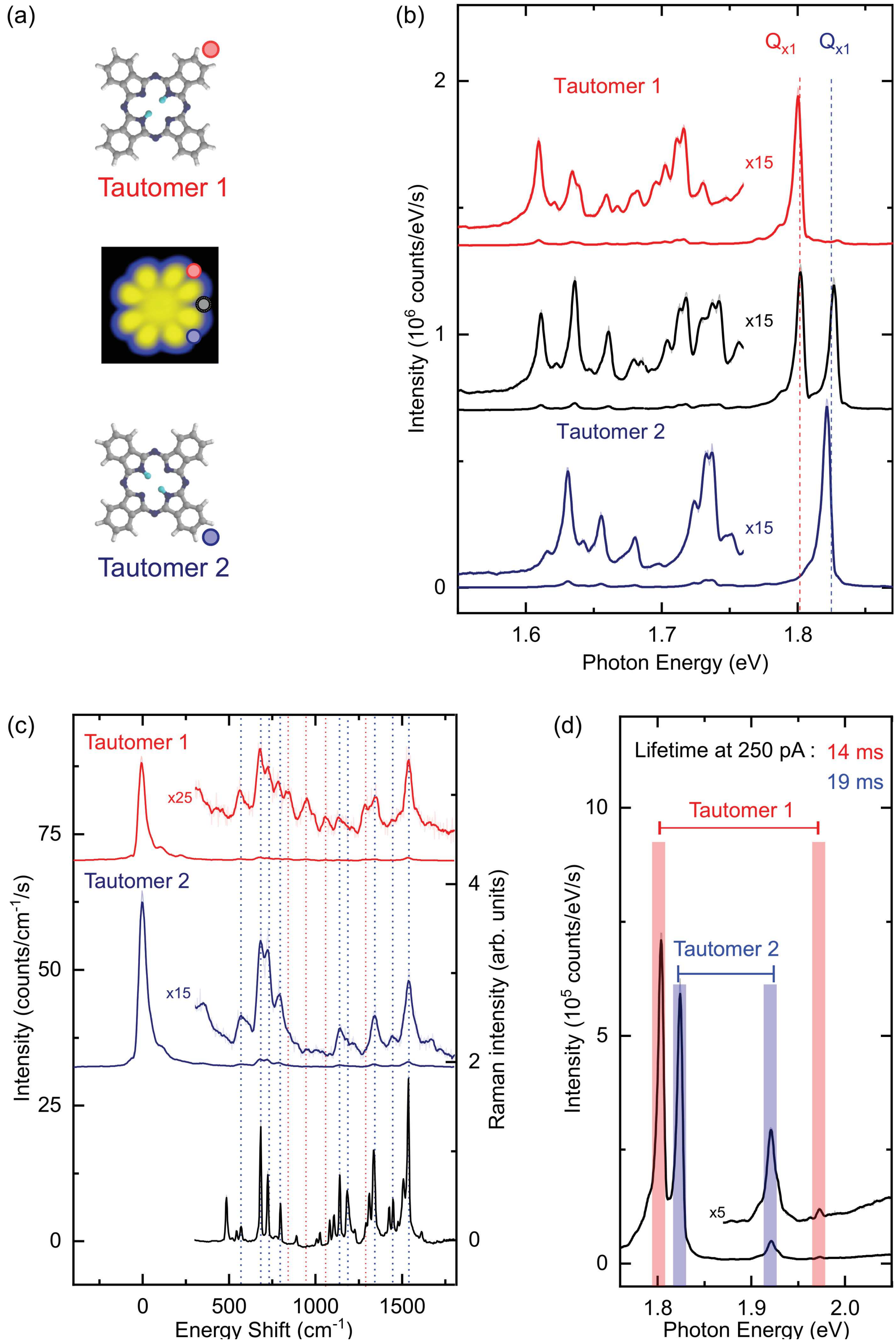

**Figure 4.9: Vibrational signature of the $H_2$Pc tautomers revealed by HRFM** (a) Sketch depicting the selective excitation of each tautomer fluorescence. (b) STM-F spectra recorded at the position indicated in (a). (c) STM-F spectra associated with each tautomer plotted as a function of the energy shift with respect to the $Q_x$ line and compared to a Raman spectrum recorded on a $H_2$Pc powder. (d) STM-F spectrum showing the substantial difference in the $Q_x - Q_y$ gap of the two tautomers.

# Conclusion

In this chapter, we carried out STM-F experiments on single ZnPc molecules decoupled from an Ag(111) substrate by a thin layer of NaCl. STM-F spectra recorded on linear arrangements of ZnPc molecules present a main emission line which sharpens, shifts towards lower energy, and becomes more intense with the number of molecules. Thanks to this narrowing, a well-resolved set of peaks is observed in the lower energy region. Each of these peaks appears at an invariant energy shift with respect to the main emission line, suggesting that their emission originates from the same excited state. Based on a comparison between the STM-F spectrum, a Raman spectrum recorded on a ZnPc powder, and a fluorescence spectrum acquired in photo-luminescence experiments on frozen matrices, one concludes that these peaks correspond to vibronic emissions of the ZnPc molecule. Based on DFT calculations, each vibronic peak was attributed to a specific vibrational mode. This spectrum thus constitutes an accurate chemical signature of the probed species, at the single-molecule level, information that cannot be obtained with a conventional STM approach. An analysis of the whole STM-F spectrum as a function of tip position was conducted to unravel the impact of the different supra-molecular excitonic modes on the vibronic signal. Independently of the tip position, the vibronic peaks always appear at a constant energy shift with respect to the lower energy supra-molecular excitonic mode and do not seem to be impacted by the emission intensity of this latter. A more specific study reveals that the intensities of the vibronic peaks change as a function of the tip position. Interestingly, this spatial variation seems to be strongly related to the vibrational-mode symmetry. HRFM maps realized for each vibronic peak confirm this observation. Modes belonging to the same irreducible representation present a similar pattern, which reflects the associated symmetry. Finally, the uncorrelated patterns observed between the main and vibronic emission lines are discussed in the framework of the vibronic coupling theory. In this picture, the vibration motion of the molecule induces contamination of the vibronic transition by a superposition of transition dipole moments associated with higher excited states of the molecule. Consequently, the vibronic emission carries characteristic of this superposition determined by symmetry rules and therefore presents a pattern reflecting its symmetry, and which is different from the main emission line pattern.

Finally, our method provides a way to obtain without light excitation a molecular chemical fingerprint. Moreover, we showed that this fingerprint varies when we address a sub-part of the molecule. The capability to obtain such optical information together with a high spatial resolution shows that Hyper-Resolved Fluorescence Microscopy constitutes a powerful method to get insight in physical phenomena at a scale unreachable by other conventional techniques.

# Chapter 5

# Electrofluorochromism at the single-molecule level

The interplay between the redox state and the optical properties of molecules is important for applications in displays, sensors, and molecular-bases memories [1]. Understanding this interplay is also fundamentally important for biological phenomenon such as photosynthesis, where molecules redox states play a role in the intermolecular energy transfer. The optical properties of the different redox state of molecules are generally addressed by spectroelectrochemistry, which consists in probing the optical properties of a large number of molecules in electrochemical cells [52]. Recent results reported a single molecule level sensitivity with such technique [48]. However, obtaining at the single-molecule level a chemical signature such as vibronic, on those systems is still challenging. Such signatures have recently been obtained via Surface Enhanced Raman Spectroscopy [23, 130], but at the cost of direct contact between the electrodes and the molecule, which may alter the intrinsic properties of this latter. In another hand, the STM environment has shown that it constitutes an ideal platform to control and probe the charge state of atoms or molecules [99, 115, 114] with atomic-scale precision. Therefore, combining this approach with STM-F spectroscopy constitutes a convenient way to investigate the interplay between the redox states and optical properties of a single molecule.

In this chapter, I report STM-F experiments carried out on single Zinc-phthalocyanine molecules adsorbed on a NaCl/Au(111) sample. In addition to the fluorescence line associated to the neutral ZnPc molecule, STM-spectra reveal a sharper and more intense emission line in the lower energy region which is attributed to the fluorescence emission of the radical cation of ZnPc. STM-F spectroscopy allows obtaining a vibronic fingerprint of the charged molecule, which is significantly different from the one of the neutral species. The respective emission of the two redox species is controlled by tuning the NaCl thickness, and the plasmonic response of the STM junction. A study of the STM-F spectra as a function of voltage, tunneling current, the tip-molecule distance, and the metallic substrate is conducted to understand the fluorescence excitation mechanism of the two redox species. Finally, a phenomenological approach to the luminescence mechanism is proposed.

## 5.1 STM-F spectroscopy on a zinc phthalocyanine molecule

### 5.1.1 Presentation of the system

Fig. 5.1(a) presents a sketch of the experiment where the fluorescence of a ZnPc molecule decoupled from a gold Au(111) by a 3-ML of NaCl, is excited by the tip of an STM. The differential conductance spectrum $dI/dV$ recorded on a single molecule, reveals the energy positions of the HOMO and LUMO orbitals, whose STM images are presented in the inset (Fig. 5.1(b)). One can notice that these images are identical to those acquired on a NaCl/Ag(111) substrate (see the previous chapter). However, compared to this case, the energy positions of the corresponding orbital are rigidly shifted towards higher voltage ($\approx$ 1 eV). This difference reflects the higher work function of Au(111) ($\approx$ + 0,8 eV) compare to Ag(111). Fig. 5.1(c) shows an STM-F spectrum recorded at a positive voltage ($V$ = +2 V) on a single ZnPc molecule at the position indicated by a cross in the STM image of Fig. 5.1(b). This spectrum reveals an intense emission line at $\approx$ 1.89 eV (labelled $X^0$) with a width of $\approx$ 20 meV, which correspond to the fluorescence emission of the molecule [83, 129], and weaker intensity vibronic features in the lower energy region. An STM-F spectrum recorded at a negative voltage ($V$ = -2.5 V) presents the same emission line (Fig. 5.1(d)), but whose intensity is reduced by a factor of 30 compared to the spectrum recorded at positive voltage. Additionally, a sharper (line width of $\approx$ 10 meV) and more intense emission line is observed at $\approx$ 1.52 eV (labeled $X^+$), and which has not been reported in previous STM-F studies [129, 134, 132] carried out on the same molecule. This energy is in excellent agreement with the fluorescence energy of ZnPc radical cation (ZnPc$^+$) reported by experimental and theoretical studies [86, 74, 102].

To better understand these observations Fig. 5.1(e), (f) show energy sketches depicting the excitation mechanism at both voltage polarities. At positive voltage (Fig. 5.1(e)) the fluorescence emission of the neutral molecule ($X^0$ in Fig. 5.1(c)) is excited by an energy transfer from inelastic tunneling electrons, traversing the junction from the tip to the sample. Similarly, at negative voltage, the fluorescence emission of the neutral molecule ($X^0$ in Fig. 5.1(d)) is excited by inelastic electrons starting from the sample to the tip. However, at sufficiently low voltage ($V$ = -2.5 V) a second process may occur. In this situation, an electron can be extracted from the molecule, driving the molecule in a positively charged state (ZnPc$^+$). Due to the NaCl decoupling, this charge can be stabilized for another inelastic event to occur (Fig. 5.1(f)). This inelastic electron transfers its energy to the charged molecule, which undergoes an excitation-emission cycle. One can note that the observation of both contributions in the spectrum, *i.e*, emission of the charged and neutral molecule, recorded at negative voltage suggests a blinking between the two redox species.

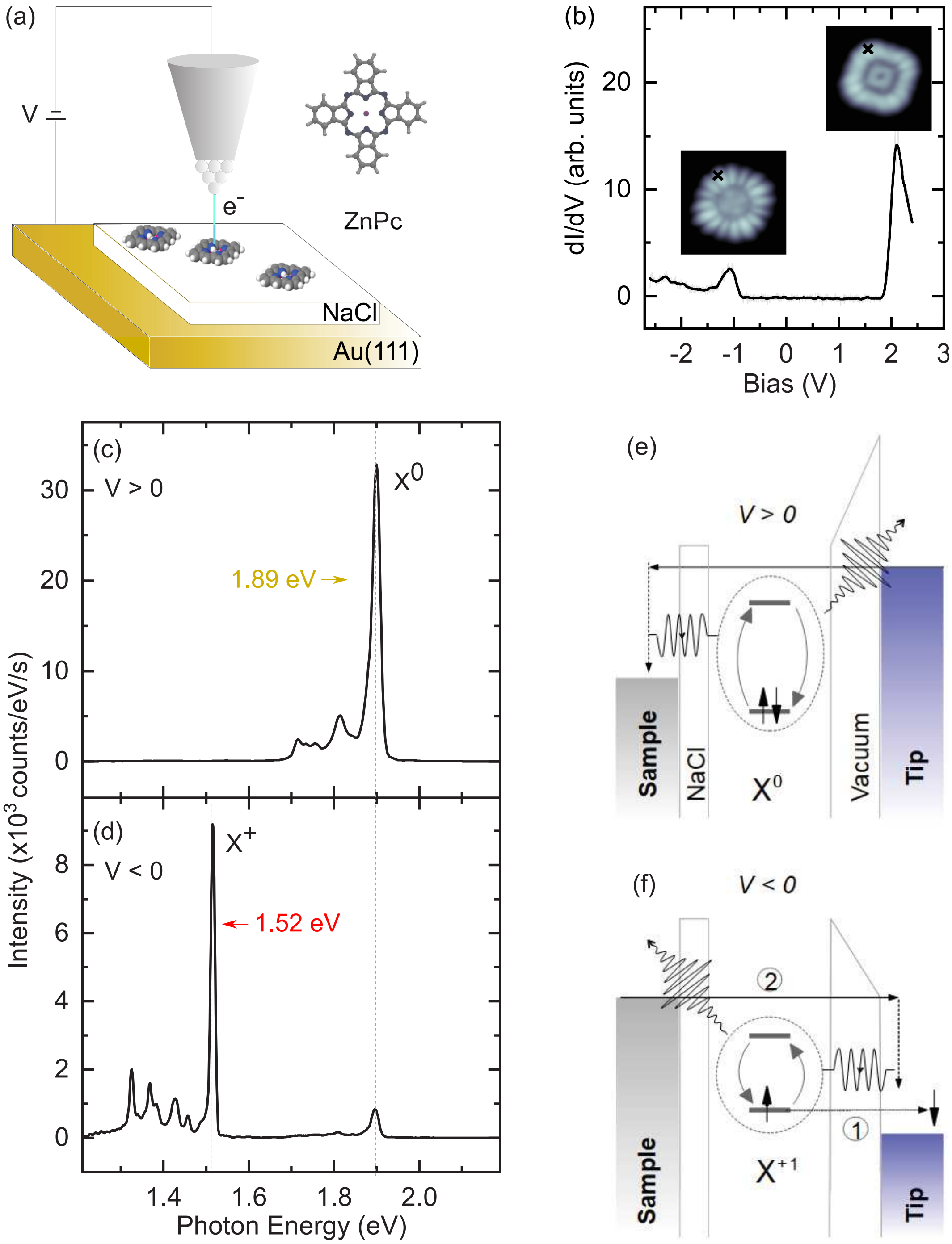

**Figure 5.1: STM-F spectroscopy of the two redox states of a single ZnPc molecule** (a) Sketch of the experiment. (b) Differential conductance spectrum recorded on single ZnPc adsorbed on a 3-ML NaCl/Au(111) sample. Inset : STM images ($2.9 \times 2.9$ nm$^2$; $I$ = 30 pA) of the HOMO ($V$ = -1V) and the LUMO ($V$ = +1.85 V). (c) STM spectrum at positive voltage ($V$ = +2 V; $I$ = 300 pA; acquisition time $t$ = 300 s) recorded at the position indicated in (b). (d) STM spectrum at negative voltage ($V$ = -2.5 V; $I$ = 300 pA; acquisition time $t$ = 300 s) recorded at the position indicated in (b). (e) and (f) Energetic sketch depicting the excitation mechanisms at both polarity. Note that the states are not the HOMO-LUMO states but the ground and excited states ($S_0$ and $S_1$) of the molecule. The sketch in (f) represents an hybrid representation : an electron is extracted from the HOMO, which thus modify the optical $S_0 - S_1$ gap.

These proposed mechanisms will be discussed further in the last section of this chapter. One can already stress on the fact that the formation of the radical cation is only possible at negative voltage, which explains why we do not observe its fluorescence in the spectrum realized at positive voltage.

The fluorescence of the charged molecule presents a line-width of $\approx 10$ meV, which is twice smaller than the one of the neutral molecule ($\approx 20$ meV). In a very similar configuration, Zhang *et al.* [132] reported a value of $\approx 1$ ns for the neutral ZnPc excited state lifetime. By assuming that the line-width is lifetime limited, this value would lead to a line-width of $\approx 1$ $\mu$eV, which is not what we observed experimentally. Therefore, one can state that the width of the emission lines are not lifetime limited but rather reflects the dephasing due to the interactions between the emitter and the surface phonons. Fatayer *et al.* [35] have recently reported an experimental and theoretical study which shows that charging a single molecule induces an important reorganization of the NaCl below this latter. Therefore, this reorganization may reduce the dephasing and explains the significant fluorescence line-width reduction observed between the neutral and the charged species.

The observations of charged atoms or molecules on such insulating films was reported in many STM and AFM studies [99, 128, 115, 67, 36, 43, 35, 34], where charged effect could always be associated to features in the images or the differential conductance spectrum. In our case, such features are not observed in this latter nor in the images but only revealed via the fluorescence spectra.

### 5.1.2 Vibrational signature of the charged molecule

The investigations of the previous paragraphs confirm that it is possible to obtain the fluorescence signals of the two redox states of a single ZnPc molecule. In the previous chapter, we demonstrated that STM-F spectroscopy could provide an effective vibronic fingerprint of the probed species, which is extremely sensitive to the molecular structure. Fig. 5.2(a) presents an STM-F spectrum of the charged ZnPc molecule, plotted as a function of the energy shift with respect to the $X^+$ line. This STM-F spectrum reveals a well-resolved series of peaks which correspond to vibronic emission of the radical cation of ZnPc. A comparison with the vibronic spectrum of the neutral molecule [1](Fig. 5.2(b)) shows that the vibronic fingerprint of the molecule is strongly affected by its redox state. The energy position of the ZnPc$^+$ vibronic lines is only slightly shifted compared to those of ZnPc, the respective intensities, however, are strongly modified. To understand this strong modification, our collaborator Alex Boeglin at the IPCMS, developed a finite difference method base on time-dependant DFT calculations. These calculations evaluate the respective intensities of the vibronic lines by taking into account the Franck-Condon contributions for the vibrational modes belonging to the $A_1g$ representation, and the Herzberg-Teller contributions for the $A_1g$, $B_1g$, and $B_2g$ modes. A fair agreement is observed between theory and experiment. Overall, one can notice that modes belonging

---

[1] Note that this spectrum has been recorded on a tetramer of ZnPc molecules (see chapter 3 for details).

to the $B_1g$ representation present similar intensities in the two redox species spectra. For the charged molecule the $B_2g$ vibronic lines are enhanced while $A_1g$ lines are reduced compared to the neutral molecule. To understand that vibronic lines appear nearly at the same energy for the two redox states, our collaborator Hervé Bulou performed DFT calculation to obtain the optimized geometry of the two redox species. Fig. 5.2(c) shows the optimized geometry for the neutral molecule. A nearly identical geometry is found for the charged molecule. Indeed, a histogram of the bond length difference between ZnPc and ZnPc$^+$ reveals changes of less than 0.01 Å(Fig. 5.2(c)). This shows that the backbone of the molecule is extremely rigid, which explains that the vibronic modes for ZnPc and ZnPc$^+$ appear nearly at the same energy.
These observations show that even though the molecular structure is slightly affected by charging, one can unambiguously distinguish the two redox species through their vibronic spectra. Such vibrational information averaged over many charged molecules can be obtained from Raman spectroscopy, performed in electrochemical cell [13, 113]. Recent results reported that vibronic spectra of redox species could be addressed by Surface Enhanced Raman Spectroscopy at the single-molecule limit [23, 130]. However, in this case, the molecule is in direct contact with the electrodes, which may alter its intrinsic properties. Thanks to the excellent decoupling provide by NaCl, STM-F spectroscopy constitute a convenient method to obtain an accurate fingerprint of two redox species of a single molecule. The other advantage of our approach compared to those mentioned above is that the molecule is in a highly controllable environment, which can be easily modified. The next section proposes to investigate this aspect.

## 5.2 Control of the respective emission of the charged and neutral molecule

The previous section demonstrated that STM-F spectroscopy constitutes a convenient way to obtain simultaneously the optical signals of the different redox states of a single molecule. The observation of the two contributions in the fluorescence spectra suggests a blinking between the two species. Additionally, one can notice the notable energy difference between these two contributions, which raise questions about the coupling efficiency between these two contributions and the NCP. In this section, we demonstrate control of the lifetime of the two redox species, and their respective emission lifetime.

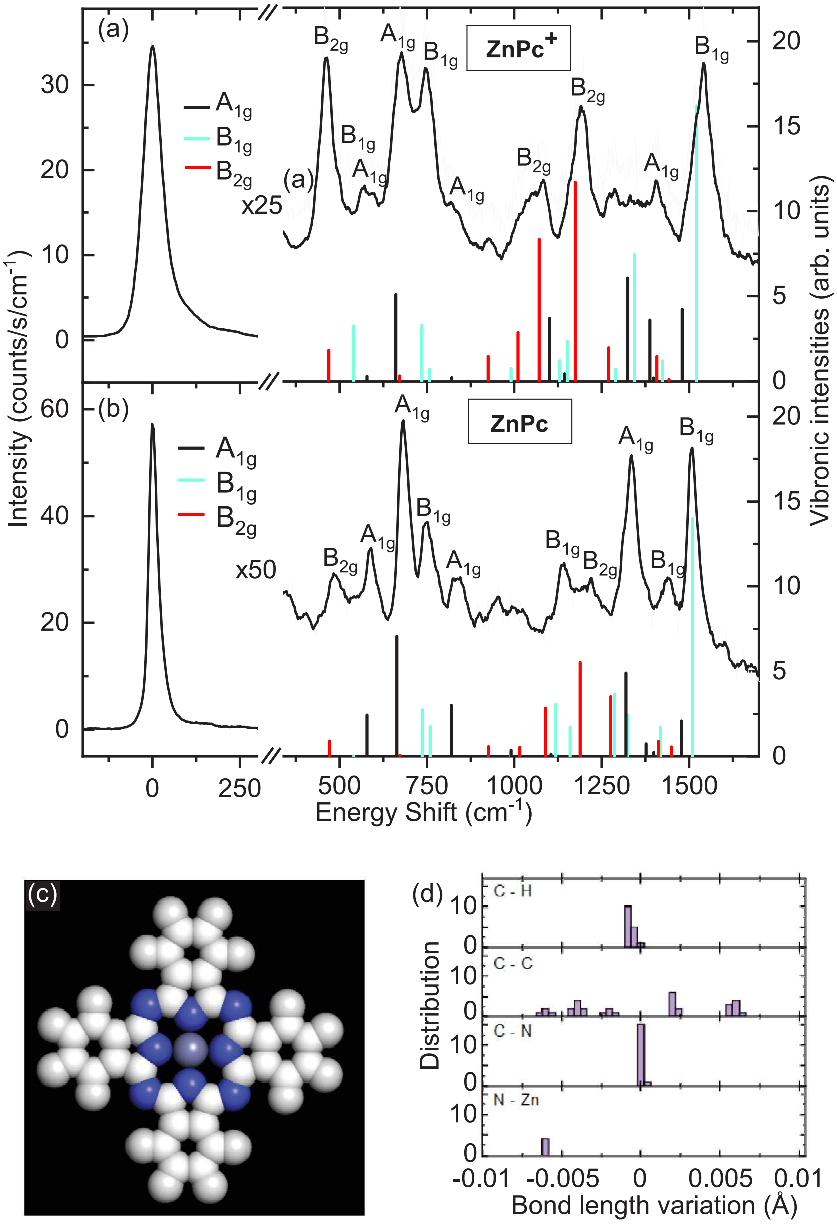

**Figure 5.2: Vibronic fingerprint of the two redox species** (a) STM-F spectrum ($V$ = -2.5 V; $I$ = 300 pA; acquisition time $t$ = 180 s) of the ZnPc$^+$ plotted as a function of the energy shift from the $X^+$ line. (b) STM-F spectrum ($V$ = -2.5 V; $I$ = 750 pA; acquisition time $t$ = 300 s) recorded on a tetramer of ZnPc (see previous chapter)to obtain the vibronic fingerprint of the neutral ZnPc molecule. (c) DFT-optimized geometry of the ZnPc molecule. (d) Histogram of the bond length variation between the two redox species.

### 5.2.1 Charge lifetime

Fig. 5.3(a) shows a sketch of the experiment, where we followed the evolution of the STM-F spectra as a function of the number of NaCl atomic layers separating the molecule from the Au(111) surface. STM-F spectra recorded on the bare metal (spectrum 0) and the molecule adsorbed on 1, 2, 3, and 4 atomic layers of NaCl (spectra labelled 1, 2, 3, and 4 respectively) are displayed Fig. Fig. 5.3(b).

For a single molecule adsorbed on a single NaCl layer, except a reduction of the intensity, the spectrum (labelled 1) is similar to the one recorded on the bare metal, which is characteristic of the plasmonic cavity. This observation suggests that the molecular fluorescence is quenched in this case, reflecting the poor decoupling offered by a single layer of NaCl. For another molecule decoupled by two atomic layers of NaCl, the spectrum (labelled 2) reveals the two fluorescence contributions $X^0$ and $X^+$, which present a similar intensity. For a molecule adsorbed on three layers of NaCl, the spectrum (labelled 3) shows that the $X^+$ contribution dominates the $X^0$ one. This latter becomes even not observable in the spectrum recorded on a molecule adsorbed on four atomic layers of NaCl (spectrum 4). At negative voltage, the electrons traverse the junction from the sample to the tip. Therefore, the lifetime of the charged molecule depends on two concomitant processes. While the probability to charge the molecule relies essentially on the tip-molecule distance, the probability to neutralize the molecule depends on the molecule-sample distance. When the insulating layer thickness increases, the corresponding tunneling barrier becomes larger, and consequently the probability to neutralize the molecule decreases. Meanwhile, since the measurement are performed at constant current, the tip has to get closer to the surface to compensate for this larger barrier. Therefore, the tip-molecule distance decreases, and then the probability to charge the molecule increases. Finally, increasing the NaCl thickness leads the molecule to spend more time in its charged state. Similar observations have been reported by Steurer *et al.* [114] on single gold atoms on NaCl insulating films.

One can conclude that these observations suggest that the ratio between the intensity of the $X^0$ and $X^+$ lines, reflect the relative time spend in the neutral and charged species.

One can make another remark regarding the evolution of the intensity of both lines as a function of the number of NaCl layers. Except for the 4ML spectrum (spectrum 4) where the $X^0$ contribution disappear, one can notice an increase of the emission intensity as a function of the NaCl thickness for both lines. The increasing of the insulating NaCl layers has two consequences. First, it allows a reduction of the fluorescence quenching due to the hybridization between the molecule and the metallic substrate states. Secondly, a reduction of the tip-sample distance due to the constant current condition, and therefore an increase of the volume density of plasmonic mode in the junction leading to a higher Purcell enhancement. Similar observations have been reported about the fluorescence of a single ZnPc molecule on Ag(100) by Zhang *et al.* [132]. Note that in this latter paper only the fluorescence contribution from the neutral molecule is reported. The fact that we see only the $X^+$ contribution in the 4ML spectrum suggests that the molecule spends most of its time in the charged state for this case.

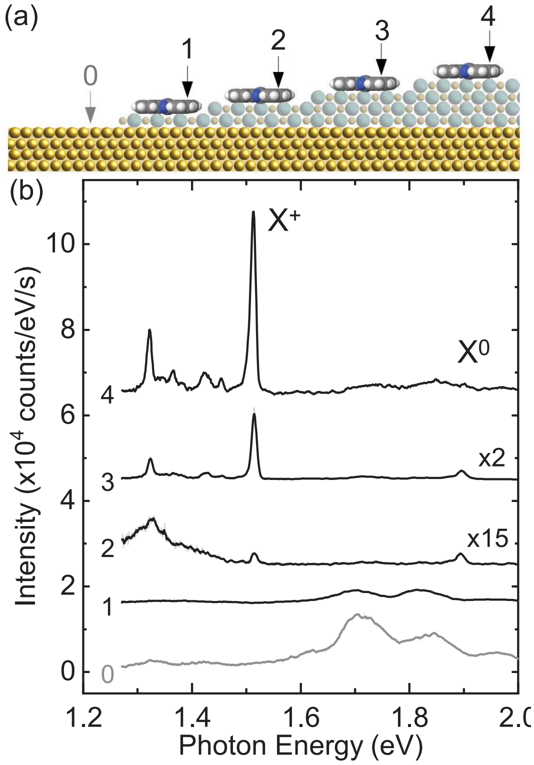

**Figure 5.3: Influence of the insulator thickness on the otpical response of the two redox species** (a) Sketch depicting the experiment where STM-F spectra are recorded on a single ZnPc molecule adsorbed on 0, 1, 2, 3, and 4 atomic layers of NaCl. (b) STM-F spectra ($V$ = -2.5 V; $I$ = 300 pA) recorded on a single molecule adsorbed on 1ML ($t$ = 300 s), 2ML ($t$ = 180 s), 3ML ($t$ = 120 s), 4ML ($t$ = 10 s). The spectrum labeled 0 is recorded on the bare Au(111) surface.

### 5.2.2 Emission lifetime

Next, we studied the interplay between the NCP and the fluorescence emission of both redox states.

Fig. 5.4 (a) and (b) present STM-F spectra recorded on a single ZnPc molecule adsorbed on 3ML of NaCl (black spectra) and spectra recorded far away from the molecule which constitutes the NCP response (green and red spectra). This response can be tuned by tip indentation in the surface sample, which modifies the tip apex geometry. Comparison between Fig. 5.4 (a) and Fig. 5.4 (b) shows that the presence of high density of plasmonic modes around the energy of the $X^0$ (Fig. 5.4 (a)) or the $X^+$ (Fig. 5.4 (b)) lines amplifies their emission. This is a consequence of the Purcell effect [91], which has been reported in other STM-F studies [92, 20]. Here we used this property to tune the respective emission of the two redox states of the molecule, by controlling their respective emission lifetime.

Eventually, we normalized the spectra recorded on the molecule by their associated NCP response (Fig. 5.4 (c)). This procedure reveals a linear dependence of the emission lines intensities with NCP intensity, which confirms our interpretation. Furthermore, one can notice that upon this normalization the $X^+$

becomes dominant. This observation suggests either that the transition dipole moment associated to the fluorescence of the cationic species is much stronger than the neutral one, or that the molecule spends most of its time in the cationic form, or the excitation efficiency of the fluorescence of the charged molecule is much stronger than the one of the neutral molecule.

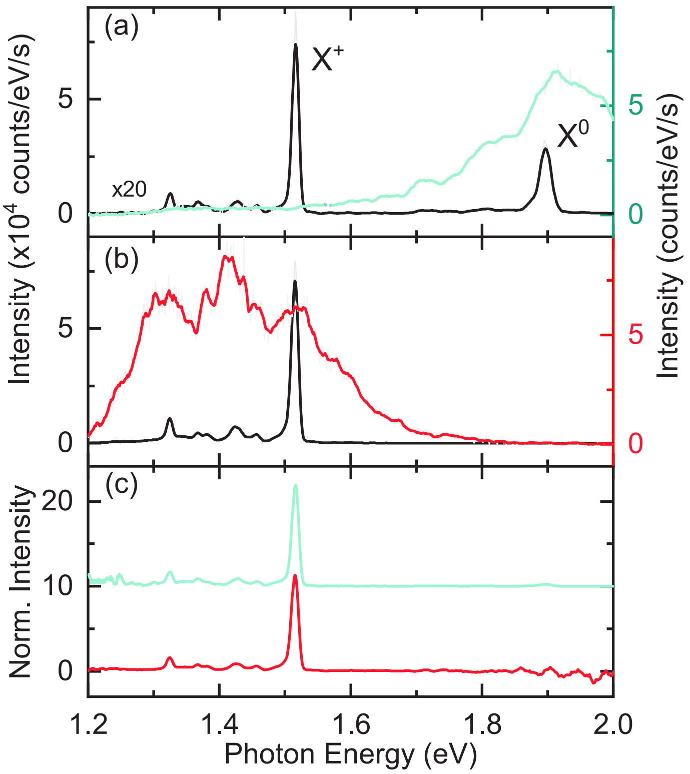

**Figure 5.4: Influence of the NCP on the optical response of the two redox species** (a) STM-F spectra ($V$ = -2.5 V; $I$ = 300 pA) recorded on the single molecule (dark line; $t$ = 300 s), and on the NaCl (blue line; $t$ = 60 s) to provide the NCP response. (b) STM spectra of the ZnPc molecule (dark line) and of the NCP (red line). (c) ZnPc spectra normalized by the corresponding NCP response.

Finally, one can control the respective lifetime of the two redox species of a single molecule, as well as their emission lifetimes, by tuning respectively, the insulator thickness and the plasmonic response of the STM junction, and in the same time monitor their optical response via STM-F spectroscopy.

## 5.3 Mechanism

In this section, we investigate the excitation mechanism of the $X^0$ and $X^+$ contributions as a function of different parameters. In the first part, we investigate the evolution of these lines as a function of the applied voltage on two different substrates (Au(111) and Ag(111)). We also investigate the current dependency, which essentially informs us about the excitation efficiency (*i.e* how many electrons do we need to excite the fluorescence emission of one photon). In the second part, we focus on the impact of the energy level alignment on the

$X^0$ line. Then we investigate the plasmon-exciton coupling of both $X^0$ and $X^+$ lines as a function of tip-molecule lateral distance. Finally, we propose a phenomenological mechanism in an attempt to rationalize the experimental observations.

### 5.3.1 Impact of the metallic substrate on the fluorescence

#### Voltage dependency

Fig. 5.5 presents series of STM-F spectra recorded on a single ZnPc molecule adsorbed on 3ML on NaCl for a Au(111) gold substrate (Fig. 5.5(a)) and for a Ag(111) silver substrate (Fig. 5.5(b)). Comparison between these two series shows that the emission is dominated by the $X^+$ contribution for a gold substrate, while it is dominated by the $X^0$ one for a silver substrate. In fact, for silver the $X^+$ contribution can be observed only for a voltage $V <$ -2.5 V (Fig. 5.5(c)). As we mentioned paragraph 5.1.1, the main difference between the two metallic substrates is the higher work function ($\approx$ + 0.8 eV), which induce a rigid shift of the $dI/dV$ spectrum towards higher voltage in the case of Au(111) compared to Ag(111). To investigate how this impacts the respective emission of the $X^+$ and $X^0$ contributions, Fig. 5.5(c) and (d) shows a comparison between the $dI/dV$ spectrum and the integrated intensity for both emission contributions as a function of voltage.

For Au(111), one can observe an onset at $V$ = -2.2 V for the $X^+$ line. This onset is much larger than the energy of the $X^+$ line ($h\nu \approx$ 1.52 eV) suggesting it rather matches the energy required to charge the molecule. Interestingly, the $X^0$ contribution follows the same trend as a function of the voltage. One can remarks that this onset can not be correlated to a specific feature in the $dI/dV$ spectrum.

For the case of Ag(111), an onset at $V$ = -2.5 V is observed for the $X^+$ line [2]. For the $X^0$ contribution, however, a first onset is observed between at $\approx$ -1.9 V. At this voltage, the transport does not occur through the HOMO orbital.

---

[2] Note that for a voltage $V >$ -2.5 V, the integrated intensity is non zero because it is slightly impacted by the strong emission of the $X^0$ contribution.

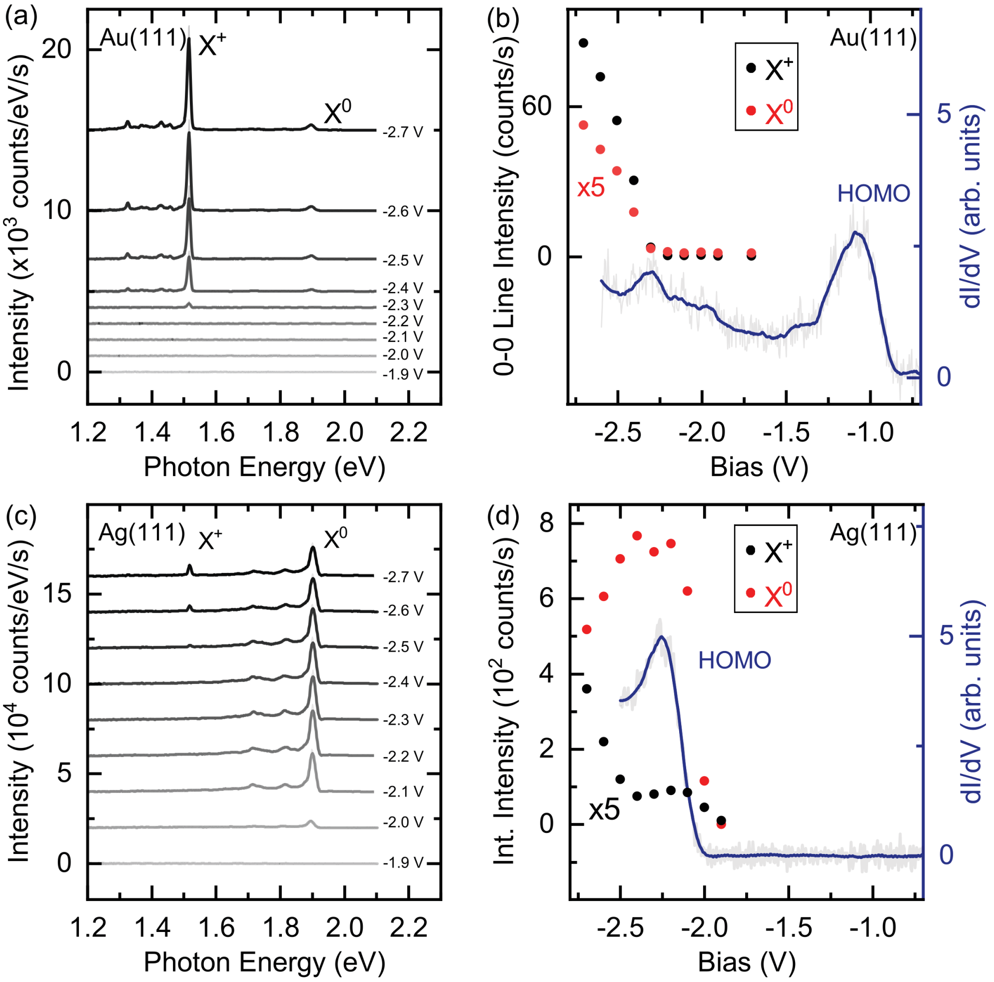

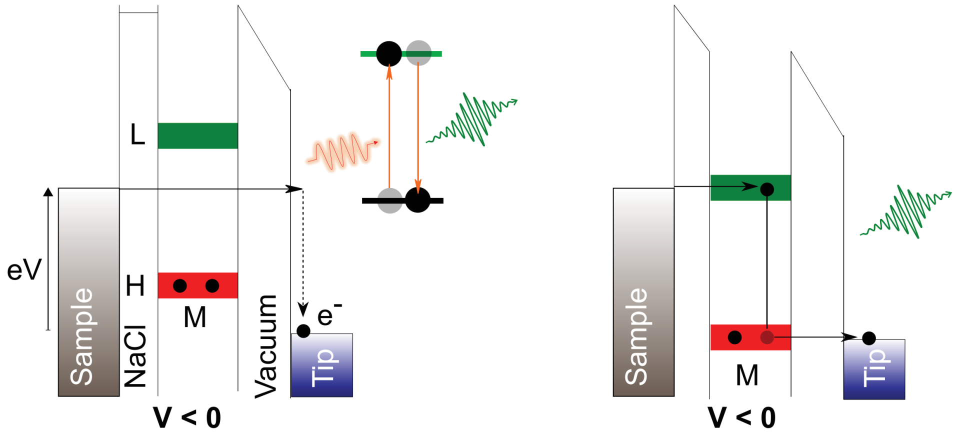
(e) Energy transfer mechanism

(f) Carrier injection mechanism

**Figure 5.5: Voltage dependency of the $X^0$ and $X^+$ lines on Au(111) and Ag(111) substrate.** (a) Series of STM-F spectra recorded on a single ZnPc molecule adsorbed on a 3ML NaCl/Au(111) sample at different voltage ($I$ = pA; acquisition time $t$ = 180 s). (b) Integrated intensity of the $X^+$ (bin : 1.50-1.54 eV) and $X^0$ (bin : 1.85-1.95 eV) lines as function of $V$, compared to the $dI/dV$ spectrum. (c) Series of STM-F spectra recorded on a single ZnPc molecule adsorbed on a 3ML NaCl/Ag(111) sample at different voltage ($I$ = pA; acquisition time $t$ = 60 s). (b) Integrated intensity of the $X^0$ and $X^+$ lines as function of $V$, compared to the $dI/dV$ spectrum. (e) Energy sketch depicting the energy transfer mechanism. (f) Energy sketch depicting the carrier-injection mechanism.

In this situation, it has been suggested that fluorescence excitation is driven by an energy transfer from an inelastic electron (Fig. 5.5(e)) [16, 20, 29]. Then, a second onset is observed at $V$ < -2.1 V which correspond to the HOMO onset, where the $X^0$ intensity strongly increases. In this situation, the transport is strongly modified by the presence of the HOMO orbital, which becomes the dominant transport channel. This change of emission regime has been interpreted as a change of the excitation mechanism [49, 129, 16], where the carrier-injection (CI) mechanism becomes dominant over the ET mechanism once tunneling through the HOMO orbital is possible (Fig. 5.5(f)). However, the CI mechanism, which involves a sequential injection of an electron in the LUMO and a hole in the HOMO, needs a specific alignment of the LUMO and the HOMO, with the Fermi level of the sample and the tip respectively [92, 129]. This means that under a voltage $V$, the LUMO (resp. HOMO) has to shift with respect to the sample (resp. tip) Fermi level to becomes resonant with this latter (Fig. 5.5(f)). Such scenario is possible only if the voltage drop in the junction is equally shared between the region separating the molecule from the metal (*i.e* the NaCl), and the one separating the molecule from the tip (*i.e* the vacuum). However, it has been shown that in such STM junction the voltage drops only occurs in the vacuum side [101], which means that the LUMO and LUMO orbitals energy positions are almost fixed with respect to the Fermi level of the sample. In the next paragraph, we will discuss another type of carrier-injection mechanism proposed by different authors [16, 80], that overpass this problem.

Finally, if the slightly different onset for the $X^+$ line observed for gold and silver can be rationalized by a different energy position of the HOMO orbital (*i.e* it is easier to extract an electron from the HOMO in the case of gold), the difference observed for the $X^0$ line between both substrate, suggests a possible different excitation mechanism.

### Current dependency

To investigate the hypothesis of a different mechanism on gold or silver, Fig. 5.6(a) and (c) presents a series of STM-F spectra recorded at different current for both substrates. For both cases, spectra are recorded at $V$ = -2.5 V. Fig. 5.6(b) and (d) shows the integrated intensity for the $X^0$ and $X^+$ lines as a function of the current for gold and silver. Note that for silver the $X^+$ line was not observed for this series, possibly due to a weak plasmonic response at this energy.
For silver, the emission intensity for the $X^0$ line presents a slightly super-linear behaviour ( $I^{1.1}$), similar to what we observed in chapter 3 for $H_2Pc$, and similar to what has been reported in other studies [132]. If a linear dependence, suggesting mono-electronic excitation, may be expected, one has to keep in mind that the plasmonic cavity changes when the current changes. Indeed, when the current increases the tip gets closer to the molecule, and consequently, the volume density of the plasmonic field is stronger at the position of the molecule. This suggests an enhancement of the radiative decay of the molecular excitation, when the current increases, explaining the super-linear behaviour.
For the case of gold, the emission intensity for the $X^+$ line presents a slightly super-quadratic behaviour ( $I^{2.4}$). This can be rationalized by considering the

$X^+$ emission as a two electrons process, where first an electron is extracted from the molecule, and then a second electron excited the fluorescence of the positively charged molecule. Surprisingly, the $X^0$ contribution follows also a super-quadratic behaviour ( $I^{2.2}$) suggesting also a two electrons process in this case. One can remarks that this observation is consistent with the similar voltage onset observed for the $X^0$ and $X^+$ contributions in this case, which may indicate a connection between the two fluorescence lines.

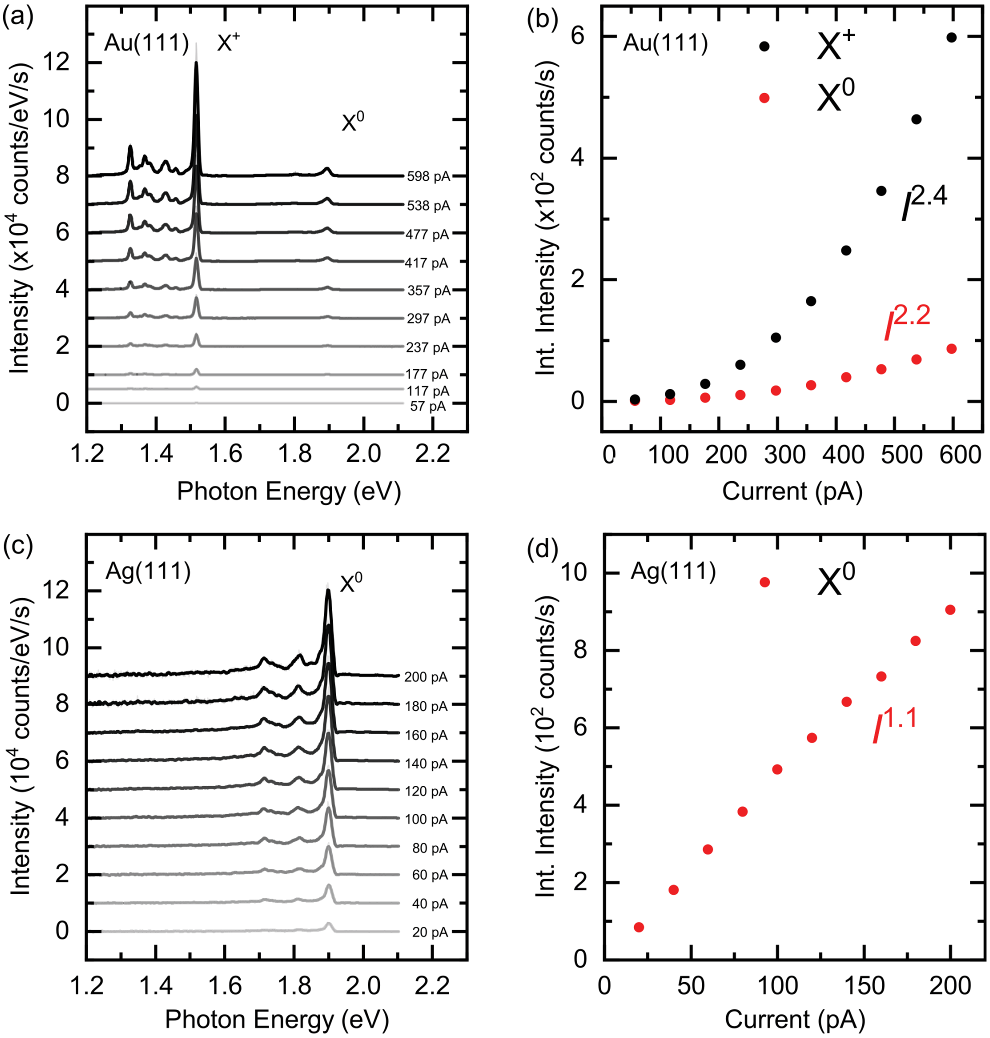

**Figure 5.6: Current dependency of the $X^0$ and $X^+$ lines on Au(111) and Ag(111) substrate.** (a) STM-F spectra ($V$ = -2.5 V) at different current, recorded on a single ZnPc molecule adsorbed on a 3ML NaCl/Au(111) substrate (b) Integrated intensity of the $X^+$ (bin : 1.50-1.54 eV) and $X^0$ (bin : 1.85-1.95 eV) lines as function of $I$. (c) STM-F spectra ($V$ = -2.5 V) at different current, recorded on a single ZnPc molecule adsorbed on a 3ML NaCl/Ag(111) substrate (d) Integrated intensity of the $X^0$ (bin : 1.85-1.95 eV) line as function of $I$.

### 5.3.2 Impact of the energy level alignment

We now focus on the dependence of the fluorescence emission, especially the $X^0$ contribution, as a function of the voltage polarity. Fig. 5.7 presents an overview of the different STM-F spectra that can be obtained on a ZnPc single molecule, depending of the sample (Top part : Au(111), Bottom part Ag(111)), and the polarity ($V < 0$ Fig. 5.7(a) and $V < 0$ Fig. 5.7(c)). Note that all of these STM-F spectra are recorded on 3ML of NaCl for both substrates.

As we mentioned before, at $V$ = -2.5 V the STM-F spectrum recorded for a gold substrate presents en emission dominated by the $X^+$ contribution, while it is dominated by the $X^0$ contribution for the case of silver (Fig. 5.7(a)). At $V$ = +2.5 V, a spectrum recorded for gold shows an intense $X^0$ contributions while almost no emission is observed for the case of silver (Fig. 5.7(c)). This quasi-absence of emission at positive voltage has been reported in several studies realized on silver substrate [129, 49]. These observations together with the rigid shift observed in the $dI/dV$ between gold and silver (Fig. 5.7(b)) suggest that the energy level alignment plays an important role in the different emission regime that we observed for the $X^0$ line. To highlight this effect we indicate in Fig. 5.7(b) the voltage which corresponds to the energy of the $X^0$ contribution at both polarity (dashed line). For gold, the energy position of the LUMO ($\epsilon_L^{Au}$ $\approx$ 2.1 eV) is above the energy of the $X^0$ contribution ($h\nu$ = 1.9 eV), while it is below for the case of silver ($\epsilon_L^{Ag} \approx 1$ eV). Similarly, the strong $X^0$ contribution observed for the silver substrate compare to gold (Fig. 5.7(a)), corresponds also to a situation where the absolute value of the energy position of the HOMO ($\epsilon_H^{Ag} \approx 2.3$ eV) is above the $X^0$ energy, while it is below for gold ($\epsilon_H^{Au} \approx 1$ eV).

One can resume these observations as follows. At an acquisition voltage of $V$ = +2.5V (resp. $V$ = -2.5V), the transport is mainly occurring through the LUMO channel (resp. HOMO). Therefore, an important part of the overall tunneling electrons will have an energy of around $\epsilon_L$ (resp. $|\epsilon_H|$). These electrons will be able to participate in the fluorescence excitation only if their energy (*i.e* the orbital energy) is greater than the fluorescence energy.

Note that these observations are compatible with a recent mechanism [80, 16], which consider that the $X^0$ emission (at negative voltage) results from a two-step excitation process. In a first step, when the Fermi level of the tip becomes resonant with the HOMO orbital, an electron can be extracted from the molecule (Fig. 5.7(d)). Consequently, the molecule becomes positively charged which induce a shift towards lower energy of the LUMO orbital, due to a reorganization of the electronic structure. Due to this shift, the Fermi level of the sample may be resonant with the LUMO, and then an electron may be injected in this latter, leading to a creation of an electron-hole pair in the molecule. Even though it has not been proposed by the authors, one can imagine a similar situation at a positive voltage, where an electron injected in the LUMO induce a shift of the HOMO towards the higher energy, which allows extracting an electron from the HOMO to build the electron-hole pair (Fig. 5.7(e)). In this picture, the shift of the LUMO (resp. HOMO) towards the Fermi level of the sample $E_F$ (resp. tip) at negative voltage (resp. positive) is facilitated by the fact that the LUMO (resp. HOMO) is already shifted towards $E_F$ on silver (resp. gold). Therefore, it is consistent with the observation of a strong $X^0$ line at negative voltage (resp. positive) on silver (resp. gold). However, one can still stress that in this picture the shift of the LUMO (resp. HOMO) always corresponding to the value needed to be resonant with the Fermi level of the sample (resp. tip).

Alternatively, one can imagine another mechanism which does not necessarily need this *ad hoc* shift. This mechanism relies on the following considerations. First, it has been demonstrated in many studies [16, 49, 20, 57, 29] that when the transport is not dominated by tunneling through orbital channel (*i.e* at $e|V| < \epsilon_L$, $|\epsilon_H|$ ), an inelastic electron can effectively excite the molecule fluorescence (ET mechanism). Second, once the transport is dominated by a molecular orbital channel, the fluorescence is observed only if this channel allows electrons to have an energy higher than the fluorescence line.
In this mechanism, electrons participating to the transport through a molecular orbital may undergo an inelastic transition which will resonantly excite the optical transition of the molecule (Fig. 5.7(f) and (g)). Since the transport is dominated by this selective orbital channel, the amount of inelastic electrons able to excite the fluorescence are significantly increased compare to the case where the transport through the orbital channel cannot occur ($e|V| < \epsilon_L$, $|\epsilon_H|$), which may explain the different intensity regime observed between these two situations.

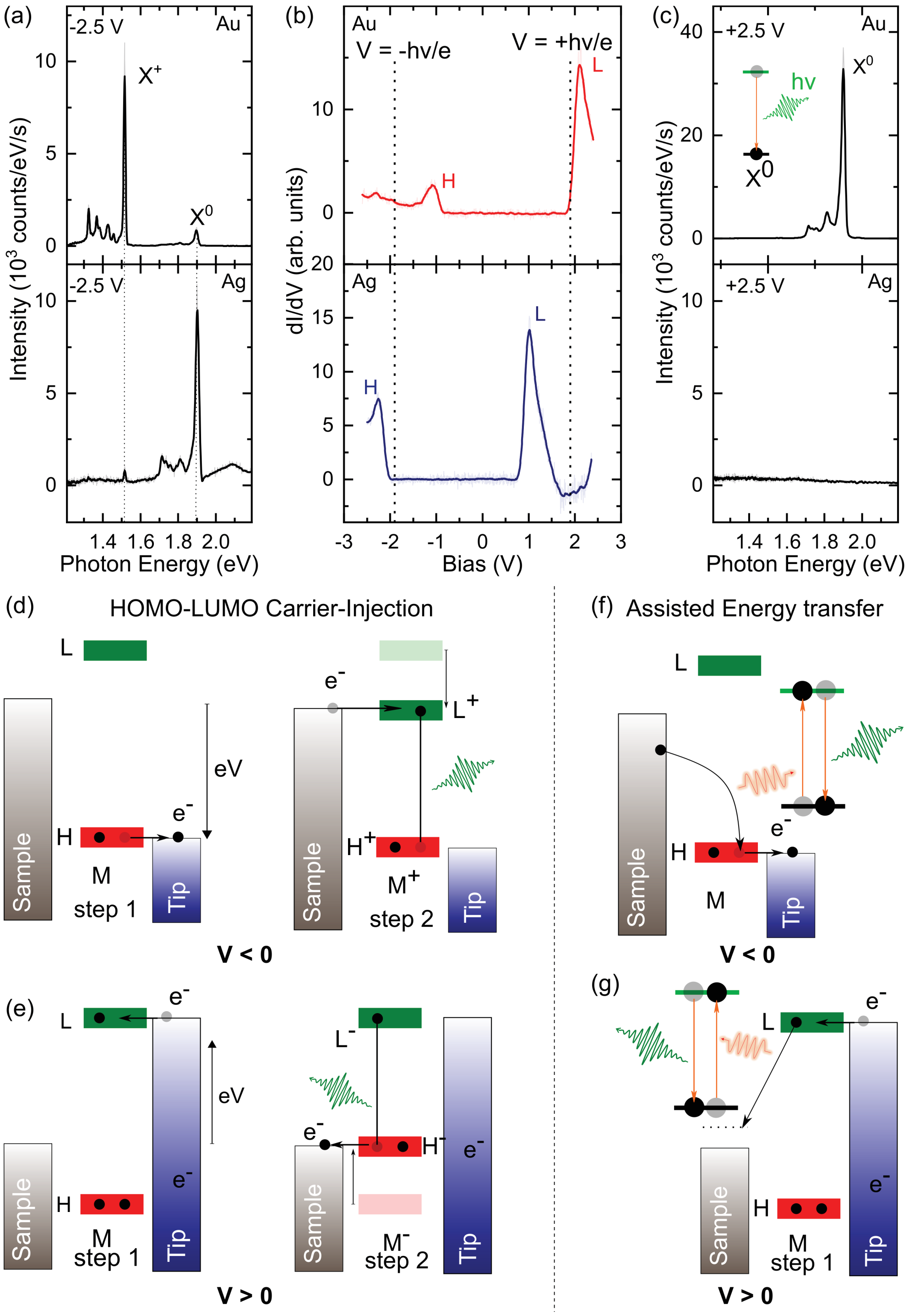

**Figure 5.7: Emission regimes as a function of the voltage polarity** (a) STM-F spectra at negative voltage ($V$ = -2.5 V), recorded for a molecule adsorbed on a three layers NaCl on Au(111) and Ag(111). (b) $dI/dV$ spectra for Au(111) and Ag(111). The dashed lines highlight the respective energy position of the molecular orbitals compare to the fluoresence energy ($X^0$ line). (c) STM-F spectra recorded at positive voltage ($V$ = + 2.5 V) on Au(111) and Ag(111). (d) and (e) Sketches depicting the carrier-injection mechanism [16, 79] involving an energy shift of the LUMO or the HUMO upon charging. (f) and (g) Sketches depicting an assisted energy transfer when one of the electrons participating to the transport through a molecular orbital transfer its energy to excite the molecular fluorescence.

### 5.3.3 Plasmon-exciton coupling

To have a complete picture of the excitation mechanism, here we investigate the evolution of the $X^0$ and $X^+$ contributions as a function of the tip-molecule lateral distance. Fig. 5.8(a) and (b) presents a sketch of the experiments where a series of STM-F spectra are recorded by progressively approaching the tip laterally to the molecule. At negative voltage (Fig. 5.8(c)), Fano resonances at the energy of the $X^0$ contribution [33] are observed once the tip is located at a distance $< 0.5$ nm of the molecule edge. Such features have been also reported in other STM-F experiments (see paragraph 2.3.2 in chapter 2) [50, 134, 57], and are a signature of the plasmon-exciton coupling. Interestingly, except for a small variation of the peak shape, this contribution does not change substantially when the tip is moved above the molecule. Unlike the observations reported by Imada *et al.* [50], the intensity of the $X^0$ contribution does not increase drastically. Conversely, the $X^+$ contribution is only observable once the tip is located above the molecule. These observations show that even though the NCP-exciton coupling is observable in the spectrum when the tip is not located directly above the molecule, the charging process can occur only if an electron tunnels from the molecule to the tip, which needs an overlap between the tip and molecule orbitals. Additionally, one can point out that this result is another confirmation that the $X^+$ contribution corresponds to the ZnPc$^+$ fluorescence.

Eventually, we performed the same measurement at a negative voltage (Fig. 5.8(d)). Interestingly, the $X^0$ contribution is only observed once a direct overlap between the tip and molecule is possible. This suggests that the "at distance" plasmon-exciton coupling, such the one observed at negative voltage, does not occur in this case. This observation is extremely surprising because if one can understand that a direct excitation needs specific conditions, such as energy level alignment (see 5.3.2), it should not be the case for a plasmon-induced excitation [20, 50, 134, 57, 26, 108].

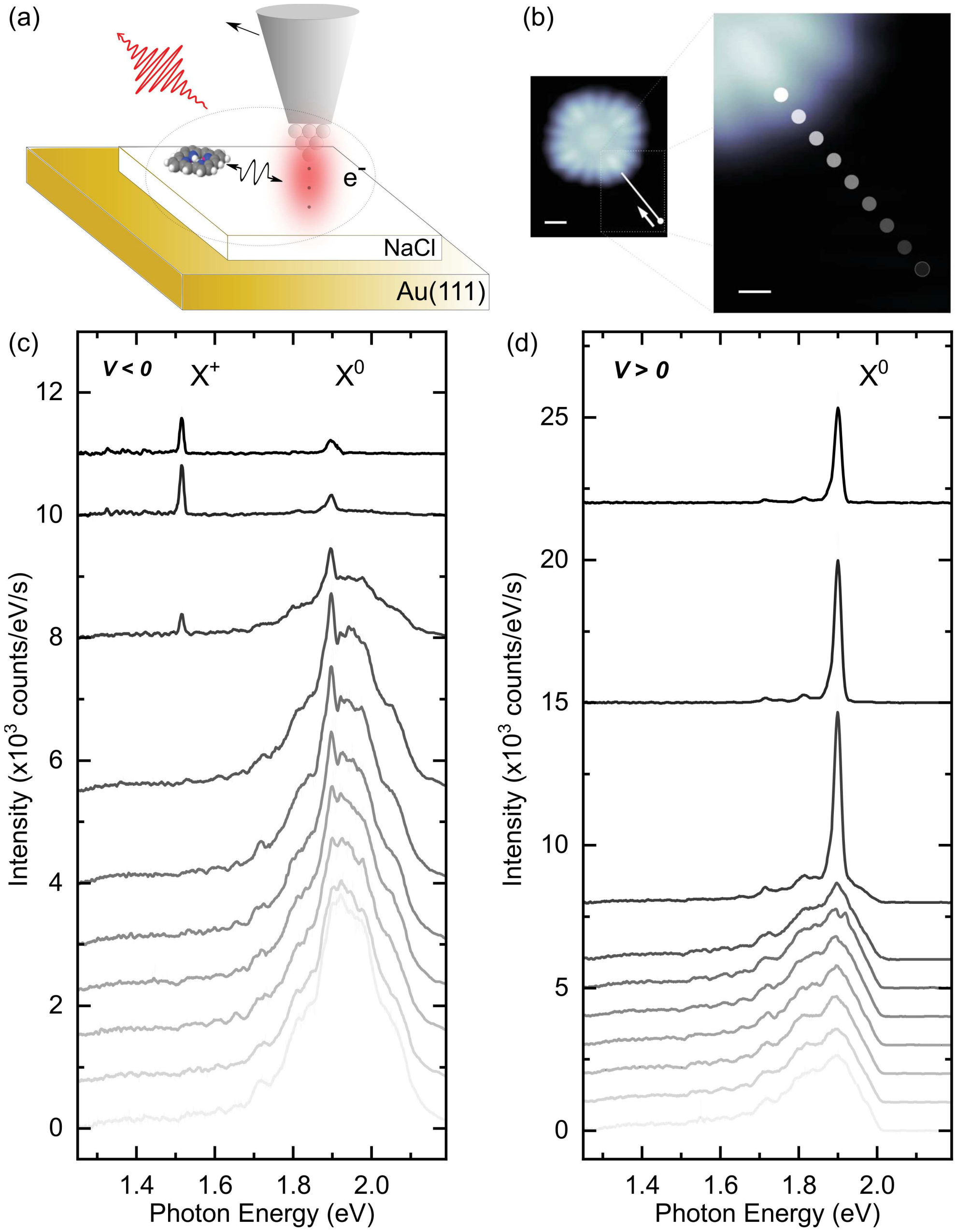

**Figure 5.8: Evolution of the plasmon-exciton coupling as a function of the tip-molecule lateral distance.** (a) Sketch of the experiment. (b) STM images ($V$ = -2.5 V; $I$ = 30 pA) where are indicated the acquisition positions of the STM-F spectra of (c) and (d). (c) Series of STM-F spectra recorded at the position indicated in (b) at negative voltage ($V$ = -2.5 V; $I$ = 180 pA; $t$ = 180 s). (d) Series of STM-F spectra recorded at the position indicated in (b) at positive voltage ($V$ = + 2 V; $I$ = 60 pA; $t$ = 180s).

### 5.3.4 General mechanism

The previous investigation of this section has highlighted not less than five different behaviours in the luminescence properties of a single ZnPc molecule in an STM junction :

- The $X^0$ contribution intensity on silver has a slightly super-linear current dependency, that we attributed to a one-electron process slightly affected by the decay probability which varies as a function of the tip-molecule vertical distance.
- The $X^+$ contribution intensity on gold has a slightly super-quadratic current dependency, that we attributed to a two-electrons process.
- The $X^0$ contribution intensity on gold has also a slightly super-quadratic current dependency, which cannot be explained so far.
- A remote excitation of $X^0$ contribution via the plasmon-exciton coupling when the tip is laterally away from the molecule.
- An intriguing suppression of this plasmon-exciton coupling at positive voltage.

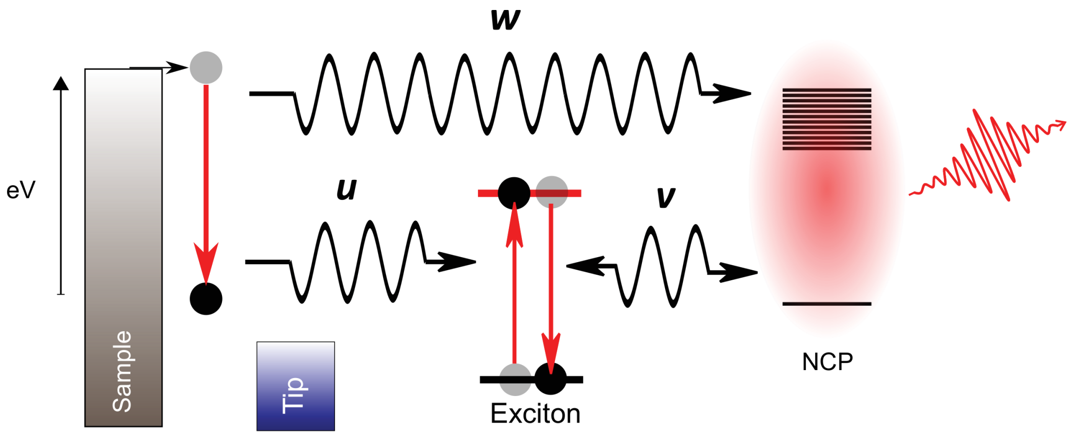

**Figure 5.9: Phenomenological model**

Giving a universal luminescence mechanism is complicated. One can propose a phenomenological model (Fig. 5.9) taking into account the above observations. This model is described by three coupling constant which parametrically depends on several parameters describing the total system: $\{$ molecule + NCP + tunneling electrons $\}$.

- The constant **u** which described the interaction between the tunneling electrons and the molecule. This constant depends on the respective position of the tip with respect to the molecule. This distance dependency could results from two aspects: the needed spatial overlap between the molecule and tip orbitals if we consider a carrier injection mechanism or the range of the dipole-dipole interaction if we consider a direct energy transfer between the inelastic electron and the molecule. **u** depends also on the alignment of the energy level of the molecule in the junction with respect to those of the electrodes (spectral overlap). Finally, it also possibly depends on the transition dipole moment associated with the molecule and the inelastic electrons if we consider a direct energy transfer mechanism. One cannot exclude also an effect of the NCP modes density on this process.

- The constant **w** which described the interaction between inelastic electrons and the NCP modes of the STM junction. This essentially depends on the density of NCP modes in the junction, and the transition dipole moment associated with the inelastic transition.
- The constant **v** which described the coupling between the exciton and the NCP. If it plays a role essentially on the emission where the tip is located on the molecule, it also plays a role on the excitation when the tip is located away from the molecule. Moreover, one cannot exclude an effect on the excitation where the tip is located above the molecule. This constant depends on the transition dipole moment of the molecule, the density of NCP modes, the distance between the molecule and the tip (in the three directions of space), and the polarity of the voltage.

Finally, the position of the molecule in the STM junction will strongly modify the ratio between the different coupling constant. One can distinguish two regimes. A first regime, where the tip is above the molecule (where **u**, **v** are strong compare to **w**). And a second regime, where the tip is outside of the molecule (where **u** becomes negligible compared to **w**, and **v**).

This change of regime is well illustrated in Fig. 5.8(b) where we pass from a broadband emission spectrum dominated by the NCP, outside of the molecule, to a flat spectrum without NCP contributions, dominated by the molecular emission once the tip is above the molecule.

## Conclusion

In this chapter, we carried out STM-F spectroscopy experiments on single ZnPc molecules adsorbed on a NaCl/Au(111) sample. STM-F spectra recorded on a single ZnPc molecule reveal an emission line attributed to the fluorescence emission of the molecule and a more intense emission line in the lower energy region. Based on a comparison with literature and a study of the STM-F spectra as a function of the voltage polarity, this emission line is attributed to the fluorescence of the radical cation of ZnPc. STM-F spectroscopy allows obtaining a vibronic spectrum of the charged molecule. A comparison with the one of the neutral molecule shows substantial differences in terms of respective intensity. This shows that an unambiguous chemical fingerprint of the two single-molecule redox states can be obtained with STM-F spectroscopy. Furthermore, control of the lifetime of the charged molecule and the radiative decay probability probabilities of the molecule is performed by tuning, respectively, the insulator thickness and the plasmonic response of the STM junction. A comparative study between gold and silver substrate, for the light intensity of both redox states contributions as a function of voltage and current, is realized to investigate the excitation mechanism. It appears that the orbitals frontiers energy level alignment with respect to the Fermi levels of the electrodes plays an important role in the excitation of both contributions. Moreover, depending on the substrate different excitation mechanism seems to be involved for the neutral molecule fluorescence excitation. Besides, an investigation of the plasmon-exciton coupling as a function of the tip-molecule lateral distance, reveals a voltage polarity of the at-distance plasmon-exciton coupling. Eventually, the experimental observations are resumed in a generic phenomenological luminescence mechanism.

Finally, our method provides a way to address the interplay between the redox states and the optical properties of a single molecule, with atomic-scale precision. This capability may be highly valuable in the elucidation of energy conversion mechanisms, involving light-driven redox reaction, such as those implicated in the photosynthesis or photo-voltaic cells.

# Conclusion

When I arrived in the team as a fresh master student, only a few experiments of single molecules luminescence induced by STM were reported in the literature [92, 15, 65, 96, 20]. Due to the difficulty to assign luminescence spectra with available spectroscopic data, a wide range of questions were unsolved. The experimental configuration using NaCl as an insulator, developed by Zhang *et al.* [129], has allowed a big step forward in the understanding of STM-Induced light emission from single molecules experiments. Especially, for the first time, an unambiguous single-molecule fluorescence signal could be obtained in a highly controllable environment.

However, if we consider the possibility to effectively obtain an optical spectrum at the molecular, and even the sub-molecular level, an inevitable question arises: What is the physical meaning of an optical spectrum at this scale? This question was central during my PhD and has to lead the works presented in this manuscript.

The first experimental chapter is probably the most fundamental one to understand this central question. The experiments presented in this chapter have been carried out on single $H_2Pc$ molecules decoupled from an Ag(111) surface by a thin layer of NaCl. By addressing precisely with the STM tip different sub-part of a single molecule, a duplication of its main fluorescence lines is observed. A spatial mapping of these lines, that we term Hyper-Resolved Fluorescence Microscopy, is performed and reveal a "dipole-like" patterns directed along one of the molecular axes. A theoretical model taking into account the novel concept of picocavity, where the last atoms of the STM tip apex allow to confine the plasmonic modes of the STM junction in a scale much smaller than the molecule size, is used to reproduce the experimental maps. The excellent agreement between the HRFM maps and the theory, first confirms the existence of such a picocavity in our STM junction, and second, gives an unprecedented insight in the understanding of the physical origin of the spatial resolution achieved in STM-F experiments. This resolution relies essentially on the close to atomic-scale modulation of the emission efficiency, due to the coupling between the molecular transition dipole moment, and the plasmonic modes confined in the picocavity. This shows that HRFM, more than an exotic technique using electron rather than photon to excite the fluorescence, can be considered as an optical microscopy technique with close to atomic-scale resolution. Thanks to the optical images provided by this microscopy, the duplicated lines observed in the STM-F spectra can be attributed to the fluorescence emission of the two tautomers of the $H_2Pc$ molecule. A temporal analysis of the fluorescence signal of each tautomer is carried out, to perform a complete tracking of the tautomerization dynamic. Finally, a mechanism of tautomerization involving the excitonic state of the molecule is proposed.

With the knowledge acquired regarding the origin of the sub-molecular variation observed in the STM-F spectra, the second experimental chapter proposes to investigate the lower energy region of the fluorescence spectrum. As the lines observed in this region are associated with specific vibrational modes of the molecule, such spectra are usually considered as a chemical fingerprint of the probed species. This chemical signature is usually addressed by Raman or low-temperature fluorescence spectroscopy, over a large number of molecules where the individual molecular fingerprint is diluted in the averaged signal. Obtaining such fingerprint at the single-molecule level, and even the sub-molecular level is motivated by two considerations. First, since the vibrational modes of a molecule are extremely sensitive to subtle variation of the molecular structure, the vibronic spectrum of a molecule can act as an effective probe of its local environment. Second, from a fundamental point of view, addressing the vibronic spectrum of a sub-part of a molecule rises intriguing questions about the physical meaning of a chemical fingerprint at this scale. The experiments presented in this chapter are carried out on ZnPc molecules decoupled from an Ag(111) surface by a thin layer of NaCl. STM-F spectroscopy realized on linear arrangements of individual molecules reveals a narrowing of the main emission line, due to the inter-molecular dipole-dipole coupling, which allows observing a well-resolved series of peaks. Based on a comparison with spectroscopic data available on this molecule, these peaks are assigned to vibronic emission of the ZnPc molecule. This shows that a chemical fingerprint can be obtained without light excitation and at the single-molecule level. HRFM maps of these vibronic lines, reveals a pattern specific to the corresponding vibrational mode symmetry, and which is different from the pattern observed for the main emission lines. This result demonstrates that a vibronic fingerprint, which is often considered as a signature of the probed species, varies when we address sub-part of the molecule. Finally, these observations are rationalized in the framework of the vibronic coupling theory. In this framework, the molecular vibration affects the electronic structure of the molecule, and thus slightly modify the first excited state of the molecule. This new excited state can be built on a linear combination of higher energy excited states of the molecule. Therefore, the transition dipole moment associated with a vibronic transition carries the character of the transition dipole moments associated with transitions from higher excited states, which is revealed in the vibronic HRFM maps patterns.

The third experimental chapter proposes to investigate the interplay between the redox states of a single molecule and its optical properties, which is a key step in the understanding of energy transfer mechanisms at play in biological phenomenon such as photosynthesis, or in technology such as organic photovoltaic cells. The experiments of this chapter are carried out on single ZnPc molecules adsorbed on a NaCl/Au(111) substrate. STM-F spectra recorded on a single molecule reveal two emission lines. The first emission lines, already observed on an Ag(111) substrate in the previous chapter, correspond to the fluorescence of the ZnPc molecule. Based on a comparison with spectroscopic data available in the literature, and a study of the STM-F spectra as a function of the voltage polarity, this second line which is sharper, and more intense is attributed to the fluorescence of the radical cation of the ZnPc molecule. Vibronic spectroscopy is used to obtain a chemical fingerprint of the charged molecule, which is significantly different from the neutral one. By tuning, respectively, the NaCl layer thickness and the STM nanocavity plasmonic response, complete control of the respective emission of both redox states is performed. A detailed analysis of the different parameters impacting the fluorescence emission of both redox species is carried out to identify the different excitation mechanisms. Finally, the mechanism is more generally discuss for the case of the neutral fluorescence to attempt providing a bigger picture of the STM-F experiments on single molecules.

From a fundamental point of view, the works performed in the framework of this thesis, allowed to investigate the light-matter interaction processes at a scale forsaken by conventional optical methods. We could explain how and why a single-molecule optical spectrum, especially its vibronic part, varies when we address a sub-part of the molecule. From a more applied point of view, we showed that HRFM together with temporal measurement is a valuable tool to follow the dynamic of simple chemical reaction such as the prototypical tautomerization reaction presented in this thesis. In another hand, the capability to control the redox properties of a single-molecule and in the same time probe its optical response may find application in the elucidation of energy conversion mechanism involving light-driven redox reaction, at play in processes such as photosynthesis.

Finally, the essence of Hyper-Resolved Fluorescence Microscopy is contained in the unique capability to confine, and control light with a close to atomic-scale precision in an entirely known environment. This capability will be extremely valuable in the growing field of nanophotonic, and we can predict future adaptation on this experimental approach with purely optical excitation source without any losses of spatial resolution. On the other hand, using electrons as an excitation source offers many possibilities. In particular, using functionalized tip such as magnetic tip [125] would allow accessing to the triplet state of the molecule. This possibility could help to obtain a better understanding of the interplay between fluorescence and phosphorescence process at the atomic scale.

# Bibliography

[1] P. Audebert and F. Miomandre. “Electrofluorochromism: from molecular systems to set-up and display”. In: *Chem. Sci.* 4 (2013), p. 575.

[2] M. Barbry et al. “Atomistic near-field nanoplasmonics: Reaching atomic-scale resolution in nanooptics”. In: *Nano Letters* 15.5 (2015), pp. 3410–3419. ISSN: 15306992. DOI: `10.1021/acs.nanolett.5b00759`.

[3] J. Bardeen. “Tunnelling from a Many-Particle Point of View”. In: *Phys. Rev. Lett.* 6 (2 Jan. 1961), pp. 57–59. DOI: `10.1103/PhysRevLett.6.57`. URL: `https://link.aps.org/doi/10.1103/PhysRevLett.6.57`.

[4] R. Berndt et al. “Photon Emission at Molecular Resolution Induced by a Scanning Tunneling Microscope”. In: *Science* 262.5138 (1993), pp. 1425–1427. DOI: `10.1126/science.262.5138.1425`. eprint: `https://science.sciencemag.org/content/262/5138/1425.full.pdf`. URL: `https://science.sciencemag.org/content/262/5138/1425`.

[5] Richard Berndt. “Photon Emission From the Scanning Tunneling Microscope”. 1992, p. 0.

[6] Richard Berndt, James K. Gimzewski, and Peter Johansson. “Inelastic tunneling excitation of tip-induced plasmon modes on noble-metal surfaces”. In: *Phys. Rev. Lett.* 67 (27 Dec. 1991), pp. 3796–3799. DOI: `10.1103/PhysRevLett.67.3796`. URL: `https://link.aps.org/doi/10.1103/PhysRevLett.67.3796`.

[7] Schrader Bernhard. *Infrared and Raman spectroscopy, Methods and applications.* Wiley, 1995.

[8] G. Binnig et al. “7 × 7 Reconstruction on Si(111) Resolved in Real Space”. In: *Phys. Rev. Lett.* 50 (2 Jan. 1983), pp. 120–123. DOI: `10.1103/PhysRevLett.50.120`. URL: `https://link.aps.org/doi/10.1103/PhysRevLett.50.120`.

[9] G. Binnig et al. “Surface Studies by Scanning Tunneling Microscopy”. In: *Phys. Rev. Lett.* 49 (1 July 1982), pp. 57–61. DOI: `10.1103/PhysRevLett.49.57`. URL: `https://link.aps.org/doi/10.1103/PhysRevLett.49.57`.

[10] M G Blaber, M D Arnold, and M J Ford. “A review of the optical properties of alloys and intermetallics for plasmonics”. In: *Journal of Physics: Condensed Matter* 22.14 (Mar. 2010), p. 143201. DOI: `10.1088/0953-8984/22/14/143201`. URL: `https://doi.org/10.1088%2F0953-8984%2F22%2F14%2F143201`.

[11] Jose Manuel Blanco et al. “First-principles simulations of STM images: From tunneling to the contact regime”. In: *Phys. Rev. B* 70 (8 Aug. 2004), p. 085405. DOI: `10.1103/PhysRevB.70.085405`. URL: `http://link.aps.org/doi/10.1103/PhysRevB.70.085405`.

[12] Hannes Böckmann et al. “Near-Field Enhanced Photochemistry of Single Molecules in a Scanning Tunneling Microscope Junction”. In: *Nano Lett.* 18.1 (2018), pp. 152–157. DOI: `10.1021/acs.nanolett.7b03720`. eprint: `https://doi.org/10.1021/acs.nanolett.7b03720`. URL: `https://doi.org/10.1021/acs.nanolett.7b03720`.

[13] Nadezda A. Brazhe et al. “In Situ Raman Study of Redox State Changes of Mitochondrial Cytochromes in a Perfused Rat Heart”. In: *PLOS ONE* 8.8 (Aug. 2013), pp. 1–9. DOI: `10.1371/journal.pone.0070488`. URL: `https://doi.org/10.1371/journal.pone.0070488`.

[14] By R Hanbury Brown. “Correlation between Photons in two Coherent Beams of Light”. In: *Nature* 27 (1956), pp. 27–29.

[15] Chi Chen et al. “Viewing the Interior of a Single Molecule: Vibronically Resolved Photon Imaging at Submolecular Resolution”. In: *Phys. Rev. Lett.* 105 (21 Nov. 2010), p. 217402. DOI: `10.1103/PhysRevLett.105.217402`. URL: `https://link.aps.org/doi/10.1103/PhysRevLett.105.217402`.

[16] Gong Chen et al. “Spin-Triplet-Mediated Up-Conversion and Crossover Behavior in Single-Molecule Electroluminescence”. In: *Phys. Rev. Lett.* 122 (17 May 2019), p. 177401. DOI: `10.1103/PhysRevLett.122.177401`. URL: `https://link.aps.org/doi/10.1103/PhysRevLett.122.177401`.

[17] Gong Chen et al. “Spin-Triplet-Mediated Up-Conversion and Crossover Behavior in Single-Molecule Electroluminescence”. In: *Phys. Rev. Lett.* 122 (17 May 2019), p. 177401. DOI: `10.1103/PhysRevLett.122.177401`. URL: `https://link.aps.org/doi/10.1103/PhysRevLett.122.177401`.

[18] J. C. Chen. *Introduction to Scanning Tunneling Microscopy*. Oxford Science Publications, 2008.

[19] Rohit Chikkaraddy et al. “Single-molecule strong coupling at room temperature in plasmonic nanocavities”. In: *Nature* 535.7610 (2016), pp. 127–130. ISSN: 14764687. DOI: `10.1038/nature17974`. URL: `http://dx.doi.org/10.1038/nature17974`.

[20] Michael C. Chong et al. “Narrow-Line Single-Molecule Transducer between Electronic Circuits and Surface Plasmons”. In: *Phys. Rev. Lett.* 116 (3 Jan. 2016), p. 036802. DOI: `10.1103/PhysRevLett.116.036802`. URL: `https://link.aps.org/doi/10.1103/PhysRevLett.116.036802`.

[21] Michael C. Chong et al. “Ordinary and Hot Electroluminescence from Single-Molecule Devices: Controlling the Emission Color by Chemical Engineering”. In: *Nano Letters* 16.10 (2016). PMID: 27652517, pp. 6480–6484. DOI: `10.1021/acs.nanolett.6b02997`. URL: `https://doi.org/10.1021/acs.nanolett.6b02997`.

[22] Michael C. Chong et al. “Ordinary and Hot Electroluminescence from Single-Molecule Devices: Controlling the Emission Color by Chemical Engineering”. In: *Nano Letters* 16.10 (2016). PMID: 27652517, pp. 6480–6484. DOI: `10.1021/acs.nanolett.6b02997`. eprint: `https://doi.org/10.1021/acs.nanolett.6b02997`. URL: `https://doi.org/10.1021/acs.nanolett.6b02997`.

[23] Emiliano Cortés et al. “Monitoring the Electrochemistry of Single Molecules by Surface-Enhanced Raman Spectroscopy”. In: *J. Am. Chem. Soc.* 132 (2010), p. 18034.

[24] M. F. Cromie, C. P. Lutz, and D. M. Eigler. “Confinement of electrons to quantum corrals on a metal surface”. In: *Science* 262 (0 Jan. 1993), pp. 218–220. DOI: `10.1126/science.262.5131.218`. URL: `https://doi.org/10.1126/science.262.5131.218`.

[25] W. Deng et al. “STM-induced photon emission from self-assembled porphyrin molecules on a Cu(100) surface”. In: *The Journal of Chemical Physics* 117.10 (2002), pp. 4995–5000. DOI: `10.1063/1.1498471`. eprint: `https://doi.org/10.1063/1.1498471`. URL: `https://doi.org/10.1063/1.1498471`.

[26] Z. C. Dong et al. “Generation of molecular hot electroluminescence by resonant nanocavity plasmons”. In: *Nature Photonics* 4.1 (2010), pp. 50–54. DOI: `10.1038/nphoton.2009.257`. URL: `http://dx.doi.org/10.1038/nphoton.2009.257`.

[27] Z.-C. Dong et al. “Tunneling electron induced photon emission from monolayered H2TBP porphyrin molecules on Cu(100)”. In: *Surface Science* 532-535 (2003), pp. 237–243. ISSN: 0039-6028. DOI: `https://doi.org/10.1016/S0039-6028(03)00162-6`. URL: `http://www.sciencedirect.com/science/article/pii/S0039602803001626`.

[28] Benjamin Doppagne et al. “Electrofluorochromism at the single-molecule level”. In: *Science* 361.6399 (2018), pp. 251–255. ISSN: 0036-8075. DOI: `10.1126/science.aat1603`. URL: `https://science.sciencemag.org/content/361/6399/251`.

[29] Benjamin Doppagne et al. “Vibronic Spectroscopy with Submolecular Resolution from STM-Induced Electroluminescence”. In: *Phys. Rev. Lett.* 118 (12 Mar. 2017), p. 127401. DOI: `10.1103/PhysRevLett.118.127401`. URL: `https://link.aps.org/doi/10.1103/PhysRevLett.118.127401`.

[30] L. Douillard and F. Charra. “High-resolution mapping of plasmonic modes: photoemission and scanning tunneling mluminescence microscopies”. In: *J. Phys D: Appl. Phys* 568.44 (2011), p. 464002.

[31] A. Eisfeld and J.S. Briggs. “The J- and H-bands of organic dye aggregates”. In: *Chemical Physics* 324.2 (2006), pp. 376–384. ISSN: 0301-0104. DOI: `https://doi.org/10.1016/j.chemphys.2005.11.015`. URL: `http://www.sciencedirect.com/science/article/pii/S030101040500563X`.

[32] I. Ekvall et al. “Preparation and characterization of electrochemically etched W tips for STM”. In: *Measurement Science and Technology* 10 (11 Nov. 1999), p. 0. DOI: 10.1088/0957-0233/10/1/006. URL: https://iopscience.iop.org/article/10.1088/0957-0233/10/1/006.

[33] U. Fano. “Effects of Configuration Interaction on Intensities and Phase Shifts”. In: *Phys. Rev.* 124 (6 Dec. 1961), pp. 1866–1878. DOI: 10.1103/PhysRev.124.1866. URL: https://link.aps.org/doi/10.1103/PhysRev.124.1866.

[34] Shadi Fatayer et al. “Molecular structure elucidation with charge-state control”. In: *Science* 365.6449 (2019), pp. 142–145. ISSN: 0036-8075. DOI: 10.1126/science.aax5895. eprint: https://science.sciencemag.org/content/365/6449/142.full.pdf. URL: https://science.sciencemag.org/content/365/6449/142.

[35] Shadi Fatayer et al. “Reorganization energy upon charging a single molecule on an insulator measured by atomic force microscopy”. In: *Nature Nanotechnology* doi.org/10.1038/s41565-018-0087-1 (2018). DOI: https://doi.org/10.1038/s41565-018-0087-1.

[36] I. Fernández-Torrente et al. “Gating the Charge State of Single Molecules by Local Electric Fields”. In: *Phys. Rev. Lett.* 108 (3 Jan. 2012), p. 036801. DOI: 10.1103/PhysRevLett.108.036801. URL: https://link.aps.org/doi/10.1103/PhysRevLett.108.036801.

[37] G. Fisher. *Vibronic Coupling : The interaction between the Electronic and Nuclear Motions*. Academic Press, London, 1984.

[38] A. Fragner et al. “Resolving Vacuum Fluctuations in an Electrical Circuit by Measuring the Lamb Shift”. In: *Science* 322.5906 (2008), pp. 1357–1360. ISSN: 0036-8075. DOI: 10.1126/science.1164482. eprint: https://science.sciencemag.org/content/322/5906/1357.full.pdf. URL: https://science.sciencemag.org/content/322/5906/1357.

[39] M. J. Frisch et al. “Gaussian 09 Revision D.01”. In: (). Gaussian Inc. Wallingford CT 2009.

[40] D. J. Gardiner and P. R. Graves. *Practical Raman Spectroscopy*. Springer-Verlag. ISBN 978-0387502540., 1989.

[41] J. K. Gimzewski et al. “Photon emission with the scanning tunneling microscope”. In: *Zeitschrift für Physik B Condensed Matter* 72.4 (Dec. 1988), pp. 497–501. DOI: 10.1007/BF01314531. URL: https://doi.org/10.1007/BF01314531.

[42] Leo Gross. “Recent advances in submolecular resolution with scanning probe microscopy”. In: *Nature Chemistry* 3.4 (2011), pp. 273–278. ISSN: 17554330. DOI: 10.1038/nchem.1008.

[43] Leo Gross et al. “Measuring the Charge State of an Adatom with Non-contact Atomic Force Microscopy”. In: *Science* 324.5933 (2009), pp. 1428–1431. ISSN: 0036-8075. DOI: 10.1126/science.1172273. eprint: https://science.sciencemag.org/content/324/5933/1428.full.pdf. URL: https://science.sciencemag.org/content/324/5933/1428.

[44] Christoph Große et al. “Dynamic control of plasmon generation by an individual quantum system”. In: *Nano Letters* 14.10 (2014), pp. 5693–5697. ISSN: 15306992. DOI: 10.1021/nl502413k.

[45] Christoph Große et al. “Nanoscale Imaging of Charge Carrier and Exciton Trapping at Structural Defects in Organic Semiconductors”. In: *Nano Letters* 16.3 (2016). PMID: 26871739, pp. 2084–2089. DOI: 10.1021/acs.nanolett.6b00190. URL: https://doi.org/10.1021/acs.nanolett.6b00190.

[46] S. Heidorn et al. “Influence of Substrate Surface-Induced Defects on the Interface State between NaCl(100) and Ag(111)”. In: *J. Phys. Chem. C* 117.31 (2013), pp. 16095–16103. DOI: 10.1021/jp405297h. eprint: https://doi.org/10.1021/jp405297h. URL: https://doi.org/10.1021/jp405297h.

[47] S. Heinze et al. “Prediction of bias-voltage-dependent corrugation reversal for STM images of bcc (110) surfaces: W(110), Ta(110), and Fe(110)”. In: *Phys. Rev. B* 58 (24 Dec. 1998), pp. 16432–16445. DOI: 10.1103/PhysRevB.58.16432. URL: https://link.aps.org/doi/10.1103/PhysRevB.58.16432.

[48] Caleb M. Hill, Daniel A. Clayton, and Shanlin Pan. “Combined optical and electrochemical methods for studying electrochemistry at the single molecule and single particle level: recent progress and perspectives”. In: *Phys. Chem. Chem. Phys.* 15 (48 2013), pp. 20797–20807. DOI: 10.1039/C3CP52756E. URL: http://dx.doi.org/10.1039/C3CP52756E.

[49] Hiroshi Imada et al. “Real-space investigation of energy transfer in heterogeneous molecular dimers”. In: *Nature* 538.7625 (2016), pp. 364–367. ISSN: 14764687. DOI: 10.1038/nature19765. URL: http://dx.doi.org/10.1038/nature19765.

[50] Hiroshi Imada et al. “Single-Molecule Investigation of Energy Dynamics in a Coupled Plasmon-Exciton System”. In: *Phys. Rev. Lett.* 119 (1 July 2017), p. 013901. DOI: 10.1103/PhysRevLett.119.013901. URL: https://link.aps.org/doi/10.1103/PhysRevLett.119.013901.

[51] Larkin P. J. *Infrared and Raman spectroscopy, Principles and spectral interpretation*. Elsevier, 1989.

[52] Wolfgang Kaim and Jan Fiedler. “Spectroelectrochemistry: the best of two worlds”. In: *Chem. Soc. Rev.* 38 (12 2009), pp. 3373–3382. DOI: 10.1039/B504286K. URL: http://dx.doi.org/10.1039/B504286K.

[53] J. G. Keizer, J. K. Garleff, and P. M. Koenraad. “Simple and efficient scanning tunneling luminescence detection at low-temprature.” In: *Review of Scientific Instruments* 80 (11 2099), p. 0. DOI: 10.1063/1.3274675. URL: https://aip.scitation.org/doi/10.1063/1.3274675.

[54] Kensuke Kimura et al. “Selective triplet exciton formation in a single molecule”. In: *Nature* 570.7760 (2019), pp. 210–213. DOI: 10.1038/s41586-019-1284-2. URL: http://dx.doi.org/10.1038/s41586-019-1284-2.

[55] Nagao Kobayashi et al. "Synthesis, Spectroscopy, and Electrochemistry of Tetra-tert-butylated Tetraazaporphyrins, Phthalocyanines, Naphthalocyanines, and Anthracocyanines, together with Molecular Orbital Calculations". In: *Chem. Eur. J.* 10.24 (2004), pp. 6294–6312. DOI: `10.1002/chem.200400275`. eprint: `https://onlinelibrary.wiley.com/doi/pdf/10.1002/chem.200400275`. URL: `https://onlinelibrary.wiley.com/doi/abs/10.1002/chem.200400275`.

[56] Jörg Kröger et al. "Fano Description of Single-Hydrocarbon Fluorescence Excited by a Scanning Tunneling Microscope". In: *Nano Lett.* 18.6 (2018), pp. 3407–3413. DOI: `10.1021/acs.nanolett.8b00304`. eprint: `https://doi.org/10.1021/acs.nanolett.8b00304`. URL: `https://doi.org/10.1021/acs.nanolett.8b00304`.

[57] Jörg Kröger et al. "Fano description of single-hydrocarbon fluorescence excited by a scanning tunneling microscope". In: *arXiv:1801.07143* (2018).

[58] Jens Kügel et al. "Remote Single-Molecule Switching: Identification and Nanoengineering of Hot Electron-Induced Tautomerization". In: *Nano Lett.* 17.8 (2017), pp. 5106–5112. DOI: `10.1021/acs.nanolett.7b02419`. eprint: `https://doi.org/10.1021/acs.nanolett.7b02419`. URL: `https://doi.org/10.1021/acs.nanolett.7b02419`.

[59] Klaus Kuhnke et al. "Atomic-Scale Imaging and Spectroscopy of Electroluminescence at Molecular Interfaces". In: *Chemical Reviews* 117.7 (2017). PMID: 28294599, pp. 5174–5222. DOI: `10.1021/acs.chemrev.6b00645`. eprint: `https://doi.org/10.1021/acs.chemrev.6b00645`. URL: `https://doi.org/10.1021/acs.chemrev.6b00645`.

[60] Takashi Kumagai et al. "Thermally and Vibrationally Induced Tautomerization of Single Porphycene Molecules on a Cu(110) Surface". In: *Phys. Rev. Lett.* 111 (24 Dec. 2013), p. 246101. DOI: `10.1103/PhysRevLett.111.246101`. URL: `https://link.aps.org/doi/10.1103/PhysRevLett.111.246101`.

[61] Barnes W. L., Dereux A., and Ebbesen T. "Surface plasmon subwavelength optics". In: *Nature* 0.424 (2003), pp. 824–830. DOI: `10.1038/nature01937`. URL: `https://www.nature.com/articles/nature01937`.

[62] V. P. LaBella et al. "Atomic Structure of the $\mathrm{GaAs}(001) - (2 \times 4)$ Surface Resolved Using Scanning Tunneling Microscopy and First-Principles Theory". In: *Phys. Rev. Lett.* 83 (15 Oct. 1999), pp. 2989–2992. DOI: `10.1103/PhysRevLett.83.2989`. URL: `https://link.aps.org/doi/10.1103/PhysRevLett.83.2989`.

[63] J. N. Ladenthin et al. "Force-induced tautomerization in a single molecule". In: *Nature Chem.* 8 (2016), p. 935.

[64] John Lambe and S. L. McCarthy. "Light Emission from Inelastic Electron Tunneling". In: *Phys. Rev. Lett.* 37 (14 Oct. 1976), pp. 923–925. DOI: `10.1103/PhysRevLett.37.923`. URL: `https://link.aps.org/doi/10.1103/PhysRevLett.37.923`.

[65] Joonhee Lee et al. "Vibronic Motion with Joint Angstrom–Femtosecond Resolution Observed through Fano Progressions Recorded within One Molecule". In: *ACS Nano* 8.1 (2014). PMID: 24261832, pp. 54–63. DOI: `10.1021/nn405335h`. eprint: `https://doi.org/10.1021/nn405335h`. URL: `https://doi.org/10.1021/nn405335h`.

[66] Joonhee Lee et al. "Visualizing vibrational normal modes of a single molecule with atomically confined light". In: *Nature* 568.7750 (2019), pp. 78–82. DOI: `10.1038/s41586-019-1059-9`.

[67] Thomas Leoni et al. "Controlling the Charge State of a Single Redox Molecular Switch". In: *Phys. Rev. Lett.* 106 (21 May 2011), p. 216103. DOI: `10.1103/PhysRevLett.106.216103`. URL: `https://link.aps.org/doi/10.1103/PhysRevLett.106.216103`.

[68] Peter Liljeroth, Jascha Repp, and Gerhard Meyer. "Current-Induced Hydrogen Tautomerization and Conductance Switching of Naphthalocyanine Molecules". In: *Science* 317.5842 (2007), pp. 1203–1206. ISSN: 0036-8075. DOI: `10.1126/science.1144366`. eprint: `https://science.sciencemag.org/content/317/5842/1203.full.pdf`. URL: `https://science.sciencemag.org/content/317/5842/1203`.

[69] Markus Lippitz, Florian Kulzer, and Michel Orrit. "Statistical Evaluation of Single Nano-Object Fluorescence". In: *ChemPhysChem* 6 (2005), p. 770.

[70] Zhongqiang Liu et al. "Theoretical investigation of the molecular, electronic structures and vibrational spectra of a series of first transition metal phthalocyanines". In: *Spectrochim. Acta A* 67.5 (2007), pp. 1232–1246. ISSN: 1386-1425. DOI: `http://dx.doi.org/10.1016/j.saa.2006.10.013`. URL: `http://www.sciencedirect.com/science/article/pii/S138614250600583X`.

[71] Brahim Lounis and Michel Orrit. "Single-photon sources". In: *Reports on Progress in Physics* 68.5 (Apr. 2005), pp. 1129–1179. DOI: `10.1088/0034-4885/68/5/r04`. URL: `https://doi.org/10.1088%2F0034-4885%2F68%2F5%2Fr04`.

[72] Boris Luk'Yanchuk et al. "The Fano resonance in plasmonic nanostructures and metamaterials". In: *Nature Materials* 9.9 (2010), pp. 707–715. ISSN: 14764660. DOI: `10.1038/nmat2810`. URL: `http://dx.doi.org/10.1038/nmat2810`.

[73] Yang Luo et al. "Electrically Driven Single-Photon Superradiance from Molecular Chains in a Plasmonic Nanocavity". In: *Phys. Rev. Lett.* 122 (23 June 2019), p. 233901. DOI: `10.1103/PhysRevLett.122.233901`. URL: `https://link.aps.org/doi/10.1103/PhysRevLett.122.233901`.

[74] John Mack, Nagao Kobayashi, and Martin J. Stillman. "Magnetic circular dichroism spectroscopy and TD-DFT calculations of metal phthalocyanine anion and cation radical species". In: *Journal of Porphyrins and Phthalocyanines* 10.10 (2006), pp. 1219–1237. DOI: `10.1142/S1088424606000594`. eprint: `http://www.worldscientific.com/doi/pdf/10.1142/S1088424606000594`. URL: `http://www.worldscientific.com/doi/abs/10.1142/S1088424606000594`.

[75] Kazuyuki Meguro et al. “Origin of multiple peaks in the light emission spectra of a Au(111) surface induced by the scanning tunneling microscope”. In: *Phys. Rev. B* 65 (16 Apr. 2002), p. 165405. DOI: 10.1103/PhysRevB.65.165405. URL: https://link.aps.org/doi/10.1103/PhysRevB.65.165405.

[76] P. Merino et al. “Exciton dynamics of C 60 -based single-photon emitters explored by Hanbury Brown-Twiss scanning tunnelling microscopy”. In: *Nature Communications* 6 (2015), pp. 1–6. ISSN: 20411723. DOI: 10.1038/ncomms9461.

[77] Pablo Merino et al. “A Single Hydrogen Molecule as an Intensity Chopper in an Electrically Driven Plasmonic Nanocavity”. In: *Nano Lett.* 19.1 (2019), pp. 235–241. DOI: 10.1021/acs.nanolett.8b03753. eprint: https://doi.org/10.1021/acs.nanolett.8b03753. URL: https://doi.org/10.1021/acs.nanolett.8b03753.

[78] Andrey E. Miroshnichenko, Sergej Flach, and Yuri S. Kivshar. “Fano resonances in nanoscale structures”. In: *Rev. Mod. Phys.* 82 (3 Aug. 2010), pp. 2257–2298. DOI: 10.1103/RevModPhys.82.2257. URL: https://link.aps.org/doi/10.1103/RevModPhys.82.2257.

[79] Kuniyuki Miwa et al. “Effects of molecule-insulator interaction on geometric property of a single phthalocyanine molecule adsorbed on an ultrathin NaCl film”. In: *Phys. Rev. B* 93 (16 Apr. 2016), p. 165419. DOI: 10.1103/PhysRevB.93.165419. URL: https://link.aps.org/doi/10.1103/PhysRevB.93.165419.

[80] Kuniyuki Miwa et al. “Many-Body State Description of Single-Molecule Electroluminescence Driven by a Scanning Tunneling Microscope”. In: *Nano Lett.* 19.5 (2019), pp. 2803–2811. DOI: 10.1021/acs.nanolett.8b04484. eprint: https://doi.org/10.1021/acs.nanolett.8b04484. URL: https://doi.org/10.1021/acs.nanolett.8b04484.

[81] W. E. Moerner and L. Kador. “Optical detection and spectroscopy of single molecules in a solid”. In: *Phys. Rev. Lett.* 62 (21 May 1989), pp. 2535–2538. DOI: 10.1103/PhysRevLett.62.2535. URL: https://link.aps.org/doi/10.1103/PhysRevLett.62.2535.

[82] W. E. Moerner and Michel Orrit. “Illuminating Single Molecules in Condensed Matter”. In: *Science* 283.5408 (1999), pp. 1670–1676. ISSN: 0036-8075. DOI: 10.1126/science.283.5408.1670. eprint: https://science.sciencemag.org/content/283/5408/1670.full.pdf. URL: https://science.sciencemag.org/content/283/5408/1670.

[83] Ciaran Murray et al. “Visible luminescence spectroscopy of free-base and zinc phthalocyanines isolated in cryogenic matrices”. In: *Phys. Chem. Chem. Phys.* 13 (39 2011), pp. 17543–17554. DOI: 10.1039/C1CP22039J. URL: http://dx.doi.org/10.1039/C1CP22039J.

[84] A V Naumov. "Low-temperature spectroscopy of organic molecules in solid matrices: from the Shpol'skii effect to laser luminescent spectromicroscopy for all effectively emitting single molecules". In: *Physics-Uspekhi* 56.6 (2013), p. 605. URL: `http://stacks.iop.org/1063-7869/56/i=6/a=605`.

[85] Tomáš Neuman et al. "Coupling of Molecular Emitters and Plasmonic Cavities beyond the Point-Dipole Approximation". In: *Nano Letters* 18.4 (2018), pp. 2358–2364. ISSN: 15306992. DOI: `10.1021/acs.nanolett.7b05297`.

[86] Tebello Nyokong, Zbigniew Gasyna, and Martin J. Stillman. "Phthalocyanine .pi.-cation-radical species: photochemical and electrochemical preparation of [ZnPc(-1).+ in solution". In: *Inorganic Chemistry* 26.4 (1987), pp. 548–553. DOI: `10.1021/ic00251a012`. eprint: `http://dx.doi.org/10.1021/ic00251a012`. URL: `http://dx.doi.org/10.1021/ic00251a012`.

[87] M. Orrit and J. Bernard. "Single pentacene molecules detected by fluorescence excitation in a p-terphenyl crystal". In: *Phys. Rev. Lett.* 65 (21 Nov. 1990), pp. 2716–2719. DOI: `10.1103/PhysRevLett.65.2716`. URL: `https://link.aps.org/doi/10.1103/PhysRevLett.65.2716`.

[88] K. Perronet et al. "Single-molecule fluctuations in a tunnel junction: A study by scanning-tunnelling-microscopyï¿½induced luminescence". In: *EPL (Europhysics Letters)* 74.2 (2006), p. 313. URL: `http://stacks.iop.org/0295-5075/74/i=2/a=313`.

[89] J M Pitarke et al. "Theory of surface plasmons and surface-plasmon polaritons". In: *Reports on Progress in Physics* 70.1 (Dec. 2006), pp. 1–87. DOI: `10.1088/0034-4885/70/1/r01`. URL: `https://doi.org/10.1088%2F0034-4885%2F70%2F1%2Fr01`.

[90] E. Prodan et al. "A Hybridization Model for the Plasmon Response of Complex Nanostructures". In: *Science* 302.5644 (2003), pp. 419–422. ISSN: 0036-8075. DOI: `10.1126/science.1089171`. eprint: `https://science.sciencemag.org/content/302/5644/419.full.pdf`. URL: `https://science.sciencemag.org/content/302/5644/419`.

[91] E. M. Purcell, H. C. Torrey, and R. V. Pound. "Resonance Absorption by Nuclear Magnetic Moments in a Solid". In: *Phys. Rev.* 69 (1-2 Jan. 1946), pp. 37–38. DOI: `10.1103/PhysRev.69.37`. URL: `https://link.aps.org/doi/10.1103/PhysRev.69.37`.

[92] X. H. Qiu, G. V. Nazin, and W. Ho. "Vibrationally Resolved Fluorescence Excited with Submolecular Precision". In: *Science* 299.5606 (2003), pp. 542–546. ISSN: 0036-8075. DOI: `10.1126/science.1078675`. eprint: `https://science.sciencemag.org/content/299/5606/542.full.pdf`. URL: `https://science.sciencemag.org/content/299/5606/542`.

[93] "Quantum electrodynamics at room temperature coupling a single vibrating molecule with a plasmonic nanocavity". In: *Nature Communications* 10.1 (2019), pp. 1–7. ISSN: 20411723. DOI: `10.1038/s41467-019-08611-5`. URL: `http://dx.doi.org/10.1038/s41467-019-08611-5`.

[94] "Quantum mechanical effects in plasmonic structures with subnanometre gaps". In: *Nature Communications* 7 (2016). ISSN: 20411723. DOI: `10.1038/ncomms11495`.

[95] H. Raether. "Surface plasmons". In: ().

[96] Gaël Reecht et al. "Electroluminescence of a Polythiophene Molecular Wire Suspended between a Metallic Surface and the Tip of a Scanning Tunneling Microscope". In: *Phys. Rev. Lett.* 112 (4 Jan. 2014), p. 047403. DOI: `10.1103/PhysRevLett.112.047403`. URL: `https://link.aps.org/doi/10.1103/PhysRevLett.112.047403`.

[97] R. W. Rendell and D. J. Scalapino. "Surface plasmons confined by microstructures on tunnel junctions". In: *Phys. Rev. B* 24 (6 Sept. 1981), pp. 3276–3294. DOI: `10.1103/PhysRevB.24.3276`. URL: `https://link.aps.org/doi/10.1103/PhysRevB.24.3276`.

[98] R. W. Rendell, D. J. Scalapino, and B. Mühlschlegel. "Role of Local Plasmon Modes in Light Emission from Small-particle Tunnel Junctions". In: *Phys. Rev. Lett.* 41 (25 Dec. 1978), pp. 1746–1750. DOI: `10.1103/PhysRevLett.41.1746`. URL: `https://link.aps.org/doi/10.1103/PhysRevLett.41.1746`.

[99] Jascha Repp et al. "Controlling the Charge State of Individual Gold Adatoms". In: *Science* 305.5683 (2004), pp. 493–495. ISSN: 0036-8075. DOI: `10.1126/science.1099557`. eprint: `http://science.sciencemag.org/content/305/5683/493.full.pdf`. URL: `http://science.sciencemag.org/content/305/5683/493`.

[100] Jascha Repp et al. "Imaging Bond Formation Between a Gold Atom and Pentacene on an Insulating Surface". In: *Science* 312.5777 (2006), pp. 1196–1199. ISSN: 0036-8075. DOI: `10.1126/science.1126073`. eprint: `https://science.sciencemag.org/content/312/5777/1196.full.pdf`. URL: `https://science.sciencemag.org/content/312/5777/1196`.

[101] Jascha Repp et al. "Molecules on Insulating Films: Scanning-Tunneling Microscopy Imaging of Individual Molecular Orbitals". In: *Phys. Rev. Lett.* 94 (2 Jan. 2005), p. 026803. DOI: `10.1103/PhysRevLett.94.026803`. URL: `https://link.aps.org/doi/10.1103/PhysRevLett.94.026803`.

[102] Angela Rosa and Giampaolo Ricciardi. "A time-dependent density functional theory (TDDFT) interpretation of the optical spectra of zinc phthalocyanine $\pi$-cation and $\pi$-anion radicals". In: *Canadian Journal of Chemistry* 87.7 (2009), pp. 994–1005. DOI: `10.1139/V09-066`. eprint: `https://doi.org/10.1139/V09-066`. URL: `https://doi.org/10.1139/V09-066`.

[103] F. Rossel, M. Pivetta, and W.-D. Schneider. "Luminescence experiments on supported molecules with the scanning tunneling microscope". In: *Surface Science Reports* 65.5 (2010), pp. 129–144. DOI: `10.1016/j.surfrep.2010.06.001`. URL: `http://infoscience.epfl.ch/record/161535`.

[104] Mikhail V. Rybin et al. “Purcell effect and Lamb shift as interference phenomena”. In: *Scientific Reports* 6.October 2015 (2016), pp. 1–9. ISSN: 20452322. DOI: 10.1038/srep20599.

[105] K. Sakamoto et al. “Light emission spectra of the monolayer-island of C60 molecules on Au(111) induced by scanning tunneling microscope”. In: *Surface Science* 502-503 (2002), pp. 149–155. ISSN: 0039-6028. DOI: https://doi.org/10.1016/S0039-6028(01)01924-0. URL: http://www.sciencedirect.com/science/article/pii/S0039602801019240.

[106] Kevin J. Savage et al. “Revealing the quantum regime in tunnelling plasmonics”. In: *Nature* 491.7425 (2012), pp. 574–577. ISSN: 00280836. DOI: 10.1038/nature11653.

[107] N. L. Schneider et al. “Light emission from a double-decker molecule on a metal surface”. In: *Phys. Rev. B* 84 (15 Oct. 2011), p. 153403. DOI: 10.1103/PhysRevB.84.153403. URL: https://link.aps.org/doi/10.1103/PhysRevB.84.153403.

[108] Natalia L. Schneider and Richard Berndt. “Plasmonic excitation of light emission and absorption by porphyrine molecules in a scanning tunneling microscope”. In: *Phys. Rev. B* 86 (3 July 2012), p. 035445. DOI: 10.1103/PhysRevB.86.035445. URL: https://link.aps.org/doi/10.1103/PhysRevB.86.035445.

[109] Tigran V. Shahbazyan. “Exciton–Plasmon Energy Exchange Drives the Transition to a Strong Coupling Regime”. In: *Nano Letters* 19.5 (2019). PMID: 30973738, pp. 3273–3279. DOI: 10.1021/acs.nanolett.9b00827. eprint: https://doi.org/10.1021/acs.nanolett.9b00827. URL: https://doi.org/10.1021/acs.nanolett.9b00827.

[110] “Single molecule SERS and detection of biomolecules with a single gold nanoparticle on a mirror junction”. In: *Analyst* 138.16 (2013), pp. 4574–4578. ISSN: 13645528. DOI: 10.1039/c3an00447c.

[111] “Single-molecule optomechanics in "picocavities"”. In: *Science* 354.6313 (2016), pp. 726–729. ISSN: 10959203. DOI: 10.1126/science.aah5243.

[112] I.I. Smolyaninov. “Photon emission from a layer of copper phthalocyanine molecules on a gold (111) film surface induced by STM”. In: *Surface Science* 364.1 (1996), pp. 79–88. ISSN: 0039-6028. DOI: https://doi.org/10.1016/0039-6028(96)00581-X. URL: http://www.sciencedirect.com/science/article/pii/003960289600581X.

[113] William A. Steen, Kavita M. Jeerage, and Daniel T. Schwartz. “Raman Spectroscopy of Redox Activity in Cathodically Electrodeposited Nickel Hexacyanoferrate Thin Films”. In: *Appl. Spectrosc.* 56.8 (Aug. 2002), pp. 1021–1029. URL: http://as.osa.org/abstract.cfm?URI=as-56-8-1021.

[114] W. Steurer et al. “Manipulation of the Charge State of Single Au Atoms on Insulating Multilayer Films”. In: *Phys. Rev. Lett.* 114 (3 Jan. 2015), p. 036801. DOI: 10.1103/PhysRevLett.114.036801. URL: https://link.aps.org/doi/10.1103/PhysRevLett.114.036801.

[115] Ingmar Swart, Tobias Sonnleitner, and Jascha Repp. “Charge State Control of Molecules Reveals Modification of the Tunneling Barrier with Intramolecular Contrast”. In: *Nano Letters* 11.4 (2011). PMID: 21428431, pp. 1580–1584. DOI: `10.1021/nl104452x`. eprint: `http://dx.doi.org/10.1021/nl104452x`. URL: `http://dx.doi.org/10.1021/nl104452x`.

[116] Ingmar Swart et al. “Controlled lateral manipulation of molecules on insulating films by STM”. In: *Nano Letters* 12.2 (2012), pp. 1070–1074. ISSN: 15306984. DOI: `10.1021/nl204322r`.

[117] C. Cohen Tannoudji, B. Diu, and F. Laloé. *Mecanique Quantique*. Hermann, 1997.

[118] J. Tersoff and D. R. Hamann. “Theory of the scanning tunneling microscope”. In: *Phys. Rev. B* 31 (2 Jan. 1985), pp. 805–813. DOI: `10.1103/PhysRevB.31.805`. URL: `https://link.aps.org/doi/10.1103/PhysRevB.31.805`.

[119] Sol Triebwasser, Edward S. Dayhoff, and Willis E. Lamb. “Fine Structure of the Hydrogen Atom. V”. In: *Phys. Rev.* 89 (1 Jan. 1953), pp. 98–106. DOI: `10.1103/PhysRev.89.98`. URL: `https://link.aps.org/doi/10.1103/PhysRev.89.98`.

[120] Vladimir A. Ukraintsev. “Data evaluation technique for electron-tunneling spectroscopy”. In: *Phys. Rev. B* 53 (16 Apr. 1996), pp. 11176–11185. DOI: `10.1103/PhysRevB.53.11176`. URL: `https://link.aps.org/doi/10.1103/PhysRevB.53.11176`.

[121] Mattin Urbieta et al. “Atomic-Scale Lightning Rod Effect in Plasmonic Picocavities: A Classical View to a Quantum Effect”. In: *ACS Nano* 12.1 (2018). PMID: 29298379, pp. 585–595. DOI: `10.1021/acsnano.7b07401`. eprint: `https://doi.org/10.1021/acsnano.7b07401`. URL: `https://doi.org/10.1021/acsnano.7b07401`.

[122] Silvia Völker and J.H. van der Waals. “Laser-induced photochemical isomerization of free base porphyrin in an n-octane crystal at 4.2 K”. In: *Mol. Phys.* 32.6 (1976), pp. 1703–1718. DOI: `10.1080/00268977600103021`. eprint: `https://doi.org/10.1080/00268977600103021`. URL: `https://doi.org/10.1080/00268977600103021`.

[123] T Wang et al. “Excitation of propagating surface plasmons with a scanning tunnelling microscope”. In: *Nanotechnology* 22.17 (Mar. 2011), p. 175201. DOI: `10.1088/0957-4484/22/17/175201`. URL: `https://doi.org/10.1088%2F0957-4484%2F22%2F17%2F175201`.

[124] Martin Wersäll et al. “Observation of Mode Splitting in Photoluminescence of Individual Plasmonic Nanoparticles Strongly Coupled to Molecular Excitons”. In: *Nano Letters* 17.1 (2017). PMID: 28005384, pp. 551–558. DOI: `10.1021/acs.nanolett.6b04659`. eprint: `https://doi.org/10.1021/acs.nanolett.6b04659`. URL: `https://doi.org/10.1021/acs.nanolett.6b04659`.

[125] R. Wiesendanger. “Spin mapping at the nanoscale and atomic scale”. In: *Rev. Mod. Phys.* 81 (2009), p. 1495.

[126] Katherine A. Willets and Richard P. Van Duyne. “Localized Surface Plasmon Resonance Spectroscopy and Sensing”. In: *Annual Review of Physical Chemistry* 58.1 (2007), pp. 267–297. DOI: 10.1146/annurev.physchem.58.032806.104607. URL: https://doi.org/10.1146/annurev.physchem.58.032806.104607.

[127] S. W. Wu, G. V. Nazin, and W. Ho. “Intramolecular photon emission from a single molecule in a scanning tunneling microscope”. In: *Phys. Rev. B* 77 (20 May 2008), p. 205430. DOI: 10.1103/PhysRevB.77.205430. URL: https://link.aps.org/doi/10.1103/PhysRevB.77.205430.

[128] S. W. Wu, N. Ogawa, and W. Ho. “Atomic-Scale Coupling of Photons to Single-Molecule Junctions”. In: *Science* 312.5778 (2006), pp. 1362–1365. ISSN: 0036-8075. DOI: 10.1126/science.1124881. eprint: http://science.sciencemag.org/content/312/5778/1362.full.pdf. URL: http://science.sciencemag.org/content/312/5778/1362.

[129] Yang Zhang et al. In: *Nature* 22.2 (2016), pp. 137–141. ISSN: 10282092. DOI: 10.1007/s13398-014-0173-7.2.

[130] Stephanie Zaleski et al. “Observing Single, Heterogeneous, One-Electron Transfer Reactions”. In: *J. Phys. Chem. C* 119 (2015), p. 28226.

[131] Anatoly V. Zayats, Igor I. Smolyaninov, and Alexei A. Maradudin. “Nano-optics of surface plasmon polaritons”. In: *Physics Reports* 408.3 (2005), pp. 131–314. ISSN: 0370-1573. DOI: https://doi.org/10.1016/j.physrep.2004.11.001. URL: http://www.sciencedirect.com/science/article/pii/S0370157304004600.

[132] Li Zhang et al. “Electrically driven single-photon emission from an isolated single molecule”. In: *Nature Communications* 8.1 (2017), pp. 1–7. ISSN: 20411723. DOI: 10.1038/s41467-017-00681-7. URL: http://dx.doi.org/10.1038/s41467-017-00681-7.

[133] R Zhang et al. “Chemical mapping of a single molecule by plasmon-enhanced Raman scattering.” In: *Nature* 498.7452 (2013), pp. 82–6. DOI: 10.1038/nature12151. URL: http://www.ncbi.nlm.nih.gov/pubmed/23739426.

[134] Yao Zhang et al. “Sub-nanometre control of the coherent interaction between a single molecule and a plasmonic nanocavity”. In: *Nature Communications* 8.May (2017), pp. 1–7. ISSN: 20411723. DOI: 10.1038/ncomms15225. URL: http://dx.doi.org/10.1038/ncomms15225.

# List of Figures

1 Carte HRFM de la raie $Q_x$ de fluorescence de la molécule de $H_2Pc$ 7

1.1 STM image of the surface reconstruction of Si(111) with STM . . 21
1.2 Description by Binnig and Rohrer of the working principle of the STM. . . . . 22
1.3 Origin and description of the tunnel current. . . . . 22
1.4 Electronic standing waves probed by STM. . . . . 24
1.5 Description of a STM junction and model of Bardeen. . . . . 24
1.6 Sketch of the tip geometry assumed by Tersoff and Hamann. . . 29
1.7 Description of a metal-metal tunnel junction. . . . . 31
1.8 Operation of STM imaging. . . . . 33
1.9 Tunneling through molecular orbitals. . . . . 34
1.10 Voltage dependency of STM images. . . . . 34
1.11 Scheme of the LT-STM Omicron. . . . . 36
1.12 **Sketch of the optical setup.** . . . . . 38
1.13 Transmission and efficiency of the optical components. . . . . 39
1.14 Comparison of the three different gratings. . . . . 40

2.1 Light emission from a metal-insulator-metal junction. . . . . 44
2.2 Influence of the tip shape and composition of the STM junction on the STM-LE spectrum. . . . . 45
2.3 Description of the Surface Plasmon Polariton (SPP). . . . . 46
2.4 Dispersion relation of SPP (dark line). . . . . 47
2.5 Description of Localized Surface Plasmons confined in the sub-wavelength size tip apex. . . . . 48
2.6 Formation of nanocavity plasmons. . . . . 49
2.7 Light emission process in a metal-metal junction. . . . . 50
2.8 Decay of a molecular excitation in a plasmonic nanocavity. . . . 51
2.9 STM-LE on $C_{60}$ molecules adsorbed on a Au(111) surface. . . . . 53
2.10 Timeline of STM-Induced single molecule fluorescence experiments. . . . . 56
2.11 Coherent dipole-dipole coupling. . . . . 58
2.12 Evolution of the lowest energy coupling mode as a function of the number of molecules. . . . . 59
2.13 Intermolecular energy transfer via dipole-dipole interaction. . . 60
2.14 Energy transfer controlled with dipoles respective orientations. 61
2.15 Investigation of the NCP-exciton interaction as a function of the tip-molecule distance . . . . . 62
2.16 Observation of Fano resonance. . . . . 63
2.17 Single photon emission from a $ZnPc$ molecule. . . . . 65
2.18 Carrier injection mechanism at negative bias voltage. . . . . 66

2.19 Energy transfer mechanism . . . . . . . . . . . . . . . . . . . . . . . 67
2.20 STM-LE of a single $H_2Pc$ molecule as a function of the voltage. . 68

3.1 STM measurement on $\mathrm{H_2Pc}$ molecules decoupled from a Ag(111) substrate by a thin layer of NaCl. . . . . . . . . . . . . . . . . . . 72
3.2 STM-F spectroscopy of individual $\mathrm{H_2Pc}$ molecules . . . . . . . . 74
3.3 Spatial mapping of the fluorescence signal. . . . . . . . . . . . . . 75
3.4 Fluorescence process in a STM junction . . . . . . . . . . . . . . . 76
3.5 Description of the emission process . . . . . . . . . . . . . . . . . 79
3.6 Modelisation of the $Q_x$ photon map . . . . . . . . . . . . . . . . . 80
3.7 Identification of the two tautomers with Hyper-Resolved Fluorescence Microscopy. . . . . . . . . . . . . . . . . . . . . . . . . 82
3.8 Temporal tracking of the tautomerization process . . . . . . . . 84
3.9 Description of the three different behaviours observed in the STM-F spectra. . . . . . . . . . . . . . . . . . . . . . . . . . . . . 86
3.10 Influence of the molecule position on the Moiré pattern. . . . . . 88
3.11 Evolution of the tautomerization switching rate as a function of the current. . . . . . . . . . . . . . . . . . . . . . . . . . . . . 90
3.12 Voltage onset of the tautomerization process. . . . . . . . . . . . 92
3.13 Interface state on NaCl. . . . . . . . . . . . . . . . . . . . . . . . 93
3.14 Properties of the naphthalocyanine molecule ($\mathrm{H_2Nc}$). . . . . . . 94
3.15 Comparison between $\mathrm{H_2Pc}$ and $\mathrm{H_2Nc}$ . . . . . . . . . . . . . . . 95

4.1 Description of the system . . . . . . . . . . . . . . . . . . . . . . 99
4.2 Building ZnPc oligomers with tip manipulation . . . . . . . . . . 100
4.3 Narrow line emission from oligomer excitonic states. . . . . . . 101
4.4 Assignments of the vibronic lines. . . . . . . . . . . . . . . . . . 103
4.5 Spatial variation of the supra-molecular exciton emission . . . . 105
4.6 Hyper-Resolved Fluorescence Microscopy on the four excitonic coupling modes . . . . . . . . . . . . . . . . . . . . . . . . . . . 106
4.7 Impact of the excitonic coupled modes on the vibronic signal . . 108
4.8 Spatial variation of the vibronic signal. . . . . . . . . . . . . . . . 110
4.9 Vibrational signature of the $\mathrm{H_2Pc}$ tautomers revealed by HRFM 115

5.1 STM-F spectroscopy of the two redox states of a single ZnPc molecule . . . . . . . . . . . . . . . . . . . . . . . . . . . . . . 119
5.2 Vibronic fingerprint of the two redox species . . . . . . . . . . . 122
5.3 Influence of the insulator thickness on the otpical response of the two redox species . . . . . . . . . . . . . . . . . . . . . . . . . 124
5.4 Influence of the NCP on the optical response of the two redox species . . . . . . . . . . . . . . . . . . . . . . . . . . . . . . . 125
5.5 Voltage dependency of the $X^0$ and $X^+$ lines on Au(111) and Ag(111) substrate. . . . . . . . . . . . . . . . . . . . . . . . . . 127
5.6 Current dependency of the $X^0$ and $X^+$ lines on Au(111) and Ag(111) substrate. . . . . . . . . . . . . . . . . . . . . . . . . . 129
5.7 Emission regimes as a function of the voltage polarity . . . . . . 132
5.8 Evolution of the plasmon-exciton coupling as a function of the tip-molecule lateral distance. . . . . . . . . . . . . . . . . . . . . 134

5.9 Phenomenological model . . . . . . . . . . . . . . . . . . . . . . 135

# Publications and presentations

## Publications

- **B. Doppagne**, M. C. Chong, E. Lorchat, S. Berciaud, M. Romeo, H. Bulou, A. Boeglin, F. Scheurer, and G. Schull.

  *Vibronic spectroscopy with submolecular resolution from STM-Induced electroluminescence*

  **Phys. Rev. Lett. 118**, 127401 (2017)

- J. Kroeger, **B. Doppagne**, F. Scheurer, and G. Schull.

  *Fano description of single-hydrocarbon fluorescence excited by a scanning tunneling microscope*

  **Nano Letters 18**, 3407 (2018)

- **B. Doppagne**, M. C. Chong, H. Bulou, A. Boeglin, F. Scheurer, and G. Schull.

  *Electrofluorochromism at the single-molecule level*

  **Science 361**, 251-255 (2018)

- **B. Doppagne**, T. Neuman, R. Soria Martinez, L. E. Parra Lopez, H. Bulou, M. Romeo, S. Berciaud, F. Scheurer, J. Aizpurua, and G. Schull.

  *Single-molecule tautomerization tracking through space- and time-resolved fluorescence spectroscopy*

  **Nature Nanotechnology 15**, 207-211 (2020)

# Presentations

- ORAL PRESENTATION: **B. Doppagne**, M. C. Chong, E. Lorchat, S. Berciaud, M. Romeo, H. Bulou, A. Boeglin, F. Scheurer, and G. Schull.

  *Fluorescence de molécules uniques induite par STM : Vers une spectroscopie vibrationnelle de résolution spatiale sub-moléculaire*

  **Forum des microscopies à sonde locale** Montpellier, France (2017)

- POSTER: **B. Doppagne**, M. C. Chong, E. Lorchat, S. Berciaud, M. Romeo, H. Bulou, A. Boeglin, F. Scheurer, and G. Schull.

  *Vibronic Spectroscopy with Submolecular Resolution from STM-Induced Electroluminescence*

  **654. WE-Heraeus-Seminar "Topical insights into nanoscience using scanning probes"** Bad Honnef, Germany (2017)

- ORAL PRESENTATION: **B. Doppagne**, M. C. Chong, E. Lorchat, S. Berciaud, M. Romeo, H. Bulou, A. Boeglin, F. Scheurer, and G. Schull.

  *Vibronic Spectroscopy with Submolecular Resolution from STM-Induced Electroluminescence*

  **Conference Nanolight** Benasque, Spain (2018)

- ORAL PRESENTATION: **B. Doppagne**, M.C. Chong, T. Neuman, L. Parra-Lopez, E. Lorchat, S. Berciaud, M. Romeo, H. Bulou, A. Boeglin, F. Scheurer, J. Aizpurua and Guillaume Schull.

  *Fluorescence de molécules uniques induite par STM : Vers une spectroscopie de fluorescence hyper-résolue*

  **Forum des microscopies à sonde locale** Marseille, France (2019)

- POSTER: **B. Doppagne**, M.C. Chong, T. Neuman, L. Parra-Lopez, E. Lorchat, S. Berciaud, M. Romeo, H. Bulou, A. Boeglin, F. Scheurer, J. Aizpurua and Guillaume Schull.

  *Hyper-resolved fluorescence microscopy*

  **704. WE-Heraeus-Seminar "Exploring the Limits of Nanoscience with Scanning Probe Methods"** Bad Honnef, Germany (2019)

**Benjamin DOPPAGNE**

# Hyper-Resolved Fluorescence Microscopy with STM

## Résumé

Dans cette thèse, je rapporte l'utilisation d'un microscope à effet tunnel (STM) pour obtenir le spectre de fluorescence d'une molécule unique, et ainsi s'affranchir des limites inhérentes aux techniques optiques conventionnelles. Cette technique repose sur l'utilisation des électrons tunnels comme source d'excitation, et l'amplification de l'émission par les modes électromagnétiques de la cavité, formé par la pointe STM et la surface, appelés plasmons de gap. Les résultats de cette thèse, confirment que ces modes sont fortement localisés dans des volumes de l'ordre du nm$^3$, ce qui permet de pratiquer une « imagerie optique » à l'échelle sub-moléculaire. Cette technique de Microscopie de Fluorescence Hyper-Résolue nous a permis i) De suivre avec une résolution spatiale, spectrale et temporelle un processus de tautomerisation, ii) De mesurer une signature vibrationnelle résolue à l'échelle sub-moléculaire et iii) De suivre l'état redox d'une unique molécule via son signal optique.

Mots clés : STM ; Plasmonique ; Nano-optique ; Fluorescence ; Molécule unique ; Tautomerisation ; Etat redox ; Spectrocopie vibrationelle ; Electrofluorochromisme

## Résumé en anglais

In this thesis, I report the use a Scanning Tunneling Microscope to obtain the fluorescence spectrum of a single molecule, to go beyond the limitations commonly observed in conventionnal optical techniques. This technique relies on the use of tunneling electrons to excite the fluorescence of a molecule, which is amplified by electromagnetic modes of the cavity, formed by the tip and the sample, knows as gap plasmons. The results of this thesis, confirm that these modes are strongly localized within volumes of the order of 1 nm$^3$, allowing to carried out « optical imaging » at the sub-molecular scale. This Hyper-Resolved Fluorescence Microscopy technique allowed us i) To track with : spatial, spectral and temporal resolution a tautomerization process, ii) To measure a vibrationnal signature with sub-molecular resolution, and iii) To monitor the fluorescnece of a single molecule redox state.

Keywords : STM ; Plasmonics ; Nano-optics ; Fluorescence ; Single Molecule ; Tautomerization ; Redox state ; Vibrationnal spectroscopy, Electrofluorochromism